1st International Conference on

# 3DMS

3D Materials Science, 2012

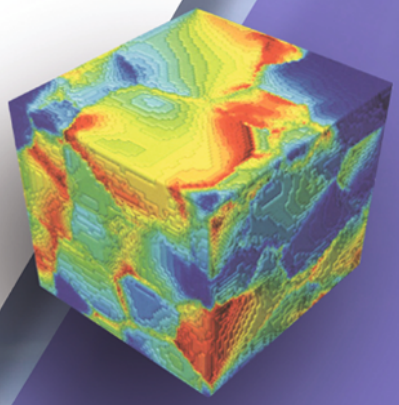

July 8-12, 2012 • Seven Springs Mountain Resort
Seven Springs, Pennsylvania, USA

## Conference Proceedings


**Edited by:**

Marc De Graef
Henning Friis Poulsen
Alexis Lewis
Jeff Simmons
George Spanos



Springer

TMS

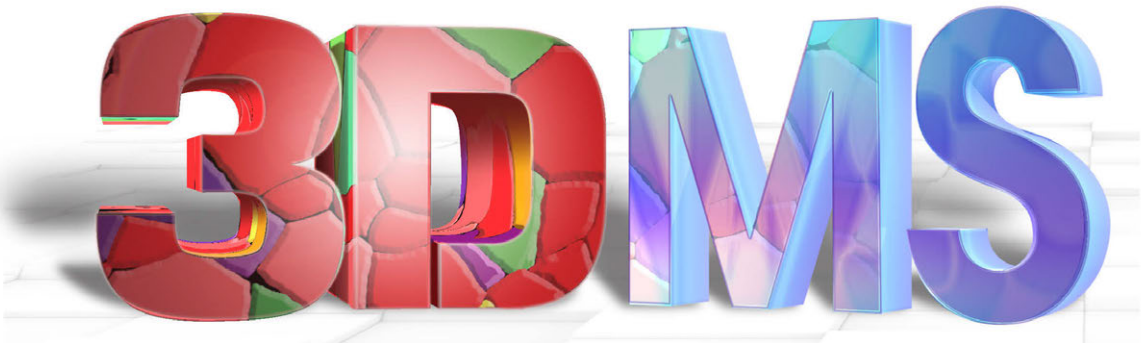


## Proceedings of the

# 1st International Conference on 3D Materials Science

***Held***

July 8-12, 2012

Seven Springs Mountain Resort

Seven Springs, Pennsylvania, USA

***Edited by***

Marc De Graef, Henning Friis Poulsen, Alexis Lewis,

Jeff Simmons, George Spanos

*Editors*
Marc De Graef
Henning Friis Poulsen
Alexis Lewis
Alexis Lewis
George Spanos

ISBN 978-3-319-48573-7 ISBN 978-3-319-48762-5 (eBook)
DOI 10.1007/978-3-319-48762-5

Chemistry and Materials Science: Professional


Published by Springer International Publishers, Switzerland, 2016
Reprint of the original edition published by John Wiley & Sons, Inc., 2012, 978-1-11847-039-8



Printed on acid-free paper

This Springer imprint is published by Springer Nature
The registered company is Springer International Publishing AG
The registered company address is: Gewerbestrasse 11, 6330 Cham, Switzerland

# TABLE OF CONTENTS
# 1st International Conference on 3D Materials Science

Preface ..... ix
About the Conference Editors/Organizers ..... xi
Organizers ..... xiii

## Perspectives on 3D Materials Science

Perspectives on Materials Science in 3D ..... 1
*D. Jensen*

## 3D Microstructure-Property Relationships

3D Investigation of Cracking Behavior in a Ni Superalloy ..... 13
*A. Deal, D. Rowenhorst, B. Laflen, I. Spinelli, T. Barbuto, Y. Huang, and T. Hanlon*

On the Three-dimensional Microstructure of Martensite in Carbon Steels ..... 19
*P. Hedström, A. Stormvinter, A. Borgenstam, A. Gholinia, B. Winiarski, P. Withers, O. Karlsson, and J. Hagström*

FIB/SEM Determination of Sub-surface Damage Caused by Micro-tribology Scratching of WC/Co Hardmetal Samples ..... 25
*M. Gee, K. Mingard, A. Gant, and H. Jones*

3D Characterization of Recrystallization Boundaries ..... 31
*Y. Zhang, A. Godfrey, N. MacDonald, and D. Juul Jensen*

Development of Fully Automated Serial-sectioning 3D Microscope and Topological Approach to Pearlite and Dual-phase Miscrostructure in Steels ..... 37
*Y. Adachi, N. Sato, M. Ojima, M. Nakayama, and Y. Wang*

Fragmentation of a Steel Ring under Explosive Loading ..... 43
*J. Schreiber, I. Smid, and T. Eden*

Quantifying the Effect of 3D Spatial Resolution on the Accuracy of Microstructural Distributions ..... 49
*G. Loughnane, R. Grandhi, R. Srinivasan, M. Uchic, M. Groeber, M. Riley, and M. Shah*

Three-dimensional Investigation of Void Growth Leading to Fracture in Commercially Pure Titanium ..... 61
*M. Pushkareva, J. Adrien, E. Maire, and A. Weck*

Quantification of Primary Phase Undercooling of Rapidly Solidified Droplets with 3D Microtomography ..... 67
*A. Ilbagi, P. Delshad Khatibi, H. Henein, C. Gandin, and D. Herlach*

3D Microstructural Architectures for Metal and Alloy Components Fabricated by 3D Printing/Additive Manufacturing Technologies ..... 73
*E. Martinez, L. Murr, K. Amato, J. Hernandez, P. Shindo, S. Gaytan, D. Ramirez, F. Medina, and R. Wicker*

Elastic Behavior of the Percolating Eutectic Structure of a High Pressure Die Cast Magnesium Alloy ..... 79
*B. Zhang, A. Nagasekhar, and C. Caceres*

Numerical Simulations of Compression Properties of SiC/Fe-20Cr Co-continuous Composites ..... 85
*L. Yu, Y. Jiang, S. Lu, H. Ru, and M. Fang*

Calculation of Lorentz Force Field of the Innovation Cathode Cell ..... 91
*Y. Jiang, L. Yu, and N. Feng*

Enumeration of Polyhedra for Grain Growth Analysis ..... 97
*T. Keller, B. Cutler, M. Glicksman, and D. Lewis*

Distribution of Carbide Particles and Its Influence on Grain Growth of Ferrite in Fe-C Alloys Containing B and V ..... 107
*T. Oikawa, and M. Enomoto*

Modeling Grain Boundary Interfaces in Pure Nickel ..... 113
*T. Turner, J. Schuren, P. Shade, and M. Groeber*

A Toolbox for Geometric Grain Boundary Characterization ..... 119
*K. Glowinski, and A. Morawiec*

3D Microstructures of $Sb_2Te_3$ Precipitates in PbTe Matrix with Prediction by a Weak Compatibility Condition ..... 125
*X. Chen, S. Cao, T. Ikeda, V. Srivastava, J. Snyder, D. Schryvers, and R. James*

In-situ Characterization of Entrainment Defects in Liquid Al-Si-Mg Alloy ..... 131
*Y. Yue, W. Griffiths, J. Fife, and N. Green*

## Image Processing and Digital Representations of 3D Microstructures

Shape Analysis and Classification of Objects ..... 137
*B. Neal, and J. Russ*

Graph Cut Approaches for Materials Segmentation Preserving Shape, Appearance, and Topology ..... 147
*J. Waggoner, J. Simmons, M. De Graef, and S. Wang*

Fitting Laguerre Tessellations to the Microstructure of Cellular Materials ..... 153
*I. Vecchio, K. Schladitz, and C. Redenbach*

Simulation of FIB-SEM Images for Segmentation of Porous Microstructures ..... 159
*T. Prill, K. Schladitz, and C. Wieser*

Handling Misalignment and Drift in 3D EBSD Data Sets ..... 165
*Y. Huang, B. Laflen, A. Deal, I. Spinelli, A. Barbuto, and T. Hanlon*

Optimizing Stochastic Process for Efficient Microstructure Reconstruction ..... 171
*S. Ryu, and D. Li*

Characterization of Pores and Cracks in Underwater Welds by µCT and Digital Optical Microscopy ..... 177
*S. Paciornik, T. Bernthaler, V. dos Santos, M. Monteiro, M. Mauricio, A. Bracarense, and E. Pessoa*

Characterization of Carbonate Rocks through X-ray Microtomography ..... 183
*D. Pilotto, S. Fontoura, S. Paciornik, and M. Mauricio*

Subgrain Boundary Identification in 3D EBSD Data through Fast Multiscale Clustering ..... 189
*B. Soe, C. McMahon, D. Golay, Z. Quadir, M. Ferry, and L. Bassman*

## Applications of 3D Experimental Techniques Across Length Scales

An Automated Multi-modal Serial Sectioning System for Characterization of Grain-Scale Microstructures in Engineering Materials ..... 195
*M. Uchic, M. Groeber, M. Shah, P. Callahan, A. Shiveley, M. Chapman, M. Scott, and J. Spowart*

Ultra Fast Tomography: New Developments for 4D Studies in Material Science ..... 203
*P. Lhuissier, M. Scheel, M. Di Michiel, E. Boller, J. Adrien, E. Maire, L. Salvo, J. Blandin, and M. Suery*

Three-dimensional Characterization of Dislocation-Defect Interactions ..... 209
*I. Robertson, J. Kacher, and G. Liu*

The Microstructure of RR1000 Nickel-base Superalloy: The FIB-SEM Dual-beam Approach ..... 215
*S. Croxall, M. Hardy, H. Stone, and P. Midgley*

3D Analysis of Phase Separation in Ferritic Stainless Steels ..... 221
*J. Odqvist, J. Zhou, W. Xiong, P. Hedström, M. Thuvander, M. Selleby, and J. Ågren*

Micro-computed Tomography, a 3D Tool for Non-destructive Visualisation and Analysis ..... 227
*E. Bongaers, and R. van den Bosch*

SEM-based Electron Tomography of Turfs Comprised of Lineal Structures ..... 233
*O. Fakron, and D. Field*

Author Index ..... 239

Subject Index ..... 241

# Preface

This volume represents a collection of papers presented at the first International Conference on 3D Materials Science, a specialty conference organized by the Minerals, Metals & Materials Society (TMS) and the conference organizers, and held at Seven Springs Mountain Resort, Seven Springs, Pennsylvania, USA from July 8-12, 2012.

The aim of the first International Conference on 3D Materials Science was to bring together world leaders in the field, at a time when 3D materials characterization and analysis techniques are moving beyond initial qualitative measurements and into an era where full 3D quantification of microstructures is becoming the norm. While many of the early challenges of data collection have been overcome, either by the development of new software and hardware or by automation, new techniques are steadily being introduced and improved upon, and many challenges in the processing, storage, sharing, and analysis of 3D data exist. This workshop sought to bring together the community to share ideas and tools, and to roadmap the future directions of 3D Materials Science.

The conference covered research in Applications of 3D Experimental Techniques across Length Scales (including both Destructive and Non-Destructive techniques), Image Processing of 2D and 3D Microstructural Data, Digital Representations of 3D Microstructures, Storage and Sharing of 3D Data, Microstructure-Property Relationships in 3D, 3D Interfaces and Microstructural Evolution, and Future Directions in 3D Materials Science. The conference included a plenary session and 20 invited presentations from prominent international speakers working in the research areas listed, nearly 60 oral presentations, and nearly 100 poster presentations including a special student poster session. The International Advisory Committee represented 11 countries, and the speakers and poster presenters represented 25 different countries, making this a truly international conference.

This proceedings collection contains high-impact research contributions representing the poster, oral, invited, and plenary sessions. The high quality of the research presented at the conference is reflected in these manuscripts. It is the aim of editors of this volume, the conference organizers, and TMS, that this conference, and the proceedings contained herein, serve to bring together the 3D Materials Science community to maximize cooperative interaction and advance the field in a meaningful way.

# About the Conference Editors/Organizers

## Marc De Graef

Professor Marc De Graef is Professor of Materials Science and Engineering at Carnegie Mellon University in Pittsburgh, PA. He joined the faculty in March 1993 after a post-doctoral period in the Materials Department at the University of California at Santa Barbara. He received his BS and MS degrees in physics from the University of Antwerp (Belgium) in 1983, and his Ph.D. in physics from the Catholic University of Leuven (Belgium) in 1989. He is co-director of the J. Earle and Mary Roberts Materials Characterization Laboratory. He served on the Board of Directors of TMS, received the 2012 TMS Educator Award, and is a Fellow of the Microscopy Society of America. His research interests lie in the area of microstructural characterization of structural intermetallics and magnetic materials, with a strong emphasis on 3-D characterization. His experimental approaches include scanning and transmission electron microscopy, focused ion beam microscopy, and x-ray and electron tomography. On the theoretical side he has an interest in the physics of shapes, and in the quantitative simulation of electron scattering imaging modalities.

## Henning Friis Poulsen

Professor Henning Friis Poulsen joined the section for "neutron and x-ray materials physics" at the Technical University of Denmark in January 2012. Prior to this, Poulsen was a research professor at the Risø National Laboratory for Sustainable Energy in Denmark, where he headed the Centre of Excellence: "metalstructures in four dimensions". His research has focused on the development of synchrotron and TEM based 3D and 4D characterization techniques and their applications within materials science and engineering, in particular metallurgy. He currently holds an Advanced Grant from the European Research Council. Poulsen was granted a Dr. Techn. degree from the Technical University of Denmark in 2004. He received his PhD in Physics from the University of Copenhagen, his MS in Engineering from the Technical University of Denmark and his BS in Mathematics and Physics from the University of Copenhagen.

## Alexis C Lewis

Dr. Alexis C. Lewis is a staff scientist at the US Naval Research Laboratory in Washington, DC, where she began as a National Research Council Postdoctoral Associate in 2003, and was promoted to Materials Research Engineer in 2005. Her research focuses on three-dimensional characterization of materials, with a focus on 3D crystallography, and measuring structure-property relationships through experiment and simulation. Dr. Lewis is the former chair of the TMS Advanced Characterization, Testing, and Simulation committee, as well as a member of the Mechanical Behavior and the Women in Materials Science and Engineering Committee of TMS. She is a member of TMS, ASM and MRS. Dr. Lewis received her SB in Materials Science and Engineering from MIT in 1997, and her PhD in Materials Science and Engineering from the Johns Hopkins University in 2003.

**Jeff Simmons**

Dr. Jeff Simmons is a scientist at the Materials and Manufacturing Directorate of the Air Force Research Laboratory. He has a B.S. degree in Metallurgical Engineering from the New Mexico Institute of Mining and Technology and M.E. and Ph.D. Degrees in Metallurgical Engineering and Materials Science and Materials Science, respectively, from Carnegie Mellon University. After receiving his Ph.D. in 1992, he joined the Materials Directorate at Wright Patterson AFB as a post doctoral researcher and as a research contractor. In 1998, he joined the Air Force Research Laboratory as a research scientist. During his tenure, he has worked on both basic research as well as engineering applications in the aerospace industry. His research interests are in 3-D Materials Science, particularly in development of advanced algorithms for production and analysis of large image datasets. He has published and has organized symposia in the Materials Science and Signal Processing fields on applications of electronic imaging algorithms towards the analysis of digital microscopy. Other research interests have included mathematical representations of microstructures, mesoscale modeling of microstructure development (Phase Field), atomistic modeling of defect properties, and computational thermodynamics. Non-research experience has included leading teams to develop analytical tools for digital data, integration of computer resources for materials simulations, computer security, and network design as well as manufacturing, particularly in machining applications. He has overseen execution of Air Force contracts in Integrated Computational Materials Science and Engineering (ICMSE). Dr. Simmons is a member of the TMS committees of Advanced Characterization, Testing, and Simulations (ACTS) and has served as its chair, Phase Transformations, and Integrated Computational Materials Engineering (ICME). He is a member of TMS, ACM, and the IEEE Computer and Signal Processing Societies.

**George Spanos**

Dr. George Spanos, TMS Technical Director, is responsible for the technical direction of TMS, located at the society's headquarters in Warrendale, PA. In addition, he contributes to the development and execution of the society's strategic plan. He received his B.S. (1982), M.E. (1985) and Ph.D. (1989) degrees in Metallurgical Engineering and Materials Science from Carnegie Mellon University. In 1989 he joined the Naval Research Laboratory (NRL) as a staff scientist, in 1994 was promoted to Section Head (Microstructural Evolution Section) at NRL, and in June of 2010 joined TMS as their Technical Director. Dr. Spanos is author/co-author of 92 technical publications which have been cited more than 1,500 times, in the field of phase transformations, processing-structure-property relationships, 3D materials analyses, and ICME. Some of his past and present professional affiliations include: member of the Board of Governors of Acta Materialia Inc. (2008-2010), past chairman (1999) and member (1996-1999) of the Joint Commission for Metall. and Materials Trans., Chairman (1995-1996) and Key Reader (1992 - present) of the Board of Review of Metall. and Materials Trans. A, and member of a number of TMS committees. Some of his awards include: Fellow of ASM-International (2004), Marcus A. Grossman Award for best article in Metall. and Mat. Trans. for authors under 40 (2001), two Technology Transfer Awards at NRL (2000, 2005), NRL 2009 Commanding Officer's Award for Achievement in Equal Employment Opportunity (EEO).

## Conference Organizers

| | |
|---|---|
| Marc De Graef | Carnegie Mellon University, USA |
| Henning Friis Poulsen | Risø National Laboratory and DTU, Denmark |
| Alexis Lewis | U.S. Naval Research Laboratory, USA |
| Jeff Simmons | U.S Air Force Research Laboratory, USA |
| George Spanos | TMS, USA |

## 3DMS International Advisory Committee

| | |
|---|---|
| Dominique Bernard | ICMCB - Pessac, France |
| Charles Bouman | Purdue University, USA |
| Jean-Yves Buffiere | INSA de Lyon, France |
| Larry Drummy | Air Force Research Laboratory, USA |
| Masato Enomoto | Ibaraki University, Japan |
| Hamish Fraser | Ohio State University, USA |
| Andrew Godfrey | Tsinghua University, China |
| Helio Goldenstein | University of São Paulo, Brazil |
| Dorte Juul-Jensen | Risø/ DTU National Laboratory, Denmark |
| Milo Kral | University of Canterbury, New Zealand |
| Paul Midgely | University of Cambridge, UK |
| Barry Muddle | Monash University, Australia |
| Ty Pollack | AFRL London, UK |
| Claudia Redenbach | University Kaiserslautern, Germany |
| Katja Schladitz | Fraunhofer ITWN, Germany |
| David Seidman | Northwestern University, USA |
| Gary Shiflet | University of Virginia, USA |
| Marco Stampanoni | ETH Zurich, Switzerland |
| Philip Withers | University of Manchester, UK |

1st International Conference on 3D Materials Science
*Edited by: Marc De Graef, Henning Friis Poulsen, Alexis Lewis, Jeff Simmons, George Spanos*
***TMS (The Minerals, Metals & Materials Society), 2012***

# PERSPECTIVES ON MATERIALS SCIENCE IN 3D

D. Juul Jensen

Materials Science and Characterization Section, Department of Wind Energy, Technical University of Denmark, Risø Campus, DK-4000 Roskilde, Denmark

## Keywords

3D techniques, 3DXRD, recrystallization, challenges for 3D science, success of 3D science

## Abstract

Materials characterization in 3D has opened a new era in materials science, which is discussed in this paper. The original motivations and visions behind the development of one of the new 3D techniques, namely the three dimensional x-ray diffraction (3DXRD) method, are presented and the route to its implementation is described. The present status of materials science in 3D is illustrated by examples related to recrystallization. Finally, challenges and suggestions for the future success for 3D Materials Science relating to hardware evolution, data analysis, data exchange and modeling are discussed.

## Materials Science in 3 and 4D

The Materials Science theme generally aims at linking materials processing with materials properties and performances. The key to understanding this link is typically in the materials microstructure, and microscopy, in particular electron microscopy, is by far the most valuable experimental tool for microstructure investigations. All the microscope techniques are by nature 2D (x, y) techniques which actually limit the microstructure information obtained by these methods and have led to misinterpretations and mistakes [e.g. 1]. Transmission electron microscopy does allow 2 ½ D (x, y, thin z section) characterizations both by tomography and diffraction techniques [e.g. 2-4].

Another third dimension, namely time, t, has been studied by electron microscope techniques (x,y,t), so the evolution of a specific microstructure during for example deformation or annealing has been studied by implementing stress rigs and furnaces in the microscope [e.g. 5-7]. Such measurements clearly reveal the microstructural evolution in the sample surface, but uncertainties of course always exist if the observations are affected by the free surface, and bulk phenomena occurring below the inspected surface may suddenly appear – e.g. a nucleus may

form below the surface and grow to be seen in the inspected surface. So clearly 3D (x, y, z) and 4D (x, y, z, t) techniques are the way forward for many types of experiments.

3D techniques are not new. Serial sectioning has been used for decades [e.g. 9, 10], x-ray methods have long been used for local bulk characterization [e.g. 11, 12] and neutron diffraction has been used to determine for example average textures and residual stresses in large bulk sample volumes [e.g. 13, 14].

What is new is that within the last 10-20 years, the scientific community has really realized the need for 3D and 4D techniques and has devoted significant efforts to advance the existing 3D/4D methods and to develop new unique techniques. The goals in these efforts include: much easier, less manpower-requiring operations; better spatial resolution; non-destructive methods; fast measurements. This has led to a whole suite of modern 3D and 4D techniques, and 3D/4D results are reported in more and more publications. The techniques behind the most frequently published 3D/4D results are in two groups: advanced serial sectioning and x-ray methods. The serial sectioning methods encompass semi-automatic and fully automatic mechanical sectioning, which microstructural inspection in optical as well as scanning electron microscopes [e.g. 15-18], high resolution focused ion beam sectioning in the scanning microscope [e.g. 19-20] and sectioning by lasers [21]. The new x-ray methods include three dimensional x-ray diffraction (3DXRD) for fast non-destructive orientation measurements [e.g. 22-24] and 3D polychromatic x-ray micro diffraction for high spatial resolution orientation measurements [25-27] as well as techniques where slits[28] and collimators [29] are used to get the third dimension.

## 3DXRD – From Idea to Implementation

The vision was to develop a technique allowing non-destructive measurements in selected local *µ-sized* volumes within the *bulk* of $mm^3$-$cm^3$ samples. It was motivated by the need to study local deformation and recrystallization phenomena occurring in the bulk *in-situ,* while samples were deformed or annealed. For example for recrystallization (which may be considered as a very well known and well documented process, which is used intensely in the industry) it is remarkable that real key phenomena are not known, e.g. where do the nuclei form and with what crystallographic orientations, how do the annealing-induced boundaries surrounding the nuclei and recrystallizing grains migrate and interact with all the deformation-induced dislocation boundaries and what parameters are of importance here.

A basic requirement for developing a technique to fulfill the described vision is a beam which can penetrate deeply (>1 mm) in materials and which is so intense that even diffraction signals from µ-sized volume elements can be distinguished from the background. High energy x-rays from synchrotrons provide such a beam. When the energy of the x-rays is about 80 keV, the penetration depth (defined as the depth at which the transmitted intensity is 10 %) is 5mm in steel and 4 cm in aluminium. A very intense beam on the sample is obtained by focusing.

For us the route towards the implementation of the vision started by hiring an expert in high energy x-rays (Henning F. Poulsen), who collected the scientific ideas and together with the scientists behind the ideas started to define specifications etc. for the dream 3DXRD instrument. The first paper describing the idea behind the 3DXRD microscope and the first set of preliminary data was published already in 1995 [22]. During the following years, various beam lines at HASYLAB in Hamburg, Germany and at the European Synchrotron Radiation Facility (ESRF) in Grenoble, France were used for further development of the 3DXRD technique and for testing the equipment for different types of experiments [e.g. 30]. Following a workshop held in February 1998 at ESRF on the use of the 3DXRD technique it was decided to build a dedicated hutch (measuring area) for a permanent installation of a 3DXRD microscope at the Materials Science beamline ID11. The agreement was that ESRF should build the hutch with all the necessary installations, while Risø should develop, build and install the microscope. The optics should be developed as a joint-venture. After completion, the 3DXRD microscope should become an ESRF instrument in the sense that potential users may apply for beamtime on it using the regular ESRF application procedure, and that the instrument, therefore, is available to anybody interested having a qualified research proposal.

The 3DXRD microscope was commissioned during the summer 1999 and has been in regular operation ever since. During the recent years, it has been upgraded to obtain finer spatial resolution including moving it to a new experimental hutch. Our group now is not directly involved in the operation of the 3DXRD instrument. We contribute with ideas, some software development and as “large” users via a series of approved so-called long-term proposals, which have allowed us around 4-6 weeks beamtime per year since year 2000.

The described process (from instrument builders to large users) is believed to be optimal as the best operation of beamline instruments is by scientists at the synchrotron and our role is of course to be materials scientists using the 3DXRD for key experiments and ambassadors helping the ESRF staff spreading the knowledge about the 3DXRD’s experimental possibilities.

## Need for 3D and 4D Tools in Recrystallization Studies

Nucleation of recrystallization is very difficult to study experimentally; the nuclei are small and few, so large data sets are typically needed to get statistically sound data. Furthermore, if the issue is to study nucleation sites or orientation relationships between nuclei and parent site in the deformed sample, static 2D measurements suffer from the so-called “lost-evidence” problem [31], namely that when a nucleus is observed with a 2D (x, y) technique, it is impossible to see what was there before the nucleus formed so the exact nucleation site or orientation relationship is unknown. Also results obtained by in-situ annealing measurements in e.g. a SEM (x, y, t) may be problematic to interpret due to surface effects.

So far, few studies have been published on 3D/4D observations of nucleation: The relationship between nuclei and large second phase particles have been quantified by careful serial sectioning of Al-1.2 wt Mn [32] and Al 3004 [18]. In both cases results obtained by 2D methods were confirmed namely that large particles are preferential nucleation sites. However, the agreement is only qualitative in the sense that 2D observations lead to quite different quantitative results than 3D [18]. Serial sectioning was also used to map the spatial distribution of nucleation sites [17], and the results were used as input for modeling of the effects of nuclei clustering on the recrystallization kinetics and grain size distribution. It was shown that even weak clustering has clear effects on both recrystallization kinetics and size distribution [33].

In order to predict the recrystallization texture and understand the various nucleation mechanisms, it is important to know which crystallographic orientations the nuclei have at the various nucleation sites. It is generally assumed that nuclei form with orientations present at the nucleation sites in the deformed state. However, other publications report on formation of nuclei with new orientations which are not seen in the deformed microstructure [e.g. 8, 34-36]. With the classical 2D or the serial sectioning 3D method one can only guess which orientations were present at the exact nucleation sites before the annealing.

Only 4D investigations can quantify if nuclei may form with orientations different from those present at the nucleation sites prior to annealing. 3DXRD has been used for such investigations [37, 38] and it was shown that nuclei with new orientations do form and their orientations cannot be explained by twinning up to second order. The data were analyzed for relationships between the new nuclei orientations and the rotation axis across deformation induced dislocation boundaries in the deformed parent grains. The results suggest that the origin for the formation of nuclei with new orientations relates to the misorientation distribution in the deformed parent grain and that the misorientation axes between a nucleus and the parent grain may be identical to a misorientation axes across dislocation boundaries within that grain [38].

During recrystallization the grains grow by boundary migration through the deformed matrix. Whenever two grains impinge, the boundary motion will stop. Further migration would be defined as grain growth. Generally, it is supposed that the velocity of boundary motion, v, is proportional to the driving force F as expressed by the relationship:

$$v = M F$$

where M is the mobility. For recrystallization, the driving force F is assumed to be given by the stored energy in the deformed microstructure ($F_D$) which typically is orders of magnitude larger than the driving force related to boundary curvature during grain growth. Whereas several grain growth experiments have confirmed the validity of eq (1) [e.g. 39, 40] much less is done for recrystallization. The few recrystallization experiments focusing on this issue have all been done by static stereological 2D characterizations which either confirm eq (1) [e.g. 41, 42] or found a power-law relationship between v and F [43], i.e. another simple relationship.

In-situ 2D investigations during recrystallization as well as ex-situ 2D characterizations of the same surface area after a series of consecutive annealing treatments, however reveal very complex boundary migration and velocities which locally deviate significantly from that predicted using average F and M values in eq (1) [7, 44]. Whether this is a real effect or a consequence of the 2D character of the experiment cannot be proven. 4D (x, y, z, t) experiments are required.

The migration of a boundary surrounding a single recrystallizing grain through a weakly deformed single crystal matrix has been studied in-situ by 3DXRD [45]. These measurements also reveal a very complex boundary migration process. It is found that:

1) Flat facets may form, which migrate forward at the same rate for extended periods of time.

2) The non-faceted segments of the boundary do not migrate at a constant rate through the relatively homogeneous deformed matrix of the single crystal. On the contrary, segments of the boundary move forward for a while then stop, move again etc. (stop-go motion).

3) Local protrusions and retrusions typically form locally on the migrating boundary.

As these results are observed directly in 4D, they cannot be due to experimental artifacts. Standard recrystallization theories and models (e.g. eq (1)) do not describe the 4D results well and have to be revised. For this purpose the 3DXRD measurements have to be supplemented by detailed microscopical investigations in order to understand what is going on. An example of some of this work is given elsewhere in these proceedings [43]. Also an experiment has been performed using the 3D polychromatic x-ray micro diffraction method at APS. This technique has a much better spatial resolution than the 3DXRD and thus allows for direct observations of effects of the local deformed microstructure on migration of recrystallization boundaries, which is considered instrumental for establishment of improved recrystallization theories and models.

## Challenges and Suggestions for the Future Success of 3D Materials Science

Indication of success for 3D/4D characterizations already exist; i) results have been published which prove that 2D is not enough and some new physical mechanisms have been suggested based on 3D/4D data, ii) several of the experimental techniques have been further advanced and can now be considered as relatively mature and iii) the 3D/4D community is growing from the initial stage when it was mostly the group(s) behind a given technique, who was using that technique.
There is still, however, a long way to go before 3D/4D will be widely used. This is not unusual, and history has shown that some degree of commercialization often is needed. The electron back scattering pattern (EBSP) technique for example was developed over many years in individual

universities/national laboratories but not until two companies were created focusing on the EBSP method and in particular the data analysis, EBSP became a "need to have" technique in most materials science laboratories in academia and industry. Clearly of course the companies realized correctly that the EBSP technique fulfills a general scientific need of sufficient importance to base a business model on. And the companies they contributed significantly to the field by developing easy, user-friendly and fast experimental measurements and even more important, they developed systems for easy data analysis and beautiful data presentation.

Little commercialization has yet been realized for the 3D/4D methods, except from the RoboMet which is based on mechanical serial sectioning combined with optical microscopy and FIB in the SEM. In my opinion, this is not because there is not sufficient scientific need for the 3D/4D methods – some users may have been scared off because of the present complexities with the methods, but the need *is* there.

In the following some major obstacles and suggestions for the future shall be discussed.

1. There are many principally different 3D/4D methods

One data analysis system can therefore not be developed which serves them all. The raw data analysis and e.g. the alignment procedure needed to get serial sections in register are different. So this part of the data analysis clearly has to be developed by the instrument builders or in very close collaboration with these. From thereon, however, the 3D/4D data analysis and representation could (should) be united. The data sets are large, which may be a challenge in its own right, but other communities – in particular the game industries do handle far larger sets, and it might be an idea to learn from them. The whole 3D/4D materials society would benefit, if a company would take up this challenge (or the society could unite to work on just one representation system). Another challenge here is that in present days' publication channels, it is hard to visualize 3D/4D data. This would mean that in the papers we do not only have to focus on pretty pictures but also on specific scientific points; which may actually be an advantage for this field.

2. The 3D/4D community is scattered

The scientific focus is broad, which this conference also illustrates. It might be an advantage to keep the community close together, not only by meeting at conferences, but also via establishments of networks. This should be networks focusing on technique development, on science-technique questions/possibilities and on data representation and visualization. Web-based sharing of information and tools may be a way forward.

3. Some of the 3D/4D methods only operate at large international facilities

Here it is either very costly to get beamtime or if the usual peer-reviewed beamtime application procedure is used, it is hard to get beamtime – success rates below 10% is not unusual and in all

cases the time from idea to experiment is very long. This clearly limits the widespread use of these 3D/4D methods, and it is expected that this will always be the case in spite of the fact that more large scale facilities are being built. One might think of making some of the measurements faster more standard, so some kind of block allocation system might be put into place as parts of the biology community have done. But generally, an advice is only to use the 3D/4D techniques at the large scale facilities when it is really needed, i.e. the results cannot be obtained in any other way and always be very well prepared with optimal and well characterized samples for the 3D/4D experiment at the large scale facility.

4. Data analysis takes months, if not years

This is in particular true for the 3D/4D technique at the large scale facilities. Some *on-line* data visualization is extremely important, which can guide the next measurements and the user can avoid losing some of the precious beamtime on useless data. This has been implemented on some of the beamlines, e.g. on APPS 34-ID for the 3D polychromatic x-ray micro diffraction technique. Easier data analysis may be a compromise between constantly improving the experimental techniques to reach new possibilities and keeping to some fixed standards, which can be used for series of measurements. Also here establishment of communities between technique developers and scientific users could help getting this balance right.

## Concluding Remarks

The 3D/4D journey has so far been fantastic. Occasionally, it has been hair-raising to look inside the materials and see things which have hitherto been hidden and not possible to observe with other techniques. We are, however, in my opinion now at a critical stage, where we have to bring 3D/4D investigations beyond the demonstration stage and produce series of scientifically important results, which in term will stimulate the modeling and physical understanding. Challenges include firm establishment of the 3D/4D community(-ies), treatment of huge data sets, capturing methods to visualize the data and extract the scientifically important information, prescribing joint protocols to exchange data, not only between the different techniques, but also between experiments and models, i.e. creating a lively database, which stores all the data, keeps track of their associations and evolves as new experiments or modeling results are available. With the goal of overcoming these challenges it seems necessary to join not only the 3D/4D communities but also to create strong links to the ICME (Integrated Computational Materials Engineering) community, which deals with some of the same scientific and industrial needs for materials results which go beyond what can be obtained by 2D experimental methods.

**Acknowledgements**

The Danish National Research Foundation is acknowledged for funding the Danish Chinese Center for Nanometals, within which this work has been performed.

**References**

1. G. Spanos, D.J. Rowenhorst, S. Chang and G.B. Olsen, "3D Characterization of Microstructures in Metallic Systems by Serial Sectioning". Proc. 31st Risø International Symposium on Materials Science. Eds N. Hansen et al., (2010), 159-170.

2. J.S. Barnard, J. Sharp, J.R. Tong and P.A. Midgley, "High-Resolution Three-Dimensional Imaging of Dislocations", *Science,* 313 (2006), 319-319.

3. J.S. Barnard, J. Sharp, J.R. Tong and P.A. Midgley, "Three-Dimensional Analysis of Dislocation Networks in GaN using Weak-Beam Dark-Field Electron Tomography", *Philosophical Magazine,* 86 (2006), 4901-4922.

4. H.H. Liu, S. Schmidt, H.F. Poulsen, A. Godfrey, Z.Q. Liu, J. Sharon and X. Huang, "Three-Dimensional Orientation Mapping in the Transmission Electron Microscope", *Science,* 332 (2011), 833-834.

5. X.D. Zhang, A. Godfrey, G. Winther, N. Hansen and X. Huang, "In-Situ TEM Compression of Submicron-Sized Single Crystal Copper Pillars". Proc. 31st Risø International Symposium on Materials Science. Eds. N. Hansen et al., (2010), 489-496.

6. Y. Zhang, A. Godfrey and D. Juul Jensen, "Local Boundary Migration during Recrystallization in Pure Aluminium", *Scripta Mater.,* 64 (2011), 331-334.

7. E. Anselmino, "Microstructural effects on grain boundary motion in AlMn alloys" (PhD Thesis, Delft Univ. Techn), (2007).

8. T.J. Sabin, S. Schmidt, H.O. Sørensen, G. Winther, H.F. Poulsen, L. Margulies, C. Gundlach, and D. Juul Jensen, „Direct Non-Destructive Observation of Bulk Nucleation in 30 % Deformed Alluminium, *Scripta Mater.,* 61 (2009), 875-878.

9. M.A. Mangan, P.D. Lauren and G.J. Shiflet, "Three-Dimensional Reconstruction of Widmanstatten Plates in Fe – 12.3 Mn – 0.8 C", *Journal of Microscopy,* 188 (1997), 36-41.

10. R.A. Vandermeer and P. Gordon, "Edge-Nucleated, Growth Controlled Recrystallization in Aluminium, *Trans Metall. Soc. AIME*, 215 (1959), 577-588.

11. D.K. Bowen "Application of Synchrotron X-ray Methods for the Characterization of Deformed and Recrystallized Microstructures", Proc. 5th Risø International Symposium on Materials Science. Eds. N. Hessel Andersen et al., (1984), 1-17.

12. A.B.C. Dadson and R.D. Doherty, "Transmission Pseudo – Kossel (TK) Studies of the Structure of Hot-Deformed (Dynamically Recovered) Polycrystalline Aluminium", *Acta Metall. Mater.,* 40 (1992), 345-352.

13. D. Juul Jensen and J.K. Kjems, "Apparatus for Dynamical Texture Measurements by Neutron Diffraction Using a Position Sensitive Detector". *Textures and Microstructures,* 5 (1983), 239-251.

14. T. Lorentzen and J.B. Ibsø "Neutron-Diffraction Measurements of Residual Strains in Offshore Welds", *Mat. Sci. Eng. A,* 197 (1995), 209-214.

15. J.E. Spowart, "Automatic Serial Sectioning for 3D Analysis of Microstructures", *Scripta Mater.,* 55 (2006), 5-10.

16. D.J. Rowenhorst, A.C. Lewis and G. Spanos, "Three-Dimensional Analysis of Grain Topology and Interface Curvature in a Beta-Titanium Alloy", Acta Materialia 58 (2010), 5511-5519.

17. Z. Sükösd, K. Hanneson, G.L. Wu and D. Juul Jensen, "3D Spatial Distribution of Nuclei in 90 % Cold Rolled Aluminium, *Mat. Sci. Forum,* 558-559, (2007), 345-350.

18. Y.H. Zhang, D. Juul Jensen, Y. Zhang, F.X. Lin, Z.Q. Zhang and Q. Liu, "3D Investigation of Recrystallization Nucleation in a Particle-Containing Al Alloy", *Submitted for publication.*

19. M.D. Uchic, M.A. Groeber, D.M. Dimiduh, J.P. Simmonds, "3D Microstructioral Characterization of Nickel Superalloys via Serial-Sectioning using Dual Beam FIB-SEM", *Scripta Mater.,* 55 (2006), 23-28.

20. S. Zaefferer, S.I. Wright and D. Raabe, "Three-Dimensional Orientation Microscopy of a Focused Ion Beam-Scanning Electron Microscope: A New Dimension of Microstructure Characterization", *Metallurgical and Materials Transactions A-Physical Metallurgy and Materials Science,* 39A (2) (2008), 374-389.

21. M.L.P. Echlin, A. Mottura, C. Torbet and T.M. Pollock, "A New TriBeam System for Three-Dimensional Multimodal Materials Analysis", *The Review of Scientific Instruments*, 83 (2) (2012), 023701.

22. H.F. Poulsen and D. Juul Jensen, "Synchrotron Radiation Diffraction: A Novel Tool for Recrystallization Studies in Bulk μm Sized Local areas". Proc. 16$^{th}$ Risø International Symposium on Materials Science: Microstructural and Crystallographic Aspects of Recrystallization. Edited by N. Hansen et al., (1995), 503-508.

23. H.F. Poulsen, *"ThreeDimensional X-ray Diffraction Microscopy"* (Springer Berlin, 2004).

24. D. Juul Jensen, A. Kvick, E.M. Lauridsen, U. Lienert, L. Margulies, S.F. Nielsen and H.F. Poulsen. Proc. Mat. Res. Soc. Symp., 590 (2000), 227-240.

25. G. Ice, "Letting the Grains Show Their Strains. *Materials World*, May 2000, 20-21.

26. B.C. Larson, W. Yang, G.E. Ice, J.D. Budai and J.Z. Tischler, "Three Dimensional X-ray Structural Microscopy of Submicrometre Resolution", *Nature*, 415 (2002), 887-890.

27. G.E. Ice, B.C. Larson, W. Yang, J.D. Budai, J.Z. Tischler, J.W.L. Pang, R.I. Barabash and W. Liu, "Polychromatic X-ray Microdiffraction Studies of Mesoscale Structure and Dynamics", *J. Synchrotron Rad.*, 12 (2005), 155-162.

28. H.J. Bunge, L. Wcislak, H. Klein, U. Garbe and J.R. Schneider, "Texture and Microstructure Imaging in Six-Dimensions with High-Energy Synchrotron Radiation", *J. Appl. Cryst.*, 36 (2003), 1240-1255.

29. T. Wroblewski, O. Clauss, H.-A. Crostack, A. Ertel, F. Fandrich, Ch. Genzel, K. Hradil, W. Ternes and E. Woldt, "A new Diffractometer for Materials Science and Imaging at HASYLAB Beamline G3", *Nucl. Instr. Meth. A*, 428 (1999), 570-582.

30. H.F. Poulsen, S. Garbe, T. Lorentzen, D. Juul Jensen, F.W. Poulsen, N.H. Andersen, T. Frello, R. Feidenhans'l and H. Graafsma, "Applications of High-Energy Synchrotron Radiation for Structural Studies of Polycrystalline Materials", *J. Synchrotron Rad.*, 4 (1997), 147-154.

31. B. Duggan, "The Problem of Lost Evidence" (Term Discussed at the ICOTOM 11 Conference held in Xian, China, 1996).

32. H. Weiland, T.N. Rouns and J. Liu, "The Role of Particle Stimulated Nucleation during Recrystallization of an Aluminium – Manganese Alloy", *Z. Metall kde*, 85 (1994), 592-597.

33. S. Storm and D. Juul Jensen, "Effects of Clustered Nucleation on Recrystallization", *Scripta Mater.*, 60 (2009), 477,480.

34. H. Paul, J.H. Driver and Z. Jasienski, "Shear Banding and Recrystallization Nucleation in a Cu-2% Al Alloy Single Crystal", *Acta Materialia*, 50 (2002), 815-830.

35. S.R. Skjervold and N. Ryum, "Orientation Relationships in a Partially Recrystallized Polycrystalline AlSi-Alloy", *Acta Materialia*, 44 (1996), 3407-3419.

36. G.L. Wu and D. Juul Jensen, "Orientations of Recrystallization Nuclei Developed in Columnar-Grained Ni at Triple Junctions and a High-Angle Grain Boundary", *Acta Mater.*, 55 (2007), 4955-4964.

37. A.W. Larsen, H.F. Poulsen, L. Margulies, C. Gundlach, Q.F. Xing, X. Huang and D. Juul Jensen, "Nucleation of Recrystallization Observed in-situ in the Bulk of Deformed Metals", *Scripta Mater.*, 53 (2005), 553-557.

38. S.S. West, S. Schmidt, H.O. Sorensen, G. Winther, H.F. Poulsen, L. Margulies, C. Gundlach and D. Juul Jensen, „Direct Non-Destructive Observation of Bulk Nucleation in 30% Deformed Aluminum", *Scripta Mater.*, 61 (9) (2009), 875-878.

39. G. Gottstein and L.S. Shvindlerman, "On the True Dependence of Grain Boundary Migration Rate on Drive Force", *Scripta Met. Mat.*, 27 (1992), 1521-1526.

40. R. Viswanathan and G.L. Bauer, "Kinetics of Grain Boundary Migration in Copper Bicrystals with (001) Rotation Axes", *Acta Metall.*, 21 (1973), 1099-1109.

41. R.A. Vandermeer, "Dependence of Grain Boundary Migration Rates on Driving Force", *Trans AIME*, 233 (1965), 265-267.

42. R.A. Vandermeer, D. Juul Jensen and E. Woldt, "Grain Boundary Mobility during Recrystallization of Copper", *Met. Mat. Trans*, 28A (1997), 749-754.

43. B.B. Rath and H. Hu, "Effect of Driving Force on the Migration of High-Angle Tilt Grain Boundaries in Aluminium Bicrystals, *Trans TMS AIME*, 245 (1969), 1577-1585.

44. Y.B. Zhang, A. Godfrey, Q. Liu, W. Liu and D. Juul Jensen, "Analysis of the Growth of Individual Grains during Recrystallization in Pure Nickel", *Acta Mater.*, 57 (2009), 2631-2639.

45. S. Schmidt, S.F. Nielsen, C. Gundlach, L. Margulies, X. Huang and D. Juul Jensen, "Watching the Growth of Bulk Grains during Recrystallization of Deformed Metals", *Science*, 305 (2004), 229-232.

46. Y. Zhang, G. Godfrey, N. MacDonald and D. Juul Jensen, "3D Characterization of Recrystallization Boundaries" (in these proceedings).

1st International Conference on 3D Materials Science
*Edited by: Marc De Graef, Henning Friis Poulsen, Alexis Lewis, Jeff Simmons, George Spanos*
***TMS (The Minerals, Metals & Materials Society), 2012***

# 3D Investigation of Cracking Behavior in a Ni Superalloy

Andrew Deal[1], David Rowenhorst[2], Brandon Laflen[1], Ian Spinelli[1],
Tony Barbuto[1], Yuchi Huang[1], Timothy Hanlon[1]

[1]GE Global Research; 1 Research Circle; Niskayuna, NY 12309
[2]The U.S. Naval Research Laboratory; 4555 Overlook Avenue SW, Washington, DC 20375

## Abstract

The high temperature fatigue performance of Ni-base superalloys is critical to gas turbine applications and as such, requires a more fundamental understanding when designing and producing turbine components. To investigate the relationship to local microstructure, a fatigue specimen was cycled under conditions designed specifically to result in intergranular propagation. Prior to failure, the test was interrupted and a 3D data set was reconstructed destructively from optical and EBSD slices taken from around the tip of the growing crack. The data set was investigated to understand the character of grain boundary planes along the crack front with respect those of the bulk material.

## Introduction

Gas turbines demand exceptional high temperature material performance. Standard operation imposes complex cyclic stress states and corrosive environments, making alloy design crucial to component life. Consequently, it is no misnomer that the class of alloys suited for gas turbine applications are called 'superalloys.' In service Ni superalloys must survive a number of engine cycles in the range of 15,000 or 150,000, depending on the application, and this expected life is currently set through curves generated by thorough mechanical testing. To supplement this data and understand the microstructural effects on life, an effort to explore the three-dimensional nature of a crack tip was initiated. Methodology and preliminary results are discussed here.

## Mechanical Testing

A Ni-base superalloy fatigue specimen with rectangular cross section (0.400” wide by 0.168” thick), known as a KB bar, was prepared with a 7-mil deep by 14-mil wide EDM surface flaw in the center of the gage section. An image of a KB bar is shown in Figure 1. The specimen blank was fully solutioned and aged, prior to finish-machining. A room temperature pre-crack sequence was imposed at 10Hz under a constant $\Delta K$ of 14.25ksi*in$^{1/2}$ (R = 0.05) to extend a fatigue crack from the EDM starter flaw. The test temperature was then elevated to 1300°F and a trapezoidal cyclic waveform was imposed with 1-second ramps and a 360-second hold at peak stress. This combination of temperature, stress, and waveform resulted in a fully intergranular fatigue failure mode. Crack length measurements were made throughout with a reversing DC electrical potential drop system. The test was interrupted prior to failure, and the specimen was prepared for serial sectioning to analyze the microstructure adjacent to the main crack.

To prepare the sample, a section of the KB bar containing the fatigue crack was mounted in a conductive phenolic compound, ground, and polished in longitudinal cross-section. The grinding was controlled so that the plane of the final polish was approximately transversely centered in the bar, capturing the deepest part of the crack. Additionally, the cross-section was mounted

away from the mount center and a flat was polished into the side of the mount for positioning in the SEM and the optical bench.

## Data Acquisition

Once the mount was prepared, a serial sectioning routine similar to [1] was applied to generate data for 3D reconstruction and analysis. First, four Knoop micro-indents were set in a rectangular array surrounding the crack tip using a Clemex JS-2000 micro-indenter. The initial width of each indent was measured and recorded to provide a baseline for measuring material removal. Next the mount was positioned in a Struer's Prepamatic-2 autopolisher and nominally 1.0μm of material was removed. A modified Kalling's etch was applied to delineated the grain boundaries and a multi-image optical montage of the entire crack tip was taken on a Zeiss Axio Observer Z1.m microscope, with a 0.11μm pixel size. The indent widths were measured again after the polish and imaging, and the removal depth was calculated using the geometry of the indent. This sequence was repeated five times, with fresh indents being applied every other slice in a rotating pattern. Once the fifth cycle was completed the flat of the sample was placed in a Camscan 44 W-filament SEM on a 20° pre-tilted wedge with affixed stoppers for accurate sample positioning. This positioning provided a 70° tilt of the sample plane for EBSD mapping. Once the SEM was evacuated, the accelerating voltage was set to 20kV and sample was positioned to map the region of interest. Before scanning, the filament was allowed to equilibrate for a minimum of 3 hours in order to minimize drift during mapping. Finally a 1631x1259 pixel map, with a step size of 0.75 μm, was performed. The map took approximately 13 hours to complete at a scan rate of 44 points/second. The entire sub-process of 5 optical analyses and one EBSD analysis was repeated over the course of 4 months to produce ~150 individual optical slices and ~30 EBSD maps for the 3D reconstruction, schematically shown in Figure 1.

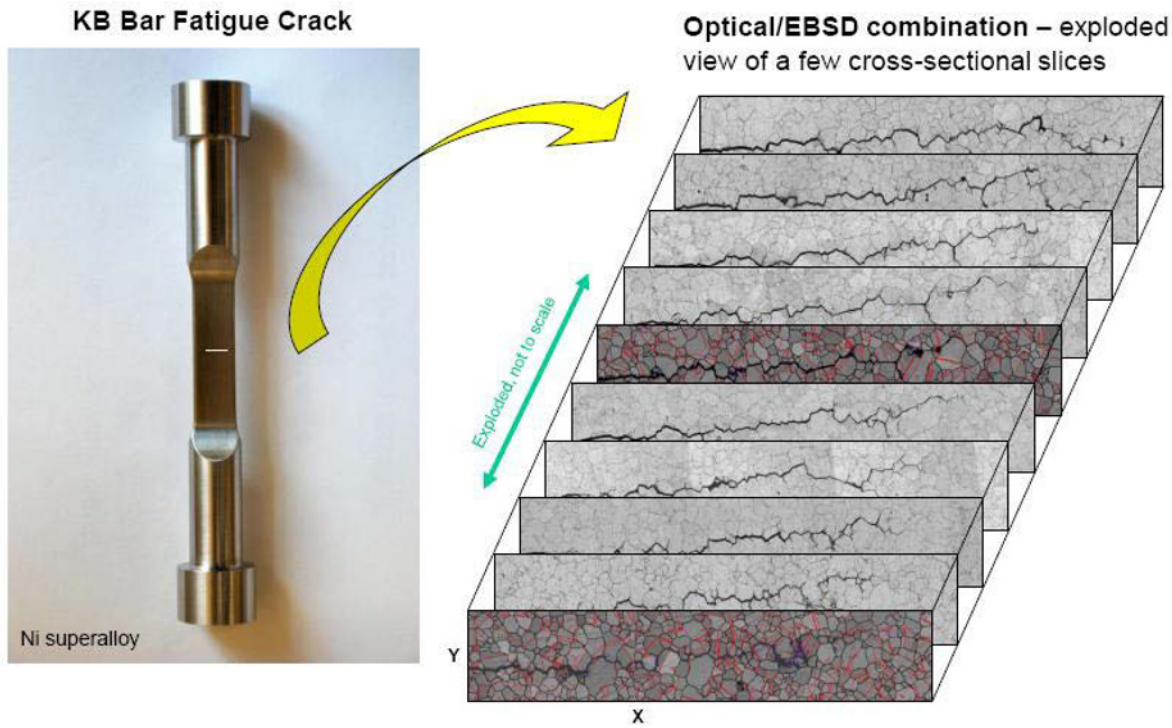


**Figure 1** – Schematic representation of KB bar crack 3D reconstruction

## Results

Figure 2 shows the removal rate histogram for the 150 slices. The standard deviation of the mechanical material removal was 0.21µm, and the overall average was 1.01µm, within 1% of the target. A typical optical montage and a corresponding EBSD map are shown in Figure 3. The optical montages generally did not reveal twin boundaries. Some are visible, but most are not. However, twins were well captured by the EBSD maps, which will eventually allow for their incorporation into the reconstruction. The percentage of correctly indexing points in the EBSD maps was generally 95% or more. Cleanup was applied to the data to fill in grain boundaries, but care was taken to avoid filling the crack to aid in crack extraction. In Figure 3, ~3.5% of points were generated from the cleanup routine, with red indicating a Σ3 boundary, black indicating a regular grain boundary, green representing the remaining unindexed area.

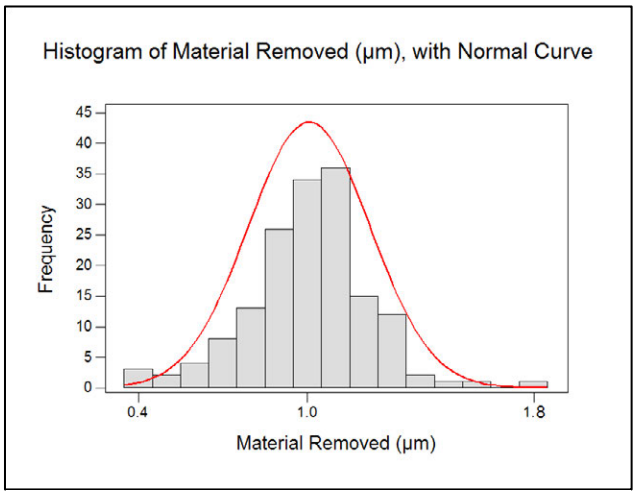


**Figure 2** – Histogram of sectioning measurements

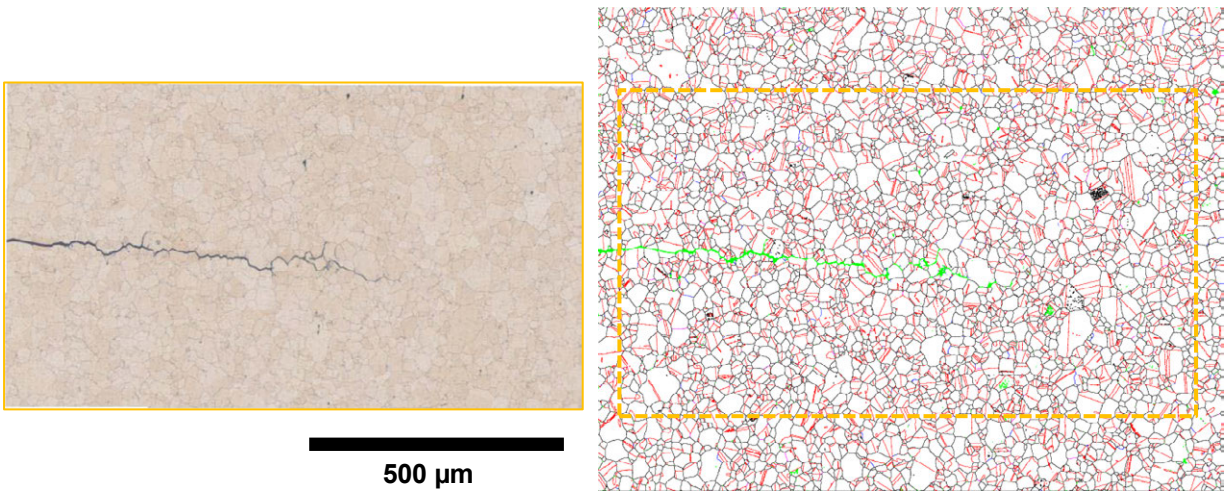


**Figure 3** – Typical optical montage (L) and EBSD map (R). Black, red, and green in the map signify regular boundaries, special boundaries, and unindexed points, respectively.

## Data Reconstruction

To reconstruct the 3D volume, first the individual optical tiles from each slice were montaged using the Zeiss software. The optical images were then stacked and aligned within the computer using in-house registration routines. The misalignments between the sections primarily consisted of translations, with very small rotational misalignments. The translations were determined by the maximum in the cross-correlation of the images.

Next the EBSD scans were aligned with the optical images. While the task of matching two images of the same identical area might seem easier than aligning different sections, the alignment of the two image modalities proved to be more challenging. One difficulty was that the EBSD images had small inherent distortions. These distortions were likely due to small amounts of drift, minor errors in dynamic focus or electron beam raster alignment to the sample, and some small sample positional errors. For more information on distortions in EBSD maps, see [2]. While careful data collection methods minimized these distortions, when directly comparing small features over a large area, such as the interface of a crack, even small image distortions led to significant misalignment of the images.

To align the two datasets, the optical image was treated as the baseline image, and its sister EBSD image was undistorted to achieve the highest degree of overlap with it. The EBSD image was undistorted using a second-degree polynomial with separate coefficients for the x and y directions, leading to a 12 parameter optimization. The coefficients of the polynomials were determined using a Nelder and Mead optimization algorithm, which maximizes a given generic function given a set of adjustable parameters. The optimized function in this case measured the degree of overlap in the two images using mutual information.

Mutual information is a concept borrowed from the field of information technology which determines probability that a set of pixels contain the same information, regardless of the independent values of the pixels. The mutual information of two images is related to the image entropy, H of the image defined by:

$$H = -\sum_{i=0}^{255} p_i \ln(p_i)$$

where $p_i$ is the probability that a pixel within the image has an intensity of i, within the a range of 0 to 255. The joint entropy of two images, im1 and im2, measures the degree of correlation between the two images and is similar to the concept of the entropy of mixing in solutions, is given by:

$$H(im1,im2) = -\sum_{j=0}^{255}\sum_{i=0}^{255} p_{i,j} \ln(p_{i,j})$$

where pi,j is the probability that if im1 has an intensity of i then im2 has the probability of having intensity j. The mutual information, MI, between the two images is then given by:

$$MI(im1,im2) = H(im1) + H(im2) - H(im1,im2)$$

Thus, if the amount of shared information between the two images increases, the value of the MI will increase, regardless of the exact values of the features within the images. For further information on the use of mutual information for data alignment see [3].

The mutual information between the optical image and the “Band Contrast” image from the EBSD data was maximized, since both of these imaging modes provided strong contrast at the

location of the crack, as well as at the location of the grain boundaries. The initial guess for the modifications of the EBSD images was given by the ratio in pixel size of the two images, and a manual estimation of the translations for the first optical image/EBSD image pair. Subsequent initial guesses for the polynomial coefficients were given by the previous pair's solution.

Once the EBSD images were aligned to the optical images, they were combined into a single reference frame in the VTK framework for analysis.

## Analysis

Initial analysis focused on the crystallographic nature of the opposing crack surfaces. Consequently, the crack was extracted from the optical portion of the 3D volume. Lines of EBSD data, spaced roughly every 5µm, were superimposed onto the extraction surface from the fully reconstructed volume. Next, a surface normal was estimated for each point on the crack surface in the volume reference frame. This was accomplished using in-house software, which was developed with VTK and designed to analyze 3D surfaces. The crystallographic normals were then calculated at points that contained EBSD data. These data, over 200,000 directions, are plotted in the [001] pole figure in Figure 4. There was a slight preference for <111> normal directions, which correspond to {111} planes along the crack surface. This begged the question as to whether there was a significant twin content in the crack path, which required analysis of the boundary planes themselves.

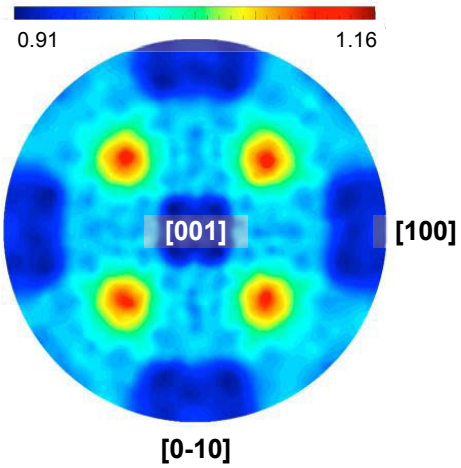


**Figure 4** – [001] pole figure of surface normal directions. Scale is multiples of a random distribution.

To analyze the boundary planes that the crack followed, crystallographic normal directions from opposite sides of the crack were grouped in pairs and analyzed. Specifically, each point on one side of the crack was projected along its normal direction (in the volume reference frame) to the closest point on the opposite side, creating a pair. The two crystallographic surface planes of a pair and the axis/angle disorientation obtained from a pair's EBSD data were used to classify the crack boundary points into eight categories, which were color coded for visual representation:

- RED: Twin boundary = Σ3 disorientation with both boundary planes equal to {111}
- ORANGE: Σ3 boundary with only one {111} plane (1st plane)
- YELLOW: Σ3 boundary with only one {111} plane (2nd plane)
- MAGENTA: Σ3 boundary with no {111} plane on either side
- GREEN: Regular (non-Σ3) twist boundary with both boundary planes equal to {111}
- CYAN: Regular boundary with only one {111} plane
- BLUE: Regular boundary with no {111} plane on either side
- WHITE: Not a grain boundary

The tolerance for the Σ3disorientation was initially set to 5° for both the angle and axis. A 10° tolerance was also used for comparison. Results are shown graphically in Figure 5. The majority of planes that the crack followed were regular boundaries with either no {111} plane on either side of the crack (BLUE), or only one {111} plane (CYAN). The type with the next

highest frequency was a Σ3 boundary with no {111} plane on either side (MAGENTA). Virtually no twins (RED) or Σ3 boundaries with a single {111} plan (ORANGE, YELLOW) were present, although a small amount of regular twist boundaries (GREEN) were detected. The results suggest that the crack proceeded almost exclusively along regular boundaries.

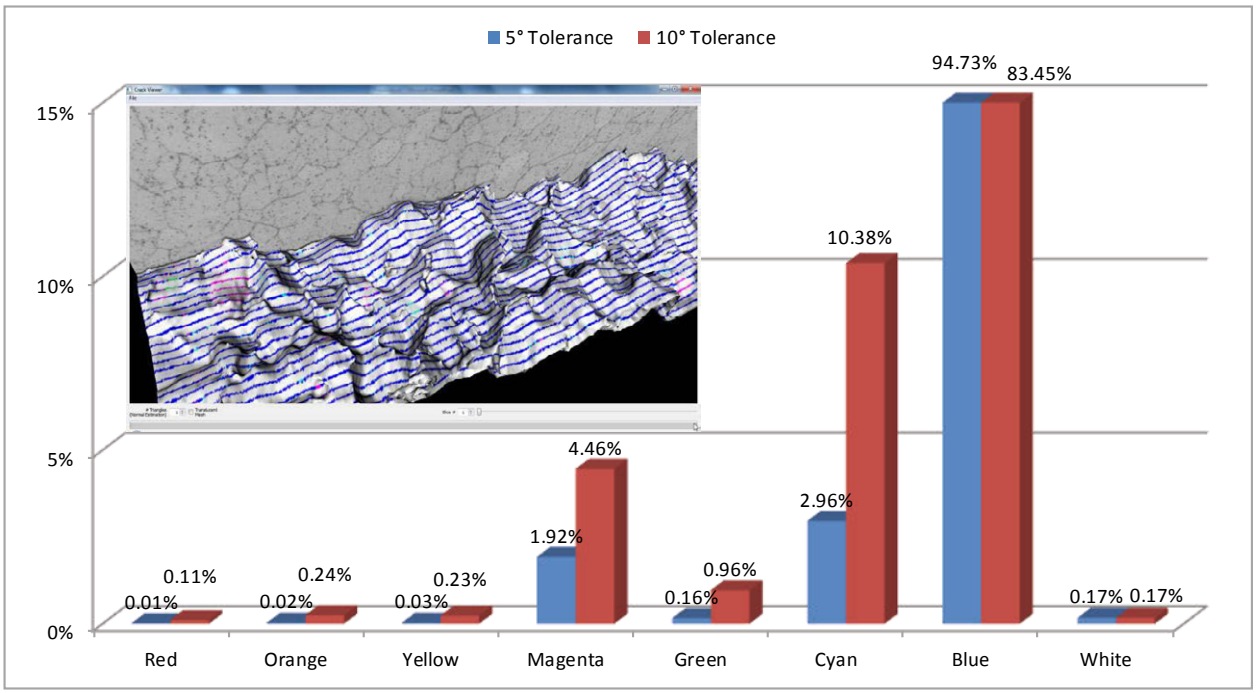


**Figure 5** – Chart of boundary distribution. Inlaid image is a top-down view of the crack surface, with boundary coloring on the EBSD points and a single optical image orthogonal to the surface. See text for key.

## Future Work

The authors plan to compare the data in Figures 4 and 5 to similar distributions obtained from the bulk portion of the 3D volume away from the crack surface. This will help determine whether the crack actively followed a regular boundary path or simply encountered the bulk distribution of boundary types along its trajectory. To accomplish this, segmentation of the grain boundaries in the optical data and incorporation of the twin boundaries from the EBSD data are both currently in progress.

**References:**


[1] Lewis, A.C. , Bingert, J.F., Rowenhorst, D.J., Gupta, A., Geltmacher, A.B., Spanos, G. "Two- and three-dimensional microstructural characterization of a super-austenitic stainless steel" Materials Science and Engineering A 418 (2006) 11–18.

[2] Nolze, G. "Image distortions in SEM and their influences on EBSD measurements." Ultramicroscopy 107 (2007) 172–183.

[3] Gulsoy, E. B., Simmons, J. P., De Graef, M. "Application of joint histogram and mutual information to registration and data fusion problems in serial sectioning microstructure studies." Scripta Materialia, 60 (2009) 381–384.

1st International Conference on 3D Materials Science
*Edited by: Marc De Graef, Henning Friis Poulsen, Alexis Lewis, Jeff Simmons, George Spanos*
***TMS (The Minerals, Metals & Materials Society), 2012***

# ON THE THREE-DIMENSIONAL MICROSTRUCTURE OF MARTENSITE IN CARBON STEELS

Peter Hedström[1], Albin Stormvinter[1], Annika Borgenstam[1], Ali Gholinia[2], Bartlomiej Winiarski[2], Philip J. Withers[2], Oskar Karlsson[3] and Joacim Hagström[3]

[1] Department of Materials Science and Engineering, KTH Royal Institute of Technology 100 44 Stockholm, Sweden
[2] School of Materials, University of Manchester, Grosvenor Street, M1 7HS, U.K.
[3] Swerea KIMAB AB, Box 55970, 102 16 Stockholm, Sweden

Keywords: Martensite, Carbon steels, Serial sectioning, Three-dimensional microstructure

## Abstract

The mechanical properties of high-performance steels are often reliant on the hard martensitic structure. It can either be the sole constituent e.g. in tool steels, or it can be part of a multi-phase structure as e.g. in dual-phase steels. It is well-known that the morphology of martensite changes from lath to plate martensite with increasing carbon content. The transition from lath to plate is however less known and in particular the three-dimensional (3D) aspects in the mixed lath and plate region require more work. Here the current view of the 3D microstructure of martensite in carbon steels is briefly reviewed and complemented by serial sectioning experiments using a focused ion beam scanning electron microscope (FIB-SEM). The large martensite units in the Fe-1.2 mass% C steel investigated here are found to have one dominant growth direction, less transverse growth and very limited thickening. There is also evident transformation twinning parallel to the transverse direction. It is concluded that more 3D analysis is required to understand the 3D microstructure of martensite in the mixed lath and plate region and to verify the recently proposed 3D phase field models of martensite in steels.

## Introduction

Martensite with its inherent hardness is an important constituent in high-performance steels. It can either be used as the sole constituent, or as one constituent in a composite structure. One example of a composite structure is the dual-phase steels with pro-eutectoid precipitation of the soft ferrite phase and the subsequent formation of the hard martensite upon quenching. The dual-phase structure has a good compromise between strength and toughness, but this can also be achieved in pure martensitic steels after tempering. The properties of martensite are a consequence of its intricate structure with favored crystallographic relations between adjacent units, rich deformation structure and varying morphology. All of these microstructural features are dependent on the alloy composition.

The current understanding of martensite in steels is to a large extent based on two-dimensional (2D) experimental characterization and materials modeling. The rapid development of different three-dimensional (3D) tools is however generating new ways to improve our knowledge about intricate polycrystalline structures. There are a number of groups that are working on serial sectioning techniques and the outlook and methodology has been reviewed several times lately,

see e.g. [1]. In addition, there are large activities in 3D X-ray visualization, see e.g. [2]. Despite this the 3D nature of martensite has received little attention to date. The available reports are most often concerned with composite aspects [3] rather than the martensite microstructure itself.

In the modeling area there have been a number of recent reports utilizing 3D phase field modeling to simulate the martensitic transformation and the martensite structure. For instance Kundin et al. [4] modeled a Fe-Ni alloy forming butterfly martensite and found good agreement with 2D experimental work. Yeddu et al. developed a 3D phase field model for a Fe-0.3 mass% C steel [5]. They presented simulation results on morphology and crystallography in 3D [6]. This inspired us to undertake 3D characterization to enable sound comparison and validation of the modeling. It is particularly interesting to study the mixed region where both lath and plate martensite can coexist. This paper reports our initial experimental efforts targeted on this interesting regime on a 1.2 mass% C steel, which is thought to be close to the upper bound of the mixed region [7]. Here, the current understanding of martensite in carbon steels is briefly reviewed and complemented by 3D serial sectioning experiments.

## Martensite In Carbon Steels

Lath martensite is the dominant microstructure in low carbon steels, see Figure 1a. The lath is the smallest unit and it can be considered as a single crystal with very high dislocation density [8]. The lath is narrow in two dimensions and extended in the third. The typical width of a lath unit as found in 2D sections is a few hundred nanometers. The laths are arranged parallel to each other with only small crystallographic misorientations of about 1 to 3° between the individual laths. In low-carbon steels the second smallest unit is considered to be the sub-block [9], which consists of laths from one distinct crystallographic variant, i.e. one of the 24 possible martensite orientations given by the Kurdjumov-Sachs orientation relationship (K-S OR) [8]. The next structural level is the block, which is built-up of two different sub-blocks with a low degree of misorientation [9]. The packet is the next hierarchical level where all martensite units are formed on the same habit plane.

When increasing the carbon content the morphology of martensite will change with much less distinct packets and blocks, and in general it seems like the structural units become finer up to about 0.7 mass% C, see Figure 1b. The second distortion will now more often occur via twinning and more twins are found at this carbon content [8], though they can also be found for low-carbon martensite. The martensite morphology at intermediate carbon contents is often referred to as butterfly martensite due to the frequent observations of two units forming together with a distinct angle between them. In addition to the small units found at this carbon content one can occasionally find larger units and these are especially common at prior austenite grain boundaries (Figure 1b).

At high carbon contents, > about 1.2 mass% C (Figure 1c), the martensite units will frequently appear as lenses with a distinct midrib, and the second distortion will mostly occur by twinning [8]. The twinning close to the midrib is called transformation twinning, but also deformation twinning is found when the martensite units have widened [10]. The lens units arrange in plate groups (4 variants in the K-S OR) to accommodate stresses. Moreover, they typically arrange in a zig-zag pattern due to autocatalysis of subsequent units.

The 3D characterization of martensite in carbon steels started with the work by Krauss and Marder [11]. They investigated an Fe-0.2 mass% C alloy and studied the morphology of martensite using serial sectioning and light optical microscopy (LOM). They found most individual units to be lath-shaped, but they also found some of 2D rectangular morphology, which they claimed could be consistent with the lath morphology if the etchant is not able to etch the boundaries within such units or if the resolution of the LOM is too low to resolve that the rectangles actually comprise several units. More recently Rowenhorst et al. [12] investigated the 3D morphology and crystallography of coarse martensite formed in a HSLA steel (0.07 mass% C). They used a combination of LOM and electron backscattered diffraction (EBSD) together with serial sectioning and showed that it was a misconception from 2D analysis that coarse martensite was plate-shaped. Instead they found the shape to be lath-like with the length being considerably larger than the width and thickness. They presented a methodology to study the crystallographic interfaces in 3D, but they did not present any detailed analysis of the interfaces thus found. Morito et al. [13] investigated the morphology and crystallography of sub-blocks of martensite in ultra-low carbon lath martensitic steel by EBSD. They found that the blocks contain one dominant sub-block and many minor sub-blocks and that the crystallographic relation between these are [011]/10.5º. The minor sub-block had a plate morphology with about 10 µm width and was connected to the other minor sub-blocks within one block. Morito et al. [9] investigated the 3D morphology of blocks and packets in one ultra low carbon steel and one steel having 0.493 mass% C. They found that some martensite units had a sponge-like morphology. Liu et al. [14] investigated the martensite morphology in a steel having 1.37 mass% C using serial sectioning and LOM. They found the martensite morphology to be a flat ellipsoid and claimed that this was quite different from the general view of martensite morphology in high-carbon steel.

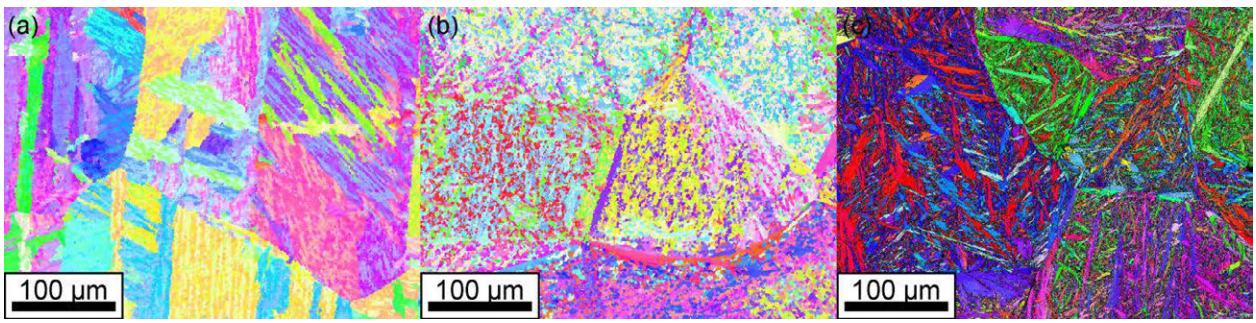

Figure 1: EBSD inverse pole figure micrographs from austenitized and quenched steels a) IF steel (1.0 µm step size) b) 0.75 mass% C (1.0 µm step size) c) 1.20 mass% C (0.3 µm step size)

## Serial Sectioning Experiments

An Fe-1.2 mass% C alloy was investigated by serial sectioning using a Zeiss Auriga dual-beam FIB-SEM. The 1 mm thick sample was austenitized at 1100°C and subsequently quenched in brine. Prior to mounting in the FIB-SEM the sample was mechanically polished. Fiducial marks were generated on the surface to allow post-processing alignment. Sections were taken every 250 nm and a total of 46 sections were studied using chanelling contrast imaging. The 3D reconstructions were performed in the software IMOD [15].

## Results and Discussion

Figures 2a-c show three out of 46 sections. The microstructure consists of both small and large martensite units, which is typical for a plate-like martensite morphology, since the large martensite units forming first will restrict growth of the units forming later on [8]. Three of the larger martensite units found in the observed volume have been selected for 3D reconstruction. These units were selected, since they have a rather clear homogeneous contrast with a distinct interface with the adjacent units. The units are displayed in green, cyan and red and marked 1, 2 and 3 respectively in Figures 2a-c. The transformation twinning is clearly seen in some sections of the larger units, see Figure 2a - unit 2 (cyan) and Figure 2c – unit 1 (green). In the surrounding smaller units it is much more difficult to distinguish the morphology and also any potential transformation twinning due to the varying contrast possiby due to additional deformation and lattice rotation by dislocation formation or deformation twinning [10].

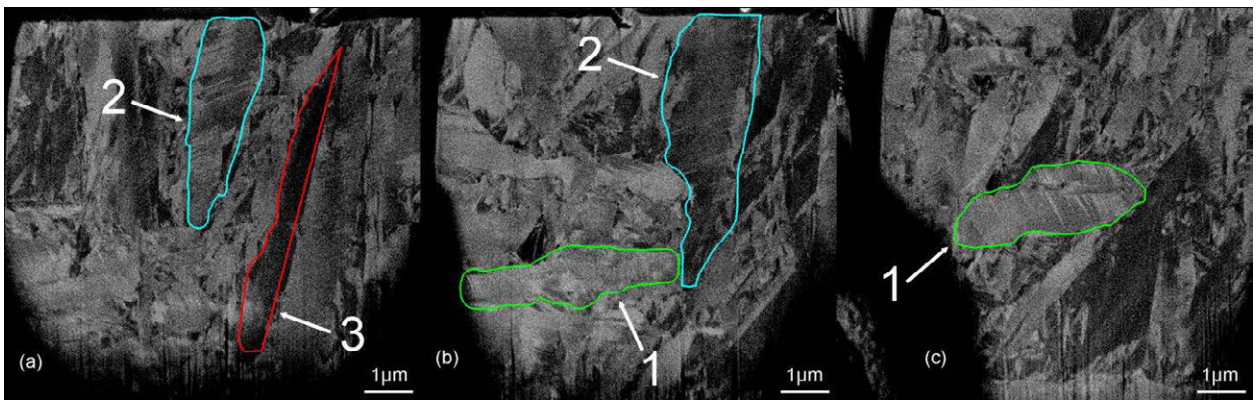

Figure 2: FIB serial sections for Fe-1.2 mass% C austenitized and quenched in brine. The three units that were reconstructed in 3D are colored in green (1), cyan (2) and red (3) respectively. (a) Section # 10 (b) Section # 20 (c) Section # 39.

Figures 3a-c show 3D reconstructions of the three martensite units observed in the sectioned volume (Figures 2a-c). The units have one dominant growth direction, less transverse growth and a very limited thickening. Since only a limited volume may be examined by the slice and view technique in a FIB-SEM it is difficult to completely enclose a fully developed large martensite unit. Hence, it is therefore not fully disclosed whether the units should be characterized as plate-shaped or as coarse laths [12]. It should however be emphasized that in the nomenclature of lath martensite the lath refers to the small single crystalline units with very high dislocation density, as mentioned earlier. Therefore we prefer to describe the units in Figure 3 as plate-shaped, but with one elongated direction. When comparing to the work by Liu et al. [14] for a Fe-1.37 mass% C steel they showed a rather similar appearance of the units, though the difference between length and transverse direction is more pronounced in the present work.

To generate a fuller view of the 3D structure of martensite, especially in the mixed lath and plate region [15], it is necessary to follow-up with more complete studies in 3D also considering the crystallographic information. It is possible that our current views of martensite, which are almost exclusively obtained from 2D sections could be improved considerably by further investigations on 3D features such as martensite-martensite and martensite-austenite interfaces, morphology of martensite units in the mixed region, and internal strain distribution. Therefore further 3D-

chanelling contrast imaging to study substructure and morphology coupled with 3D-EBSD to better understand the grouping of crystallographic units and accomodation effects is planned.

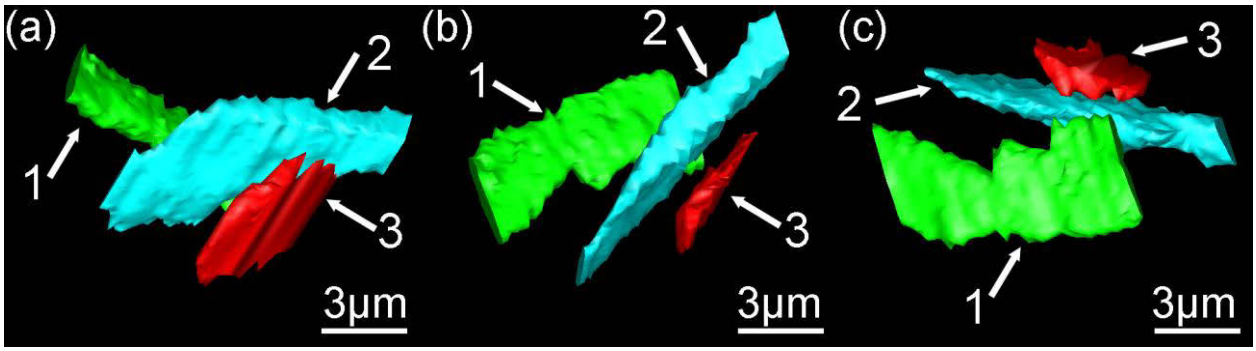

Figure 3: 3D reconstruction of three martensite units based on the serial sectioning imaging. (a)-(c) display the reconstructed martensite units viewed from different angles.

## Concluding Remarks

3D martensite characterization is scarce in the literature and this may limit our understanding of martensitic microstructures in carbon steels. To fully understand the morphological and crystallographic nature of the transition from lath to plate martensite with carbon content as well as for verification of the recent 3D phase field modeling, more 3D characterization work is required. The recent advances in 3D serial sectioning techniques provide a basis for such work and we have presented initial serial sectioning experiments for a high-carbon martensitic steel. It is found that large martensite units have one dominant growth direction, less transverse growth and a very limited thickening. The morphology of smaller units is more difficult to define possibly due to additional deformation.

## Acknowledgements

This work was performed within the VINN Excellence Center Hero-m, financed by VINNOVA, the Swedish Government Agency for Innovation Systems, Swedish Industry and KTH Royal Institute of Technology. The authors are grateful to Zeiss, Oberkochen and Drs. Fredrik Lindberg and Malin Tornberg for help with the serial sectioning experiments. An EPSRC-NPL grant is also acknowledged EP/I029605/1.

## References

[1] S. Zaefferer and S.I. Wright. “Three-dimensional orientation microscopy by serial sectioning and EBSD-based orientation mapping in a FIB-SEM”, Electron backscatter diffraction in materials science, ed. A.J. Schwartz, M. Kumar, B.L. Adams and D.P. Field (New York, NY: Springer, 2009) 109-122.

[2] H.F. Poulsen, *Three-dimensional X-ray Microscopy - Mapping Polycrystals and their Dynamics* (Heidelberg, Germany: Springer, 2004).

[3] P. Hedström, U. Lienert, J. Almer and M. Odén. ”Elastic strain evolution and ε-martensite formation in individual austenite grains during in situ loading of a metastable stainless steel”, Mater. Lett. 62 (2008) 338.

[4] J. Kundin, D. Raabe and H. Emmerich. “A phase-field model for incoherent martensitic transformations including plastic accommodation processes in the austenite”, J. Mech. Phys. Solids 59 (2011) 2082.

[5] H.K. Yeddu, A. Malik, J. Ågren, G. Amberg, A. Borgenstam. ”Three-dimensional phase-field modeling of martensitic microstructure evolution in steels”, Acta Mater. 60 (2012) 1538.

[6] H.K. Yeddu, A. Borgenstam, P. Hedström and J. Ågren. ”A phase-field study of the physical concepts of martensitic transformations in steels” Mater. Sci. Eng. A 538 (2012) 173.

[7] A. Stormvinter, P. Hedström and A. Borgenstam. ” Investigation of Lath and Plate Martensite in a Carbon Steel”, Solid State. Phenom. 172-174 (2011) 61.

[8] Z. Nishiyama. *Martensitic Transformation*. (New York, NY: Academic press, 1978).

[9] S. Morito, Y. Edamatsu, K. Ichinotani, T. Ohba, T. Hayashi, Y. Adachi, T. Furuhara, G. Miyamoto, N. Takayama. “Quantitative analysis of three-dimensional morphology of martensite packets and blocks in iron-carbon-manganese steels”, J. Alloy. Compd., http://dx.doi.org/10.1016/j.jallcom.2012.02.004.

[10] A. Stormvinter, P. Hedström and A. Borgenstam. ”Automatic phase and orientation mapping combined with classical transmission electron microscopy to study the development of martensite in high-carbon low alloy steels”, Submitted 2012.

[11] G. Krauss and A.R. Marder. “The morphology of martensite in iron alloys” Metall. Trans. 2 (1971) 2343.

[12] D.J. Rowenhorst, A. Gupta, C.R. Feng and G. Spanos, “3D Crystallographic and morphological analysis of coarse martensite: Combining EBSD and serial sectioning” Scripta Mater. 55 (2006) 11.

[13] S. Morito, Y. Adachi and T. Ohba. “Morphology and Crystallography of Sub-Blocks in Ultra-Low Carbon Lath Martensite Steel” Mater. Trans. 50 (2009) 1919.

[14] Y. Liu, G. Zhang and W. Li, “A study of martensitic morphology by parallel multiple-layers sectioning”, Acta Metall. Sin. 46 (2010) 930.

[15] J.R. Kremer, D.N. Mastronarde and J.R. McIntosh. “Computer visualization of three-dimensional image data using IMOD”, J. Struct. Biol. 116 (1996) 71.

1st International Conference on 3D Materials Science
*Edited by: Marc De Graef, Henning Friis Poulsen, Alexis Lewis, Jeff Simmons, George Spanos*
***TMS (The Minerals, Metals & Materials Society), 2012***

# FIB / SEM DETERMINATION OF SUB-SURFACE DAMAGE CAUSED BY MICRO-TRIBOLOGY SCRATCHING OF WC/Co HARDMETAL SAMPLES

M G Gee, K P Mingard, A J Gant, H G Jones

National Physical Laboratory
Hampton Road, Teddington
TW11 0LW, United Kingdom

Keywords: FIB-SEM, Micro-tribology, Abrasion simulation, WC/Co Hardmetals

## Abstract

WC/Co hardmetals are composite materials that are used in many wear resistant applications. Micro-tribology experiments were carried out on polished samples of WC/Co as model single point abrasion tests to determine the microstructural mechanisms of wear. The mechanisms of wear included plastic deformation and micro-fracture of the WC grains leading to fragmentation of the grains with re-embedment in the binder phase to form layers covering and protecting further damage to the surface.
Ion beam milling with FIB / SEM sectioning and 3D reconstruction was used to characterise the sub-surface damage that occurred beneath scratches. It was found that specific WC grains at the surface fractured, with an increasing number of fragmented grains as the severity of the test parameters was increased. This led to an increased thickness of the re-embedded layer.

## Introduction

WC/Co hardmetals are widely used in applications where resistance to severe abrasion is required such as mining bits, concrete forming tools, and materials handling components. They are two phase materials with the hard WC embedded in a matrix of cobalt metal binder phase. Previous studies have examined the laboratory scale abrasion testing of these materials under a range of test conditions from lightly loaded abrasion contacts with fine abrasive, to heavily loaded abrasion contacts with large hard abrasive particles [1-3].
More recent work has focused on the use of scratch testing as a method for making single point tests to simulate abrasion [4-7]. These experiments have determined that the mechanisms of wear under these conditions include plastic deformation of the WC grains and Co binder phase, microfracture of the WC grains and removal of WC grains, and fragmentation of WC grains with re-embedment of these fragments into the binder phase to form surface layers of nanostructured material on the surface. This re-embedment mechanism is likely to enhance the wear resistance of the surface.
This paper describes the results of an examination of these nanostructured surface layers by FIB-SEM that has the aim of developing an understanding of their formation so that the manufacturers of these materials can optimize their structure for better wear resistance.

## Materials and Methods

The materials that were investigated were WC-Co hardmetals with 11 wt % Co binder phase and grain sizes of 2 μm (mars 11d) and 5 μm (mars 11E), supplied by Marshalls Hardmetals Ltd.

Micro-tribology experiments were carried out with a new micro-tribometer developed for in situ observation of wear damage [8]. The scratches examined in this paper were carried out in the laboratory on samples with a polished surface prepared by standard metallographic techniques. The test conditions were 250 mN or 400 mN as specified, use of diamond indenters with 20 μm or 30 μm radius as specified, a test speed of 100 μm $s^{-1}$ and a track length of 3 mm.
The worn surfaces of the micro-scratches were examined in a high resolution scanning electron microscope, using in lens and conventional secondary detectors to form images.
Selected areas on the scratches were also examined in an Auriga 60 FIB-SEM. Multiple slices were machined perpendicular to the scratch direction to form 3D images stacks of the examined areas. The milling conditions were 30 kV and 2 nA for the gallium ion beam. Images of the sections were taken between ion beam milling of the slices using the secondary in-lens detector and the SESI detector (in secondary electron mode) of the Auriga system. The electron beam voltage was 5 kV, and a tilt correction of 36 $^{o}$ was applied to correct for the tilt of the milled face of the sample. This meant that the surface part of the image had an apparent tilt of 18 $^{o}$.

## Results

Surface examination

Figure 1 shows an example of the evolution of the surface damage at the surface of micro-scratches [7]. After 50 passes there is considerable fracture to the WC grains with some areas where the WC grains have completely fragmented. There is also evidence of plastic deformation in the WC grains as evidenced by slip line traces on the surfaces of some of the grains. After 100 passes further fracture had occurred to the WC grains, and the layer of fragmented and re-embedded WC now covers most of the surface.

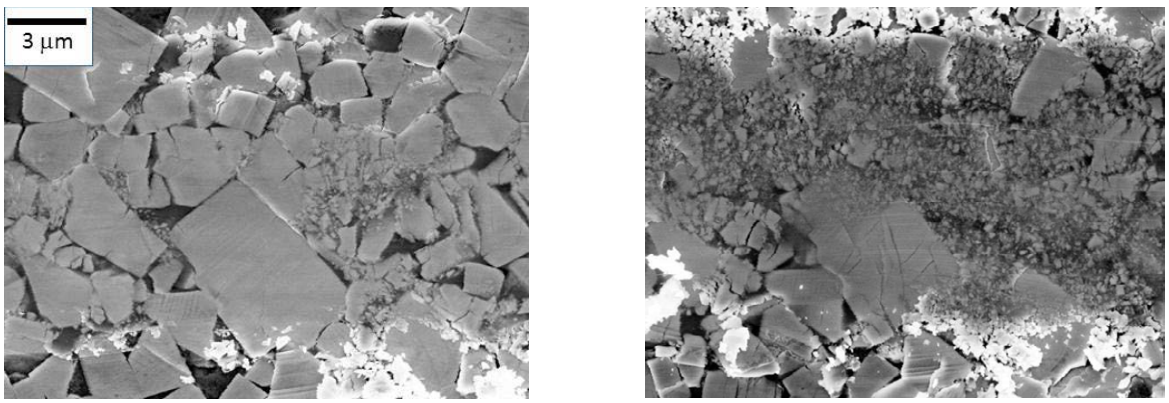


a) b)

Figure 1. Micro-tribology multi-pass scratch on mars11d hardmetal with 30 μm radius indenter and applied load of 400 mN, a) 50 passes, b) 100 passes. Note that a) and b) are exactly the same area of the sample.

FIB-SEM examination

The build-up in damage beneath the micro-scratch as the number of passes increased was examined in a sequence of FIB-SEM analyses. Figure 4b shows the start of a trench machined across a micro-scratch. Figure 2a shows the surface of a ten pass microscratch. There is considerable cracking of the WC grains within and to the edge of the micro-scratch. There is also clear indication of severe damage in the binder phase regions. The FIB sections (Figure 2b) show that the WC cracking does not extend far into the surface. Slip line traces, orientated with the

crystallographic directions of the WC grains were also often observed. Little fragmentation of WC grains has occurred.

As the number of repeat passes increased to 100 more damage took place, with fragmentation of some WC grains and re-embedment into the cobalt binder phase in localized areas (Figure 3). Figure 3a shows that debris has been pushed out from the scratch (Figure 3a). In some cases cracks were formed below and roughly parallel to the surface of the sample (Figure 3b). More fracture of the WC grains occurred with cracks penetrating further below the surface. A particular example of this is shown in Figures 3c and 3d where a crack in a large grain appears to cross the full grain in Figure 3c, but in an image taken when a further 800 nm of material has been removed can be seen to have only partially cracked the large WC grain.

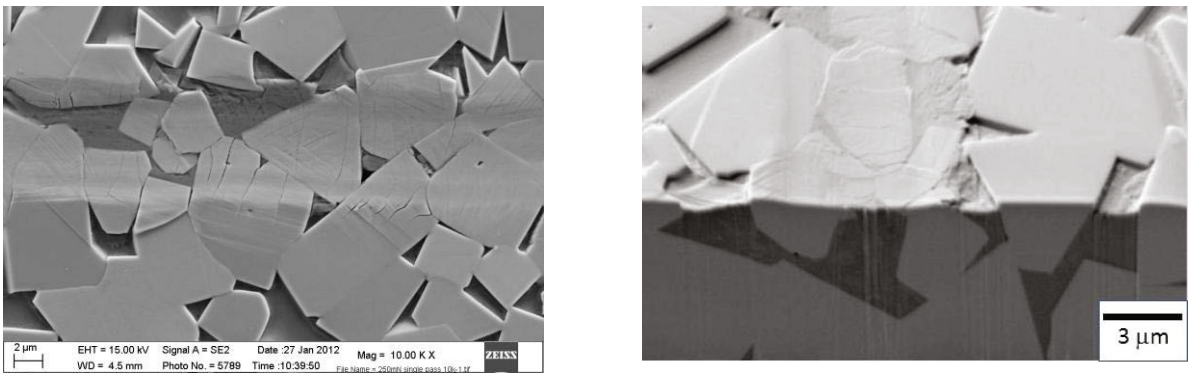


a) b)

Figure 2. Micro-tribology 10 pass scratch on mars11E hardmetal with 20 µm radius indenter and applied load of 250 mN

Figure 4 shows micro-scratches that had been subjected to 200 repeat passes. Figure 4a shows the surface of a micro-scratch revealing considerable fracture damage to most of the WC grains on the surface of the scratch. In some areas the WC gains have been crushed and the resulting fragments have re-embedded into the binder phase. There is also material pressed out to the edges of the scratch. The contrast between the WC grains and the binder phase in the centre of the scratch is much less than outside the scratches. Previous work has shown that this is due to a layer of Co rich material that covers the surface of the scratch [7].
By contrast, the scratch shown in Figure 4b is almost completely covered by a layer of WC grain fragments embedded in cobalt binder phase. The FIB sectioning shows that these layers do not have a uniform depth, and are very thin in places, but extend a few µm below the surface in other places (Figures 4c and 4d). Cracking was also observed in some of these regions.

Scratch dimensions

The FIB sectioning of the surface enables the measurement of the profile of the surface to be measured. The FIB-SEM analyses made on the micro-scratches were always made perpendicular to the sample surface, facilitating these measurements which were made with Image J 1.44P software (http://imagej.nih.gov/ij).
Table 1 gives the results of some of these measurements. The scratch width only increased slowly with the number of scratch passes from 8.3 µm for a single pass scratch to 9.4 µm for a 200 pass scratch. This corresponds to average contact pressures of 9.3 GPa for the single pass scratch decreasing to 7.1 GPa for the 200 pass scratch. The radius of the base of the scratch was also calculated from the width and depth of the scratch. The estimated radius was found to be

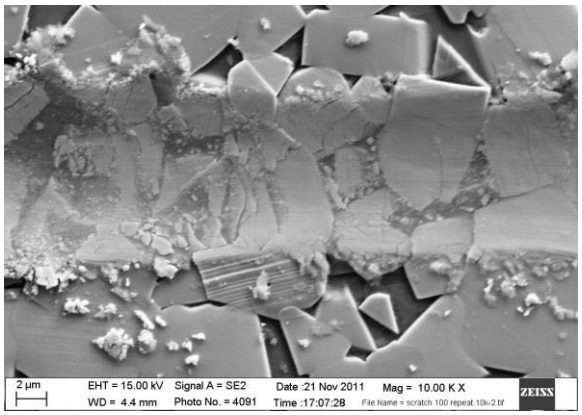


a)

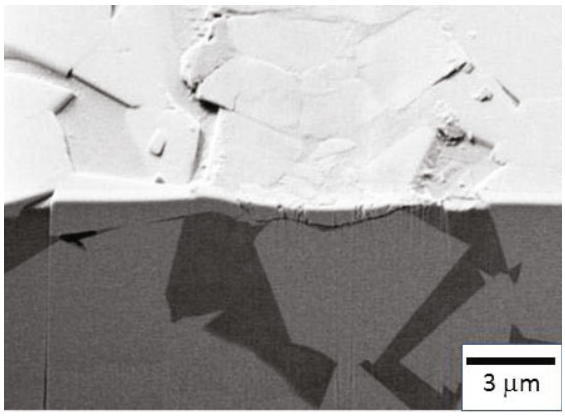


b)

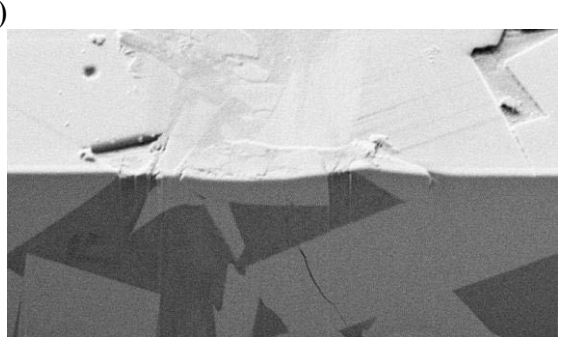

c)

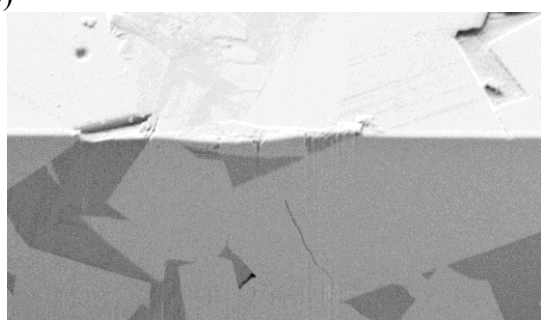

d)

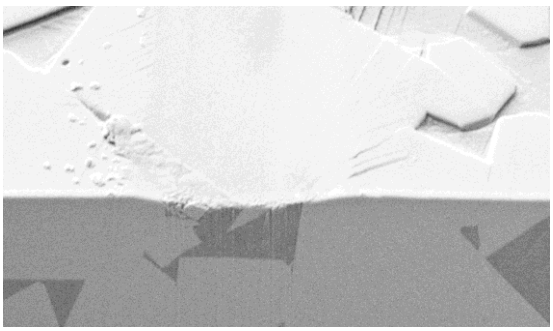

e)

Figure 3. Micro-tribology 100 pass scratch on mars11E hardmetal with 20 µm radius indenter and applied load of 250 mN

near to he actual radius of the indenter, within the uncertainty of measurement. This means that the geometry of the scratch was conformal with the shape of the indenter.

## Discussion

The results shown in this paper show the benefits of FIB-SEM for sub-surface characterization. The ability to target features of interest on a surface and to see how the surface features extend beneath the surface gives key information on mechanisms of damage that could not be achieved in any other way. This includes the measurement of scratch depth which traditionally could only be carried out through laboriously prepared cross-sections through the sample.

Measurements of the scratches showed that there was not much increase in width or depth of the scratch as the number of passes increased. The average pressure calculated from the scratch width thus declines relatively slowly from an initial pressure of 9.3 GPa for a single pass scratch to 7.7 GPa for a 200 pass scratch. The conformal contact conditions, with the scratch geometry

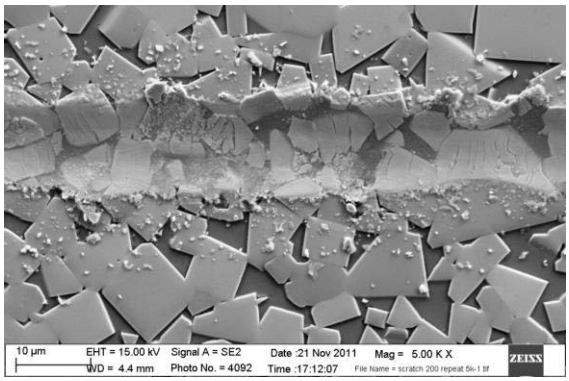


a)


b)

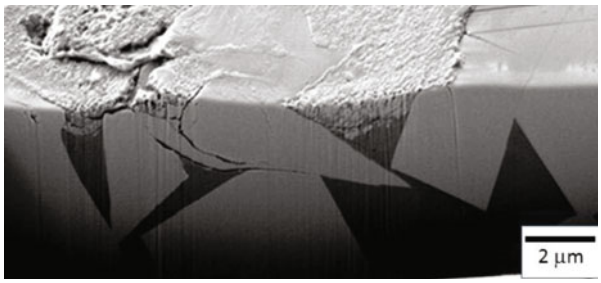


c)

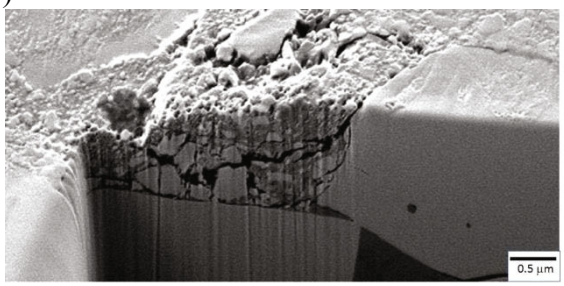


d)

Figure 4. Micro-tribology multi-pass scratch on mars11E hardmetal with 20 µm radius indenter, applied load of 250 mN and 200 passes, a) surface of scratch, b) start of milling across scratch, c) and d) cross-section across scratch

Table 1, Measurements of scratch parameters. Values are means of 5 measurements.

| Passes | Value | | | Standard Deviation of Value | | | Contact Pressure, GPa |
|---|---|---|---|---|---|---|---|
| | Scratch Width, µm | Scratch Depth, µm | Estimated Radius of Probe, µm | Scratch Width, µm | Scratch Depth, µm | Estimated Radius, µm | |
| 1 | 8.3 | 0.44 | 19.7 | 0.3 | 0.05 | 5 | 9.3 |
| 10 | 8.5 | 0.40 | 22.6 | 1.2 | 0.05 | 8 | 8.8 |
| 100 | 8.8 | 0.46 | 21.0 | 0.9 | 0.07 | 5 | 8.3 |
| 200 | 9.4 | 0.51 | 22.0 | 0.7 | 0.03 | 3 | 7.1 |

the same as the indenter geometry, shows that the indenter sinks into the WC/Co sample until the load transmitted through the moving indenter is accommodated by the sample. Further passes of the scratch over the sample increase the damage and reduce the capability of the sample to support the test load so that the width and therefore the depth of the scratches gradually increase with number of passes. Measurements of the dimensions of features will depend critically on the calibration of the magnification, tilt angle and tilt angle correction, so care needs to be taken to address these issues.

The initial deformation that takes place on the first pass scratch is cracking of the WC grains and deformation of the cobalt. These allow overall deformation to take place accommodating the shape of the indenter, with some material squeezed out to the side of the scratch. As further passes take place, more fracture and fragmentation of the WC grains occurs, with re-embedment of many of the fragments in binder phase forming layers of material on the surface of the scratch. Some material is removed completely from the scratch to form debris at the sides of the scratch.

In the FIB work presented in this paper, the surfaces of the scratches were not protected by laying down a metal on the surface before FIB sectioning. An advantage of this was that the surface of the scratch could be observed simultaneously with the FIB section allowing for an

understanding of how sub-surface damage contributed to surface features. Some rounding of the edge of the FIB section was seen. This did mean that it was difficult to define the edge of the scratch accurately on the FIB cross section, so that measurement accuracy, would be improved if a protective metal layer was deposited before FIB sectioning.
Much more work needs to be carried out before a full understanding of the processes of damage during abrasion of WC/Co hardmetals can be developed. Thus the response of different compositions of hardmetals to micro-tribology scratches needs to be examined to give information on how the mechanism of the formation of structured layers depends on microstructure. More FIB-SEM sectioning of selected fragmented areas would provide 3D datasets of the fragmented and layered regions. EBSD analysis of the re-embedded areas would also give important information about the crystallinity and plastic deformation of the carbide fragments in the fragmented regions.

## Conclusions

FIB-SEM sectioning has been successfully applied to the examination of the sub-surface structure of damage caused to a WC/Co hardmetal by micro-tribology scratches. It was found that when a single pass took place, fracture of the WC grains and deformation of the cobalt binder phase took place. As the number of passes increased, fracture to the WC grains increased leading to fragmentation and re-embedment of the WC fragments in the binder phase giving structured layers that covered the samples.

## Acknowledgements

The authors would like to thank the UK National Measurement Office for funding.

## References

1. A J Gant, M G Gee and A T May, **Microabrasion of WC-Co Hardmetals in Corrosive Media**, Wear, 256(2004)954-962.
2. A J Gant, M G Gee and B Roebuck, **Rotating Wheel Abrasion of WC/Co Hardmetals**, Wear, 258(2004)178-188
3. M.G Gee, A. Gant, B Roebuck, **Wear mechanisms in abrasion and erosion of WC/Co and related hardmetals**, Wear 263 (2007) 137–148
4. U Beste, A Lundvall, et al. **Micro-scratch evaluation of rock types - A means to comprehend rock drill wear**. Tribology International 37 (2004) 203-210.
5. S Ndlovu, K Durst, M Goken, **Investigation of the sliding contact properties of WC-Co hard metals using nanoscratch testing**, Wear 263 (2007) 1602–1609
6. M G Gee, **Model Scratch Corrosion Studies for WC/Co Hardmetals**, Wear 268 (2010) 1170–1177
7. M G Gee and L Nimishakavi, **Model Single Point Abrasion Studies on WC/Co Hardmetals**, Proceedings of 17th Plansee Seminar 2009 vol 3 pp AT7/1-7 and Int Journal of Refractory and Hard Materials, 29 (2011) 1–9
8. M G Gee, J W Nunn and A Muniz-Piniella, **Microtribology Experiments on Engineering Coatings**, Wear 271 (2011) 2673– 2680
9. M.G. Gee, K.P. Mingard And B. Roebuck, **Application of EBSD to the Evolution of Plastic Deformation in Mechanical Testing of WC/Co Hardmetal,** International Journal of Refractory and Hard Materials, 27(2009)300-312.

1st International Conference on 3D Materials Science
*Edited by: Marc De Graef, Henning Friis Poulsen, Alexis Lewis, Jeff Simmons, George Spanos*
***TMS (The Minerals, Metals & Materials Society), 2012***

# 3D CHARACTERIZATION OF RECRYSTALLIZATION BOUNDARIES

Yubin Zhang[1], Andrew Godfrey[2], Nicole MacDonald[3], Dorte Juul Jensen[1]

[1] Danish-Chinese Center for Nanometals, Materials Science and Characterization Section, Institute of Wind Energy, Technical University of Denmark, DK-4000 Roskilde Denmark
[2] Laboratory of Advanced Materials, Department of Materials Science and Engineering, Tsinghua University, Beijing 100084, P.R. China
[3] Center for Electron Nanoscopy, Technical University of Denmark, DK-2800 Kongens Lyngby, Denmark

Keywords: grain boundary, recrystallization, aluminum, protrusion/retrusion

## Abstract

A three-dimensional (3D) volume containing a recrystallizing grain and a deformed matrix in a partially recrystallized pure aluminum was characterized using the 3D electron backscattering diffraction technique. The 3D shape of a recrystallizing boundary, separating the recrystallizing grain and deformed matrix, was reconstructed. The result shows a very complex structure containing several large protrusions and retrusions. A correlation between the protrusions/retrusions and the deformed matrix in front of the boundary shows that the deformed microstructure has a very strong influence on the formation of protrusions/retrusions.

## Introduction

The migration of recrystallizing boundaries is important for the recrystallization process and, as a result, the recrystallization texture [1]. Microstructural characterization using electron microscopy and three-dimensional x-ray diffraction (3DXRD) have shown that the recrystallizing boundary and its migration are very inhomogeneous: a recrystallizing boundary migrates generally in a stop-go fashion, and consists of many protrusions and retrusions on a local scale [2-4]. Ex situ and in situ investigations [5,6] of the migration of individual recrystallizing boundaries have revealed that the formation of pro-/re-trusions may be important for the migration of recrystallization boundaries and can partly explain the observed stop-go motion. More recently phase-field model simulations [7] have provided evidence to suggest that the existence of pro-/re-trusions can lead to an increase in the migration velocity compared to a flat boundary.

Clear observations of pro-/re-trusions can be traced back to the classical work of Beck and Sperry from the 1950's [8]. However, only in the past few years, after the publication of in situ 3DXRD experiments [2] have detailed investigations focusing on these local features been reported [3-7,9-11]. These include several simulation methods: molecular dynamic simulations [12,13], phase-field simulations [7], and numerical analysis [10,11], all of which have been used to investigate the effects of heterogeneity in the deformed microstructure on the formation of pro-/re-trusions. Due to the fact that highly idealized microstructures have been used in all these simulations, none of these approaches can be applied directly for the interpretation of experimental data, because large and non-regular heterogeneities exist in the deformed matrix.

The results of previous 2D investigations suggest that the average size of pro-/re-trusions cannot simply be correlated with the stored energy in the deformed microstructure in front of recrystallizing boundary [5, 9]. It has also been suggested however that in order to fully understand the formation of pro-/re-trusions, the microstructure in the third dimension (i.e. below observed surface) also needs to be considered, because i) the mobility of the recrystallizing

boundary may depend on the boundary plane, and ii) the deformed microstructure in the third dimension may affect the formation of pro-/re-trusions [6, 9]. The present study is therefore focused on characterization of a recrystallizing boundary and the neighboring deformed microstructure in 3D.

## Experiment

The material used for this study was 99.996% pure aluminum. The material was first annealed at 550°C for 24h to obtain a grain size of several millimeters, followed by cold rolling to 50% reduction in thickness. The deformed samples were annealed at 250°C for 10 minutes to obtain partially-recrystallized microstructures. After grinding using silicon carbon paper down to 4000 followed by mechanical polishing to 1μm, the specimen was electropolished on the longitudinal sections (defined by the sample rolling direction (RD) and normal direction (ND)) in a Struers A2 solution.

3D-EBSP mappings were carried out using an FEI Helios Nanolab 600 DualBeam$^{TM}$ platform consisting of focused ion beam (FIB) and field emission gun SEM (FEGSEM) columns, and interfaced with a TSL$^{TM}$ EBSP facility (details of these techniques can be found in [14,15]). The recrystallizing boundary was by chance near one of the sample edges which was parallel to ND (see Figure 1), which minimized the milling work required to alleviate problems with shadowing during the EBSP mapping. Before the 3D serial sectioning was performed, the adjoining perpendicular rough surface, which was not electropolished, and which was connected to this edge on the transverse plane (defined by ND and the transverse direction (TD)) was cleaned using FIB by making a rough cut with a current of 20nA, followed by a final polishing with a current of 2nA. A ~1μm layer of Pt was then deposited on this surface (facing the ion beam during serial sectioning) to minimize damage from the ion beam (see Figure 1). A fiducial mark was also made on this surface next to the platinum layer, and this was used to automatically align the sample during the serial sectioning. An in-house computer program was used for the automated movement of the sample between consecutive FIB milling and EBSP mapping steps. The sample was consecutively milled perpendicular to the Pt layer using an accelerating voltage and current of 30kV and 2nA, respectively. Each milling stage removed a layer of material of 0.5 μm in thickness. In total 40 milled surfaces on the ND-RD section were mapped by EBSP using an electron beam step size, accelerating voltage and probe current of 0.5μm, 15kV and 2.1nA, respectively. During scanning the Pt layer was also mapped, and appeared as lines consisting of non-indexed points in the EBSP maps, which are ideal features for the post-mapping alignment of the EBSP maps.

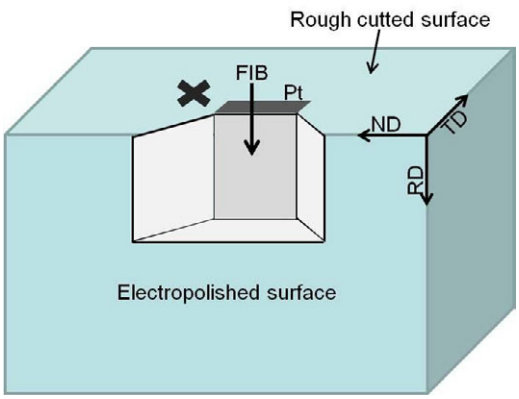


Figure1. Sketch of sample showing the geometry of milling and EBSP mapping

## Result and discussion

An EBSP map of the microstructure of a typical RD-ND section, together with its {111} pole figure is shown in Figure 2. The color code in this map is based on the RD inverse pole figure. A recrystallizing boundary consisting of several pronounced pro-/re-trusions separates the recrystallizing grain and the deformed matrix. In the deformed matrix, two set of intersecting boundaries, inclined about ±35°to RD, can be clearly seen. This is a typical deformed microstructure after medium strain deformation and some recovery of pure aluminum [16,17].
On the bottom of the map, a region corresponding to the Pt layer (see Figure 1) is seen, and this was used as the reference for sample alignment. During alignment, the rotation between any two neighboring layers was ignored and only the translation along RD was considered.
The 3-D reconstructed microstructure consisting of the 40 sections is shown in Figure 2c, in which the reconstructed RD-TD and ND-TD sections can be seen. The bands seen in the RD-ND section continue along TD and are nearly parallel to TD. This has also been reported in TEM observations [18, 19]. The pro-/re-trusions on the RD-TD section are on average more flat than those on the RD-ND section.

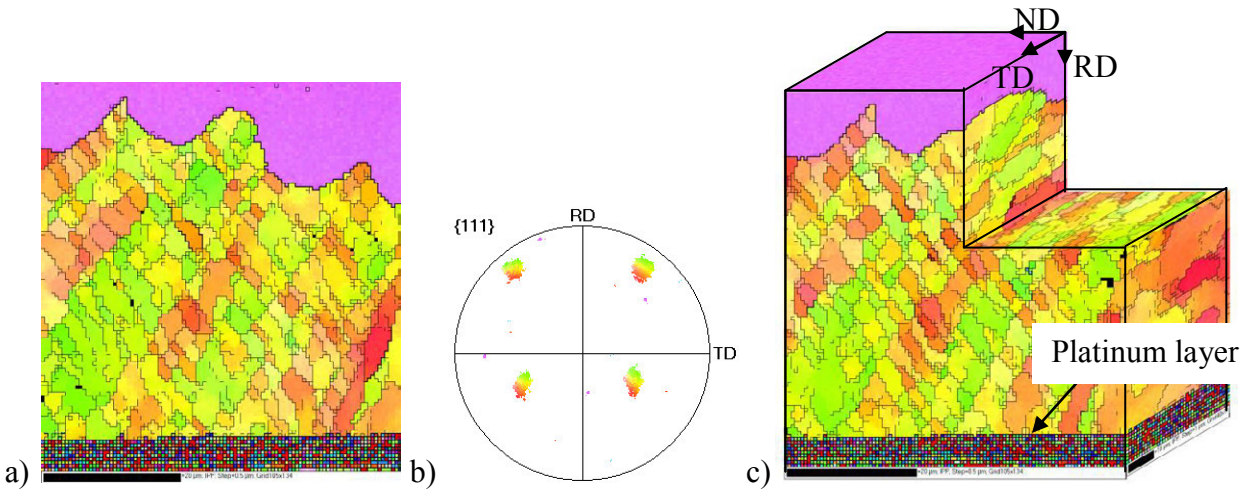


Fig. 2 EBSP map showing a typical section of the microstructure seen in a RD-ND section a) and its corresponding pole figure b); c) 3D volume showing the reconstructed microstructure.

In order to see the 3D shape of the recrystallizing boundaries, a subset of the deformed matrix in each slice was extracted from the EBSP maps, and a 3D volume of the deformed microstructure was reconstructed. In Figure 3 two different views of the reconstructed deformed microstructure are shown, in which the reconstructed top surface of this volume represents the 3D shape of the recrystallizing boundary, showing clearly heterogeneity of the pro-/re-trusions in different sample directions. It is interesting to note that in 3D the pro-/re-trusions are not isolated peaks but elongated ridges along TD. There are also some areas which are rather flat, which is in agreement with the 3DXRD observations [20] and the analysis of facet migration [4].

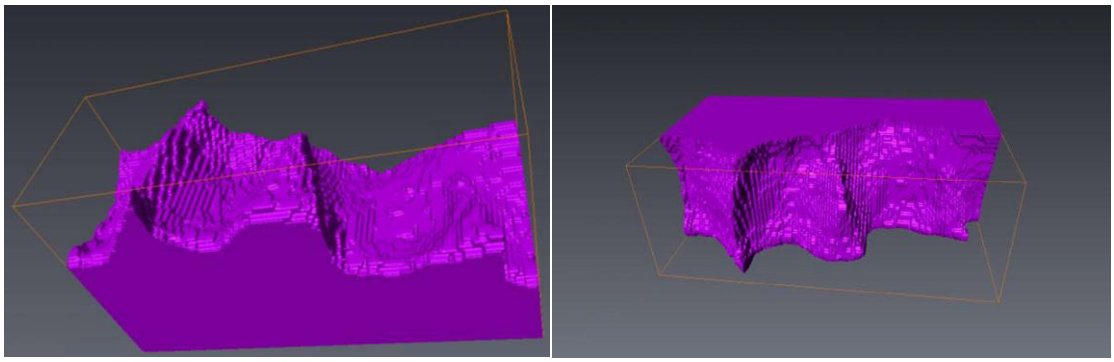

Figure 3. Two views of the recrystallizing boundary surface; the solid purple volume is the deformed matrix.

The EBSP maps contain also orientation information, from which the misorientation across the recrystallizing boundary can be obtained. Figure 4 shows the same 3D recrystallizing boundary in a new way using colors which represent the misorientations across the boundary at each location. The corresponding misorientation rotation axes and angles for all pixels on the boundary are also shown in the inverse pole figure and color bar, respectively.

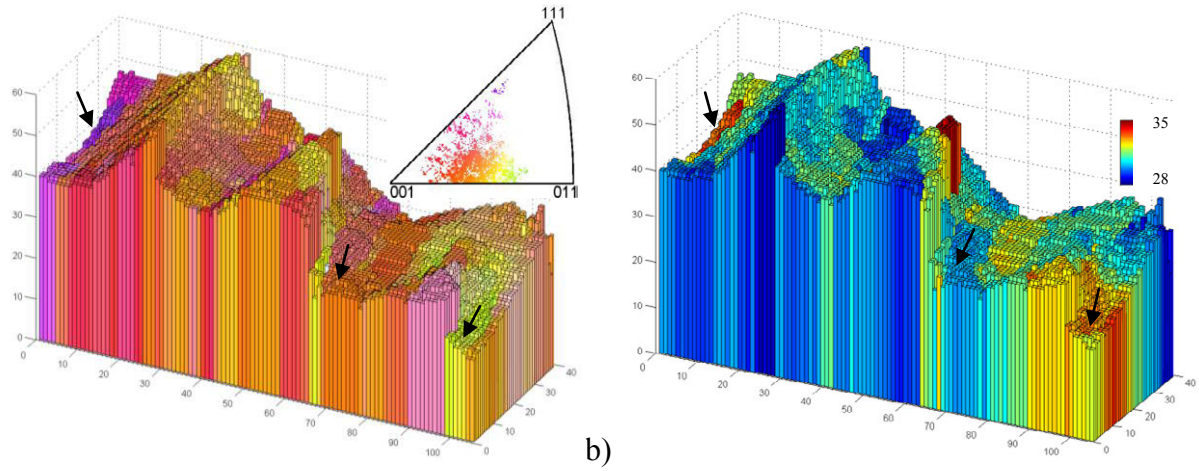


a) b)

Figure 4. The 3D recrystallizing boundary shown in different colors which are converted from the misorientation rotation axes a) and angles b). The color code for the misorientation rotation axis is the same as that used in inverse pole figure (see insert to Figure 4a), while for the misorientation angle a linear color code from blue to red was used (see insert to Figure 4b).

It can be seen that the colors (hence misorientations) at the protrusions are quite mixed. For example, the protrusions marked by black arrows have wide range of misorientation rotation axes (purple, light green or orange in the figure), and the misorientation angles can be either low or high. Similar observations are found for the boundary segments on the retrusions. Moreover, there appears to be also no systematic difference in color between the boundary segments on the protrusions and on the retrusions. This implies that there is only a relatively small difference in misorientation between segments on protrusions and on retrusions. However, it should be stressed that this does not mean that the local mobility has no effect on the formation of pro-/re-trusions. The mobility depends not only on the misorientation but also on the boundary plane, and this needs to be further analyzed before conclusions can be drawn.

Boundary pinning at solutes or second-phase particles, which is often seen in alloys, cannot be ruled out with regard to the formation of pro-/re-trusions. However, based on the frequency with which pro-/re-trusions are seen in ultra pure, normal purity and less pure materials, it is suggested that the heterogeneity in the deformed microstructure may be the main reason for the formation of protrusions/retrusions in pure materials.
In the deformed matrix, the dislocation boundaries on RD-TD section are elongated along TD and are more or less parallel to TD (Figure 2c). Two examples of extended band structures subtracted from the deformed matrix are shown in Figure 5, where 2° is used to detect dislocation boundaries. In both cases the whole band of dislocation structure is more or less parallel to TD. Figure 5 therefore clearly shows that the actual 3D bands in the deformed microstructure can reasonably be represented as by the 2D microstructure on RD-ND section. The 3D shape of the recrystallizing boundary (Figure 3) also shows a little variation along TD. This clearly indicates that the extended band deformation structure along TD has a strong influence on the 3D shape of pro-/re-trusions.

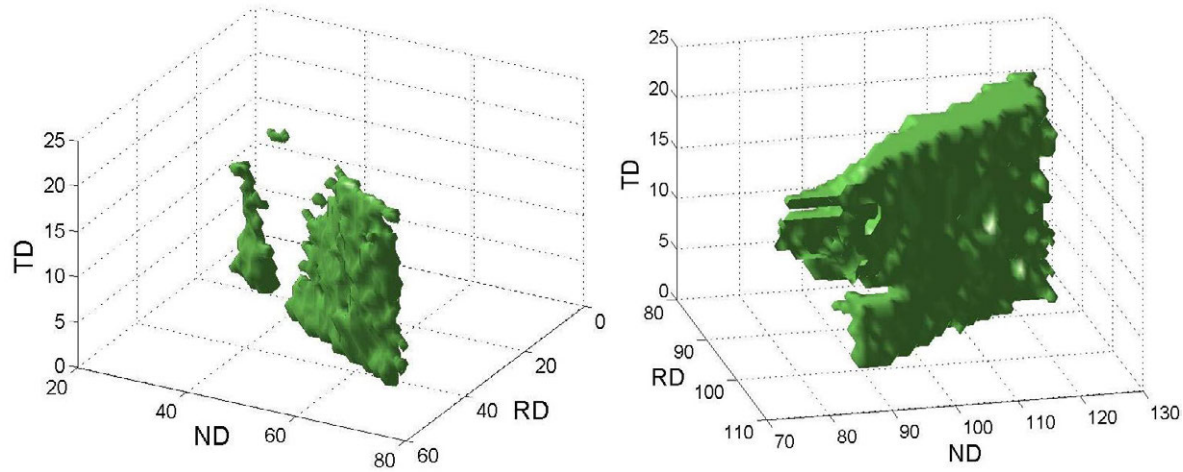


Figure 5. Two examples showing the 3D band structure in the deformed matrix.

It is important to point out that the deformed microstructure which has induced the formation of pro-/re-trusions that is seen in the microstructure, is the one which has already been ‘eaten’ at this stage. Therefore, it would be very interesting to perform experiments to observe in-situ the recrystallizing grain growing into variously oriented deformed matrices in full 3D, where the true correlation between deformed matrix and pro-/re-trusions can be obtained.

## Summary

In the present paper a 3D recrystallizing boundary and the deformed matrix in front of the boundary has been characterized using the 3D EBSP technique. The results show that the recrystallizing boundary has a very complex shape in 3D, consisting of large protrusions and retrusions. The pro-/re-trusions are more pronounced on the RD-ND section than on the RD-TD section. It has also been found that the deformed matrix has a strong influence on the formation of protrusion and retrusions.

## Acknowledgement

The authors gratefully acknowledge support from the Danish National Research Foundation and the National Natural Science Foundation of China (Grant No. 50911130230) for the Danish-Chinese Center for Nanometals, within which this work was performed.

**References:**

1. F. Haessner, *Recrystallization of metallic materials*. (Dr. Riederer Verlag GmbH Stuttgart, 1978).
2. S. Schmidt et al., "Watching the growth of bulk grains during recrystallization of deformed metals, " *Science*, 305(2004), 229-232.
3. Y.B. Zhang et al., "Analysis of the growth of individual grains during recrystallization in pure nickel, " *Acta Mater.* 2009;57: 2631-2639.
4. S. Van Boxel et al., "Monitoring grain boundary migration during recrystallisation using topotomography, " *Proceeding of the 31st Risø International Symposium* (2010), 449-456.
5. Y.B. Zhang, A. Godfrey, D. Juul Jensen, "Local boundary migration during recrystallization in pure aluminum, " *Scripta Mater.* 64(2011), 331-334.
6. Y.B. Zhang, A. Godfrey, D. Juul Jensen, "In-situ observations of migration of recrystallization boundaries in pure aluminium," *Proceeding 31st Risø International Symposium.* (2010), 497-503.
7. N. Moelans et al., to be submitted for publication.
8. P.A. Beck, P.R. Sperry, H. Hu. "The orientation dependence of the rate of grain boundary migration," *J Appl Phys* 21(1950),420-425.
9. Y.B. Zhang, A. Godfrey, D. Juul Jensen, "Measurements of the Curvature of Protrusions/Retrusions on Migrating Recrystallization Boundaries," *Computers, Materials & Continua* 14(2009), 197-207.
10. M.A. Martorano, M.A. Fortes, A.F. Padilha, "The growth of protrusions at the boundary of a recrystallized grain," *Acta Mater.* 54(2006), 2769-2776.
11. M.A. Martorano et al., "Observations of grain boundary protrusions in static recrystallization of high-purity bcc metals," *Scripta Mater* 56(2007), 903-905.
12. R.B. Godiksen et al., "Simulations of boundary migration during recrystallization using molecular dynamics," *Acta Mater.* 55(2007), 6383-6391.
13. R.B. Godiksen, S. Schmidt, D. Juul Jensen, "Molecular dynamics simulations of grain boundary migration during recrystallization employing tilt and twist dislocation boundaries to provide the driving pressure," *Modeling Simul Mater Sci. Eng.* 16(2008), 065002.
14. S. Zaefferer, S.I. Wright, D. Raabe. "Three-Dimensional Orientation Microscopy in a Focused Ion Beam–Scanning Electron Microscope: A New Dimension of Microstructure Characterization," *Metal. Mater. Trans.* 39A(2007), 374-389.
15. M.D. Uchic et al., "Three-Dimensional Microstructural characterization Using Focused Ion Beam Tomography," *MRS Bulletin.* 32(2007), 408-416.
16. X. Huang, G. Winther, "Dislocation structures. Part I. Grain orientation dependence," Phil. *Mag.*, 87(2007), 5189-5214.
17. F.J. Humphreys, M. Hatherly, *Recrystallization and Related Annealing Phenomena, second ed.* (Pergamon Press, Oxford 2004).
18. G. Winther, X. Huang, "Dislocation structures. Part II. Slip system dependence," *Phil. Mag*. 87(2007), 5215-5235.
19. D. Juul Jensen, N. Hansen, "Flow stress anisotropy in aluminium," *Acta Metall. Mater.* 38(1990),1369-1380.
20. D. Juul Jensen, D.J. Rowenhorst, S. Schmidt, "Misorientation Aspects of Growth During Recrystallization," *Mater. Sci. Forum.* 558-559(2007), 85-92.

1st International Conference on 3D Materials Science
*Edited by: Marc De Graef, Henning Friis Poulsen, Alexis Lewis, Jeff Simmons, George Spanos*
***TMS (The Minerals, Metals & Materials Society), 2012***

# DEVELOPMENT OF FULLY AUTOMATED SERIAL-SECTIONING 3D MICROSCOPE AND TOPOLOGICAL APPROACH TO PEARLITE AND DUAL-PHASE MICROSTRUCTURE IN STEELS

Yoshitaka Adachi[1], Naoko Sato[2], Mayumi Ojima[3], Makoto Nakayama[4], Yuan-Tsung Wang[5]

[1]Kagoshima University, 1-21-40 Korimoto, Kagoshima 890-0065,Kagoshima JAPAN
[2]Kyushu University, 744 Motooka, Nishi 819-0395, Fukuoka JAPAN
[3]Tokyo University, Hongo, Bunkyoku 113-8656, Tokyo, JAPAN
[4]Nakayama Denki Co. Ltd, 2-7-23 Okayamahigashi, Shijonawate 575-0003, Osaka, JAPAN
[5]China Steel Corporation, 1 Chung Kang Road, Siaogang District 81233, Kaohsiung, TAIWAN

Keywords: Fully automated serial-sectioning microscope, topology, differential geometry, pearlite, dual-phase steel

## Abstract

Using a newly developed fully automated serial-sectioning three-dimensional (3D) microscope, Genus_3D, and a conventional dual-beam SEM, we examined ferrite–martensite dual-phase and eutectoid pearlite microstructures. In particular, we consider the topology and differential geometry. Genus, Euler characteristics, Gaussian curvature, and mean curvatures were obtained from 3D reconstructions. A variation in the martensite morphology in dual-phase steel, i.e., connectivity, was examined to understand the ductile fracture mechanism. In addition, we investigated the 3D morphological variation of lamellar cementite in pearlite during spheroidizing. This 3D observation revealed many holes and fissures in cementite lamellae, which potentially accelerate the spheroidization. The disintegration of lamellar structure into particles was discussed with respect to surface area change per unit volume and local surface morphology (i.e., curvature).

## Introduction

Three-dimensional (3D) visualization of a microstructure holds promise as a key to understand its complicated morphology. Furthermore, a quantification of the 3D volume set of a microstructure is essential to correlate 3D reconstruction with the microstructure evolution mechanism as well as mechanical properties. The serial sectioning technique is a well-known procedure for obtaining 3D microstructure; focused ion beam–scannning electron microscope-electron backscatter diffraction (FIB–SEM-EBSD), or the mechanical polishing-optical microscope technique has been applied to obtain 3D serial-sectioning images. However, this sectioning approach is time consuming and it takes a week or more to capture a set of 100 sectioning images.

To quantitatively correlate 3D reconstruction with the transformation mechanism as well as mechanical properties, a mathematical evaluation of the 3D reconstruction is absolutely required[2-7)]. The remarkable benefits of 3D characterization are its ability to evaluate both the connectivity and the curvature of microstructures. Connectivity is examined by a topological approach using Euler characteristics or genus, whereas curvature is assessed by differential geometry using principal, mean, or Gaussian curvature. Here Euler characteristics and genus are

deduced by counting the number of nodes, edges, faces, and cells of 3D reconstructions that are meshed by triangulation through the Euler–Poincare formula and the Gauss–Bonnet theorem.

Although microstructures in steels are generally complicated, their evaluation in terms of average metric properties such as length, area, or volume fraction is probably inadequate to quantify the microstructural morphology. From the environmental viewpoint of conserving alloying elements, a challenging subject in steel science is the intensive control of microstructural morphology. To satisfy this requirement, it may be essential to quantitatively assess the microstructural morphology.

This study intends to understand both the spheroidization of pearlite in a eutectoid steel and the brittle fracture mechanisms of a ferrite–martensite dual-phase (DP) steel by highlighting the connectivity and local curvature of their microstructures in 3D images. In addition, a fully automated serial-sectioning 3D microscope is introduced as an efficient serial-sectioning device.

## Experimental procedure

The chemical compositions (in mass percentage) of the steels used in this study were 0.8C–Fe for the pearlite study and 0.15C–0.10Si–1.00Mn–0.86Ni–0.76Cr–0.25Mo–Fe for the DP steel study.

Hot-rolled 0.8C steel specimens were reaustenitized at 1200 °C for 30 min followed by cooling in a furnace to room temperature at 1 °C/s. Subsequently, the specimens were isothermally annealed at 700 °C for 0, 60, and 360 min followed by furnace cooling at 1 °C/s to room temperature. The hot-rolled DP steel specimen was cold rolled and subsequently annealed at 1023 K for 1.8 ks, followed by air cooling to an ambient temperature. The steel was deformed during a tensile test at room temperature until it fractured.

A double-beam SEM (SII-Zeiss XVision200DB) and a fully automated serial-sectioning 3D microscope (Genus_3D) (Fig.1) [1)] were used to observe 3D tomography of pearlite and DP microstructures, respectively. Genus_3D based on an optical microscope saves time in serial-sectioning tasks. The sectioning interval for FIB–SEM observation was set at 100 nm, and approximately 92 total sections existed for every condition. Prior to the FIB–SEM operation, 5 mm × 3 mm × 3 mm specimens were mechanically polished on two sections perpendicular to each other, to achieve a sharp edge and a damage-free surface. The FIB–SEM observation was performed without etching. For the DP microstructure, 20 serial sections were obtained with Genus_3D, for which the polishing interval was approximately 1 μm. Using Genus_3D, we can obtain 100 sectioning images reproducibly within a day. Moreover, the serial sectioning images captured by Genus_3D are well aligned because a specimen is moved only vertically toward an optical microscope lens. In addition, an image-based autofocus function has been implemented in Genus_3D, so that a sharp image is reproducibly obtained despite varying the distance between the specimen and the microscope lens. In fact, polishing, abrasive spraying, etching, rinsing, drying, and image capturing are fully computer automated. Because Genus_3D is optical microscope based, a grain size of several microns is visible; for finer microstructures, another method such as FIB–SEM should be used.

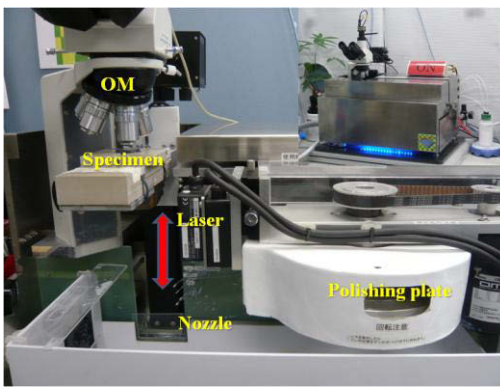

Figure 1 Fully automated serial sectioning 3D microscope "Genus_3D".

The cross section of a non-etched microstructure was observed to locate the voids just under the fracture surface and subsequently an identical region was observed after etching. The etchant

used in this study was a 3% nital solution. In the Genus_3D system, an optical microscope (Wraymer BM3400T) fitted with a digital camera (Shimadzu MOTICAM2000) was implemented.

The images acquired via serial sectioning were reconstructed to a 3D volume by stacking and aligning them with the Avizo Fire (Visualization Sciences Group) and MAVI software (Fraunhofer ITWM) packages, which provided image processing, visualization, and microstructural, and quantitative analysis.

*Surface curvature*

Two parameters can be used to characterize the surface curvature: the mean curvature, H, and the Gaussian curvature, K, given as follows:

$$\mathrm{H} = \frac{1}{2}\left(\frac{1}{\mathrm{R}_1} + \frac{1}{\mathrm{R}_2}\right) = \frac{1}{2}\left(k_1 + k_2\right) \qquad (1)$$

$$\mathrm{K} = k_1 \times k_2 \qquad (2)$$

where $k_1$ and $k_2$ represent two principal curvatures having the maximum and minimum values among all the normal curvatures, respectively. These principal curvatures are defined as $k_1 = 1/\mathrm{R}_1$ and $k_2 = 1/\mathrm{R}_2$, where $\mathrm{R}_1$ and $\mathrm{R}_2$ are the principal radii of the respective curvatures tangential to the surface patch. Figure 2 shows a map of different surface-shape contours for the mean and Gaussian curvature plots (H-K plot). This map provides us with the following information:

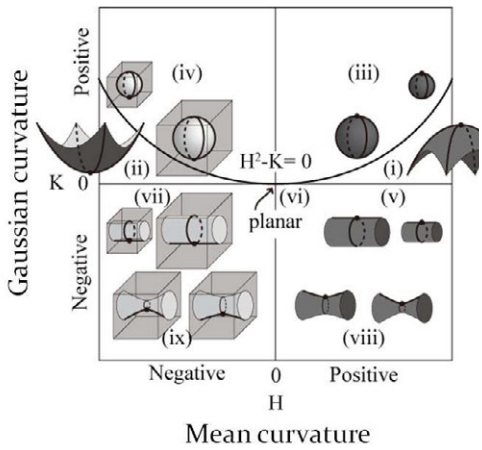


Fig.2 Mean-Gaussian curvature plot.

- Solving the Eqs. (1) and (2) provides the relationship $\mathrm{H}^2 - \mathrm{K} \geq 0$. Curvatures that lie on the parabola described by $\mathrm{H}^2 - \mathrm{K} = 0$ correspond to spherical local surface shapes, as shown in Fig. 2. If H is positive, the surface has a spherical shape of the α phase; if H is negative, the surface has a spherical shape of the β phase. Furthermore, if H = 0 and K = 0, the surface is locally flat or planar.
- If a point on the surface has a positive Gaussian curvature, the concavity of the surface is determined by the sign of H. If H is positive, the surface is concave toward the α phase; if H is negative, it is convex toward the α phase.
- An interface with K = 0 has a cylindrical surface composed of the α phase (if H is positive) or the β phase (if H is negative) and it is also equal to the cylindrical α phase within the planar β phase or the cylindrical β phase within the planar α phase.
- Saddle-shaped surfaces are characterized by a negative Gaussian curvature.

Therefore, in this study, the complex surface geometries are quantified with the probability distribution of the mean and Gaussian curvatures (the so-called H-K plot).

*Surface topology*

The topology of 3D surfaces is related to the volume integral of the Gaussian curvature ($\mathrm{K}_{total}$) by the Gauss–Bonnet theorem and can be expressed by Eq. (4):

$$g = 1 - \chi_3 = 1 - \frac{\mathrm{K}_{total}}{4\pi} \qquad (4)$$

where $g$ and $\chi_3$ are the genus and the Euler characteristic, respectively. These quantities depend only on the topology of the surface and not on its shape. For instance, the genus represents the number of holes in a closed surface. If a sphere and any other polyhedron have no holes in the

closed surface, the integral Gaussian curvatures ($K_{total}$) are equal to $4\pi$ and have a genus of zero. Attaching a hole to the structures decreases $K_{total}$ by $4\pi$ and increases the genus by 1. However, if the curvature information of a surface is not available, the Euler characteristic can also be obtained by triangulating the 3D surface and then counting the number of nodes *n*, edges *e*, faces *f*, and cells (polygon) *c* as expressed in Eq. (5):

$$\chi_3 = 1 - g = n - e + f - c \tag{5}$$

Thus, for a simple cube or a solid body, the structure is topologically equivalent to a sphere and g = 0, resulting in $\chi_3 = 1$. However, if the cube or the body is not closed, $\chi_3 \neq 1$ and Eq. (5) must be used to determine $\chi_3$. For example, if a square hole or a tunnel passes completely through a cube, the results are $n = 16$, $e = 36$, $f = 24$, and $c = 4$, giving $\chi_3 = 0$ and $g_v = 1$. Therefore, the shape would be topologically equivalent to a torus.

In addition to the quantitative measurement of the microstructure connectivity, the genus can also express shape instabilities, such as the breakage of cylindrical or long narrow ribbon structures through Rayleigh or surface energy instability, respectively. Therefore, the morphological instability of the cylinder hole or tunnel eventually decomposes into a row of spheres, a completely enclosed void is created, and the structure is topologically equivalent to a cubic void within a cube, where $n = 16$, $e = 32$, $f = 24$, and $c = 6$, resulting in $\chi_3 = 2$ and $g = -1$. In these cases, the topological characterization of holes or voids within only one independent body can be properly expressed by Eq. (5); however, it must also consider the number of independent bodies for application to topologically complex systems. The morphological instability of the structural decomposition decreases the genus by 1. Moreover, it is evident that a structure with a single void has a genus of -1. Thus, both cases decrease the genus by 1, but creating a hole in the structure increases the genus by 1. Provided that there is a relationship among *g*, *h*, *b*, and *v*, the genus (*g*) can be expressed by Eq. (6):

$$g = h - (b + v) + 1 \tag{6}$$

where *h*, *b*, and *v* denote the number of holes, independent bodies, and voids, respectively. This equation is applicable to both general and complex topological material systems. For instance, if there is one body, the genus is given by $g = h - (1 + v) + 1 = h - v$. The terms *h* and *v* correspond to continuous and discontinuous second phases embedded in a matrix phase, respectively. This means that, in general, *g* can be used as a fingerprint to determine the continuity of the second phase. However, if $b > v$, the meaning of *g* becomes more complex and a parameter to adjust the relationship among *h*, *b,* and *v*. If there are two bodies, adding a tunnel to one of them, $h = 1$, $b = 2$, and $v = 0$, gives $g = 0$ and $\chi_3 = 1$. This result is in good agreement with that calculated by Eqs. (4) and (5). In this study, we combine the Euler characteristic (Eq. (5)) and genus (Eq. (6)) to demonstrate topological characterization of the microstructure. The geometric surfaces of cementite and ferrite phases or ferrite and martensite phases, i.e., independent bodies and voids, can be triangulated and examined by calculating the number of nodes, edges, faces, and cells using the Avizo Fire or MAVI software. Then, a quantitative analysis of the topological characteristics is accomplished by examining the genus and the number of independent bodies, voids, and holes.

## Results and discussion

*a. Pearlite spheroidization*[8-10)]

Figure 3 shows a 3D reconstruction of an as-patented pearlite microstructure. A closeup view shows many holes and fissures in a cementite lamella. According to a detailed TEM examination,

when a subboundary is formed in ferrite, an adjacent cementite lamella stops growing because a specific orientation relationship between them cannot be maintained, which leads to the formation of a hole or a fissure in the cementite lamellae. With an increase in the aging period, this sheet cementite lamella disintegrates into a ribbon shape and then into a rod shape. Finally, cementite transforms its morphology to a sphere from a rod. During this morphological change, the preexisting morphological defects such as holes or fissures play a vital role, because mass transfer apparently occurs preferentially from an edge region of the hole or the fissure to a flat part because of the Gibbs–Thompson effect. The number of holes decreases with increase in the aging period (Fig. 4). This tendency is also confirmed by the H-K plot (Fig. 5), which shows a decreasing probability density in a negative Gaussian curvature region. The morphological transformation of cementite from a rod to a sphere occurs through Mullins modified perturbation mechanism. The details of this cylindrical morphology instability are not yet fully understood, however, and are being investigated as a "pinchoff" mechanism though Rayleigh instabilities[11].

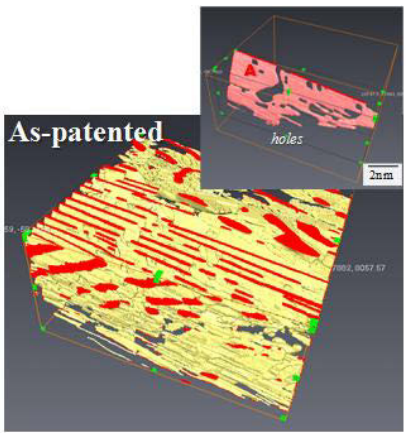


Fig.3 3D reconstruction of as-patented pearlite.

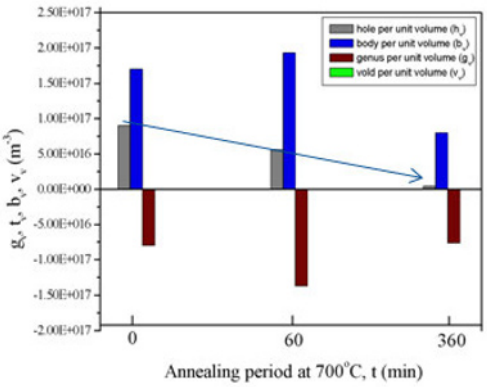


Fug.4 A change in number of genus(g), hole(t), body(b), and void(v) with annealing period.

*b. Dual phase (DP) steel*[12]

DP steels are known to possess a good balance between uniform elongation and tensile strength, but poor local elongation due to enhanced strain concentration around martensite. The ductile fracture mechanism must be examined in detail to improve local elongation. Figure 6 reveals that a relatively coarse void is preferentially formed both in the neck region of martensite and in a ferritic region adjacent to a highly curved martensite. It is also observed that a microshear band often propagates from the void along a direction tilted by approximately 45° with respect to the tensile direction. On the other hand, fractography suggests that a fracture surface consists of relatively coarse and fine voids, and a macroscopic fracture surface is almost inclined by 45° to the tensile direction (Fig.7). From these findings, it is possible that during the ductile fracture of DP steels, as shown in Fig. 8, first, a primary void (or a microcrack) is formed at the neck of martensite or in the ferritic region adjacent to the sharp martensite, and then this void induces a microshear band. With increasing strain, a secondary fine void is formed along the microshear band, and ultimately, the primary and secondary voids connect resulting in failure. The neck region in martensite, which microscopically corresponds to

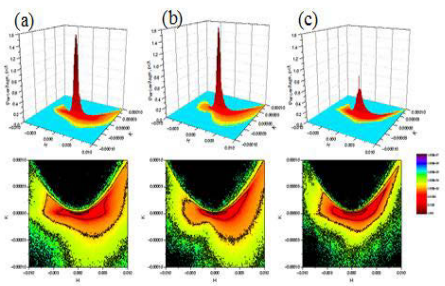


Fig.5 A change in H-K plot as a function of annealing period. (a)As patented, (b)60min, (c)360min.

a rod-shaped martensite, and a sharp tip in martensite are expressed in H < 0, K < 0 space and in H > 0, K < 0 space, respectively, in Fig. 2.

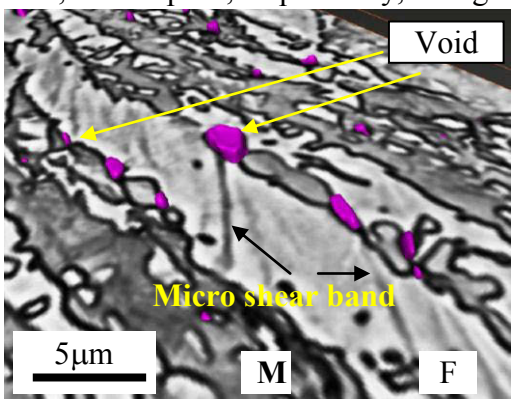


Figure 6 Preferential void formation sites in DP steel. M: martensite, F: ferrite.

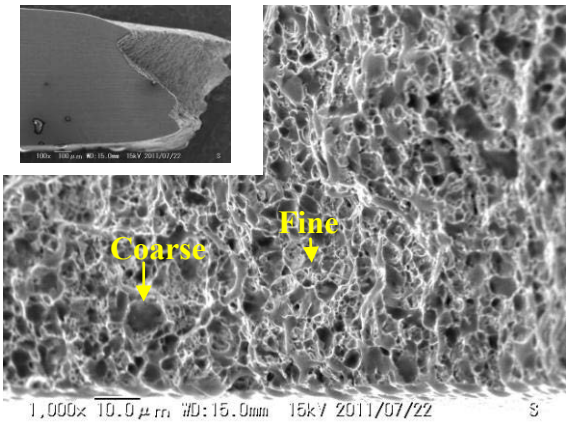


Figure 7 Fracture surface of DP steel.

## Summary

A topological approach of pearlite and a dual-phase microstructure was performed using 3D reconstructed images. 3D visualization is useful for finding a geometrical imperfection that accelerates microstructural instability upon both heating and straining. Furthermore, microstructural connectivity can be quantitatively evaluated based only on 3D images. Recent development of both FIB–SEM and a fully automated serial-sectioning 3D optical microscope has enabled the never-before-achieved investigation of a complicated microstructure.

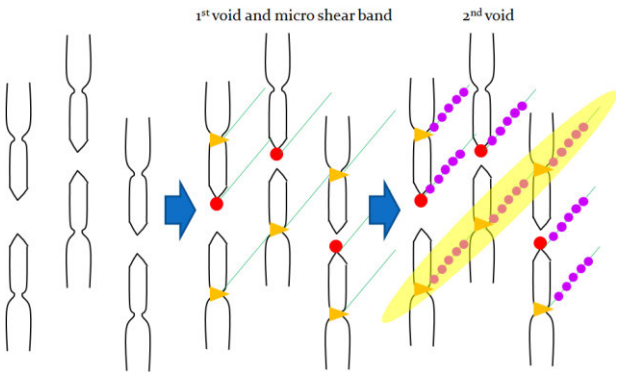


Figure 8 Schematic illustration of ductile failure mechanism in DP steel.

## Reference

1) The Business & Technology Daily News, March 15, (2011).
2) Practical Stereology, John C. Russ and Robert T. Dehoff, Plenum Press, New York.
3) R. Mendoza, K. Thornton, I. Savin, P.W. Voorhees: Acta Materialia, 54 (2006),743.
4) R. Mendoza, I. Savin, K. Thornton, P.W. Voorhees: Nat Mater, 3(2004), 385.
5) P.W. Voorhees, J. Alkemper, R. Mendoza: Adv Eng Mat., 4(2002), 694.
6) R. Mendoza, K. Thornton, I. Savin, P.W. Voorhees: Acta Materialia, 54(2006), 743.
7) P.W. Voorhees: J. Status Phys 38(1985), 231.
8) Y. Adachi, S. Morooka, K. Nakajima, Y. Sugimoto: Acta Materialia, 56(2008); 5995.
9) Y.T.Wang, Y. Adachi, K. Nakajima, Y. Sugimoto: Acta Materialia, 58 (2010), 4849.
10) Y.T.Wang, Y. Adachi, K. Nakajima, Y. Sugimoto: ISIJ International, (2012), in print.
11) L. K. Aagesen et al., Acta Materialia, 59(2011), 4922.
12) N.Sato, Y.Adachi, H.Kawata, and K.Kaneko: ISIJ International, (2012), in print.

1st International Conference on 3D Materials Science
*Edited by: Marc De Graef, Henning Friis Poulsen, Alexis Lewis, Jeff Simmons, George Spanos*
***TMS (The Minerals, Metals & Materials Society), 2012***

# FRAGMENTATION OF A STEEL RING UNDER EXPLOSIVE LOADING

Jeremy M. Schreiber[1,2], Ivi Smid[2], Timothy J. Eden[1]

[1] Applied Research Laboratory; The Pennsylvania State University

[2] Department of Engineering Science and Mechanics; The Pennsylvania State University

Keywords: Fragmentation, Finite Element Analysis, Johnson-Cook, Plasticity

## ABSTRACT

There is a great deal of interest in the behavior of metallic materials under high strain rate loading. Finite Element Analysis (FEA) could be used to model these materials with a reduction in the amount of experimentation needed for characterization. A finite element model of a metallic ring under high strain rate loading was developed using the Johnson-Cook failure model in Abaqus Computer Aided Engineering (CAE). The ring was modeled both axisymmetrically and in three dimensions. Failure was determined by defining a failure initiation value to start the process of element deletion. It was found that element deletion would occur when the failure strain initiation value was less than $1x10^{-4}$. Results of both axisymmetric and 3-D were found to be within 3% of each other with respect to maximum von Mises stress, and failure modes were identical. The effects of model changes and loading conditions are investigated.

## Introduction

Understanding the failure mechanism of high strength steels under large strain rates is of great interest. Standard practice is to build and detonate experimental test articles, collect the fragments, and examine the pattern and fragment size distribution. Most of the time, the analysis of how or where the material failed proves impossible [1,2,3,4]. Computer modeling is being used to reduce costs and improve the understanding of the failure mode. Creating a working model of the failure mode of a sample reduces the number of prototypes that need to be built and experiments to be performed. The use of a computer model will also allow for multiple simulations to be carried out. A computer model for the failure of a ring under high strain rate loading was developed using current material failure models.

## Experimental Procedure and Approach

A three dimensional ring was developed using SolidWorks computer aided drafting software. The outside dimension of the ring is approximately 80mm. Wall thickness is 7mm with a notch depth of 3.2mm. The ring was imported into Abaqus CAE to begin analysis. Partitioning in Abaqus was required to achieve the required mesh type.

Many material properties were needed to develop the model. During the initial stages of modeling, only simple elastic properties were used for the linear elastic simulations. Once plasticity and fragmentation models were introduced, additional properties were needed to model the event. Material properties for AISI 4340 are shown in Table 1.

**Table 1. Selected material properties for AISI 4340 at low strain rates [5]**

| Elastic Modulus (Pa) | Density (g/cc) | Poisson's Ratio | % Elongation | Ultimate Tensile Strength (Pa) | Yield Strength (Pa) |
|---|---|---|---|---|---|
| 205 x$10^9$ | 7.87 | 0.285 | 22 | 745x$10^6$ | 470x$10^6$ |

### Johnson-Cook Constitutive Material Model

The Johnson-Cook model is a purely empirical model that is used to represent the strength behavior of materials subjected to large strain rates, such as impulsive loading from an explosive detonation. This material model is commonly used in computer simulation of fracture and failure of materials, and is a standard model available in Abaqus CAE [6,7,8].

This model defines the yield stress, $\sigma_y$, of the material as:

$$\sigma_y = \left[A + B\varepsilon_p^n\right]\left[1 + Cln\varepsilon_p^*\right][1 - T_H^m] \quad (1)$$

Where $\varepsilon_p^n = effective\ plastic\ strain$

$$\varepsilon_p^* = normalized\ effective\ plastic\ strain\ rate$$

$$T_H^m = homologous\ temperature = \frac{(T - T_{room})}{(T_{melt} - T_{room})}$$

A, B, and C are experimentally determined material constants, where A is the basic yield stress at low strains, B is the strain-hardening effect, and C is the strain rate effect.

## Results and Discussion

### Plastic Deformation Modeling

Abaqus CAE was used in the following modeling. A dynamic, explicit model was created using the ring section. Both ends of the ring were fixed in the axial direction. Any rotation was also fixed. A time step of thirty microseconds was selected. An estimated pressure of 1.2GPa was applied to the inner wall [9,10].

Maximum von Mises stress was found to be $5.3 \times 10^8$ N/m$^2$ for this model. This exceeds the yield strength of the material in one microsecond. This suggests that the material either undergoes plastic deformation instantly, or suffers brittle fracture. The results of this model are shown in Figure 1.

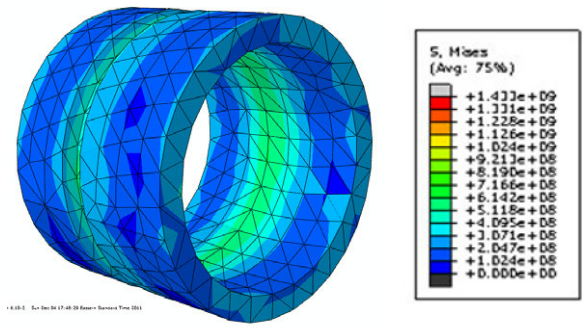


**Figure 1. Dynamic model of ring section after 30µs (stresses in Pa)**

**Axisymmetric Modeling**

An axisymmetric model was developed to reduce the calculation time of the dynamic explicit model. The run time of a three dimensional dynamic model is normally ten to twenty hours with a refined mesh. An axisymmetric model can be run in less than 30 minutes. The axisymmetric results were used in 3D model development. A 3-node linear axisymmetric triangle with Abaqus designation of CAX3 and consistent element size was used in this model. Figure 2 shows the initial and final images of the axisymmetric model.

The calculated maximum von Mises stress in this part was $4.8 \times 10^8$ N/m$^2$. The model showed unrealistic deformation at the notch area. This large deformation is due to the lack of a specified failure criterion.

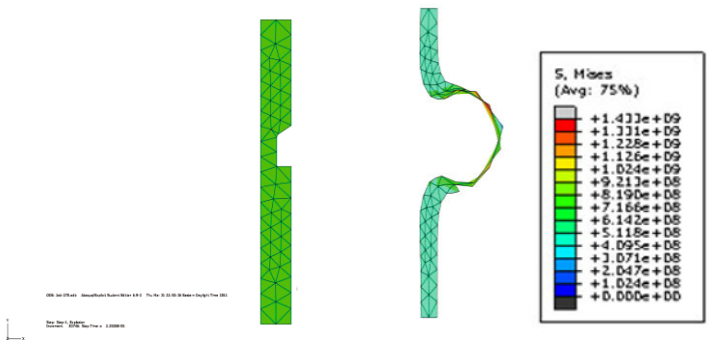


**Figure 2. Axisymmetric plastic deformation model (stresses in Pa)**

**Mesh Refinement and Instituting a 3D Fracture Model**

Mesh refinement and a fracture model were incorporated in the model. Less accurate tetrahedral elements were replaced by higher fidelity hexahedral elements. An 8-node linear brick with reduced integration and hourglass control was used. This element had Abaqus designation C3D8R. Element deletion was activated. It was necessary to determine a damage initiation value (i.e. fracture strain) for the model. When an element exceeded the specified value, it was removed from the calculation. Failure criteria based on linear displacement was used. In preceding simulations, the axisymmetric model was used to determine this value by starting at 1 and decreasing the value by one order of magnitude until no change was found. Figure 3 shows different damage initiation values with respect to failure. This shows that any damage value smaller than $1x10^{-4}$ has little additional effect on the model, and any larger does not induce fracture. $1x10^{-4}$ was used for the three dimensional calcuations. Fracture was found to occur after 45 microseconds. This value was used in the 3D model.

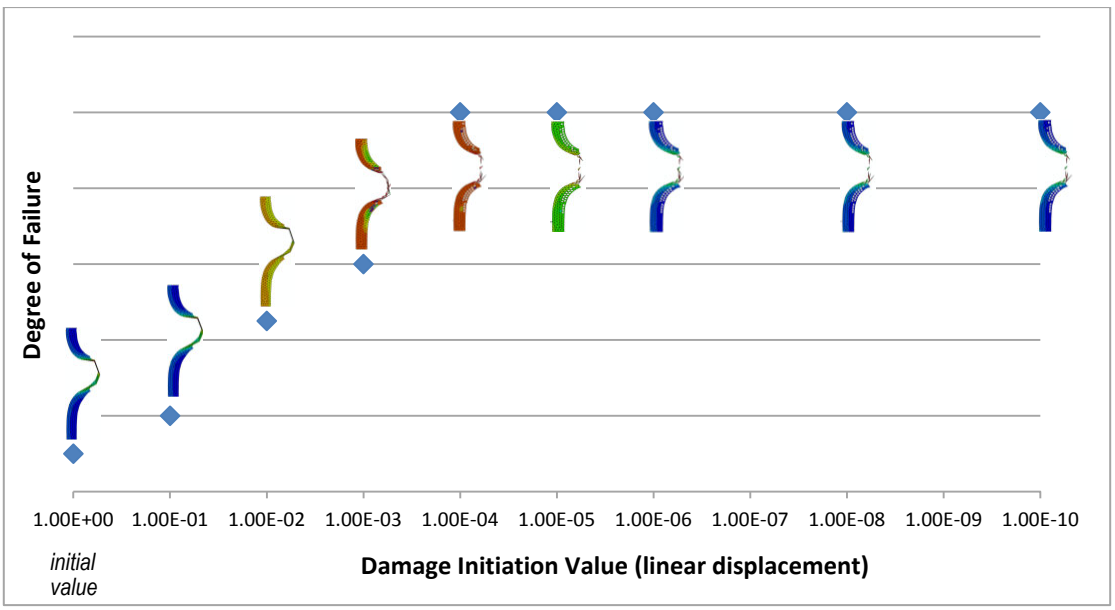


**Figure 3. Predicted failure initiation values (t = 45 µs)**

Three dimensional modeling yielded similar results to the axisymmetric modeling, but did not predict expected fragmentation behavior. The notch expanded as pressure was applied. Element deletion occurred at the notch area as expected, but did not delete any elements in the thick section of the wall. Areas surrounding the notch showed some deformation. The finite element solver may not be able to identify a failure location due to the perfect symmetry of the model. Also, J-integral failure criterion was not taken into account, and failure was initiated by linear displacement alone. In future work, microstructural changes and local texture evolution will be investigated by using x-ray diffraction lattice distortion measurements. High speed video capture will be correlated to the finite element simulations by mesh refinement and stress intensity predictions.

Using a pressure of 1.2GPa, a strain rate of $1x10^{4}$ was found. This is consistent with an explosive strain rate [11]. Figure 4 shows the results of the three dimensional failure model at 45 microseconds.

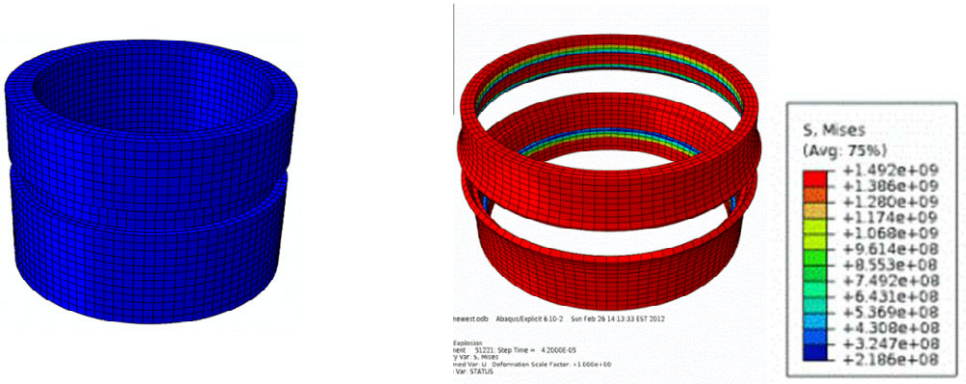


**Figure 4. Fragmentation model results (stresses in Pa)**

**Introduction of Eccentricity to Simulate Defect**

A "defect" was inserted by shifting the inner diameter 1mm to create a non-concentric ring. Figure 5 shows a top down illustration of the shift. Shifting the inner diameter of the ring thins a segment of the wall and eliminates rotational symmetry. This caused elements in the thin region to fail first. Elements around the notch area as well as the thinned region of the ring wall failed. Elements exceeding the specified damage initiation value of $1x10^{-4}$ were deleted from the calculation (not ejected outside of the view). Using a constant pressure throughout the calculation does not account for the pressure drop after an explosion. This suggests that the results may be skewed after the onset failure. Figure 6 shows the results of the calculation.

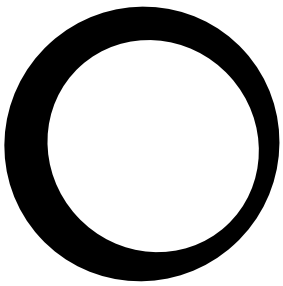

**Figure 5. Shift of inside circumference, causing eccentricity (top down view)**

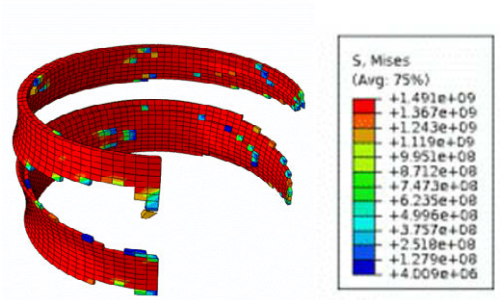


**Figure 6. Fragmentation of eccentric 3D defect model (stresses in Pa)**

## Conclusions

Three dimensional and axisymmetric computer models of an AISI 4340 steel ring were created using a finite element solver. These models were used to examine the behavior of the material under high strain rate loading. The Johnson-Cook failure model was used. The conclusions from this work are:

- Abaqus can be used to model failure using the Johnson-Cook constitutive model
- Axisymmetric modeling was used to develop parameters for 3-D

- A damage initiation value (or fracture strain) of $1x10^{-4}$ was found
- Using dynamic, explicit modeling, a three dimensional material model was created, and results were supported by an axisymmetric model
- Mesh refinement is necessary to achieve optimal results
- 3D model with full rotational symmetry produced somewhat unrealistic results
- Adding a defect such as eccentricity increases likelihood of realistic failure
- Axisymmetric modeling is consistent with three dimensional results
- Disintegration predicted to start at 45μs, with a strain rate of $1x10^{4}$
- Failure is dependent on strain rate, element size, and damage initiation value

## References


1. Stepanov, G.V. and A.V., Shirokov**.** "*Modeling of Crack Propagation Kinetics".* No. 4, Kiev : Problemy Prochnosti, 2008. 0039-2316/4204-0426.

2. Rusinek, A. and Zaera, R. "*Finite Element Simulation of Steel Ring Fragmentation Under Radial Expansion".* s.l. : International Journal of Impact Engineering, 2006, Vol. 34.

3. Campagne, L., Daridon, L. and Ahzi, S. "*A Physically Based Model for Dynamic Failure in Ductile Materials"***.** Strasbourg : Mechanics of Materials, 2004, Vol. 37.

4. Rushton, N., et al**.** "*Internal Explosive Loading of Steel Pipes".* s.l. : Thin-Walled Structures, 2008, Vol. 46.

5. AISI 4340 Steel Properties. www.matweb.com

6. Johnson, G.R., Cook, W.H. "*A Constiituitive Model and Data for Metals Subjected to Large Strains, High Strain Rates and High Temperatures".* The Hague, The Netherlands : Proc. 7th Int. Symp. on Ballistics, 1983.

7. Johnson G.R., Cook, W.H. "*Fracture Characteristics of Three Metals Subjected to Various Strains, Strain Rates, Temperatures, and Pressures".* s.l. : International Journal of Engineering Fracture Mechanics, 1985, Vol. 21.

8. Johnson-Cook Criterion. Abaqus 6.9 Analysis User's Manual. 20.2.2 Damage Initation for Ductile Metals

9. Forbes Jerry W., et.al. "*Pressure Wave Measurements During Thermal Explosion of HMX-based High Explosives".* Livermore CA : s.n.

10. Yoh, J., et al. "*Test-based Thermal Explosion Model for HMX".* s.l. : Proceedings of the Combustion Institute, 2006, Vol. 31.

11. R.W. Armstrong, S. W. (2008). High strain rate properties of metals and alloys. *International Materials Reviews*, 24.

1st International Conference on 3D Materials Science
*Edited by: Marc De Graef, Henning Friis Poulsen, Alexis Lewis, Jeff Simmons, George Spanos*
***TMS (The Minerals, Metals & Materials Society), 2012***

# Quantifying the effect of 3D spatial resolution on the accuracy of microstructural distributions

Gregory Loughnane[1], Michael Groeber[2], Michael Uchic[2], Matthew Riley[3], Megna Shah[4], Raghavan Srinivasan[1], and Ramana Grandhi[1]
[1] *Wright State University, Department of Mechanical & Materials Engineering, Dayton, OH 45433*
[2] *Air Force Research Laboratory, Materials & Manufacturing Directorate, Wright-Patterson AFB, OH 45433*
[3] *University of Idaho, Moscow, ID 83844*
[4] *UES, Inc., Dayton, OH 45432*

## Abstract

**The choice of spatial resolution for experimentally-collected 3D microstructural data is often governed by general rules of thumb. For example, serial section experiments often strive to collect at least ten sections through the average feature-of-interest. However, the desire to collect high resolution data in 3D is greatly tempered by the exponential growth in collection times and data storage requirements. This paper explores the use of systematic down-sampling of synthetically-generated grain microstructures to examine the effect of resolution on the calculated distributions of microstructural descriptors such as grain size, number of nearest neighbors, aspect ratio, and $\Omega_3$.**

## Keywords

microstructure, 3D characterization, serial sectioning, grain size

## Introduction

Three dimensional (3D) microstructure characterization techniques are required to measure many important microstructural characteristics including true size and shape, the number of features per volume, and feature connectivity [1]. Although the need for 3D characterization for 'complete' microstructural analysis is well known, it is only within the past decade that desktop computing resources—such as processor speed, memory, graphics cards, and 64-bit operating systems—have advanced to the point where materials scientists and engineers are able to readily work with the enormous data sets born of 3D characterization experiments. These aforementioned advancements in computing technology have also helped galvanize activity in the materials community to promote and adopt Integrated Computational Materials Engineering (ICME) initiatives [2-4].

A foundational experimental technology for ICME-related research is the ability to quantify the internal material state at any point during the manufacturing or utilization of engineering materials, in order to verify and validate the output of modeling and simulation tools that examine such processes. This analysis ideally includes statistically-significant data on key microstructural features such as grains, precipitates, second phases, voids, and defects. Known capability gaps for this technology area include two topics related to 3D microstructure characterization; machines to rapidly collect 3D data across the range of lengths scales that are known to affect material properties [5], and computational methods to streamline the process of

data reduction, analysis, and further re-use of data by other modeling and simulation tools. With the advent of new state-of-the-art 3D characterization systems that are addressing the need for rapid data collection, it is important to examine and investigate the sources of error associated with these characterization processes, in order to bound the uncertainty in quantitative measurements derived from such experiments.

In particular, there is little information in the materials characterization literature to guide the selection of sampling resolution for data collection in 3D. Prior guidance is particularly important for destructive experiments such as serial sectioning, where the sample volume is incrementally and irreversibly consumed during the experiment. In the serial sectioning literature, it is generally espoused that one would like a minimum of ten sections through a microstructural feature to accurately describe its size and shape, but this guidance is simply a rule-of-thumb and is wholly insufficient for quantitative microstructural analysis. Experimentalists can always strive to refine the spatial frequency of data collection, but this becomes problematic for 3D data when the collection times and storage requirements grow exponentially, often leading to considerable inefficiencies due to conservative oversampling.

This paper examines one aspect of modeling uncertainty with regards to 3D data collection, which is the effect that isotropic decrements in spatial resolution have on the accuracy of microstructural distributions that are derived from a reference data volume. Specifically, this work reports the quantitative change in the Hellinger Distance of the full distribution for the following morphological microstructure parameters: grain size in equivalent sphere diameter (ESD), grain shape as described by the two ellipsoid ratios *b/a* and *c/a*, the third moment invariant $\Omega_3$ [6], and the number of contiguous neighbors. This analysis is performed for two near log-normal grain size distributions that have been synthetically-generated and virtually down-sampled, as described in the following section.

## Methodology

The synthetic structure generation and subsequent data analysis for this study were performed using a state-of-the-art 3D materials analysis software DREAM.3D, or Digital Representation Environment for Analyzing Microstructure in 3D (dream3d.bluequartz.net). The 3D synthetic reference volumes were created using processes that are briefly described here; detailed reviews on synthetic microstructural generation methods have been reported previously [7].

The first step in the synthetic microstructure generation process is to define statistics that describe the grain size, grain shape, number of nearest neighbors, spatial orientation, crystallographic orientation and boundary character distributions for the desired volume. In this study, however, only morphological parameters are of interest and thus, the crystallographic orientation and boundary character distributions were omitted. Additionally, the number of nearest neighbors was not prescribed and was allowed to fluctuate as needed while placing the grains. Finally, the spatial orientation of the grains was assigned as random since the down-sampling was performed isotropically and not expected to be directionally sensitive. Two log-normal distributions were created for the reference grain size distributions and each volume was assigned a shape distribution that corresponded to roughly equiaxed grains. One of the grain size distributions was nearly uniform, which is termed ‘slightly log-normal’ ($\mu = 1.06$, $\sigma = 0.28$) while the other size distribution had a much heavier tail ($\mu = 0.95$, $\sigma = 0.55$), in order to examine the effect that the grain size distribution has on these uncertainty

measurements of sampling frequency. After defining reference statistical distributions, grains are generated to fill the reference volume via random sampling of these distributions. The grains are then inserted into, removed from, or moved within the volume while optimizing a number of governing criteria (e.g., space filling, grain overlap, grain size and shape, and number of neighbors). After an optimal packing is obtained, a simulated coarsening process is used to eliminate unassigned voxels that remain from the inability to densely pack the reference volume with ellipsoids. The two synthetic reference volumes are shown in Figure 1A and 1B. Note that the reference volumes contain over 4000 grains (~2000 unbiased and used for analysis), and the spatial resolution for each volume is approximately 30 voxels through the diameter of a grain of mean size. Figure 1C shows the resultant grain size distributions of the two structures. Note that the reference distributions used to determine the effect of down-sampling are the distributions shown in Figure 1C, not the input distributions used to create the volumes.

To quantify the effect of data resolution, the two reference volumes were down-sampled using the following procedure. A new voxel volume was created using MATLAB at the desired down-sampling resolution. Voxels in the new volume were assigned a grain identification value that corresponded to the voxel in the reference volume in which their centroid fell. Successively coarser re-samplings of the reference synthetic microstructure volume were produced in this manner (i.e., the same reference volume was always used to assign the voxel grain identification of the down-sampled volumes), and the result of the down-sampling process is shown in Fig. 2.

The morphological parameter distributions examined in this study include grain size (ESD), grain shape (b/a, c/a, $\Omega_3$), and number of neighbors. The ESD is computed using the following relation, where $N_v$ is the number of voxels that comprise the grain, $V$ is the voxel volume:

$$ESD = 2 \cdot \left(\frac{3}{4\pi} N_v V\right)^{\frac{1}{3}} \tag{1}$$

In this study, feature shape is described using aspect ratios of a best-fit ellipsoid and a second-order moment invariant (with respect to affine and/or similarity transformations) [6]. The moment invariant, denoted by $\Omega_3$, is used to further describe grain shape and is calculated using the following equation [6]:

$$\Omega_3 = \frac{V^5}{O_3} \tag{2}$$

$$O_3 = \mu_{200}\mu_{200}\mu_{200} + 2\mu_{110}\mu_{101}\mu_{011} - \mu_{200}\mu_{011}^2 - \mu_{020}\mu_{101}^2 - \mu_{002}\mu_{110}^2 \tag{3}$$

where $\mu_{pqr}$ represents the second order moments in Eq. 3 (moment order is equal to the sum of $p$, $q$ and $r$). $\Omega_3$ can be used to differentiate shapes with the same aspect ratio, and shapes become qualitatively 'less complex' and more ellipsoidal-like with increasing values of $\Omega_3$, up to the limiting case of $\Omega_3 = 2193.245$ that corresponds to spheres and ellipsoids [6]. In this study, all $\Omega_3$ values have been normalized by that of a sphere to resultant in values bounded between 0 and 1.

The nearest neighbor distribution describes the number of grains that share at least one voxel face with a reference grain. Note that voxels which only share a common edge or corner are not considered as neighbor grains in this analysis.

## Results and Discussion

The full distribution of grain size and $\Omega_3$ for the 'heavy-tailed' structure at each down-sampling resolution is shown in Figs. 3 and 4, respectively. One can observe that the grain size distribution does not change markedly with down-sampling until there is nominally 1 voxel spanning the mean grain diameter. By comparison, the $\Omega_3$ distribution is clearly affected by down-sampling even when there are as many as 20 voxels spanning the mean grain diameter. While this type of visual inspection can be informative, it is also useful to have metrics to characterize how the feature distributions are changing with down-sampling resolution. This study has used the Hellinger Distance (HD) to quantify the difference between two distributions, which is defined for discrete distributions as the following:

$$\mathrm{HD} = \sqrt{1 - \sum_{i=1}^{n} \sqrt{R_i \, S_i}} \tag{4}$$

where $R_i$ and $S_i$ correspond to the data percentage in bin $i$ for the discrete distributions $R$ and $S$. The HD is used to measure the geometric similarity between two distinct statistical distributions (models), and is bounded between 0 and 1, where a value of 0 implies that two models are identically distributed. For this work, microstructure parameter data was binned into histograms after being computed from down-sampled and reference volumes. Therefore, the HD was computed discretely using a direct comparison of histograms over the entire domain of possible parameter values [8].

A plot of the statistical analysis of the down-sampled volumes from the slightly log-normal grain size distribution is shown in Fig. 5. At 20 voxels spanning the mean grain size, the HD for most of the feature distributions are nearly equal to 0, which indicates that there is very little difference in the measured distributions. However, the shape parameter $\Omega_3$ is the most sensitive to resolution changes and requires significantly more sections through each feature to retain a low HD. This sensitivity is highlighted by the increase in the $\Omega_3$ HD from 0.11 at 20 voxels spanning the mean grain size to 0.34 at 10 voxels and 0.75 at 5 voxels. Importantly, the grain size, ellipsoid ratios *b/a* and c/a, and nearest neighbor distributions continue to match the reference volume distributions (HD < 0.1) with progressively-coarser down-sampling to as low as 5 voxels spanning the mean grain size. This resolution is considerably less than the traditional rule-of-thumb of 10 sections through the average feature. However, for sampling resolutions below 5, all of the feature distributions begin to deviate rapidly from the reference distribution, as the shape & volume for the smallest grains in the distribution are becoming strongly altered by the relative coarseness of the voxel array.

A plot of the statistical analysis of the down-sampled volumes from the heavy-tailed grain size distribution is shown in Fig. 6. The global trends in the data are similar to the slightly log-normal distribution: $\Omega_3$ is the most sensitive to changes in sampling resolution, and save for this parameter, all other distributions had HD values lower than 0.17 at 5 voxels spanning the mean grain size. Note that the heavy-tailed volume contains comparatively more small grains relative to the slightly log-normal volume. As a result, the microstructural

distributions calculated from the heavy-tailed volume are affected first by changes in resolution, given that the smallest grains will be most altered by sampling resolution changes.

This study highlights the intrinsic effect of sampling resolution on the accuracy of microstructural distributions derived from 3D data. The virtual down-sampling experiments show that the probability distributions for grain size, number of neighbors, and ellipsoid ratio can be collected at relatively coarse resolutions with little alteration. Conversely, selected shape descriptors such as $\Omega_3$ require high spatial resolution data. Although the methodology outlined herein has only been used to quantify one source of uncertainty, this method can be extended to examine many other sources data uncertainty, and will likely be especially effective with regards to improved analysis of destructive experimental methods like serial sectioning. For example, this approach could be used to optimize the selection of anisotropic sampling resolution (e.g., higher in-plane resolution relative to the sectioning depth), or examine the impact of variability within the serial sectioning process (planarity, parallelism, uniformity). While these concepts are not explored here and are left to future work, these types of studies should improve both data quality and experimental efficiencies.

## References


[1] DeHoff, R.T., J. Microsc. 131 (1983) 259–263.

[2] Materials Genome Initiative for Global Competitiveness, June 2011

[3] Allison, J., "Integrated Computational Materials Engineering: A Perspective on Progress and Future Steps," Journal of Materials, Vol. 63, No. 4, April, 2011, pp. 15-18.

[4] Christodoulou, J., "Dynamic 3D Digital Structure: Program Overview," *Journal of Materials*, Vol. 61, No. 10, 2009, p. 21.

[5] Uchic, M.D., Groeber, M.A., and Rollet, A.D., "Automated Serial Sectioning Methods for Rapid Collection of 3-D Microstructure Data," *Journal of Materials,* Vol. 63, No. 3, 2011, pp. 25-29.

[6] MacSleyne, J.P., Simmons, J.P., and De Graef, M., "On the use of moment invariants for the automated analysis of 3D particle shapes," *Modelling and Simulation in Materials Science and Engineering*, Vol. 16, April, 2008,

[7] Groeber, M.A., *Computational Methods for Microstructure-Property Relationships,* ed. Ghosh, S., and Dimiduk, D. (New York: Springer, 2011), pp. 53-97

[8] Riley, M.E., and Grandhi, R.V., "Quantification of model form and predictive uncertainty for multi-physics simulation," *Computers and Structures*, Vol. 89, Issues 11-12, June 2011, pp.1206-1213.

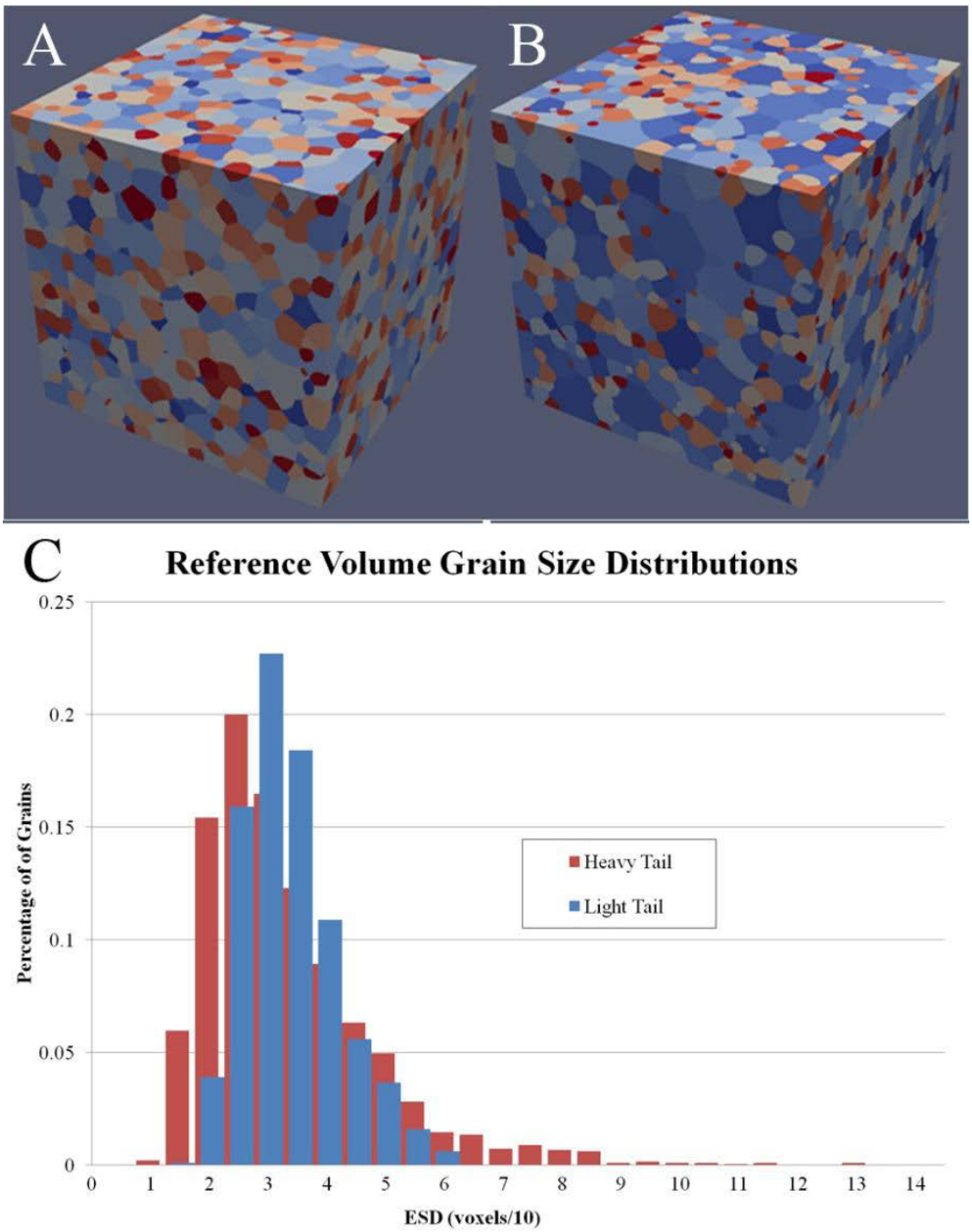


**Figure 1:** 3D renderings of the two synthetically-generated reference volumes. Panel A shows the slightly log-normal grain size distribution, while Panel B shows the heavy-tail grain size distribution. Grain coloring corresponds to unique grain IDs. Panel C plots the grain size distribution for the two volumes, and clearly shows that the heavy-tail volume has a greater number of both larger and smaller grains compared to the slightly log-normal volume.

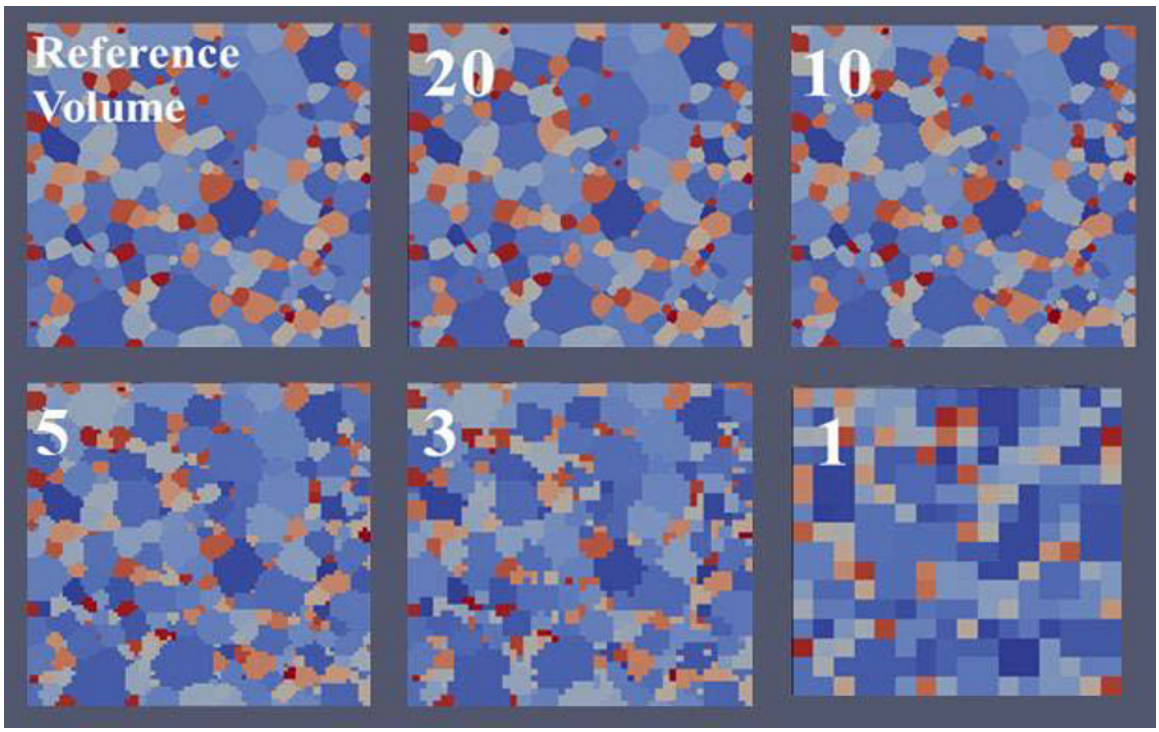


**Figure 2:** Images of successively down-sampled volumes for the heavy-tailed distribution. Spatial resolution is listed at the upper-left corner of each sub-image, which is defined as number of voxels that span the mean ESD.

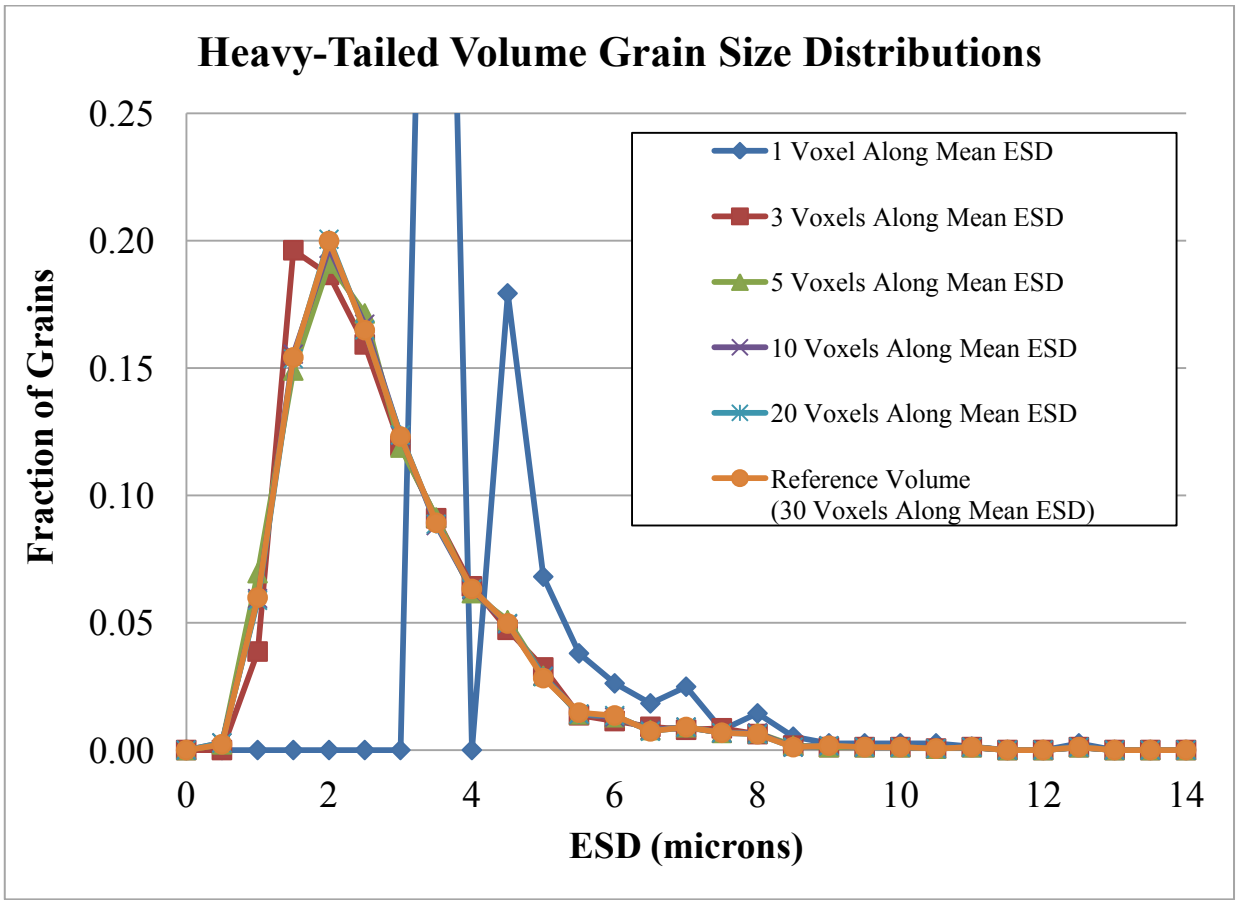


**Figure 3:** The effect of down-sampling from the reference volume on the ESD distribution is shown here for the heavy-tailed volume. Only minimal changes to the distribution are visible from down-sampling, until a down-sampling of 3 voxels along the mean ESD.

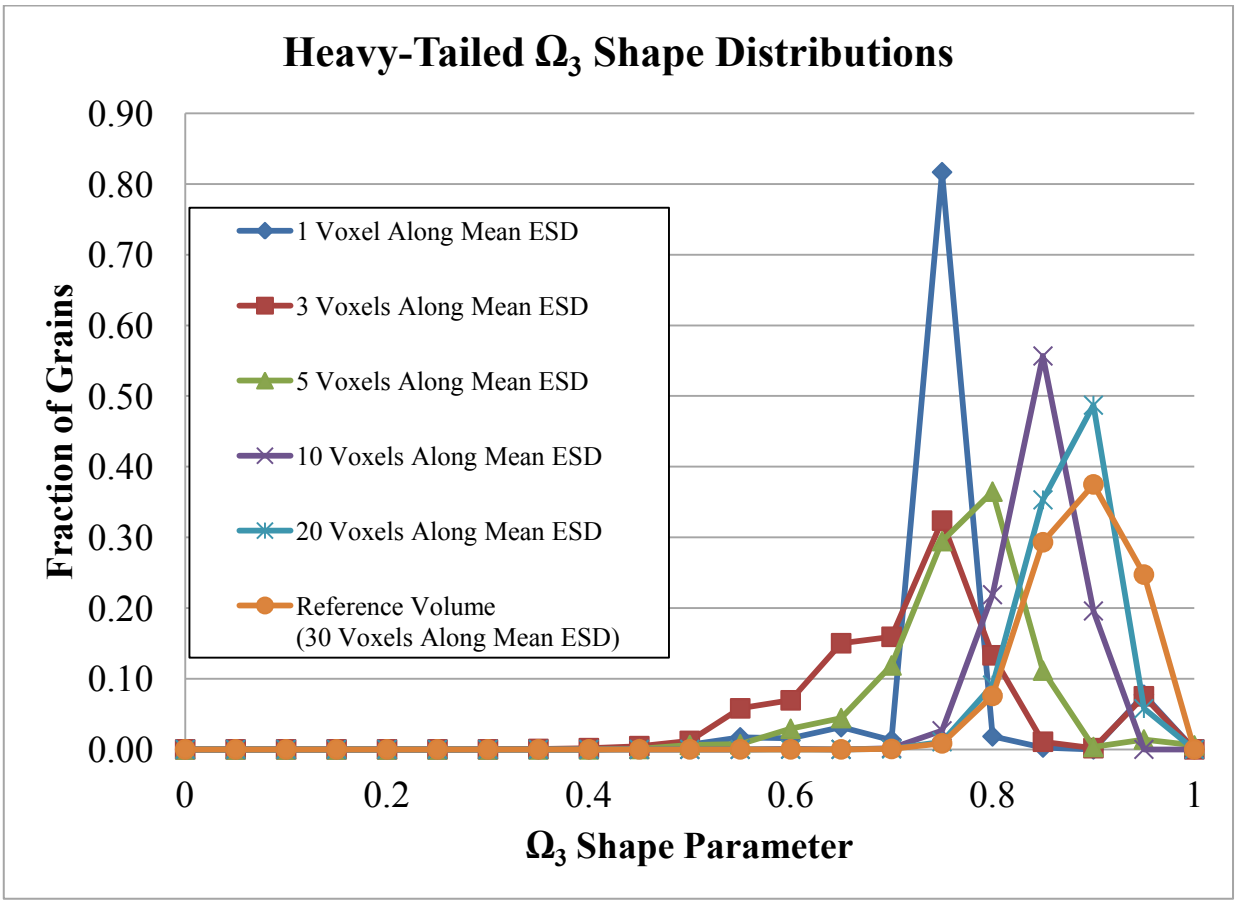


**Figure 4:** The effect of down-sampling from the reference volume on the $\Omega_3$ distribution is shown here for the heavy-tailed volume. Changes in the distribution can be seen even at a down-sampling from 30 to 20 voxels along the mean ESD.

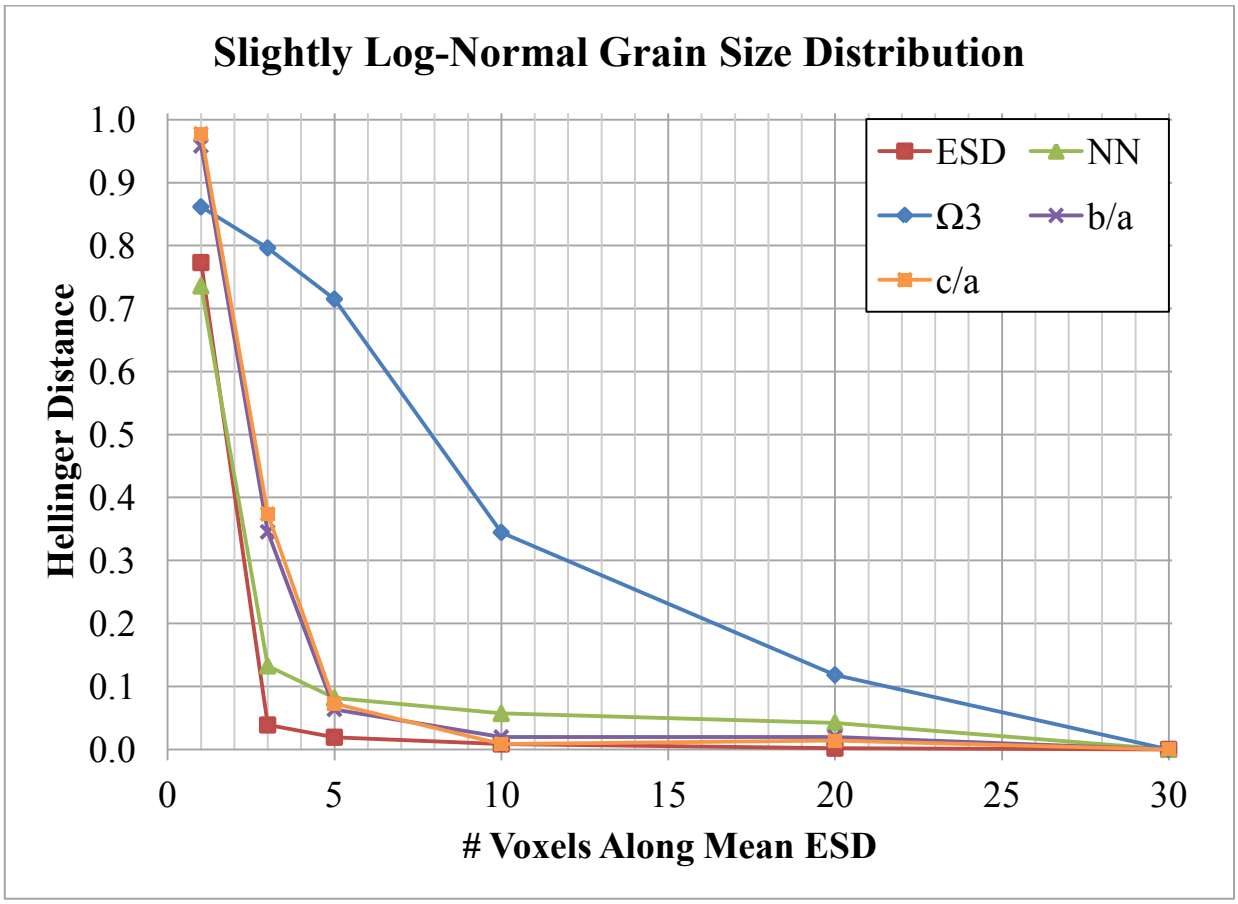


**Figure 5:**.The effect of down-sampling on the Hellinger Distance for slightly log-normal grain size distributions are illustrated here for ESD, NN, $\Omega_3$, c/a and b/a distributions. The reference volume had 30 voxels along the mean ESD, and was down-sampled all the way to 1 voxel along the mean ESD.

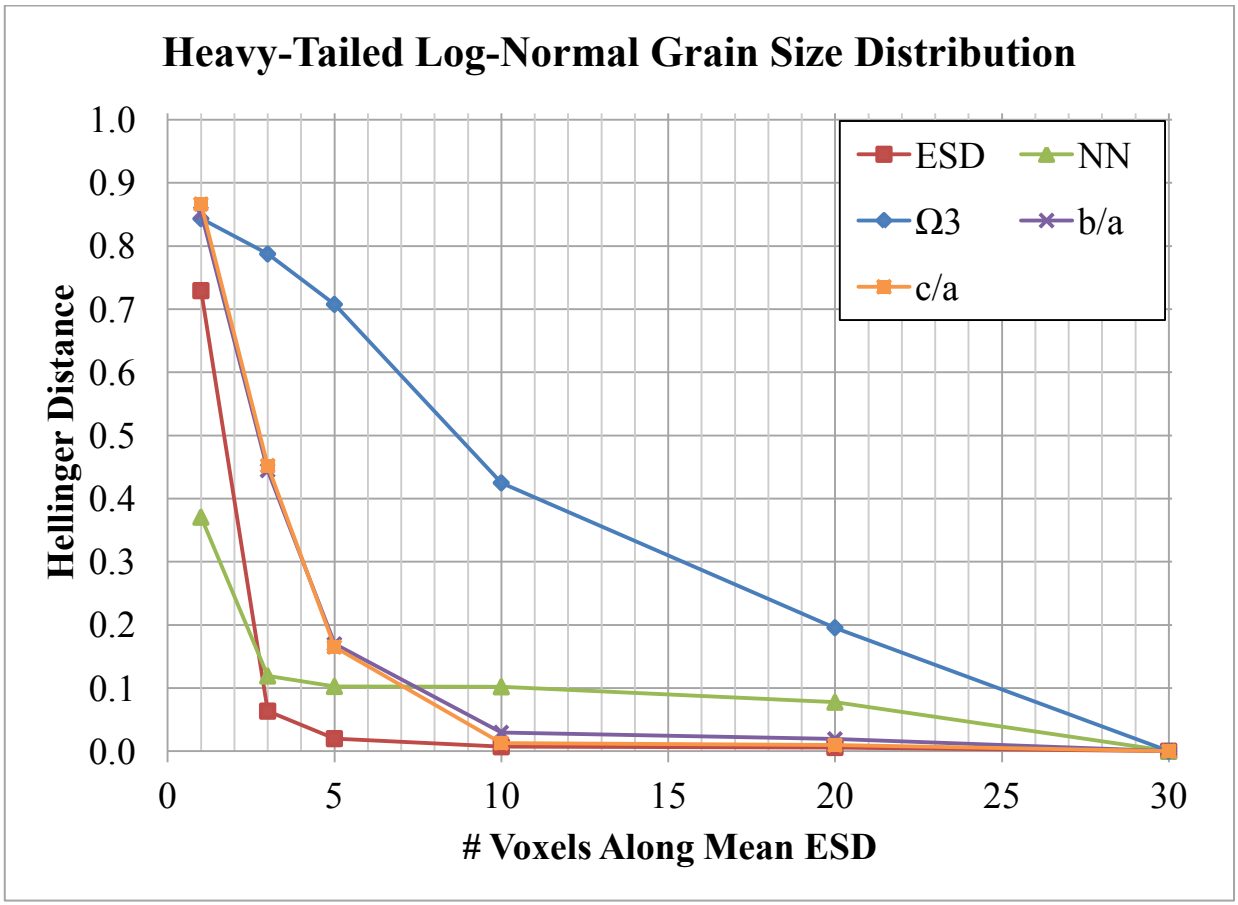


**Figure 6:** Plot of the Hellinger Distance relative to the number of voxels that span the mean ESD for the heavy-tailed log-normal grain size distribution. The effect of down-sampling on the Hellinger Distance for heavy-tailed log-normal grain size distributions are illustrated here for ESD, NN, $\Omega_3$, c/a and b/a distributions. The reference volume had 30 voxels along the mean ESD, and was down-sampled all the way to 1 voxel along the mean ESD.

1st International Conference on 3D Materials Science
*Edited by: Marc De Graef, Henning Friis Poulsen, Alexis Lewis, Jeff Simmons, George Spanos*
***TMS (The Minerals, Metals & Materials Society), 2012***

# THREE-DIMENSIONAL INVESTIGATION OF VOID GROWTH LEADING TO FRACTURE IN COMMERCIALLY PURE TITANIUM

Marina Pushkareva[1]; Jérôme Adrien[2]; Eric Maire[2]; Arnaud Weck[1*];

[1]University of Ottawa, *corresponding author: aweck@uottawa.ca
[2]INSA de Lyon

Keywords: Void growth, X-ray tomography, In-situ tensile test; Fracture

## Abstract

The fracture process of commercially pure titanium was visualized in model materials containing artificial holes. These model materials were fabricated using a femtosecond laser coupled with a diffusion bonding technique to obtain voids in the interior of titanium samples. Changes in voids dimensions during in-situ straining were recorded in three dimensions using x-ray computed tomography. Void growth obtained experimentally was compared with analytical model. The model predicted well void growth. Behavior between voids was justified in terms of grain orientation. Depending on the number of grains between voids and the grains orientation, two types of fracture behaviors were observed: i) brittle fracture when grains were in a hard orientation and when few grains were present between voids; ii) ductile fracture when grains were in a soft orientation and when several grains were present between voids.

## Introduction

Titanium is a material of importance because it is used in aerospace and biomedical applications due to its excellent mechanical and physical properties, like high specific strength, good ductility and excellent corrosion resistance.Interest has been shown towards understanding the deformation mechanisms of HCP materials, such as titanium [1-10] for aerospace applications, zirconium [11-13] for nuclear industry and magnesium [14-16] for manufacturing industries. The deformation behavior of HCPs is quite complex as it is affected by twinning and grain orientations. Different studies [2, 3] showed that grain orientation affects deformation. The misorientation of all types of the grain boundaries in titanium was found to change during deformation [2].In deciding the deformation mode in HCP materials one should consider the c/a ratio [5]: (i) when $c/a<1.632$ (Ti, Zr, Be, etc), a sufficient number of slip systems is provided by prismatic and pyramidal slip; (ii) when $1.63 < c/a < 1.73$ (Mg), only one basal slip is available; and (iii) when $c/a > 1.73$ (Zn, Cd) deformation is accommodated by basal slip and twinning. Propensity of twinning is also related to the grain size [4]: smaller grains cannot accumulate dislocations and twin boundaries, and hence twinning decreases.
The ductility is also affected by the HCP crystal structure, grain orientation and twinning. Yoo [1] proposed a relation between ductility and the ratio of elastic bulk modulus to shear modulus, K/G. High values of K/G were associated with ductility (titanium, zirconium) and low values with brittleness (magnesium). Fracture in Ti was also proposed to be a result of void nucleation, growth and coalescence. Krishna Mohan Rao et al. [10] reported fracture at room temperature by void nucleation and growth in a near-α aircraft titanium alloy. Potirniche et al. [17] reported that under uniaxial loading, voids grow in single crystals depending on the orientation of the tensile axis with respect to the crystalline lattice. A review on the effect of twinning, grain orientation

and other parameters on fracture process (experiments and modeling) was provided by Roters et al. [18].
Many models [6-9] were proposed to predict deformation mechanisms, evolution of crystallographic structure, texture, twinning, hardening and mechanical properties during deformation. However there is a lack of models to predict fracture in HCP structures. From the experimental results presented in the literature, fracture in Ti can be the result of a ductile fracture process where voids are nucleated, grow and finally coalesce. The approach taken in this paper is to verify whether standard ductile fracture models which were proven successful for some isotropic materials [21] are able to predict fracture and in particular void growth in an HCP structures such as Ti.
Experimental data on void growth and coalescence are difficult to obtain, making model validation difficult. To simplify the study of ductile fracture, titanium laser-drilled model materials similar to those of Weck et al. [21] were produced, tested and visualized using x-ray tomography. Void growth was followed in-situ and compared to the Rice and Tracey model.

## 1 Experimental methods

Commercially-pure titanium was used as the experimental material. The material was purchased from: (i) NewMetcompany in the form of thick 0.25 mm titanium foil (99.8% Ti); (ii) AlfaAesar company in the form of thin 0.032 mm titanium foil (99.7% Ti). Arrays of voids were introduced in the thin titanium foils using femtosecond laser micromachining, a new technique which allows the precise manufacturing of holes without inducing a heat affected zone around the hole. Different hole configurations were used: (i) rectangular array with intervoid spacings of 70 μm, 100 μm and 120 μm; (ii) holes at 45° with intervoid spacings of 70 μm, 100 μm and 130 μm. All samples had an initial hole diameter of 35 μm. After laser drilling the samples were polished down to a mirror finish using a 0.05 μm colloidal silica suspension. Hole containing sheets were then diffusion bonded to sheets without holes in a vacuum furnace at $10^{-5}$ torr. A typical diffusion bonding temperature and time was 1000°C during 3 hours. Two types of samples were obtained: one with a 2-dimensional array of voids inside the material and one with a 3-dimensional array of voids to obtain a more realistic void configuration.
Titanium samples were pulled in-situ in an x-ray tomography system vTomexs (INSA de Lyon, France). Tensile tests were performed at constant strain rate and at room temperature on a specially designed in situ tensile testing machine. The machine was used in tension with a load cell of 2 kN and both load and displacement were recorded during the test. During the in-situ tomography experiments, samples are deformed in tension and the test is stopped at various displacements in order to acquire a tomogram. Depending on how quickly the sample failed and on the number of interesting events occurring during the test, the number of tomograms acquired varied between samples.

## 2 Experimental results and discussion

In the following section tomograms are presented for titanium samples. True stress-strain curves are then calculated and fracture surfaces observed in a scanning electron microscope (SEM).

### 2.1 In-situ Tensile Test Results

Using the force registered during the tensile test and the smallest cross sectional area extracted from tomographic reconstructions, true stress-strain curves were constructed for all samples. To obtain the smallest cross sectional area of the samples in the neck region, the area of each section

was calculated automatically using the open source image analysis software ImageJ [22]; then the data was sorted numerically to extract the smallest cross sectional area. True stress-strain curves were calculated using the following equations:

$$\sigma = \frac{L}{A} \tag{1}$$

$$\varepsilon = ln \frac{A_0}{A} \tag{2}$$

where L is the load; A is the current cross sectional area; $A_0$ is the initial cross sectional area.
An example of true stress-strain curve is represented in Figure 1. All true stress-strain curves obtained were fitted using the classical Hollomon expression:

$$\sigma = K\varepsilon^n \tag{3}$$

where K is a constant and n the hardening exponent.
The macroscopic necking strain is given by the hardening exponent n and is represented by the intersection of the stress strain curve with the work hardening rate curve (see Figure 1). A hardening exponent of 0.15 was found for most tests which corresponds to a true necking strain of 0.15.

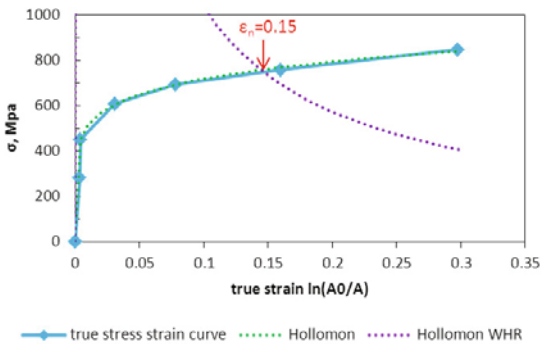


Figure 1. True stress-strain curves of commercially pure titanium sample tested in tomography containing three arrays of holes oriented at 0 degrees with respect to the tensile axis.

## 2.2 X-ray tomograms

Sample testing in X-ray tomograph permitted to visualize void growth and coalescence in three dimensions. To visualize the holes in three dimensions ImageJ was used.The visualization of holes in three-dimensions is possible because of the large differences in contrast between the matrix and the holes which allowed for a thresholding technique to be used where the voids can be separated from the rest of the material. Contrary to fractography which only provides information at fracture, tomographic reconstructions permits to follow voids' dimensions as a function of deformation in 3-dimensions. Void dimensions were measured using the ImageJ software. The macroscale tomograms are shown in Figure 2. Void dimensions evolution can be clearly seen on this figure. One can notice that during the test voids first elongate in the tensile direction and then, when coalescence starts, elongate in the transverse direction. Void growth was quantified in the different samples as a function of true strain (Figure 3). Local necking of the intervoid ligament corresponds to the moment at which voids start growing towards each other or in other word when the minor void diameter start increasing. In Figure 3b and 3d, the

corresponding true strain is approximately 0.15. It is interesting to note that this value is very close to the macroscopic necking strain obtained from the stress strain curve in Figure 1.

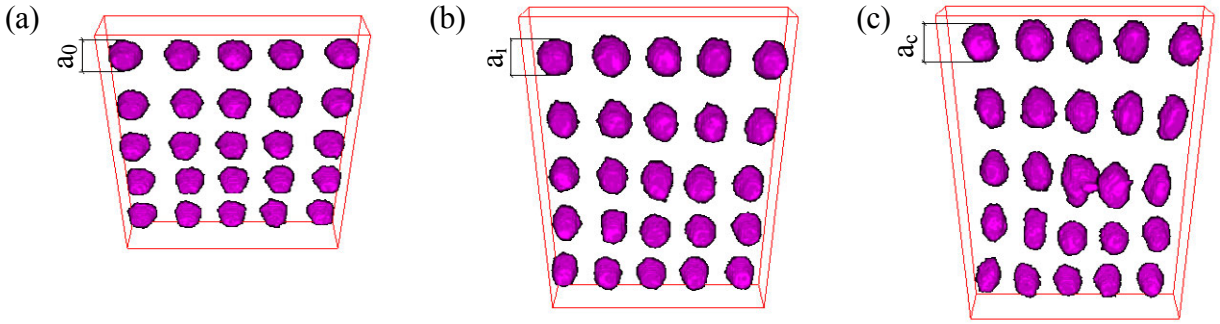


Figure 2. Tomographic reconstruction of a titanium sample containing three arrays of laser drilled holes (only one array is shown here). The sample has been tested in-situ and the tomograms correspond to the following true strains (a) 0.00, (b) 0.16, (c) 0.30. The tensile direction is vertical. Initial void diameter $a_0$ is 35 µm.

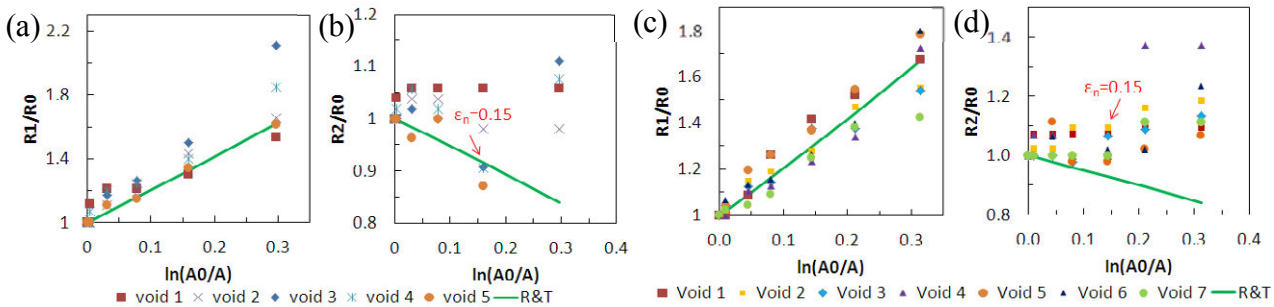


Figure 3. Comparison between the experimental results for void growth and the Rice and Tracey model for a titanium sample containing three array of holes (a and b) and one array of holes (c and d).

### 2.3 Fractography

Fracture surfaces of titanium samples tested in tomography were observed in a scanning electron microscope (SEM) and are shown in Figure 4. Figure 4a shows the whole fracture area of a sample containing 3 arrays of holes. In Figure 4b one can see that the ligament between the holes necked down to a line without any secondary void nucleation. Figure 4c shows the whole fracture area of a sample containing 1 array of holes. Figure 4d shows that the intervoid ligament broke in a brittle manner and it appears that it contains a twin. Different behaviors in the same samples may be attributed to different void interspacing and more so to different grain orientations. While comparing fracture surfaces of different samples a following trend was found: (i) brittle fracture occurs when grains were in a hard (i.e. not favorable for deformation) orientation and when few grains were present between voids; ii) ductile fracture takes place when grains were in a soft orientation and when several grains were present between voids.

## 3 Comparison with existing models

Experimental results were compared to the Rice and Tracey model [19] for void growth. The Rice and Tracey equations give the principal radii of the ellipsoidal void in the case of uniaxial tension in both tensile $R_1$ and transverse $R_2$ [20]:

$$R_1 = \exp\left(D\varepsilon_1\right) + \frac{1+E}{D}\exp\left(D\varepsilon_1\right) - 1\ R_0 \tag{4}$$

$$R_2 = \exp\left(D\varepsilon_1\right) - \frac{1+E}{2D}\exp\left(D\varepsilon_1\right) - 1\ R_0 \tag{5}$$

where

$$D = 0.558\sinh\left(\frac{3}{2}\frac{\sigma_m}{Y}\right) + 0.008\cosh\left(\frac{3}{2}\frac{\sigma_m}{Y}\right) \tag{6}$$

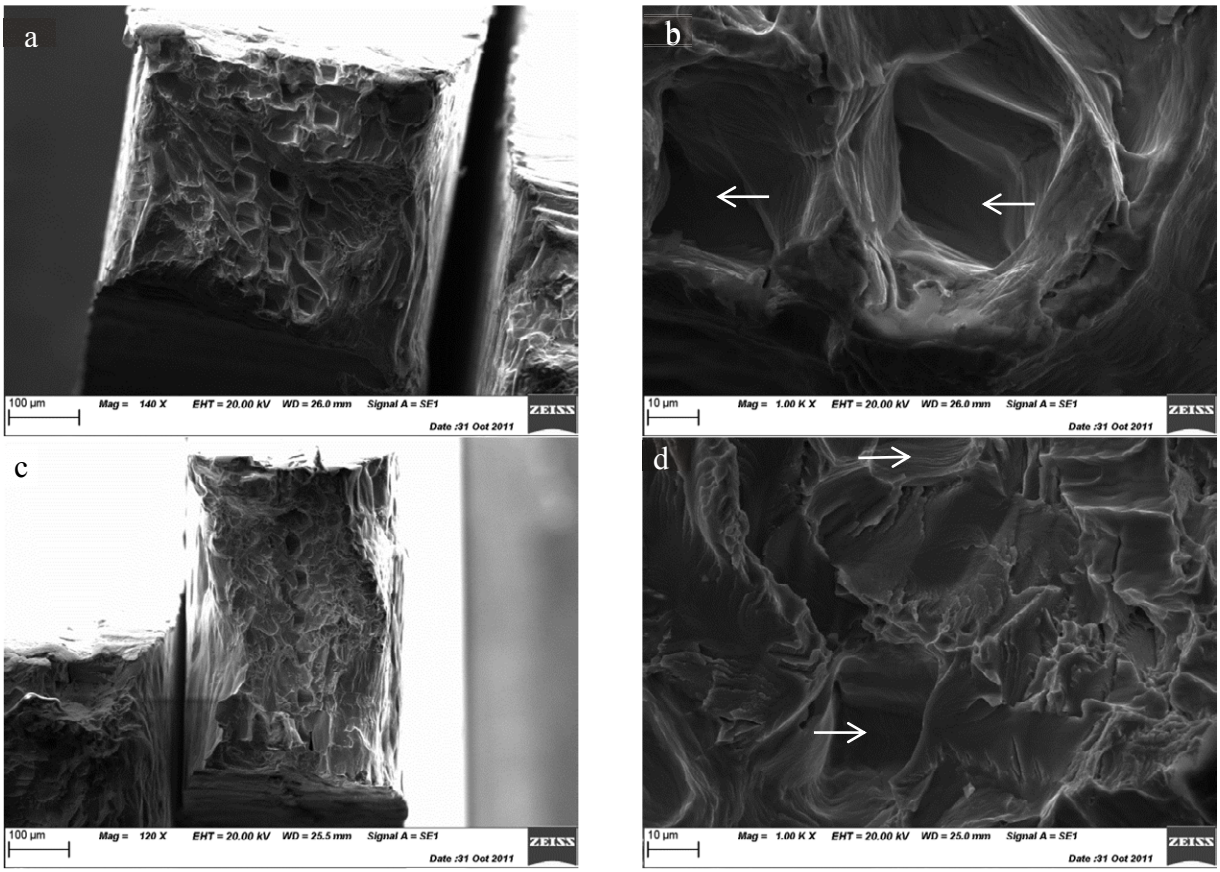


Figure 4. SEM images of the fracture surface: (a) sample with three arrays of holes; (b) a close up showing the ligament between two laser holes; (c) sample with one array of holes; (d) a close up showing transgranular fracture and a twin. Arrows show the position of the voids.

$\varepsilon_1$ is the total logarithmic strain integrated over the total strain path, $\sigma_m$ is the mean stress and $Y$ the yield stress. The parameters $D$ and $E$ are used in the Rice and Tracey model to vary the contribution of the volume and shape changing part to void growth respectively. In the case of pure titanium, because the difference between the yield stress and the ultimate tensile stress (UTS) is high (more than a factor of 2), the material is assumed to be strongly hardening and the parameter (1 + E) from equation 5 is equal to 5/3 as proposed by Rice and Tracey [19].

The curvature radius and the radius of the minimal section were measured by hand in order to determine the average stress triaxiality T in the center of the minimum cross-section, using the Bridgman formula [23]:

$$\frac{\sigma_m}{Y} = \frac{1}{3} + \ln\left(\frac{a+2r}{2r}\right) \tag{7}$$

where $a$ is the smallest cross sectional radius and $r$ the neck radius. The experimentally measured normalized void dimensions in the tensile direction (Figure 3a and c) and in the transverse direction (Figure 3b and d) are compared to the Rice and Tracey model predictions. There is a

clearly good fit between the experimental data and the model in the tensile direction. There is a good fit between the experimental data and the model in transverse direction at low strains. However the Rice and Tracey model significantly underestimates the normalized void radius at higher strains because it does not take into account coalescence.
Even though void growth is well predicted by the Rice and Tracey model in average, there is still a scatter in the data which could mean that different voids grow at different rates, possibly due to grain orientation effects and twinning.

## Conclusion

Using laser-drilled materials and x-ray computed tomography, void growth was captured in detail inside titanium samples. The Rice and Tracey model was found to give good predictions of void growth rates in the tensile direction. These results show that it is possible to obtain quantitative and reproducible information on the ductile fracture process to validate ductile fracture models for anisotropic materials such as titanium.

## References


1. M.H. Yoo, "Slip, Twinning, and Fracture in Hexagonal Close-Packed Metals," Metallurgical Transactions A, 12A (1981), 409-418.
2. D.H. Buckley, "Influence of crystal orientation on friction characteristics of titanium single crystals in vacuum" (NASA technical note, National aeronautics and administration, 1965).
3. G. Salishchev et al., "Changes in misorientations of grain boundaries in titanium during deformation," Materials Characterization, 61 (7) (2010), 732-739.
4. V.V. Stolyarov et al., "Grain refinement and properties of pure Ti processed by warm ECAP and cold rolling," Materials Science and Engineering, A343 (2003), 43-50.
5. N.P. Gurao and S. Suwas, "Evolution of crystallographic texture during deformation of submicron grain size titanium" Journal of Materials Research, 26 (4) (2011), 523-532.
6. J.J. Fundenbergert et al., "Modelling and prediction of mechanical properties for materials with hexagonal symmetry (zinc, titanium and zirconium alloys),"ActaMaterialia, 45 (10) (1997), 4041-4055.
7. A.A. Salem, S.R.Kalidindi, and S.L.Semiatin, "Strain hardening due to deformation twinning in α-titanium: Constitutive relations and crystal-plasticity modeling," ActaMaterialia, 53 (2005), 3495-3502.
8. X. Wu et al., "Prediction of crystallographic texture evolution and anisotropic stress–strain curves during large plastic strains in high purity α-titanium using a Taylor-type crystal plasticity model," ActaMaterialia, 55 (2) (2007), 423–432.
9 G. Proust, C.N. Tome and G.C.Kaschner, "Modeling texture, twinning and hardening evolution during deformation of hexagonal materials," ActaMaterialia, 55 (6) (2007), 2137–2148.
10. Y. Krishna Mohan Rao, V.V. KutumbaRao, E. Rama Rao, "Influence of microstructure on void nucleation and growth in a near-α titanium alloy IMI 685," Materials Science and Engineering A, 110 (1989) 193-202.
11. C.N. Tome, R.A. Lebensohn, U.F. Kocks, "A model for texture development dominated by deformation twinning: Application to zirconium alloys," ActaMetallurgica, 39 (11) (1991), 2667-2680.
12. R.A. Lebensohn and C.N. Tome, "A self-consistent anisotropic approach for the simulation of plastic deformation and texture development of polycrystals: Application to zirconium alloys," ActaMaterialia, 41 (9) (1993), 2611-2624.
13. G.C. Kaschner et al., "Mechanical response of zirconium—II.Experimental and finite element analysis of bent beams," ActaMaterialia, 49 (15) 2001, 3097-3108.
14. B. Bhattacharya and M. Niewczas, "Work-hardening behaviour of Mg single crystals oriented for basal slip," Philosophical Magazine, 91 (17) (2011), 2227-2247.
15. Brown D.W. et al., "Internal strain and texture evolution during deformation twinning in magnesium," Materials Science and Engineering A, 399 (1-2) (2005) 1–12.
16. A. Jain et al., "Grain size effects on the tensile properties and deformation mechanisms of a magnesium alloy, AZ31B, sheet," Materials Science and Engineering A, 486 (2008), 545–555.
17. G.P. Potirniche et al., "Lattice orientation effects on void growth and coalescence in fcc single crystals," International Journal of Plasticity 22 (2006), 921-942.
18. F. Roters et al., "Overview of constitutive laws, kinematics, homogenization and multiscale methods in crystal plasticity finite-element modeling: Theory, experiments, applications," ActaMaterialia, 58 (2010), 1152–1211.
19. J. Rice and D. Tracey, "On the ductile enlargement of voids in triaxial stress fields," Journal of the Mechanics and Physics of Solids, 17 (3) (1969), 201-217.
20. P.F. Thomason, Ductile Fracture of Metals (Oxford: Pergamon Press, 1990).
21. A. Weck et al., "Visualization by x-ray tomography of void growth and coalescence leading to fracture in model materials", ActaMaterialia, 56 (12) (2008), 2919-2928.
22. W.S.Rasband, ImageJ, U. S. National Institutes of Health, Bethesda, Maryland, USA, http://imagej.nih.gov/ij/, 1997-2011.
23. Bridgman P.W., Studies in Large Plastic Flow and Fracture, New York,McGraw-Hill: 1952.

1st International Conference on 3D Materials Science
*Edited by: Marc De Graef, Henning Friis Poulsen, Alexis Lewis, Jeff Simmons, George Spanos*
***TMS (The Minerals, Metals & Materials Society), 2012***

# QUATIFICATION OF PRIMARY PHASE UNDERCOOLING OF RAPIDLY SOLIDIFIED DROPLETS WITH 3D MICROTOMOGRAPHY

A. Ilbagi[1], P. Delshad Khatibi[1], H. Henein[1], Ch. A. Gandin[2,3] and D. M. Herlach[4]

[1]Department of Chemical and Materials Engineering, University of Alberta
Edmonton, Alberta, T6G 2G6 Canada
[2]MINES ParisTech & [3]CNRS, CEMEF UMR 7635, 06904 Sophia Antipolis, France
[4]Institut für Materialphysik im Weltraum Deutsches Zentrum für Luft- und Raumfahrt
51147 Köln, Germany

Keywords: Microtomography, Atmozation, Undercooling

## Abstract

Powders of different compositions of Al-Cu alloys were atomized in helium and nitrogen and the microstructure of the atomized droplets was examined using X-ray micro-tomography. A method was developed to remove X-ray artifacts and background noise from the particles images. The method developed involves creating a clean mask file using MATLAB image toolbox, followed by applying the mask file to the original image to achieve clean images for the particle of interest. Separate features of interest in the droplets, such as region of initial growth and primary dendrites, were investigated at the various stages of solidification. The data is used to estimate the primary phase undercooling of the droplets, which will be used in a solidification model as an input to estimate the phase fractions. The results will then be compared with the experimental results.

## Introduction

Rapid solidification techniques are of great importance due to their ability to produce various structures which are not possible to achieve in conventional solidification processes [1]. Characterization techniques such as 2D microscopy can be used to provide valuable information about solidification microstructure, but they are limited by the number of sections that can be studied from a sample; therefore, 3D visualization techniques have been utilized to gather information about the entire solidified volume. X-ray tomography is one such 3D visualization technique in which the X-ray beams from a synchrotron facility are used to construct the 3D image of the solidified body. Prasad et al. [2] used this technique to study solidification microstructure of Impulse Atomized particles of Al-5wt%Cu and Al-17wt%Cu alloys. Using this technique, nucleation sites in different particles were identified and recalescence boundaries were seen in the vicinity of the nucleation sites [3]. In this paper a methodology will be described to estimate the primary phase undercooling from the volume fraction of the recalescence region measured using tomography data.

## Experimental Procedure

All particles studied in this research were produced using Impulse Atomization (IA) technique. IA is a single fluid atomization technique in which the molten metal is pushed through several orifices by applying recurring forces. As a result, liquid ligaments emanate from the orifices and fall into a drop tube filled with inert gas. The ligaments then break into spherical droplets due to Rayleigh instability, and lose heat to the surrounding gas while falling. Eventually, the solidified

droplets are collected at the bottom of the tube. IA has been used to produce rapidly solidified metallic (or non-metallic) powders. This process can reproducibly yield powders of uniform size-distribution with cooling rate as high as $10^5$ K/s [4]. For this research, powders of Al-5wt%Cu and Al-17wt%Cu were produced using nitrogen as cooling gas.

X-Ray beams from synchrotron facilities were used to carry out computer tomography work. Observations were made on the droplets using X-ray beams of 1 μm resolution at European Synchrotron Radiation Facility (ESRF, France) and 0.37 μm resolution at Swiss Light Source (SLS, Switzerland). This non-destructive technique generated RAW files for the 3-dimensional section of the droplet. The size of each RAW file ranges from 1GB to 16GB. Analysis of the data sets involves the following steps:

1. Generate a histogram of the data
2. Locate the minimum data value between peaks. This corresponds to particle and exterior ranges of data values.
3. Do a thresholding operation on the data using the value from step 2. This generates a new data set contain 2 values, one for the particle and one for the exterior. Note that this new data set contains a variety of structures which must be cleaned.
4. Clean the thresholded data set by locating connected regions and filling in the small structures, both on the inside and outside. The result is the mask file which allows for separating the original data into particle and non-particle regions. This operation is done on each slice of the data set using 2D connection information. For more details of the technique used see [5].

## Results and Discussion

The crystallization of an undercooled melt occurs in two steps. Once nucleation has initiated solidification, the subsequent growth of the solid phase leads to the release of the heat of fusion $\Delta H_f$. In the case of rapid crystal growth a steep rise of temperature takes place, called recalescence. Assuming that solidification during recalescence occurs under near-adiabatic conditions the volume fraction solidifying during recalescence under non-equilibrium conditions can be determined by Eq. 1 [6].

$$f_R = \frac{\Delta T}{\Delta T_{hyp}} \tag{1}$$

where $\Delta T_{hyp} = \frac{\Delta H_f}{C_p^l}$ is the hypercooling limit and $C_p^l$ is the specific heat of the liquid. Prasad et al. [3] using X-ray tomography for particles of Al-Cu of both compositions identified the region of initial growth and recalescence boundaries (primary trunks). Also, the volume fraction of these regions in the droplets was evaluated. There were differences in the volume fraction of these regions observed in the Al-5wt%Cu and Al-17wt%Cu. This was believed to be caused by the difference in growth rates between the two compositions for a given undercooling.

Figure 1 shows a 2D image from tomography on a particle of Al-5wt%Cu. The regions of ultra-fine structure, representative of nucleation region, and the primary dendrite trunks are highlighted in the figure.

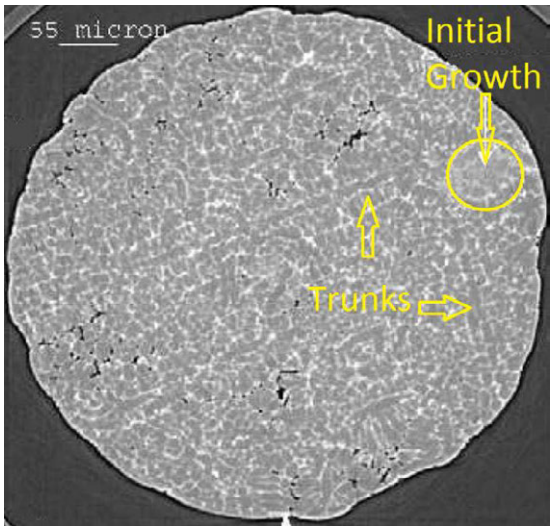


Figure 1. A 2D image from tomography on a particle of Al-5wt%Cu. The regions of ultra-fine structure and the primary dendrite trunks are highlighted in the figure.

Using stereological analysis [7] on the tomography images, the average volume fraction of nucleation and recalescence region within the particle was quantified for all the droplets (one Al-5wt%Cu droplet and four Al-17wt%Cu droplets). The calculation was done using the Cavalieri method [8]. It basically involves selecting the volumetric region containing the region of interest within the droplet and dividing that region into a fixed number of slices of known thickness. The area fraction of the feature of interest on each slice is then measured and the volume of that region for each slice is given by the product of area fraction and the slice thickness. A manual point count technique was employed for measuring the area fraction on each slice. Finally, the summation of the volume fraction for each slice gives the total volume fraction of the recalescence region for the entire droplet. Table 1 presents the results of recalescence volume fraction measurement, as well as corresponding calculated undercooling. Also, the properties of alloys used for this calculation are shown in Table 2.

Table 1.Measured recalescence volume fraction and corresponding calculated primary phase undercooling.

| Droplet Details | Al-5wt%Cu | Al-17wt%Cu (1) | Al-17wt%Cu (2) | Al-17wt%Cu (3) | Al-17wt%Cu (4) |
|---|---|---|---|---|---|
| Diameter (μm) | 660 | 480 | 490 | 450 | 420 |
| Recalescence vol. % | 19.4 ± 0.6 | 27.8 ± 2.4 | 33.3 ± 2.3 | 44.1 ± 2.2 | 32.1 ± 3.1 |
| Primary phase undercooling (K) | 64.9 ± 2.0 | 94.6 ± 8.2 | 113.3 ± 7.8 | 150.0 ± 7.5 | 109.2 ± 10.6 |

Table 2. Properties of alloys used in the calculation of primary phase undercooling.

| Alloy properties | Al-5wt%Cu | Al-17wt%Cu |
|---|---|---|
| Density (kg $m^{-3}$) | 2760 | 2870 |
| Specific heat (J $K^{-1}kg^{-1}$) | 1176.3 | 1152.9 |
| Latent heat (J $kg^{-1}$) | 393699.3 | 392247.4 |

The primary phase undercooling values shown in Table 1 were used in a solidification model to predict the phase fractions after solidification of IA particles. The details of the solidification model can be found elsewhere [9, 10]. In brief, the model assumes a uniform temperature for the entire droplet. The droplet starts falling at the atomization temperature with an initial velocity of

0.5 m/s. While the droplet continues to fall through the quiescent gas, it loses heat mainly through convection. At some user defined temperature, the nucleation of a microstructure is assumed to occur in the droplet center and to develop by radial growth of a spherical zone. At first, a dendritic microstructure is modeled, followed by a eutectic microstructure. This diffusion-based microsegregation model is coupled with diffusion in the extradendritic liquid following the model proposed by Wang and Beckermann [11]. Solidification results in latent heat release proportional to the solidification rate, and as a result the net heat content of the droplet is given by the difference between the latent heat generated and the convective heat loss. The latent heat is released until solidification is complete. Prasad et al. [10] using the interpolation of the eutectic undecoolings reported in [9] found values for the primary phase and eutectic undercooling (see Table 3). Then they used those values as input for the solidification model. The model's outcome for weight percent of eutectic microstructure was then compared with that from the experiment and reasonable match between prediction and measurements was achieved.

Table 3. Values of primary and eutectic undercooling used in [10].

| | | |
|---|---|---|
| Dendritic nucleation undercooling, $\Delta T_N^p$ [K] | | 15 |
| Eutectic nucleation undercooling, $\Delta T_N^e$ [K] | 5wt%Cu | 20 |
| | 10wt%Cu | 20 |
| | 17wt%Cu | 27.5 |

They also showed that the primary phase undercooling plays minor role in the phase fractions observed in the solidified particles. However, as it is shown in Table 1 the primary phase undercooling achieved was significantly higher than that was predicted by the previous authors (Table 3). The effect of this increase in the amount of primary phase undercooling is discussed next.

The particle size and primary phase undercoolings for the 4 particles of Al-17wt%Cu were averaged (116.8K) and used as input for the mathematical model. Also, the standard deviation of this calculation was used to find lower and higher limit for primary phase undercooling (i.e. 95K and 138K). To calculate the eutectic fraction, several different values for eutectic undercooling were also used. For Al-5wt%Cu, the eutectic undercooling reported in [10] was used along with the primary phase undercooling found in Table 1. However, for Al-17wt%Cu, the amount of eutectic undercooling used in [10], i.e. 27.5K, along with any of the primary phase undercoolings shown in Table 1 will result in complete suppression of the primary phase. This shows that the eutectic started to occur at lower temperatures than that assumed in [10]. Table 4 and 5 show the modeling results for eutectic weight fraction in Al-5wt%Cu and Al-17wt%Cu, respectively. If one does not take into account the 100 % eutectics values as they are not relevant and also does not take into account the 0 undercooling because it is expected to be some, the average wt% eutectic is 27.9% ± 2.8% for Al-17wt%Cu and is 6.3 ± 0.4% for Al-5wt%Cu. One then can average the corresponding undercooling values for primary undercooling and eutectic undercooling. The calculated values from Table 4 and 5 were then compared with that from experimental, reported in [10], equilibrium and Scheil prediction in Figure 2. From this figure it is evident that for Al-5wt%Cu, the eutectic fraction is not significantly sensitive to any of the primary phase and eutectic phase undercooling values and the model can closely predict the phase fractions. For Al-17wt%Cu, however, it seems that using 95 and 50K undercooling for primary and eutectic undercooling, respectively, results in closest eutectic fraction to that from experimental measurements. While no undercooling for both primary and eutectic phase results in overestimation of eutectic fraction, increasing the amount of undercooling for both primary and eutectic (above 95 and 50, respectively) resulted in underestimation of eutectic fraction.

Table 4. Undercooling values used as input for simulation and corresponding results of calculated primary phase and eutectic fraction for Al-5wt%Cu.

| Diameter=660μm | Gas=N2 | | |
|---|---|---|---|
| **Primary undercooling (K)** | **Eutectic undercooling (K)** | **wt% primary phase** | **wt% eutectic** |
| 0 | 0 | 92.8 | 7.2 |
| 0 | 20 | 93.1 | 6.9 |
| 65 | 0 | 93.7 | 6.3 |
| 65 | 20 | 94.0 | 6.0 |

Table 5. Undercooling values used as input for simulation and corresponding results of calculated primary phase and eutectic fraction for Al-17wt%Cu.

| Diameter = 460μm | Gas=He | | |
|---|---|---|---|
| **Primary undercooling (K)** | **Eutectic undercooling (K)** | **wt% primary phase** | **wt% eutectic** |
| 0 | 0 | 64.3 | 35.7 |
| 95 | 50 | 68.1 | 31.9 |
| 95 | 60 | 69.6 | 30.4 |
| 95 | 70 | 71.3 | 28.7 |
| 116 | 50 | 0.0 | 100.0 |
| 116 | 60 | 70.3 | 29.7 |
| 116 | 70 | 72.0 | 28.0 |
| 116 | 80 | 73.9 | 26.1 |
| 138 | 70 | 0.0 | 100.0 |
| 138 | 80 | 74.8 | 25.2 |
| 138 | 90 | 76.5 | 23.5 |

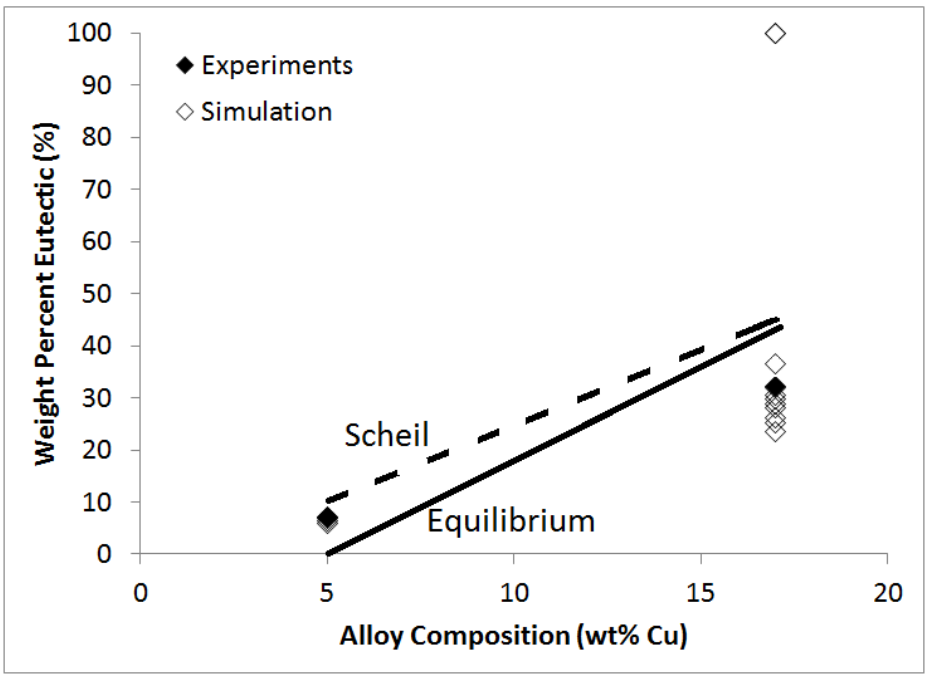


Figure 2. Comparison of weight fraction of eutectic from experimental with that from modeling, Scheil-Gulliver and equilibrium. Al-5wt%Cu particles were atomized in nitrogen and particles of Al-17wt%Cu were atomized in helium.

On the other hand, the difference between the experimental values and those predicted by Scheil-Gulliver and equilibrium shows that the primary phase and eutectic undercooling play a very important role in the final percent of eutectic in the droplets.
In order to reduce the variations in the measured volume percentage of recalescence region, higher resolution tomography is beneficial. Also, Focused Ion Beam (FIB) is being used to create multiple slices of region of interest at higher resolution.

## Summary

X-ray tomography was used to study the 3D microstructure of Al-5 and 17 wt%Cu powders. The volume fraction of recalescence region was measured and used to estimate the primary phase undercooling. It was found that the particles with higher Cu content achieve higher primary and eutectic undercooling. The results were then used as input in a solidification model to estimate the weight fraction of phases formed during solidification. Comparison between model prediction and experiments is performed considering the eutectic percent. It is found that a reasonable match between prediction and measurements can be reached by using certain levels of primary and eutectic undercooling

## Acknowledgements

Funding from the Canadian Space Agency and the Natural Sciences and Engineering research Council of Canada is acknowledged. The authors would like to thank European Synchrotron Radiation Facility (ESRF) in Grenoble, France for beam time.

## References

[1] H. Jones, Rapid Solidification of Metals and Alloys, 1982, The Institution of Metallurgists, Whetstone, London.
[2] A. Prasad, H. Henein, E. Maire, and C.A. Gandin, *X-ray tomography study of atomized al-cu droplets*, Canadian Metallurgical Quarterly, **43**(2) (2004) 273.
[3] A. Prasad, H. Henein, E. Maire, and C.A. Gandin, *Understanding the rapid solidification of al-4.3Cu and al-17Cu using X-ray tomography*, Metallurgical and Materials Transactions A, **37**(1) (2006) 249.
[4] H. Henein, *Single fluid atomization through the application of impulses to a melt*, Materials Science and Engineering A **326** (2002) 92.
[5] J. Johansson, A. Ilbagi, D. Thornton, H. Henein: "Processing 3D Data Sets from X-Ray Micro-Tomography of Impulse Atomized Al-Ni Particles," Symposium on Three-Dimensional Materials Science VI, TMS Annual Meeting, Seattle, WA, Feb. 2010.
[6] D.M. Herlach, P. Galenko, D. Holland-Moritz, "Metastable Solids from Undercooled Melts", ed. Robert Cahn, Pergamon Materials Series, (2007), 317.
[7] R.T. DeHoff and F.N. Rhines: Quantitative Microscopy, 1st ed., McGraw-Hill Book Company, New York, NY, 1968, pp. 45-53.
[8] C.V. Howard and M.G. Reed: Unbiased Stereology: 3-Dimensional Measurement in Microscopy, BIOS Scientific Publishers Limited, Oxfordshire, UK, 1998, pp. 39-44.
[9] Ch.-A. Gandin, S. Mosbah, Th. Volkmann and D. M. Herlach: Acta Mater., 56 (2008), 3023.
[10] A. Prasad, S. Mosbah, H. Henein and Ch.-A. Gandin, *A solidification model for atomization*, ISIJ International, **49**(7) (2009) 992.
[11] C. Y. Wang and C. Beckermann: Metall. Trans. A, 24 (1993), 2787.

1st International Conference on 3D Materials Science
*Edited by: Marc De Graef, Henning Friis Poulsen, Alexis Lewis, Jeff Simmons, George Spanos*
***TMS (The Minerals, Metals & Materials Society), 2012***

# 3D MICROSTRUCTURAL ARCHITECTURES FOR METAL AND ALLOY COMPONENTS FABRICATED BY 3D PRINTING/ADDITIVE MANUFACTURING TECHNOLOGIES

E. Martinez,[1,2] L. E. Murr,[1,2] K. N. Amato,[1,2] J. Hernandez,[1,2] P. W. Shindo,[1,2]
S. M. Gaytan,[1,2] D. A. Ramirez,[1,2] F. Medina,[2] R. B. Wicker[2]

[1]Department of Metallurgical and Materials Engineering
The University of Texas at El Paso, El Paso, TX 79968 USA
[2]W. M. Keck Center for 3D Innovation, The University
of Texas at El Paso, El Paso, TX 79968 USA

Keywords: Electron and Laser Beam Melting, 3D Microstructures, Metals and Alloys

## Abstract

The layer-by-layer building of monolithic, 3D metal components from selectively melted powder layers using laser or electron beams is a novel form of 3D printing or additive manufacturing. Microstructures created in these 3D products can involve novel, directional solidification structures which can include crystallographically oriented grains containing columnar arrays of precipitates characteristic of a microstructural architecture. These microstructural architectures are advantageously rendered in 3D image constructions involving light optical microscopy and scanning and transmission electron microscopy observations. Microstructural evolution can also be effectively examined through 3D image sequences which, along with x-ray diffraction (XRD) analysis in the x-y and x-z planes, can effectively characterize related crystallographic/texture variances. This paper compares 3D microstructural architectures in Co-base and Ni-base superalloys, columnar martensitic grain structures in 17-4 PH alloy, and columnar copper oxides and dislocation arrays in copper.

## Introduction

Additive manufacturing or layer-by-layer fabrication using print formats involving ink-jet technologies or other powder technologies using laser or electron beam sintering or melting are evolving as novel, modular or product-specific manufacturing concepts. The creation of 3D arrays using CAD-directed printers or selective melting of powder beds using focused, scanned laser or electron beams provides for new directional solidification concepts and prospects for novel microstructure or microstructural architecture development.

Figure 1 compares the fundamental features of electron beam melting (EBM) (Figure 1(a)) and selective laser melting (SLM) (Figure 1(b)). In these comparative additive-layer fabrication technologies, metal or pre-alloyed and atomized (rapidly-solidified) powders (Figure 2(a) and (b)) are raked or rolled into layers 50 to 100 μm thick, pre-heated, and selectively melted using a variety of beam-scan strategies [1,2]. The melt scan involves the creation of continuously

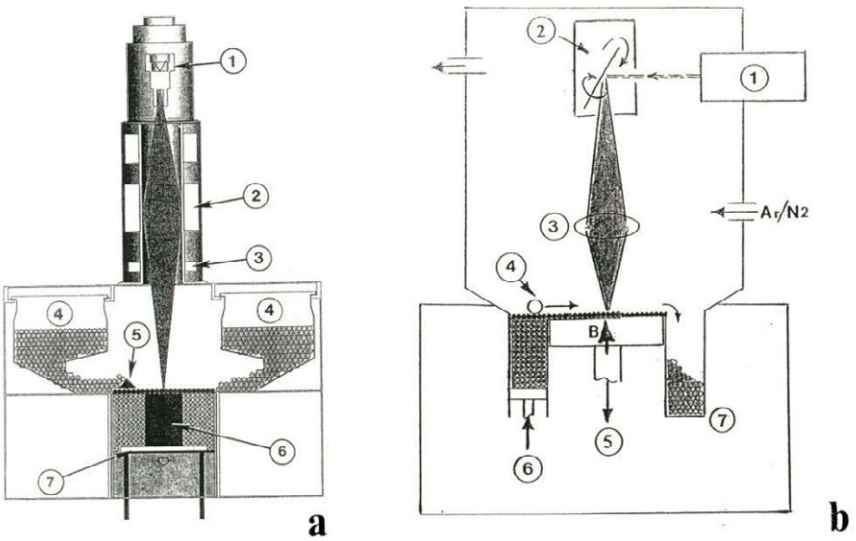


Figure 1. Schematic views for (a) electron beam melting and (b) selective laser melting. (a) Electron gun (1); beam focus and scan coils (2, 3); Powder cassettes (4), layer rake (5); building component (6); build table (7). (b) Laser source (1); scanning mirrors (2); beam focus (3); layer roller (4); build table (5); powder feed and collector containers (6, 7). The EBM system is in vacuum while the SLM system is in inert gas (Ar or $N_2$). The build direction (B) is parallel to the beam axis.

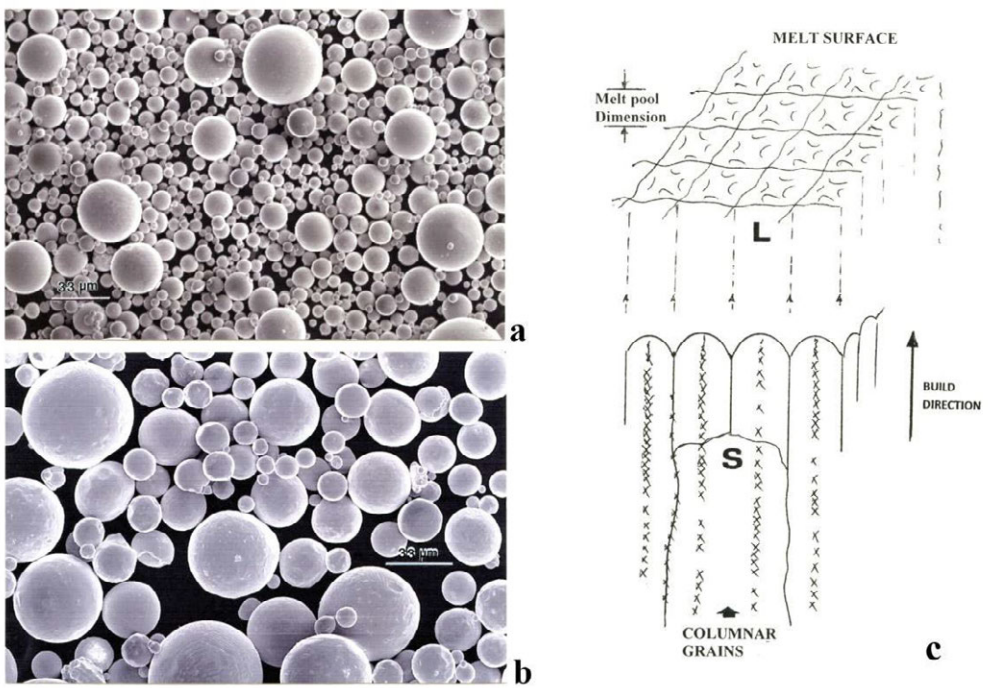


Figure 2. Examples of precursor, atomized powders: (a) copper; (b) Inconel 625 (Ni-21Cr-9Mo-3.5Nb). (c) shows a schematic representing the directional solidification of melt pools during the component building from such powders.

connected melt pools (Figure 2(c)) having nominal dimensions ranging from ~1 to 3 μm. As the melted layers cool and subsequent melt layers are created, columns of microstructures, including oriented (textured) grains are created by complex, epitaxial, directional solidification.

## Results and Discussion

Figure 3(a) shows a 3D-optical metallographic image composition for a Co-base superalloy (Co-26Cr-6Mo-0.2C; in weight percent) product fabricated by EBM. Figure 3(b) illustrates a TEM image showing the columnar $Cr_{23}C_6$ (cubic) precipitates formed within the melt (L) – solidification (S) arrays depicted schematically in Figure 2(c) [3]. Figure 4(a) and (b) compare similar 3D microstructural architectures for EBM-fabricated Cu where columnar arrays of $Cu_2O$ (cubic) precipitates were formed in contrast to the $Cr_{23}C_6$ precipitates shown in Figure 3, as a consequence of EBM fabrication [4]. The $Cu_2O$ precipitates were formed in the original copper powder in Figure 2(a).

In contrast to the columnar precipitates formed by EBM as shown for comparison in Figures 3 and 4, Figure 5 shows columnar-like martensitic (α-Fe) laths created by SLM fabrication of cylindrical components from 17-4 PH-stainless steel (pre-alloyed) powder (Fe-17Cr-4Ni-4Cu-0.5Nb in weight percent).

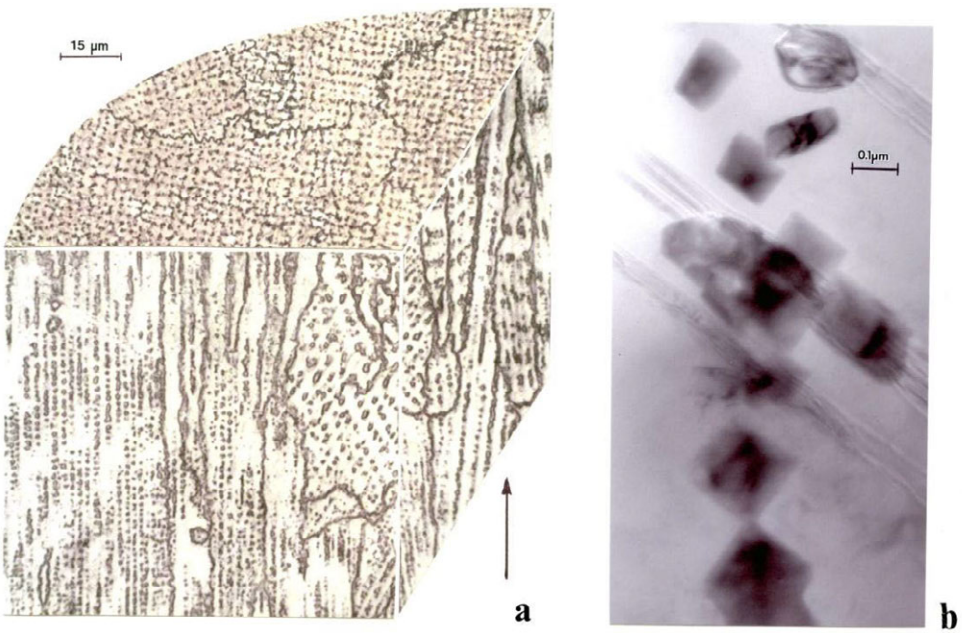


Figure 3. (a) 3D image composition for EBM fabricated Co-base superalloy. (b) Transmission electron microscopy image showing details of columnar $Cr_{23}C_6$ cubic precipitates in (a). Note build direction is shown by arrow in (a).

Figures 6 and 7 compare two Ni-base superalloys (Inconel 625 and 718, respectively) fabricated by EBM and SLM, respectively. These exhibit columnar precipitation of γ″ platelets (or disc-like platelets) having a bct structure, while the corresponding Ni-Cr matrix is fcc. In Figure 6(b),

the γ″ ($Ni_3Nb$) precipitates are coincident with the fcc matrix {111} planes, while in Figure 7(b), they are coincident with the fcc matrix {100} planes [5,6]. The orientation and morphology of the γ″ precipitates is apparent on examining the 3D TEM compositions in Figures 6(b) and 7(b), while comparisons of the 3D composites in Figures 6(a) and 7(a) provide an overall perspective for the microstructural architectures developed by both EBM and SLM fabrication [2]. Indeed, the crystallographic aspects are also demonstrated for these 3D image views on comparing corresponding XRD spectra and selected-area electron diffraction (SAED) patterns for the horizontal and vertical image planes illustrated in the 3D compositions.

It is of interest to note that in the columnar precipitation represented on comparing Figures 3, 4, 6 and 7, the precipitates are noncoherent, but are associated with dense arrays of dislocations which are a notable part of the columnar microstructures. A contributor to these dislocation microstructures (or sub-structures) involves the cooling which occurs in the layer building, and associated beam scan rates [1,2].

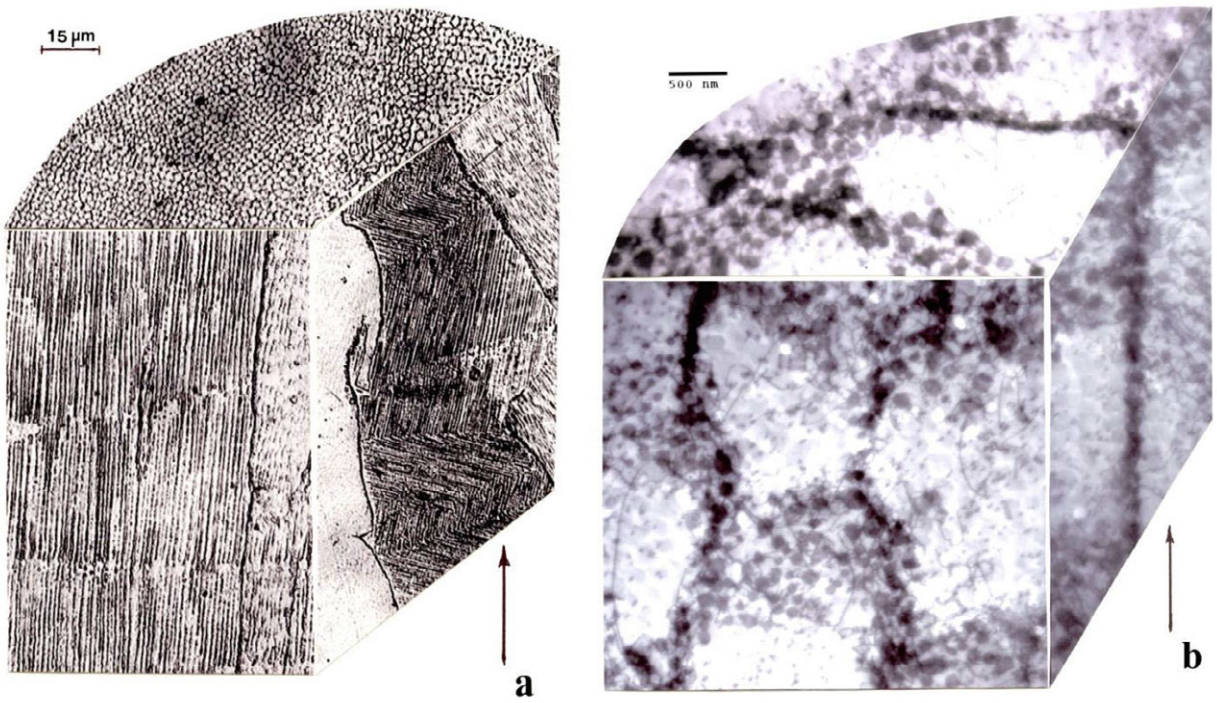


Figure 4. 3D image compositions for EBM fabricated copper components. (a) Light optical microscopy (LOM). (b) Transmission electron microscopy (TEM). Note build direction is shown by arrow in (a) and (b).

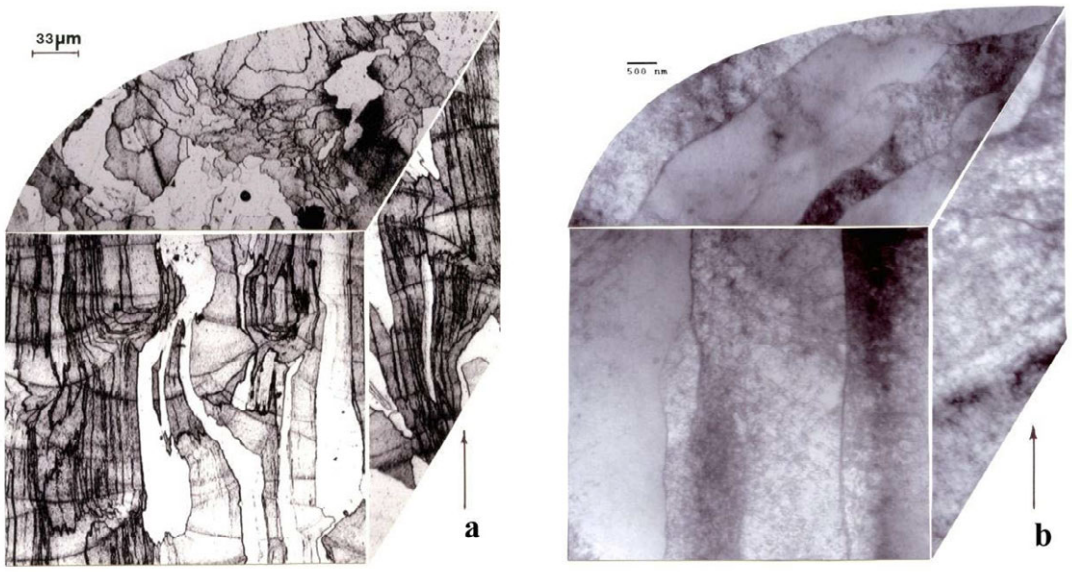


Figure 5. 3D image compositions for SLM fabricated 17-4 PH stainless steel components. Argon atomized powder was fabricated in an Ar gas environment. (a) LOM. (b) TEM. Note build direction is shown by the arrow in (a) and (b).

## Conclusions

In this paper we have provided examples for novel, directional microstructures and microstructural architectures (as columnar arrays of precipitates) using light optical micrographs and transmission electron microscope images arranged as 3D image compositions. These 3D compositions provide for three-dimensional characterization and visualization for structure-property relationships in materials fabricated by electron and laser beam technologies.

## References

1. L. Thijs et al., "A study of the Microstructure Evolution During Selective Laser Melting of Ti-6Al-4V", *Acta Materialia*, 58 (2010), 3303-3312.

2. L. E. Murr et al., "Metal Fabrication by Additive Manufacturing Using Laser and Electron Beam Melting Technologies", *Journal of Materials Science and Technology*, 28 (1) (2011) in press.

3. S. M. Gaytan et al., "Comparison of Microstructures and Mechanical Properties for Solid and Mesh Cobalt-Base Alloy Prototypes Fabricated by Electron Beam Melting", *Metallurgical and Materials Transactions*, 41A (2010), 3216-3227.

4. D. A. Ramirez et al., "Novel Precipitate-Microstructural Architecture Developed in the Fabrication of Solid Copper Components by Additive Manufacturing Using Electron Beam Melting", *Acta Materialia*, 59 (2011), 4088-4099.

5. L. E. Murr et al., "Microstructural Architecture, Microstructures, and Mechanical Properties for a Nickel-Base Superalloy Fabricated by Electron Beam Melting," *Metallurgical and Materials Transactions*, 42A (2011), 3491-3508.

6. K. N. Amato et al., "Microstructures and Mechanical Behavior of Inconel 718 Fabricated by Selective Laser Melting," *Acta Materialia* (2012), in press.

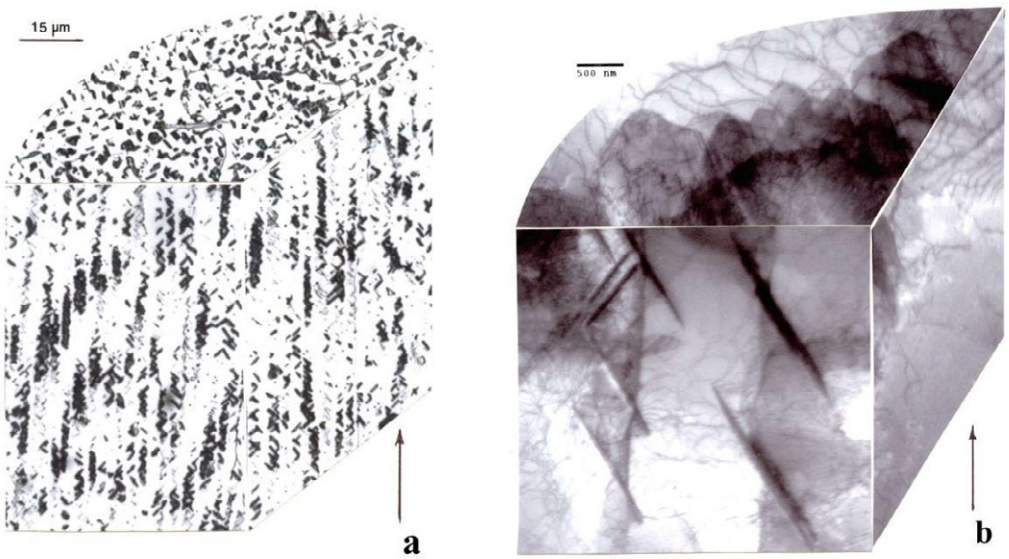


Figure 6. 3D image compositions for EBM fabricated Inconel 625. (a) LOM. (b) TEM. Note build direction shown by arrow in (a).

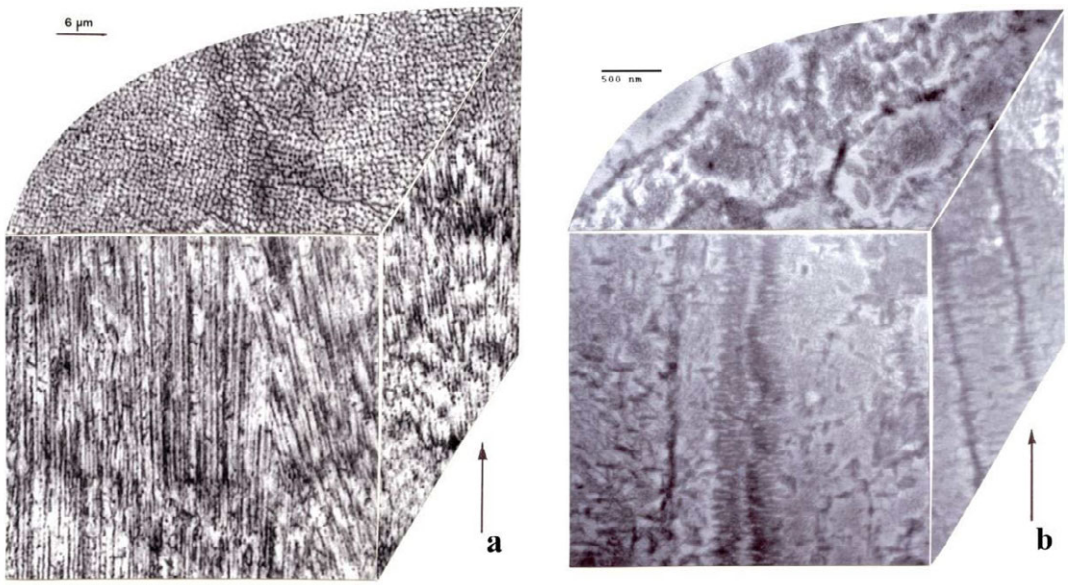


Figure 7. 3D image composition for SLM fabricated Inconel 718. (a) LOM. (b). TEM. Note build direction shown by arrow in (a) and (b).

1st International Conference on 3D Materials Science
*Edited by: Marc De Graef, Henning Friis Poulsen, Alexis Lewis, Jeff Simmons, George Spanos*
***TMS (The Minerals, Metals & Materials Society), 2012***

# Elastic Behavior of the Percolating Eutectic Structure of a High Pressure Die Cast Magnesium Alloy

Bao Zhang, Anumalasetty V. Nagasekhar, Carlos H. Caceres

ARC Centre of Excellence for Design in Light Metals, Materials Engineering
The University of Queensland, Brisbane, QLD 4072, Australia

Keywords: intermetallic network microstructure, magnesium alloys, bending-dominated behavior, stretch-dominated behavior, micro-truss lattice

## Abstract

The 3D configuration of the ($Mg_{17}Al_{12}$) $\beta$-phase intermetallic microstructure in the AZ91D alloy obtained using dual beam FIB tomography was incorporated into an FEM code and loaded in tension. The structure stiffness is consistent with bending-dominated behavior.

## Introduction

$\beta$- $Mg_{17}Al_{12}$ intermetallic forms in high-pressure die cast Mg-Al alloys when the mass content of Al exceeds 2% [1, 2] as part of the eutectic reaction occurring at the interdendritic boundaries. The eutectic in Mg-Al is divorced, and the intermetallic appears as a dispersion of isolated particles for Al concentrations below about 9%. For higher concentrations, 3D FIB [3] shows that the intermetallic forms a spatially interconnected network, akin to the structure of cellular foams [4], especially near the casting surface, or skin, because of the segregation of eutectic during the filling of the die. At the center of the cross section, or core, the degree of interconnection is less due to the accumulation of large dendritic grains solidified in the shot-sleeve, and which locally reduces the amount of eutectic.

The formation of the intermetallic network in the more concentrated Mg-Al alloys is thought to have a significant effect on the strength of the alloy, especially in thinner cast sections [5-7]. A quantitative study of the properties of intermetallic network structure is lacking, and most published calculations of the strength of hpdc Mg-Al alloys rely on order of magnitude estimates of the effect of the interdendritic intermetallic network [7]. The aim of the present work is to assess the elastic deformation behavior of the eutectic intermetallic network. To this end, previously published 3D FIB tomography data for AZ91 alloy [3]were incorporated into a finite element (FE) code and the stress-strain behavior of the structure assessed. This sort of analysis has been proven reliable in assessing the elastic response of porous ceramics [8, 9], whose spatial configuration is commonly modeled by overlapping spherical pores and solid spheres. These ideal structures resemble that of the intermetallic network of the present alloy, and it was thought that a similar analysis would shed light on the behavior of present material as well, with the non-trivial advantage that the 3D FIB data used for the modeling represents the actual structure.

## Data for Analysis

The FIB data for the analysis were obtained as described in detail in reference [3]. Briefly, with reference to Fig. 1, the volume located at the corner of the 10 x 5 $mm^2$ cross section of a high pressure die cast (hpdc) AZ91D alloy tensile specimen was sectioned into 0.25 μm thick slices,

of which the 2D secondary electron images were captured. The constituent phases in the 2D images (α-Mg and $Mg_{17}Al_{12}$) were segmented, and the data used for the 3D reconstruction of the $Mg_{17}Al_{12}$ phase using a dedicated software (AMIRA). Figure 2a shows the two constituent phases in the reconstructed volume, whereas the intermetallic structure is shown in Fig. 2b. The dimensions of the volume studied, labelled *Lx*, *Ly* and *Lz* in Fig. 2a, were 15.04, 13.46 and 14.5 $\mu m$, respectively. The fraction of $Mg_{17}Al_{12}$ in the volume studied was 12.62%, obtained with the software built-in tools.

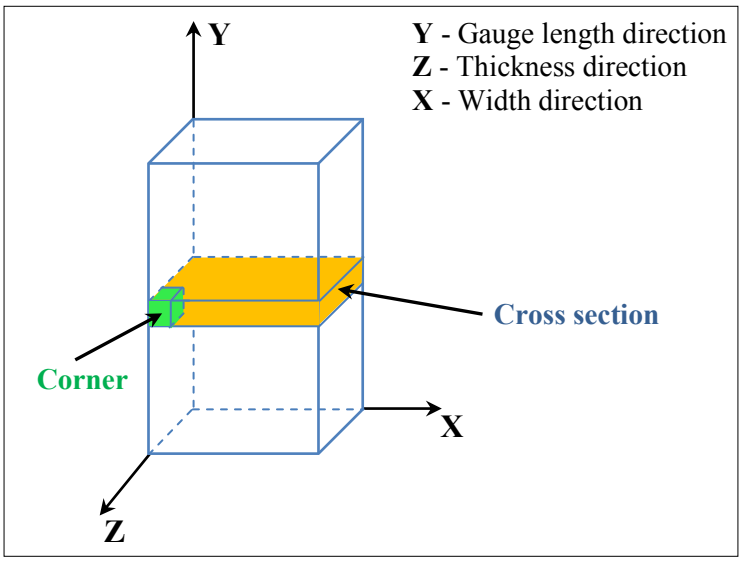


**Fig. 1 The volume studied (corner) on the tensile specimen's cross section.**

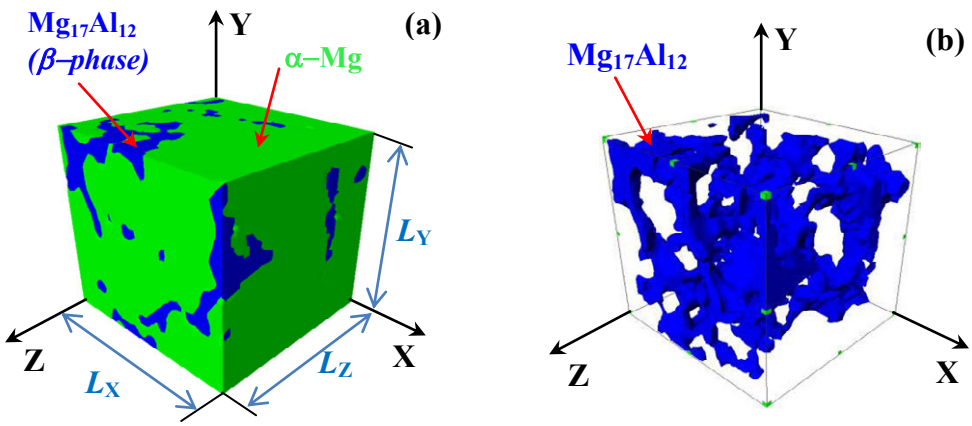


**Fig. 2: (a) the reconstructed volume; the darker phase represents the eutectic intermetallic, the lighter phase represents the (proeutectic and eutectic) α-Mg; (b) 3D image of the reconstructed eutectic intermetallic.**

## Finite Element Modelling

Figure 3 shows the grid used for the modelling. The intermetallic structure was discretised into 45,711 individual C3D4 elements. This number was high enough to ensure the convergence of the computed results. The overall structure was attached to the two rigid shells, one of which was stationary while the other could be displaced along the axis Y (tensile specimen's gauge length direction, see Fig. 1) to stretch the structure. A displacement (denoted by $\delta$) boundary condition was applied at the movable shell, and the force used to deform the structure, represented by *F*, was calculated from the model using Hooke's law.

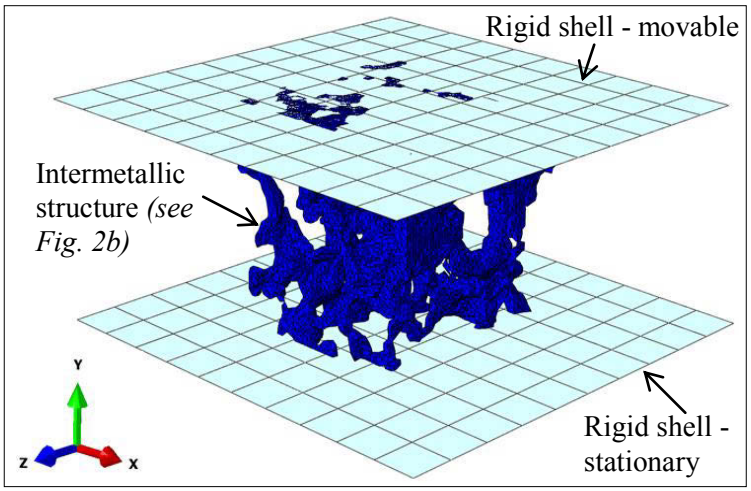


**Fig. 3 Finite element model**

The physical properties of the $Mg_{17}Al_{12}$ intermetallic used for the model are listed in Table 1. It was assumed that the eutectic intermetallic was crystallographcally isotropic. Likewise, it was also assumed that the 3D structure was isotropic.

**Table 1 Physical properties of the β-phase intermetallic, $Mg_{17}Al_{12}$ [10]**

| Density, $\rho_s$ (g/cm$^3$) | Young's modulus, $E_s$ (MPa) | Poisson's ratio, $\upsilon$ |
|---|---|---|
| 2.06 | 57300 | 0.3 |

## Results and Discussion

Figure 4 shows the stress-strain response of the intermetallic structure (denoted IS), together with four theoretically determined responses for comparison, namely, the Reuss and Voigt bounds of composites and lines representing bending- and stretch-dominated foamed structures.

The Reuss, $E_{Rs}$, and Voigt, $E_{Vt}$, bounds are the lower and upper limits to the elastic modulus of a fibre composite, and are given by eq. 1.

$$E_{Rs} = \frac{E_m E_r}{f E_m + (1-f)E_r} \qquad \text{(Reuss bound)} \qquad (1a)$$

$$E_{Vt} = f E_r + (1-f)E_m \qquad \text{(Voigt bound)} \qquad (1b)$$

where $E_m$, and $E_r$ are respectively the moduli of the matrix and the reinforcement and $f$ is the volume fraction of reinforcement. The calculations were done assuming $E_m = 0$, $Er = E_S$ (Table 1) and $f = 12.62\%$. Figure 4 shows that the IS's behavior falls within these two limits.

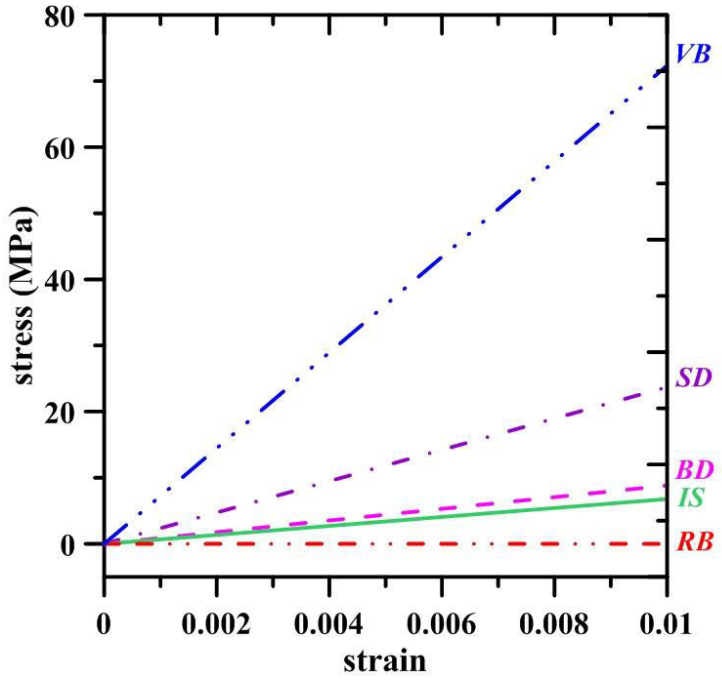


**Fig.4 The stress-strain response of the intermetallic structure (*IS*) as determined by the FE modeling, compared to the theoretically expected (eqs. 1 and 4), namely: Voigt bound *(VB)*; stretch-dominated (*SD)* and bending-dominated behavior *(BD)*; Reuss bound *(RB)*.**

Ashby and Brechet [11] defined two types of deformation behavior for cellular solids and micro-truss lattice-structures: bending-dominated and stretch-dominated. Bending-dominated corresponds to low mass efficiency, meaning a low structural modulus per unit mass in comparison with that of the stretch-dominated, which represents a high structural efficiency. The moduli, $E_{bn}$ and $E_{st}$, of structures exhibiting either behavior are approximated by eq. 2:

$$E_{bn} = E_S \left(\frac{\rho}{\rho_S}\right)^2 \qquad \text{(bending} - \text{dominated)} \qquad (2a)$$

$$E_{st} = \frac{E_S}{3}\frac{\rho}{\rho_S} \qquad \text{(stretch} - \text{dominated)} \qquad (2b)$$

where $\rho$ and $\rho_s$ represent the densities of the lattice and that of the material of which the micro-truss or cells walls are made of, respectively.

For the intermetallic structure of Fig. 2-b, the overall density $\rho$ can be related to the volume fraction of intermetallic by:

$$\rho = \rho_S f \qquad (3)$$

Substitution of eq. 3 into eq. 2 leads to:

$$E_{bn} = E_S f^2 \qquad (4a)$$

$$E_{st} = \frac{E_S f}{3} \qquad (4b)$$

Using values from table 1, lines of slopes given by Eq. 4 representing bending- and stretch-dominated behavior are included in Fig. 4; it is seen that the former very closely represents the present 3D eutectic structure.

## Conclusions

3D FIB tomography data and finite element (FE) analysis were used to evaluate the elastic deformation behavior of the eutectic intermetallic network formed in a high pressure die cast AZ91D alloy.
The stress-strain response of the intermetallic structure is consistent with the bending-dominated behavior of a cellular or micro-truss lattice-structure.

### *References*


[1] A.V. Nagasekhar, C.H. Caceres, M.A. Easton, Materials Science Forum, 618-619 (2009) 479-482.
[2] K.V. Yang, C.H. Caceres, N.A. V., M.A. Easton, Mater. Sci. Eng. A, (2012) in press.
[3] A.V. Nagasekhar, C.H. Caceres, C. Kong, Materials Characterization, 61 (2010) 1035-1042.
[4] L.J. Gibson, Ashby M. F., Proc. R. Soc. Lond. A, 382 (1982) 43-59.
[5] D. Amberger, P. Eisenlohr, M. Goken, Journal of Physics: Conference Series, 012068 (2010).
[6] C.H. Cáceres, W.J. Poole, A.L. Bowles, C.J. Davidson, Mater. Sci. Eng., 402A (2005) 269-277.
[7] C.H. Cáceres, J.R. Griffiths, A.R. Pakdel, C.J. Davidson, Mater. Sci. Eng., 402 (2005) 258-268.
[8] G. Bruno, A.M. Efremov, A.N. Levandovskyi, B. Clausen, J. Mater. Sci., 46 (2011) 161-173.
[9] A.P. Roberts, E.J. Garboczi, J. Am. Ceram. Soc, 83 (2000) 3041-3048.
[10] N. Wang, W.Y. Yu, B.Y. Tang, L.M. Peng, W.J. Ding, J. Phys. D: Appl. Phys., 41 (2008) 195408.
[11] M.F. Ashby, Y.J.M. Brechet, Acta mater, 51 (2003) 5801-5821.

1st International Conference on 3D Materials Science
*Edited by: Marc De Graef, Henning Friis Poulsen, Alexis Lewis, Jeff Simmons, George Spanos*
***TMS (The Minerals, Metals & Materials Society), 2012***

# NUMERICAL SIMULATIONS OF COMPRESSION PROPERTIES OF SiC/Fe–20Cr CO–CONTINUOUS COMPOSITES

Liang Yu[1], YanLi Jiang[1], SenKai Lu[2], HongQiang Ru[3], Ming Fang[3]

[1]Key laboratory of new processing technology for nonferrous metals & Materials, Ministry of Education, Guilin University of Technology, Guilin, 541004, China
[2]Institute of Materials Physics, Guilin Normal College, Guilin, 541004, China
[3]Key laboratory for anisotropy and texture of materials, & Materials, Ministry of Education (MOE), Northeastern University, Shenyang, 110819, China

Keywords: Micromechanical properties, Solidwork simulation, SiC/Fe–20Cr, co–continuous composite.

## Abstract

The uniaxial deformation properties of a SiC/Fe–20Cr composite where both phases are continuous have been studied using the Solidwork simulation software applied the finite element method (FEM). The simulated results have shown that the composites are relatively anisotropy. Fe–20Cr matrix and SiC network ceramic exhibit different mechanical behaviour. The ultimate stress is found near the interface of composites. The configuration of SiC has relatively great influence on intensity and distribution of stress in the composite. The material behaves in a nearly bilinear manner defined by the Young's modulus and an elastic-plastic modulus. The large deformation appears inside Fe–20Cr matrix. The elastic deformation in the ceramic is accommodated by plastic deformation in the metal phase. Fe–20Cr and SiC can restrict each other to prevent from producing the strain under the load.

## Introduction

There has been a long standing interest in the mechanical behavior of metal and ceramic matrix composites. Recently, there has been a special interest in the behavior of interpenetrating matrix, or co–continuous composites [1, 2]. The spatial topological structure has a number of special features, such as, light weight, high specific modulus and specific strength, abrasion resistance, fatigue resistance, thermal shock resistance, and low coefficient of thermal expansion and so on [3–5]. The co–continuous structures have been of great interest to mathematicians, physical scientists, material scientists, and biologists. Lots of numerical calculations have been done to predict the behavior of compression, stiffness, strength, and energy dissipation [6–15]. Our experiment shows that the co–continuous SiC/Fe–20Cr can be used as brake disk material for China railway high–speed (CRH) trains because it has the good wear properties. In this paper, we demonstrate the potential to design and fabricate a co–continuous SiC/Fe–20Cr material. In order to develop some understanding of how this co–continuous microstructure should deform, a three–dimensional FE model is developed using Solidwork2012 Simulation software to simulate the elastic and plastic behavior of the co-continuous SiC/Fe–20Cr composite [12]. The relationship between macroscopic mechanical response and geometric arrangement that holds great promise in the multifunctional design of engineering structures are also discussed [13].

## 2 Calculation Model

The co–continuous SiC/Fe–20Cr composite materials are prepared by infiltration of a molten Fe–20Cr alloy liquid into SiC network ceramic (Fig. 1(a) and (b)) under pressure using vacuum–pressure casting process (VPCP) method [10]. It can be processed to near-net shape by the use of appropriately shaped precursors. The processing and physical properties of the composite are described in greater depth in Ref [11]. Both the SiC ceramic and Fe–20Cr phases are continuous through the structure, as shown in Fig. 1(c). The volume fractions of the phases are approx. 70% Fe–20Cr and 30% SiC. Fig.1 (d) shows a typical representative section recorded in a scanning electron microscope (SEM) equipped. We can find the reaction zone between Fe–20Cr and SiC in the composites. A simple two-phase-interpenetrating cell geometry is used to represent the composite with one phase forming the structure of the cell, that being the SiC, and other phase, the Fe–20Cr, representing the material filling the cell structure. A schematic diagram of the cell for simulation is shown in Fig. 1(e). The properties of SiC reinforcement are defined as elasticity modulus is 450 GPa, Poisson ratio=0.10, density=3.15 g/cm$^3$, $\sigma_b$=200 MPa, shear modulus=192 MPa. The properties of Fe–20Cr matrix are defined as elasticity modulus=240 GPa, Poisson ratio = 0.34, density= 7.8 g/cm$^3$, $\sigma_b$=800MPa, $\sigma_s$=540 MPa, shear modulus=450 MPa.

We simulate the linear and nonlinear mechanical behavior of the SiC/Fe–20Cr composite under the load from 1.0 MPa to 2.0 MPa. The model is subjected to uniaxial compression by displacing the nodes uniformly on the top face of the cell in the Y–direction, as shown in Fig.1 (e).The *xy* plane is constrained and the opposite plane is required to displace as a plane during deformation. The perfect bonding between the two phases is assumed in the model. The Fe–20Cr behaves in an elastic perfectly-plastic manner, while SiC is modeled as an isotropic fully elastic solid.

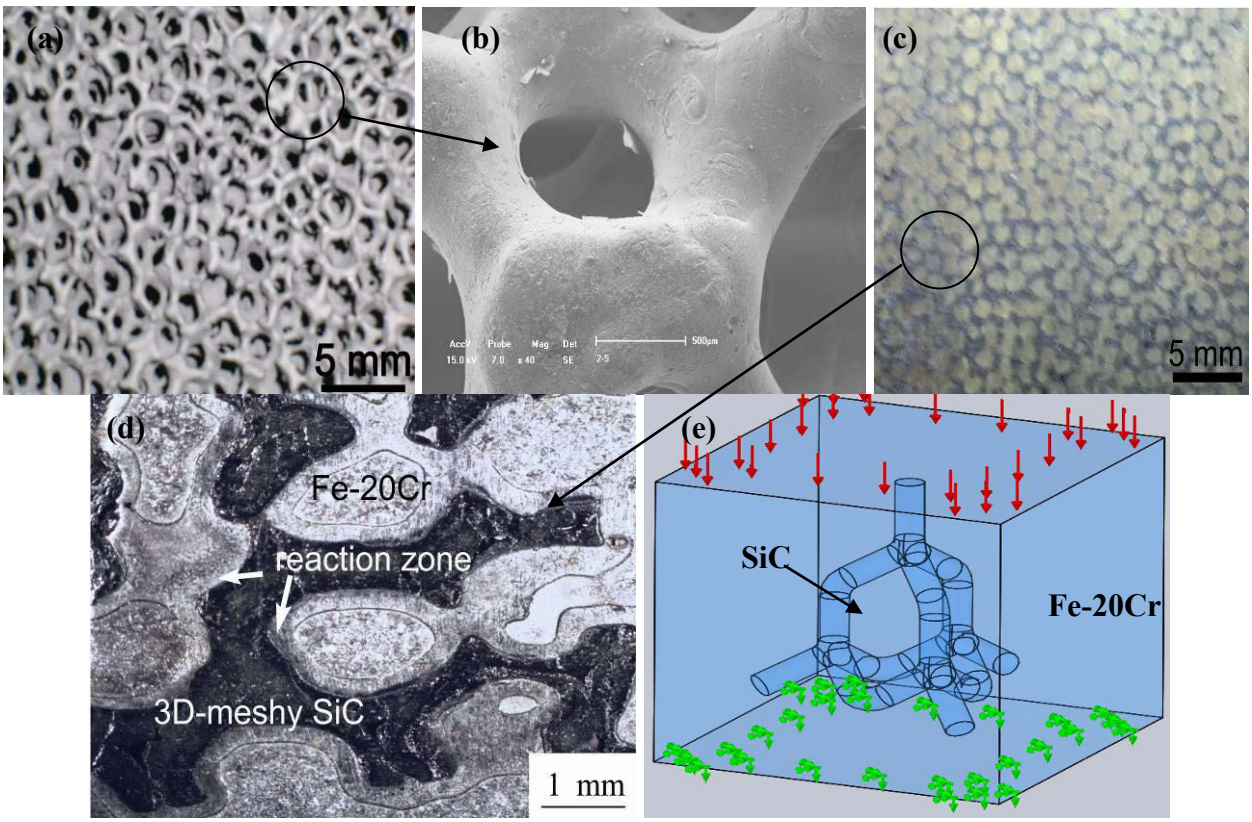


Fig. 1 SiC/Fe–20Cr co–continuous composites; (a) macro–appearance of SiC network ceramic; (b) microstructure of SiC network ceramic; (c) macro–appearance of SiC/Fe–20Cr; (d) microstructure of SiC/Fe–20Cr; (e) simulated micromechanical model (red arrow is the loading direction, green points mean the fixed surface);

## 3 Analysis of Simulation Results

The micromechanical property of SiC/Fe–20Cr composite material under the load from 1.0 MPa to 2.0 MPa is analyzed. Simulated result of the stress under load 2 MPa is showed in Fig. 2. From Fig. 2(a), the Von Mises of max stress is 8.0 MPa, the stress mainly distributes in SiC networks. From Fig. 2(b)–(d), the max stresses of X, Y, and Z–direction are 1.72 MPa, 1.04 MPa, and 1.82 MPa, respectively. The stress distribution of SiC reinforcement has relatively different in different directions. Especially, the stress goes up tremendously in near the interface boundary, the max stress appears in the interfacial boundary of the Fe–20Cr and SiC, or edge or the joints of the SiC network. However, the stress distribution of SiC network in the center of the interface and in the Fe–20Cr matrix has symmetry; essentially the stress value is constant. From above, the SiC/Fe–20Cr co–continuous composite is still relatively anisotropy. Anisotropy is another interesting property for structural materials and composites.

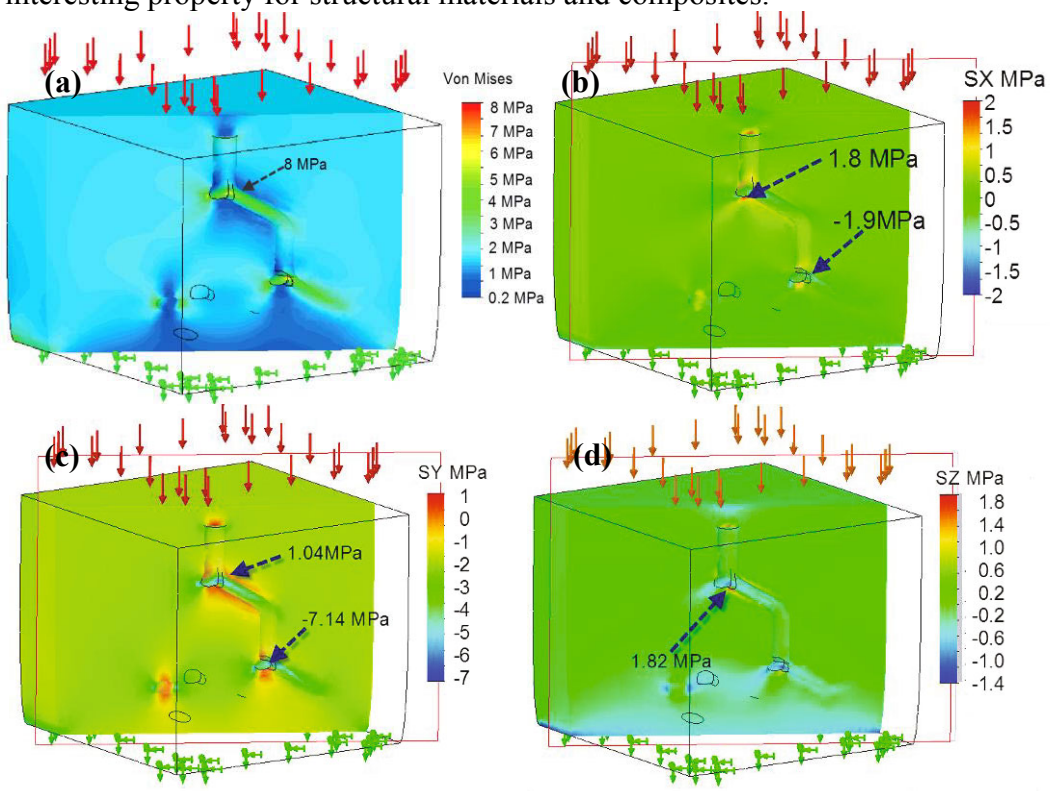


Fig. 2 Isopleths of stress of SiC/Fe–20Cr co–continuous composites with load 2 MPa; (a) Von Mises stress; (b) stress of X–direction; (c) stress of Y–direction; (d) stress of Z–direction;

Simulated result of the strain under load 2 MPa about is shown in Fig. 3. From Fig. 3(a), the max equivalence strain of the composite is $3.26\times10^{-5}$. The co–continuous structural characteristic has changed the distribution of strains of composites, which can restrict the extraneous stretch or compression, and this structural has immensely heightened the tensile strength or compression strength [16]. From Fig. 3(b)–(d), the max strains of X, Y, and Z–direction are $9.94\times10^{-6}$, $2.34\times10^{-6}$, and $9.57\times10^{-6}$, respectively. The co–continuous structure tends to induce many sub–interface and micro–cracks, and make the matrix potentially differentiate, and then decrease the effect of basic the interfacial boundary of SiC and Fe–20Cr slightly. It can be predicted that the cracks would not cross the basic the interfacial boundary but deflect along the sub–basic the interfacial boundary, which can increase crack extension energy, and improve the toughness of matrix [15]. Further, non–uniformity of strains through the cross–section of the unit cell is clearly evident in Fig. 3(b)–(d). The stress transfer and strain sharing mechanisms are particularly important for the co-continuous composites with a brittle component (SiC) since the

continuous elastomer phase (Fe–20Cr) constrains the brittle phase which increases the macroscopic failure strain by both limiting crack propagation and enabling a multitude of cracking events. Fig. 3(c) shows a positive value in the center of the SiC network at large strain which explains the observation of multiple cracking in these regions at large compressive strain with the cracks oriented parallel to the axis of applied compression. The cracking mechanism provides additional energy dissipation. The mutual support of the two co-continuous phases provides load transfer even in the face of cracking and imparts damage tolerance.

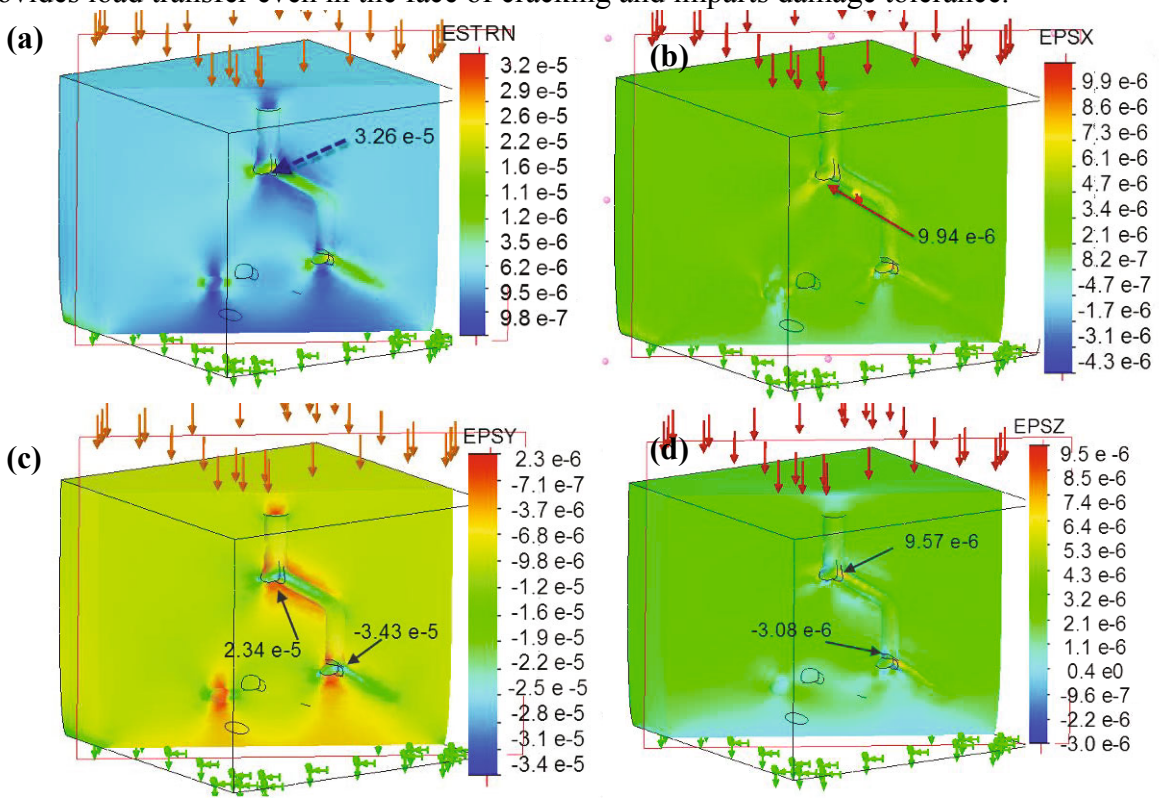


Fig. 3 Isopleths of strain of SiC/Fe–20Cr co–continuous composites with load 2 MPa; (a) Von Mises strain; (b) strain of X–direction; (c) strain of Y–direction; (d) strain of Z–direction;

Fig. 4(a) shows the results of a compression simulation that includes a loading/unloading cycle. This reveals that on loading the behavior is approximately bilinear with an elastic modulus near 312 GPa and a linear plastic modulus, of approx. 226 GPa in this case. This bilinear behavior is characteristic of all the co–continuous materials studied. Displacement contours in the URES and Y–direction of the imposed strain is shown in Fig. 4(b). The max displacements of URES and Y–direction are $2.51\times10^{-5}$ mm (Fig. 4(a)) and $2.30\times10^{-5}$ mm (Fig. 4(b)), respectively.

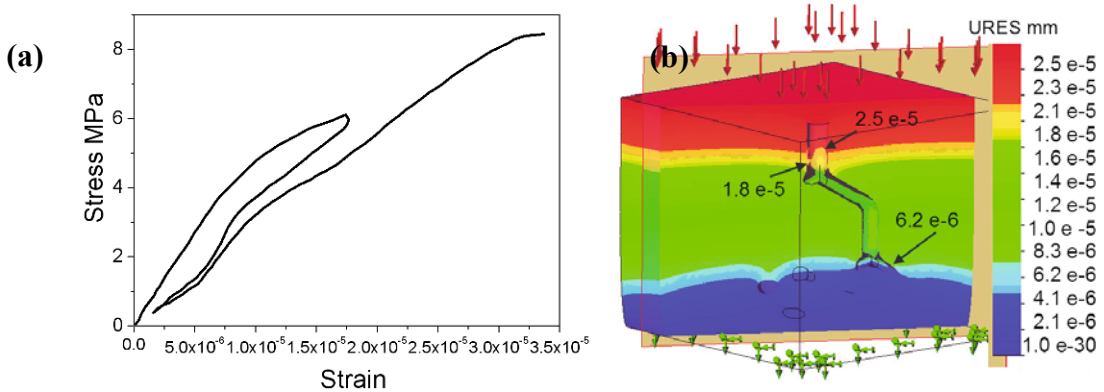


Fig. 4 Isopleths of displacement of SiC/Fe–20Cr co–continuous composites with load 2 MPa;(a) URES displacement, max $2.51\times10^{-5}$ mm; (b) displacement of Y–direction, max $2.30\times10^{-5}$ mm

The micromechanical property of SiC/Fe–20Cr composites under load from 1.0 MPa to 2.0 MPa for 20 s (Fig.5 (a)) is analyzed. From Fig. 5(b), the deformation increases with the load increasing. With the loading increasing, the stress of SiC network, the strain of Fe–20Cr matrix increase and the strength of composites is also increases. The displacement levels are higher for the Fe–20Cr compared with that of the SiC network because of Fe–20Cr has lower Young's modulus. It is clear that the apparent plasticity takes place by true plastic deformation in the metal phase and elastic accommodation in the ceramic. Compared to the conventional composites, the co-continuous composites are 3D multi-directionally reinforced, are less dependent on material distribution, and simultaneously provide relatively high stiffness, strength and energy absorption in all directions. These properties suggest co–continuous composites as excellent energy dissipative elements in advanced structures or armor by controlling volume fraction and tailoring geometric arrangements to meet different requirements [17].

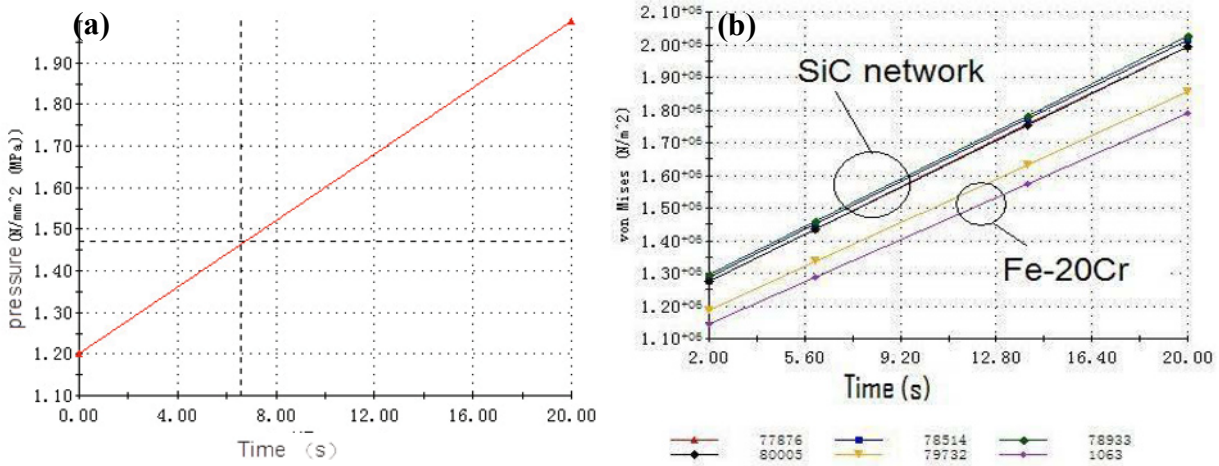


Fig. 5 The micromechanical property of SiC/Fe–20Cr composites under load from 1.0MPa to 2.0 MPa for 20 s; (a)loading curve; (b) Stress–time curve of SiC reinforcement and Fe–20Cr matrix;

## 4 Conclusions

In the paper, we have investigated the micromechanical properties of SiC/Fe–20Cr co–continuous composite under compression using Solidwork simulation software, conclusions are as the following:

(1) The composites are relatively anisotropy. Fe–20Cr matrix and SiC network ceramic exhibit different mechanical behaviour. The ultimate stress is found near the interface of composites. The configuration of SiC has relatively great influence on intensity and distribution of stress in the composite.

(2) The material behaves in a nearly bilinear manner defined by the Young's modulus and an elastic-plastic modulus. The large deformation appears inside Fe–20Cr matrix. The elastic deformation in the ceramic is accommodated by plastic deformation in the metal phase.

(3) Fe–20Cr and SiC can restrict each other to prevent from producing the strain under the load.

## 5 Acknowledgment

This work is supported by the National Natural Science Foundation of China (No. 50902018 and No. 50872018) and the Program for Changjiang Scholars and Innovative Research Team in University (IRT0713) and the Basic Research Fund of Northeastern University (N090302005)

and the Province Science and Technology in the Guangxi Offends Pass Item (1099043).

## 6 References

[1] S. H. Wang, H. R. Geng, Y. Z. Wang, B. Sun, "The Fabrication Method and Research Progress of the Reticulated Ceramic Reinforcement in Metal Matrix Composites," *Materials of Mechanical Engineering* , 29(12), (2005), 1–3.

[2] S. S Qin, "Metal–matrix Composites for Marine Applications: Development Status and Our Countermeasures," *Material Journal*, 7(10) (2003) , 68–70.

[3] R. Jhaver, H. Tippur, "Processing, compression response and finite element modeling of syntactic foam based interpenetrating phase composite (IPC)," *Materials Science and Engineering A*, 499 (2009), 507–517.

[4] L. Yu, Y. L. Jiang, H. Q. Ru, J. T. Liu, K. Luo, "Microstructures of co-continuous SiC/Fe-2Cr13 composite fabricated by vacuum-pressure casting and infiltration processes," *Advanced Materials Research* , 239-242 (2011) ,1661-1664.

[5] H. W Xing, X. M Cao, W. P. Hu, et al. "Interfacial reactions in 3D–SiC network reinforced Cu–matrix composites prepared by squeeze casting," *Materials Letters*,59(2005),1563–1566.

[6] M.J Zhao, N. Li, L. Z Zhao, X. L. Zhang, "Numerical Simulations of Compression Properties of SiC/Al Co-continuous Composites", *IFIP AICT* ,347(2011), 480–485.

[7] M. Pavese, M. Valle, C. Badini, "Effect of porosity of cordierite performs on microstructure and mechanical strength of co–continuous ceramic composites," *Journal of the European Ceramic Society*, 27 (2007), 131–141.

[8] G. Oder, M. Reibenschuh, T. Lerher, M. Sraml, B. Samec, I. Potrc, "Thermal and stress analysis of brake discs in railway vehicles," *Advanced Engineering*, 3(1) (2009), 95–102.

[9] H. Zhang, Y. Zeng, H. Zhang, F. Guo, "Computational Investigation of the Effective Thermal Conductivity of Interpenetrating Network Composites," *J. Compos. Mater,* 44(10) (2010), 1247–1260.

[10] L. Yu, Y. L. Jiang, S. K. Lu, K. Luo, H. Q. Ru, "Numerical simulation of brake discs of CRH3 high–speed trains based on Ansys," *Proceedings of the 1st World Congress on Integrated Computational Materials Engineering, ICME,* (2011), 183–188.

[11] H. Q. Ru, M. Fang, R. Q. Wang, L. Zuo, China Patent, CN200510046691. X (2006).

[12] L. Yu, Y. L. Jiang, S. K. Lu, H. Q. Ru, M. Fang, "FEM for brake discs of SiC 3D continuous ceramic reinforced 7075 aluminum alloy for CRH3 trains applying emergency braking, " *Applied Mechanics and Materials*,120(2012),51–55.

[13] L. Yu, Y. L. Jiang, H. Q. Ru, J. T. Liu, K. Luo, "Microstructures of co–continuous SiC/Fe–2Cr13 composite fabricated by vacuum–pressure casting and infiltration processes," *Advanced Materials Research*, 39–242, (2011), 1661–1664.

[14] Y. H. Ha, A. V. Richard, F. William, L. P. Costantino, Jennifer Shin, Andrew B. Smith, T. Paul, Matsudaira, Edwin L. Thomas, "Three–dimensional network photonic crystals via cyclic size reduction/infiltration of sea urchin exoskeleton", *Adv. Mater*, 16(13) (2004), 1091–1094.

[15] S. Wang, H. Geng, Y. Wang, H. Hui, "Model of compressive strength of DNSRMMCS," *Acta Material Composite*, 23 (2006), 7–11.

[16] L. F Wang, L. Jacky, E. L. Thomas, M. C. Boyce, Co-continuous composite materials for stiffness, strength, and energy dissipation", *Adv. Mater.,* 23(13)(2011), 1524–1529.

[17] G. S. Daehn, B. Starck, L. Xu, K. F. Elfishawy, J. Ringnalda, H. L. Fraser, "Elastic and plastic behavior of a co-continuous alumina/aluminum composite", *Acta mater*. 44(I), (1996), 2499261.

1st International Conference on 3D Materials Science
*Edited by: Marc De Graef, Henning Friis Poulsen, Alexis Lewis, Jeff Simmons, George Spanos*
***TMS (The Minerals, Metals & Materials Society), 2012***

# CALCULATION OF LORENTZ FORCE FIELD OF THE INNOVATION CATHODE CELL

YanLi Jiang [1], Liang Yu [1], Naixiang Feng[2]

[1]Key laboratory of new processing technology for nonferrous metals & Materials,
Ministry of Education, Guilin University of Technology, Guilin, 541004, China
[2] Key laboratory for anisotropy and texture of materials (MOE),
School of materials and metallurgy, Northeastern University, Shenyang, 110819, China

Keywords: Innovation cathode cell, ANSYS, Lorentz force

## Abstract

The mathematical models of Lorentz force field of the conventional cell and innovation cathode cell were established in the paper. The result revealed that the Lorentz force distribution of the conventional cell and innovation cathode cell was different, but the value of Lorentz force was similar, the Lorentz force in aluminum liquid in the conventional cell became higher near the surface of the cathode, while it in liquid aluminum in the innovation cathode cell decreased at first, then increased at the concave of cathode, the Lorentz force in electrolyte of the conventional cell became higher away from the surface of the cathode, while it in electrolyte under the anode bottom of the innovation cathode cell was evenly distributed, then decreased in gap of the anode. The value of the Lorentz force density in the interface of melt in the conventional and innovation cathode cell was both generally low.

## 1 Introduction

Aluminum is achieved by electrolysis in industry. Significant research also has been done on the use of the innovation cathode cell that operate with a lower anode–cathode distance (ACD) invented by Naixiang Feng of Northeastern University in 2007[1], and the voltage drop in the innovation cathode cells was reduced by about 0.38 V. Limited understanding of the innovation cathode cell has contributed to many operational problems such as power consumption, current efficiency and life of cell. The forces caused by the magnetic field and the current field have increased the importance of dynamics in the innovation cathode cell at a lower ACD. In recent years, great advance has been made toward understanding instability and the theoretical modeling of the instability in cell resulting from MHD forces[2~9], but little progress has been made in the Lorentz forces resulting from interaction between the horizontal current and the vertical magnetic field in the innovation cathode cell at a lower ACD. At reduced ACD, the horizontal current becomes larger in the aluminum of the innovation cathode cell at a lower ACD. When the current changes its direction because of the shape of the cathode, it will have a significant effect on the Lorentz force field throughout the cell. Generally, examining the flow field in the aluminum reduction cell involves the calculation of Lorentz forces [10]. In the paper, the main objective was to show the Lorentz force distribution throughout the innovation cathode cell with commercial software ANSYS.

## 2 the Model of the conventional cell and the innovation cathode Cell

### 2.1 The mathematical model

ANSYS is one of the world's leading developers of engineering simulation software, used by product designers and engineers around the world. This technology supports quick, efficient and

cost-effective product development throughout the development process-from design concept to final-stage testing, validation and production. The ultimate result is successful, innovative products and a faster return on investment for companies. The software ANSYS consists of three parts: pre-processing, calculation and post-processing. Pre-processing provides a powerful modeling and meshing tools, users can easily construct a finite element model; calculation include structural analysis, fluid dynamics and electromagnetic field analysis and so on, can simulate the interaction of multi-physical media sensitively. post-processing can give the results in color contour, gradient, vector, particle flow trace display, three-dimensional slice, transparent and translucentand graphically displayed.

In ANSYS, magnetic forces are computed by elements using the vector potential method (PLANE13, PLANE53, SOLID97, and SOLID117) and the scalar potential method (SOLID5, SOLID96, and SOLID98). Three different techniques are used to calculate magnetic forces at the element level. Magnetic forces in current carrying conductors (element output quantity FJB) are numerically integrated in Ref [2-4].

### 3.2 The physical and FEM model

The main components of the aluminum reduction cell are the anodes, the anode assemble, the liquid aluminum, the molten electrolyte, the cathode, the steel collector bars, the aluminum flexes and the air. For symmetry reasons, a half model was analyzed, as shown in Fig. 1 (air was not shown). The surface of the conventional cathode is flat, as shown in Fig. 2 (a), while there were disciplinary protrusions at the upper surface of the innovation cathode, as shown in Fig. 2 (b). In the simulation of Lorentz forces field, there were 62,873 elements and 128,213 nodes in the conventional cell (which ACD is 53 mm) and 61,972 elements and 125,976 nodes in the innovation cathode cell (which ACD is 39 mm).

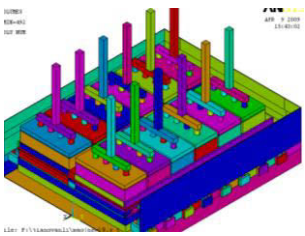

Fig 1 half physical model of innovation cathode cell

(a)

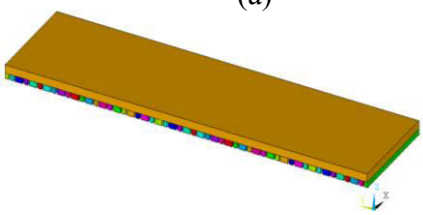

(b)

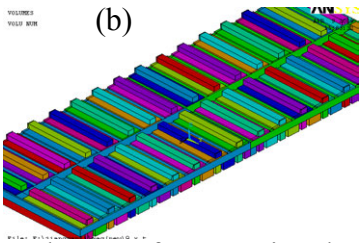

Fig 2 sketch map of cathode (a) sketch map of conventional cathode; (b) sketch map of innovation cathode

## 3 The Element Type and Load

The element types of the Lorentz forces field include the element Source 36 and the element Solid 117, represented all busbars, parts of anode assemble and others respectively.

The conventional cell and the innovation cathode cell have the same boundary conditions and loads: (1) Constrain electric scalar potential V at the top areas of the anode assemble, and set current flow equal to 168,000/2 A at one of the nodes of these areas;(2) Set reference potential equal to zero at the areas connected the steel collector bars and the aluminum flexes;(3) The boundary condition “Normal Flux” was applied in the external nodes of the air box.

## 4 The Calculated Results and Discussion

The Lorentz Force Densities in the melt in the conventional cell and in the innovation cathode cell were shown in Fig. 5. It can be seen that the value of the Lorentz force density in the interface of melt was generally low, and the maximum value of absolute value was less than 5 N. The negative and positive maximum value of X, Y, Z Lorentz force density in the interface of

melt of conventional cell were -2.5 N, 1.1 N, -0.5N, 2.2 N, -3 N and 2.3 N, while that of the innovation cathode cell were -2 N, 2.8 N, -2 N, 1.7 N, -4.2 N and 3.5 N. The minimum and maximum value of the Lorentz force density sum of interface of melt of conventional cell was 0.04 N and 3.8 N, while that of the innovation cathode cell were $8.81\times10^{-4}$ N and 5.1 N. The area of the -X Lorentz force of interface of melt of the innovation cathode cell was lower than that of the conventional cell, while the area of the Y and -Z Lorentz force is larger.

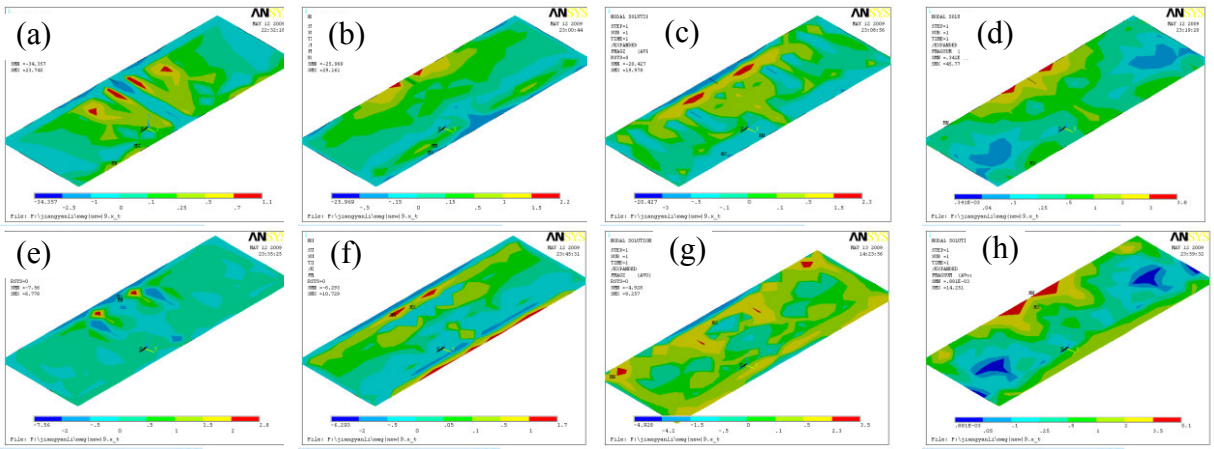


Fig. 5 LFD at interface of melt of conventional and innovation cathode cell
(a)~ (d) are $LFD_X$, $LFD_Y$, $LFD_Z$ and $LFD_{sum}$ at interface of melt of conventional cell
(e) ~ (h) are $LFD_X$, $LFD_Y$, $LFD_Z$ and $LFD_{sum}$ at interface of melt of innovation cathode cell

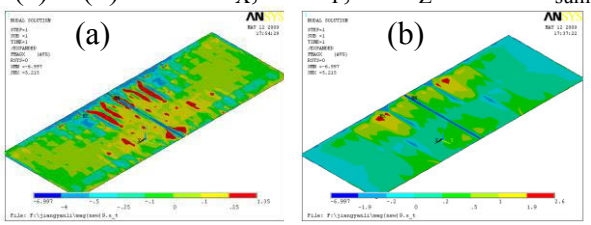


(a) z=0.872 (b) z=0.807(a)
Fig. 6 $LFD_X$ in Al of conventional cell

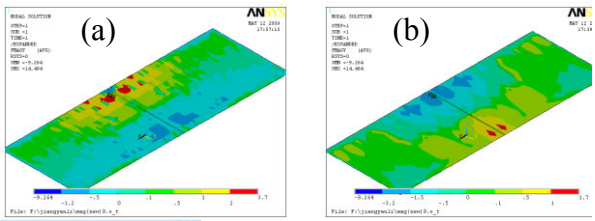


(a) z=0.872 (b) z=0.807
Fig. 7 $LFD_Y$ in Al of conventional cell

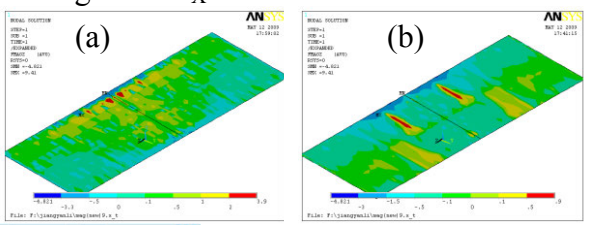


(a) z=0.872 (b) z=0.807
Fig. 8 Sectional view of $LFD_Z$ in Al of conventional cell

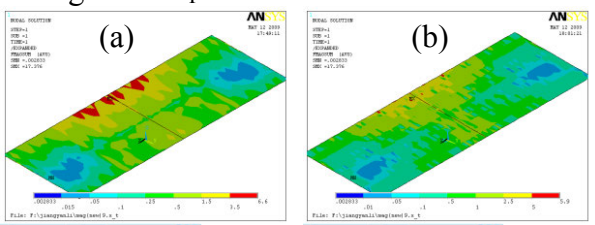


(a)z=0.872 (b)z=0.807
Fig. 9 Sectional view of $LFD_{sum}$ in Al of conventional cell

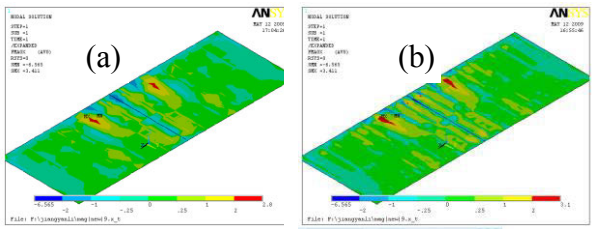


(a)z=0.92 (b)z=0.89
Fig. 10 Sectional view of $LFD_X$ in Al from the surface of convex cathode in the innovation cathode cell

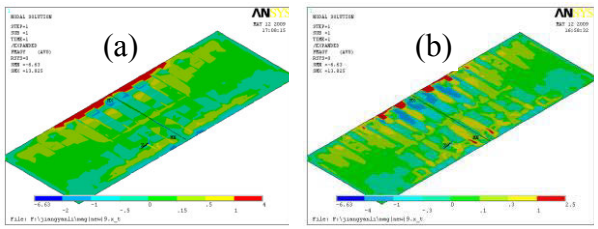


(a)z=0.92 (b)z=0.89
Fig. 11 Sectional view of $LFD_Y$ in Al from the surface of convex cathode in innovation cathode cell

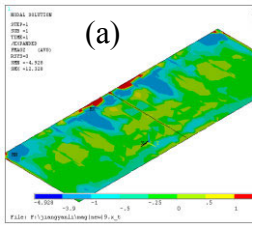


(a)z=0.92

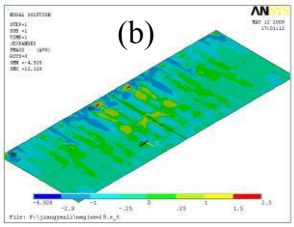


(b)z=0.89

Fig. 12 Sectional view of $LFD_Z$ in Al from the surface of convex cathode in the innovation cathode cell

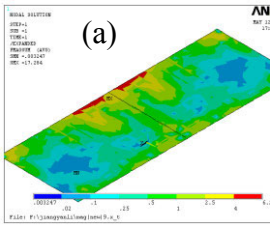


(a)z=0.92

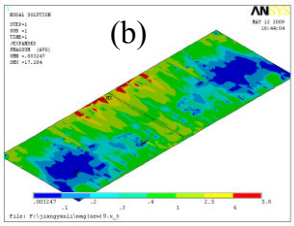


(b)z=0.89

Fig. 13 Sectional view of $LFD_{sum}$ in Al from the surface of convex cathode in innovation cathode cell

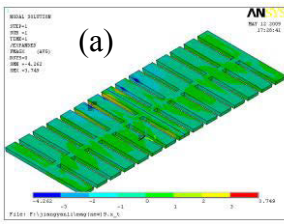


(a)z=0.92 $LFD_X$

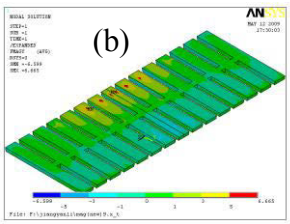


(b)z=0.89 $LFD_Y$

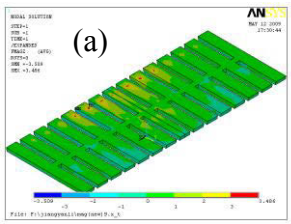


(c)z=0.92 $LFD_Z$

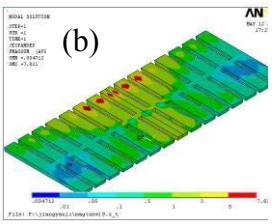


(d)z=0.89 $LFD_{sum}$

Fig. 14 LFD of aluminum in concave of cathode of the innovation cathode cell

Fig. 6~Fig. 24 were the Lorentz force density of aluminum and electrolyte of the conventional cell and the innovation cathode cell. With decreasing of the distance from the cathode surface in the aluminum of the conventional cell, the -X, +Y and +Z Lorentz force density decreased, while the +X, -Y Lorentz force density increased, and the Lorentz force density sum increased, as shown in Fig. 6~Fig. 9. With decreasing of the distance up from the surface of convex cathode in the aluminum of the innovation cathode cell, the +Y and Z Lorentz force density decreased, while the X, -Y Lorentz force density increased, the Lorentz force density sum decreased, and the area of the +X Lorentz force increase, the area of the Y and +Z Lorentz force decreased, as shown in Fig. 10~Fig. 13. While the X, Y and Z Lorentz force density of aluminum in concave of cathode of the innovation cathode cell was higher than that of aluminum of up from the surface of convex cathode in the innovation cathode cell, as shown in Fig. 14.

With the increase of the distance from the cathode surface in electrolyte under the anode bottom of the conventional cell, the X, Y and positive Z Lorentz force density increased, the Lorentz force density sum increased, and the value was the maximum in gap of the anode, as shown in Fig. 15~Fig. 19.

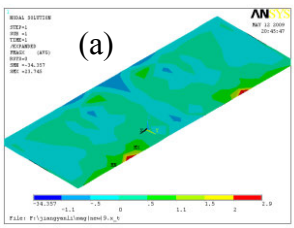


(a) z=0.942

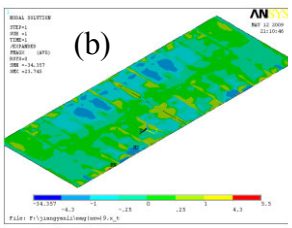


(b) z=0.966

Fig. 15 $LFD_X$ of electrolyte under the anode bottom of conventional cell

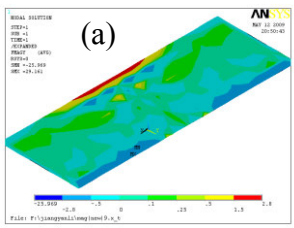


(a) z=0.942

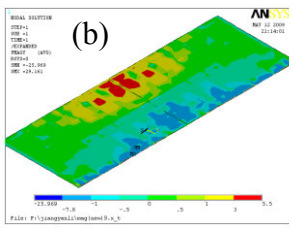


(b) z=0.966

Fig.16 $LFD_Y$ of electrolyte under the anode bottom of conventional cell

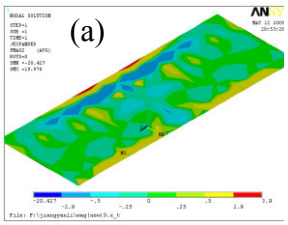


(a) z=0.942

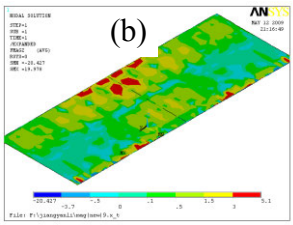


(b) z=0.966

Fig. 17 $LFD_Z$ of electrolyte under the anode bottom of conventional cell

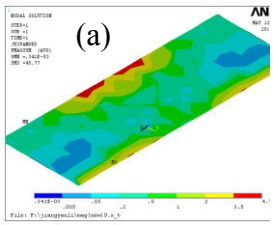


(a) z=0.942

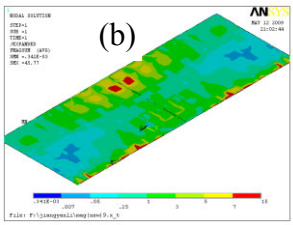


(b) z=0.966

Fig.18 $LFD_{sum}$ of electrolyte under the anode bottom of conventional cell

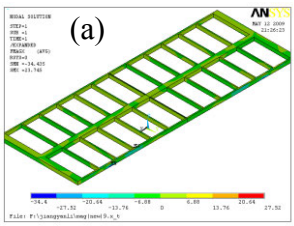


$LFD_X$

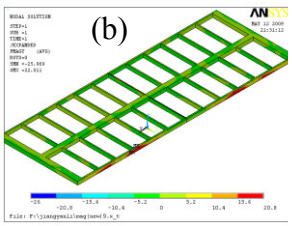


$LFD_Y$

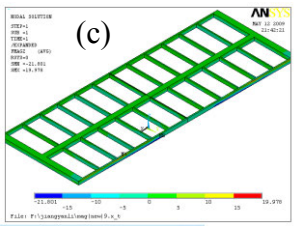


$LFD_Z$

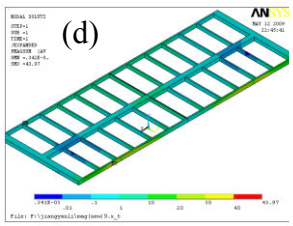


$LFD_{sum}$

Fig. 19 LFD of electrolyte in gap of anode of conventional cell

In electrolyte under the anode bottom of the innovation cathode cell, with increasing of the distance from the cathode surface, the -X, -Y and +Z Lorentz force density increased, the +X, +Y and -Z Lorentz force density decreased, while the Lorentz force density sum changed little. The Y, Z and Lorentz force density sum decreased in gap of the anode shown in Fig. 20~Fig. 24.

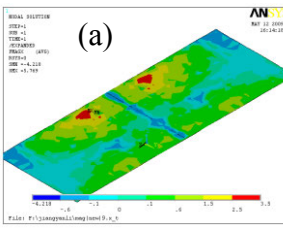


(a) z=0.964

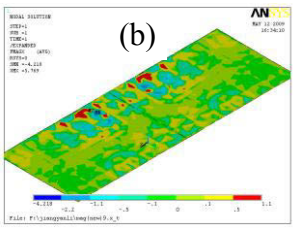


(b) z=0.977

Fig. 20 $LFD_X$ in electrolyte under the anode bottom of the innovation cathode cell

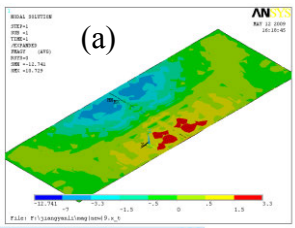


(a) z=0.964

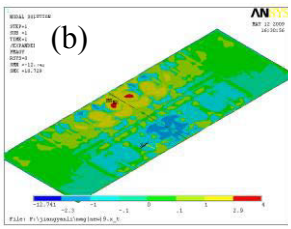


(b) z=0.977

Fig. 21 $LFD_Y$ in electrolyte under the anode bottom of the innovation cathode cell

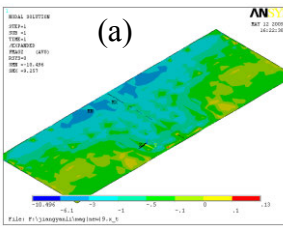


(a) z=0.964

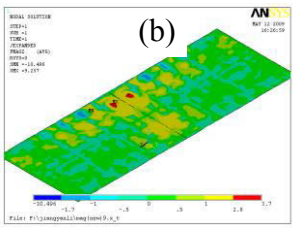


(b) z=0.977

Fig.22 $LFD_Z$ in electrolyte under the anode bottom of the innovation cathode cell

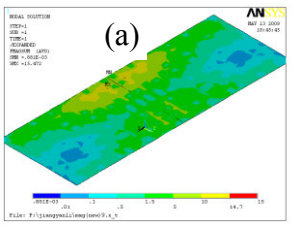


(a) z=0.964

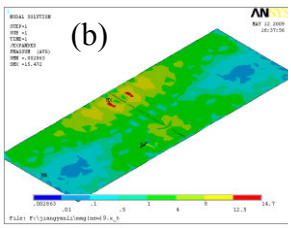


(b) z=0.977

Fig.23 $LFD_{sum}$ in electrolyte under the anode bottom of the innovation cathode cell

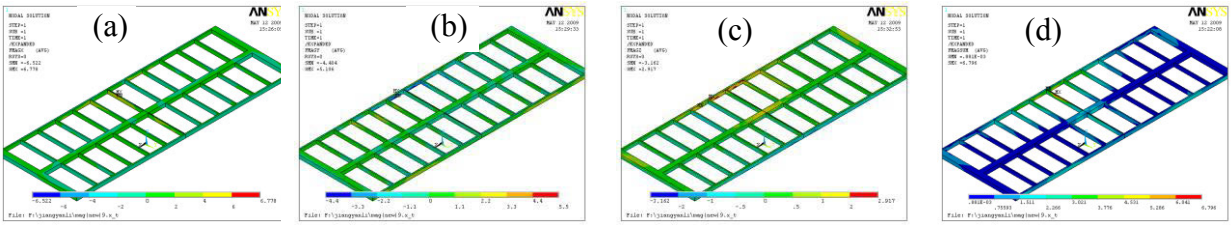


(a) $LFD_X$ (b) $LFD_Y$ (c) $LFD_Z$ (d) $LFD_{sum}$

Fig. 24 LFD in electrolyte in gap of the anode of the innovation cathode cell

## 5 Conclusions

In conclusion, the Lorentz force distribution in aluminum of the conventional cell and the innovation cathode cell was differ, but the value was similar, the Lorentz force in electrolyte of the conventional cell became higher away from the surface of the cathode, and became maximum in gap of the anode, while the Lorentz force in electrolyte under the anode bottom of the innovation cathode cell was evenly distributed, then decreased in gap of the anode. The value of the Lorentz force density in the interface of melt in the conventional and innovation cathode cell was both generally low.

## 6 Acknowledgment

This work is supported by the Research Start-up Foundation Project of Guilin University of Technology (No. 002401003330 and No. 002401003329).

## 7 References

[1] N. X Feng, J.P Peng. “Judging of the gap among our country and some leading countries from the point of view of new aluminum electrolysis technology,” Light Metals, 3, (2005), 3-5.

[2] B. K Li, X. B Zhang, S.R Zhang et al. “Study of electromagnetic field in 300KA aluminum reduction cells with innovation cathode structure”, TMS Light Metals, (2011), 1029-1033.

[3] S. Das, G. Brooks, Y. Morsi. “Theoretical investigation of the inclined sidewall design on magnetohydrodynamic (MHD) forces in an aluminum electrolytic cell”, Metallurgical and Materials Transactions B: Process Metallurgy and Materials Processing Science, 42(2011), 243-253.

[4] D. Munger, A. Vincent. “A cylindrical model for rotational MHD instabilities in aluminum reduction cells” Theoretical and Computational Fluid Dynamics, 22(2008), 363-382.

[5] M. Dupuis, V. Bojarevics, J. Freibergs. “Demonstration thermo-electric and MHD mathematical models of a 500 kA aluminum electrolysis cell: Part 2”, TMS Light Metals, (2004), 453-459.

[6] M. Kadkhodabeigi, Y. Saboohi. “A new wave equation for MHD instabilities in aluminum reduction cells”, TMS Light Metals, (2007), 345-349.

[7] S. A. Shcherbinin, A.V. Rozin, S.Yu. Lukashchuk. “The 3D modeling of MHD-stability of aluminum reduction cells”, TMS Light Metals, (2003), 373-377.

[8] M. Dupuis, V. Bojarevics, D. Richard. “Impact of the vertical potshell deformation on the MHD cell stability behavior of a 500 kA aluminum electrolysis cell”, TMS Light Metals, (2008), 409-412.

[9] D. S. Severe, A. F. Schneider, C. V. Pinto, Elton et al. “Modeling magneto hydrodynamics of aluminum electrolysis cells with ANSYS and CFX”, TMS Light Metals, (2005), 475-480.

[10] Y. L. Jiang, N. X. Feng, J. P. Peng. “Calculation of aluminum flow field at interface of molten aluminum and electrolyte in new cathode aluminum cell”, Light Metals, (2010), 409-414.

1st International Conference on 3D Materials Science
*Edited by: Marc De Graef, Henning Friis Poulsen, Alexis Lewis, Jeff Simmons, George Spanos*
***TMS (The Minerals, Metals & Materials Society), 2012***

# ENUMERATION OF POLYHEDRA FOR GRAIN GROWTH ANALYSIS

Trevor Keller[1], Barb Cutler[2], Martin Glicksman[3], Dan Lewis[1]

[1] Materials Science and Engineering Department
[2] Computer Science Department
Rensselaer Polytechnic Institute
110 8th St.; Troy, NY 12180, USA

[3] Mechanical & Aerospace Engineering
Florida Institute of Technology
150 W. University Blvd.; Melbourne, FL 32901 USA

Keywords: Polyhedral graphs, Grain growth, Monte Carlo methods

## Abstract

The advent of three dimensional data collection, grain reconstruction, and subsequent materials analysis has created opportunities to revisit problems in grain growth and polycrystalline structure. In this paper we review the relevant literature concerning the total number of polyhedral grains of a given number of faces and take the additional first steps at enumerating the topologies of the members within each set. Analysis of the dispersion in topology relative to the idealized $N$-hedra is presented. The relevance to grain growth simulations and experiments is discussed.

## Introduction

Mathematicians have proven that the total number of convex polyhedra with 4 to 15 faces is vast [1–3]; the number with 16 or more faces remains unknown. Metallurgists since C.S. Smith in the 1950's have noted that real grains apparently conform to a limited subset of the available topologies [4, 5], yet the full range of 3-vertex-connected (tri-valent) polyhedra accessible to real grains has not been characterized to date. This work is an effort to enumerate the domain of possible polyhedra as a first step towards quantitative analysis of the observed range of grain topologies in experimentally prepared and numerically simulated polycrystalline materials. Understanding the available configurations of 3-vertex-connected polyhedra may provide insights into topological selection processes that occur during grain growth.

### Background

In an infinite isotropic polycrystalline network, one expects the mean number of faces per grain to approach the ideal solution to the Kelvin problem [6]: $\langle f \rangle \approx 13.4$ [7]. Heroic efforts to reconstruct the grain structure of large polycrystalline specimens [8] and to simulate grain growth in large numerical systems [9–11] found $\langle f \rangle \approx 13.7$, with frequency distributions skewed toward greater numbers of faces than theoretically predicted.

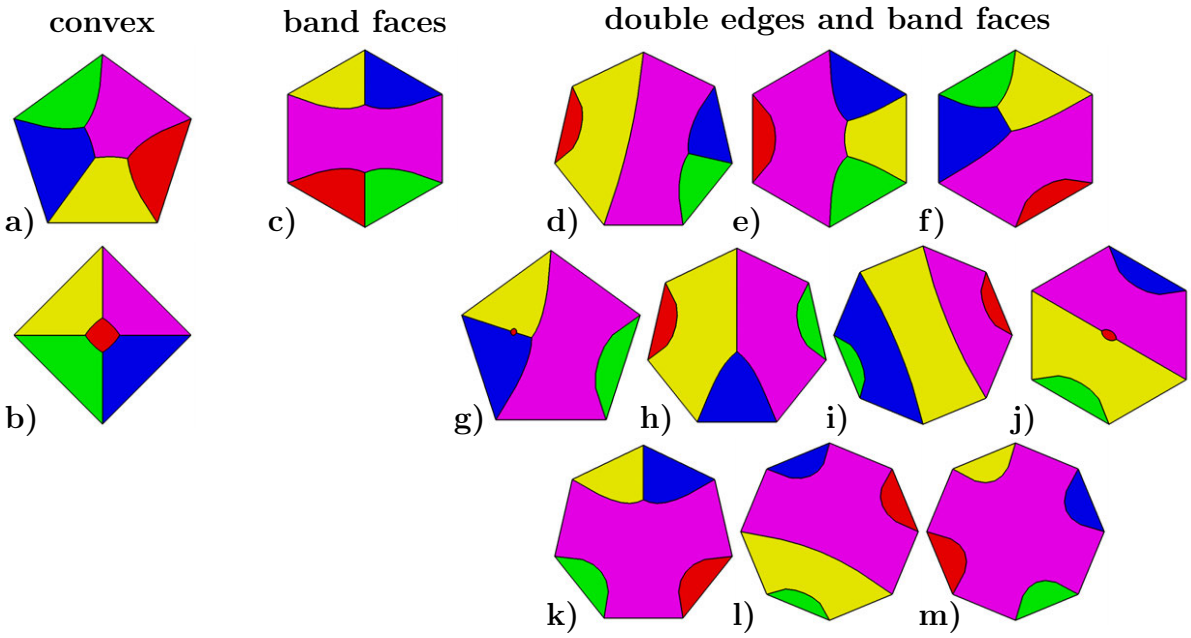


**Figure 1:** All 3-vertex-connected, 2-edge-connected planar graphs with $n = 8$ vertices, $f = 6$ faces, and $e = 12$ edges. There are only 2 unique convex polyhedra with 6 faces. Allowing highly curved faces ('band' faces), and faces with only two edges (double edges), a number of additional general curved polyhedra exist.

## Algorithm

Researchers including Federico [1], Duijvestijn [2], and Engel [3] have written about enumerating the polyhedra, convex and otherwise. By 'enumerate', the authors imply 'count the total number possible.' At the time of this writing, the authors have been unable to find plots or Schlegel diagrams of the polyhedra, except in references to an unpublished work by Duijvestijn [12] and some work by Voytekhovsky on 14- and 15- [13] and 16-hedra [14]. A Monte Carlo method was devised to compute the topologies of the set of grains in each category of $N$-hedra. This section provides the details of the present algorithm.

### Graph Structure

Each grain can be modeled by a graph of the vertices, edges, and faces—specifically, a 3-vertex-connected (3-regular, cubic), 2-edge-connected, planar graph. The graph is *3-vertex-connected*, meaning that exactly 3 edges (equivalently, 3 faces) meet at each vertex (each vertex has valence 3). Based on Plateau's rules [15], we assume that the 3-vertex-connected graphs are the only graphs of interest.

Because this graph represents a single grain rather than multiple disconnected grains, the graph must be connected, meaning each vertex can reach each other vertex by following a chain of one or more edges. Furthermore, we require that the graph must be at least 2-edge-connected, which means that at least two edges must be cut or removed to separate the graph into disconnected subgraphs. We note that singly-connected graphs

are realizable as general curved 3D polyhedra and may exist in some polycrystalline structures; however, we are currently omitting these shapes from our study. Finally the graph must be *planar*, in that the vertices and edges can be arranged and drawn on a plane such that no edges cross. The graph is not required to be a *convex planar* graph; that is, some of the polygons may be non-convex. Furthermore, the edges need not be straight; for example, the edges of a 2-sided face must be curved arcs (Figure 1d-m). Additionally, the faces of the 3D grain are not constrained to be planar and in fact two faces may share 2 or more edges (e.g., the purple face and the back face in Figure 1c). We call these faces *band faces*, because this pair of faces forms a band wrapping around the middle of the grain, separating the remaining faces into two otherwise unconnected groups.

Graph Representation

Each graph with $n$ vertices may be represented with a $n \times n$ matrix $M$, where each element $m_{ij} = 0$ if there is no edge between vertices $i$ and $j$, $m_{ij} = 1$ if there is a single edge between the vertices, and $m_{ij} = 2$ if there is a double edge. Note that $m_{ij} = m_{ji}$ and $m_{ii} = 0$. To fulfill the 3-vertex-connected property, each row (and equivalently each column) of this matrix must sum to 3. For example, the matrix on the right is a represention of the graph in Figure 2j.

$$\begin{pmatrix} 0 & 1 & 0 & 0 & 1 & 0 & 0 & 1 \\ 1 & 0 & 0 & 1 & 0 & 0 & 1 & 0 \\ 0 & 0 & 0 & 0 & 1 & 1 & 1 & 0 \\ 0 & 1 & 0 & 0 & 0 & 1 & 0 & 1 \\ 1 & 0 & 1 & 0 & 0 & 0 & 0 & 1 \\ 0 & 0 & 1 & 1 & 0 & 0 & 1 & 0 \\ 0 & 1 & 1 & 0 & 0 & 1 & 0 & 0 \\ 1 & 0 & 0 & 1 & 1 & 0 & 0 & 0 \end{pmatrix}$$

To ensure that the graph represented by the matrix is at least 2-edge-connected, we test the graph by removing a single edge from the graph and perform a flood-fill graph traversal to verify that the graph is connected. This remove-and-test operation is repeated for each edge in the graph. The more challenging and computationally expensive operation is testing if the graph is planar, which will also provide a set of faces leading to a 2D or 3D interpretation of the graph. If the graph is not symmetric, the shape can be reflected or inverted creating a mirror image polyhedron. Additionally, we note that the face set for a particular matrix is not necessarily unique. A subgraph of the polyhedron may be inverted to create a different face set, and a different polyhedron. Finally, the vertices of a polyhedron can be re-numbered, which swaps rows and columns of the matrix representation.

One method of enumerating all polyhedral shapes is to enumerate all possible matrices as described above, and discard all non 2-edge-connected graphs and non-planar graphs. However, as $n$ increases, complete enumeration becomes impractical. Furthermore, as noted above, many of these matrices yield graphs/polyhedra that are equivalent. An alternative technique is to sample the space of all possible graphs by randomly adding $e$ edges one-at-a-time until each vertex has 3 edges. However, this randomized algorithm is impractical, because as $n$ increases the number of invalid, non-planar graphs generated increases rapidly. We found that for graphs generated via this method, approximately 50% of $n$=8 vertices, 30% of $n$= 10 vertices, and 20% of $n$ = 12 vertices corresponded to valid polyhedra. Thus, we developed a more efficient algorithm to sample similarly and randomly the space of graphs by generating only planar graphs.

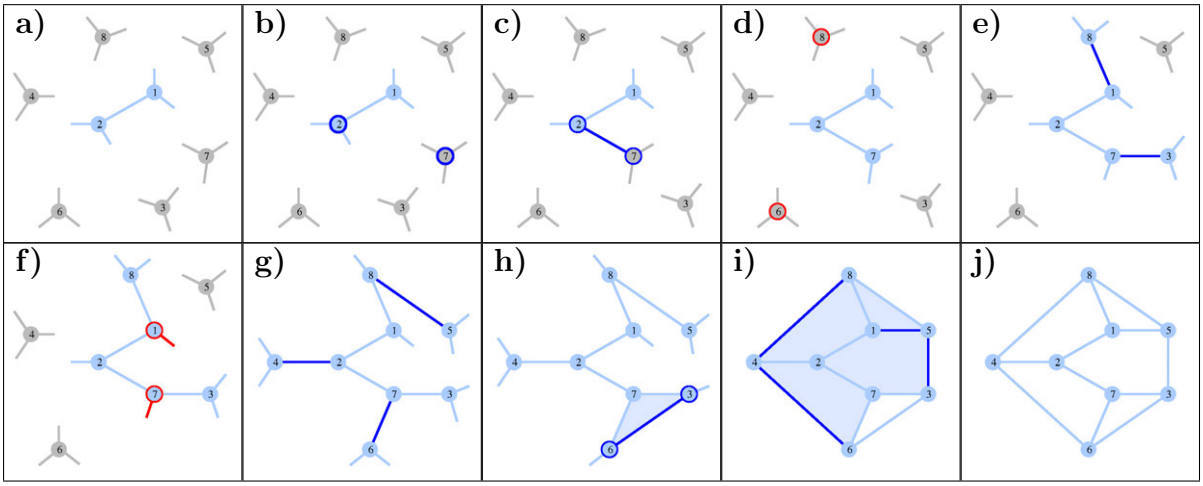


**Figure 2:** Illustration of a Monte Carlo algorithm for generating random 3-vertex-connected, 2-edge-connected planar graphs with $n = 8$ vertices, $f = 6$ faces, and $e = 12$ edges.

## Planar Graph Enumeration Algorithm

We illustrate our Monte Carlo algorithm for generating 3-vertex-connected, 2-edge-connected, planar graphs in Figure 2. We begin with a single edge connecting two vertices in the model (Figure 2a). This edge connects vertices 1 and 2, without loss of generality. Each vertex has three *receptors* that will be linked via edges to other vertices. The vertices may rotate in the plane, but the receptors maintain an established winding order; that is, a receptor cannot switch to the other side by flipping the vertex over.

On each iteration of the algorithm we randomly select two vertices that have at least one receptor open (Figure 2b) and attempt to add an edge connecting them (Figure 2c). If a vertex has more than one open receptor, we randomly select one of the open receptors. If neither of the two vertices are connected to the forming graph, we do not add that edge (Figure 2d). Note that this specific edge may be added at a later step after one or both of the vertices are first connected to the graph. Figure 2f illustrates the other type of blocked edge addition. We analyze the two proposed receptors by walking the perimeter of the current graph and making an ordered list of the open receptors and *do not* add the edge if the receptors are not adjacent in the traversal. Adding the proposed edge between these vertices would segment the remaining open receptors into two groups, forbidding the addition of future edges connecting a vertex in one group to a vertex in the other group. Note that this edge may in fact be added in a later step, if all the open receptors on one side are first connected to each other. As we progress, each time we add an edge that forms a cycle on the graph (Figure 2h), this cycle is exported as a face of the polyhedral graph.

This algorithm will only fail to generate a valid graph if the last two open receptors remaining belong to the same vertex or if the final graph is only singly-connected. The first case can be prevented with a check when adding the second-to-last edge. The second case arises in roughly one third of the generated graphs (the percentage decreases as $n$ increases), so we simply discard these graphs. Every possible 3-vertex-connected, 2-edge-connected, planar graph may be generated by this algorithm. However, the probability

**Table 1:** Fractional completion of the enumeration problem for convex polyhedra: for $f = 6$, the two convex polyhedra are Figure 1a-b. The blue italicized numbers indicate incomplete enumeration results. Total number of convex polyhedra from [3].

| $n$ | $f$ | Total Convex Graphs | Generated Convex Graphs | Generated Graphs with Band-Faces | Generated Graphs with Band- and 2-edged Faces |
|---|---|---|---|---|---|
| 4 | 4 | 1 | 1 | 0 | 1 |
| 6 | 5 | 1 | 1 | 0 | 3 |
| 8 | 6 | 2 | 2 | 1 | 10 |
| 10 | 7 | 5 | 5 | 3 | 36 |
| 12 | 8 | 14 | 14 | 15 | *193* |
| 14 | 9 | 50 | 50 | *64* | *1,075* |
| 16 | 10 | 233 | *232* | *333* | *3,561* |
| 18 | 11 | 1,249 | *1,095* | *2,117* | *1,516* |
| 20 | 12 | 7,595 | *1,577* | *1,492* | *1,733* |
| 22 | 13 | 49,566 | *3,371* | | |
| 24 | 14 | 339,722 | *269* | | |
| 26 | 15 | 2,406,841 | *237* | | |

of generating a particular graph is not uniform. We must next study and understand the distribution of polyhedra generated by this randomized enumeration algorithm and how it relates to the distribution of observable grains both in simulation and in experiments.

## Analysis

The Monte Carlo approach described here in brief has proven successful in enumerating many allowable topologies that grains can adopt: progress to date is summarized in Table 1. The reader should be cautioned that the algorithm as presented in this paper very likely provides a particular selection bias from within the set of all possible topologies. In cases where all the topological members of the set have been found this is of no practical concern. However, drawing conclusions based on the observed members of partially completed sets should be done with caution. With this in mind, we take an analytical approach based on dispersion in topological properties to classify individual polyhedral graphs without generalization to the entire population of graphs in any one set.

The Platonic solids (the regular tetrahedron, cube, and dodecahedron) have the property that all the edges and faces are identical. These few solids ($f = 4, 6, 12$) represent all the *constructible* tri-valent polyhedra with identical planar faces that can be represented in three dimensions. One of the authors (Glicksman) has introduced a method for computing the geometric properties for these idealized 'proxy' grains (the N-hedra) for an arbitrary number of faces, $3 \leq f \leq \infty$ [7]. These 'unconstructible' grains are the equivalent of the Platonic solids in that they have edge lengths (and other geometric properties) characteristic of symmetric, idealized polyhedra. We compare the results of our Monte Carlo method to these 'ideal' generalized polyhedra.

## Enumeration Progress

We begin to characterize the enumerated tri-valent polyhedra by computing the dispersion (via the standard deviation) in their number of edges per face:

$$\sigma(p) = \sqrt{\frac{1}{f}\sum_{i=1}^{f}(p_i - \bar{p})^2} \tag{1}$$

$$\bar{p} = 6 - \frac{12}{f}, \tag{2}$$

where Equation 2 is Smith's formula for the mean number of edges per face [4]. By virtue of their regularity, each of the Platonic solids has $\sigma = 0$; so, too, does each 'ideal' generalized polyhedron. For any other polyhedral graph, this statistical metric indicates how close to 'regular' it is.

By comparing the frequency with which polyhedral graphs are generated to their respective values of $\sigma$, we find that graphs with high $\sigma$ are generated far more often than those with low $\sigma$: consider Figure 3, which includes duplicate generation of the same graph in addition to isomorphs and other distinct graphs with common $\sigma$. Considering the histogram of Figure 3b with $f = 12$, an incomplete class, it is perhaps not surprising that although we have generated more than 500 topologically unique dodecahedra, the Platonic dodecahedron is not among them. Graphs with band faces and 2-edged faces (red segments in Figure 3) turn up relatively often in this work, upon occasion in grain growth simulations [16], and extremely rarely in real polyhedral networks. This difference in the proportion of band faces and 2-edged faces is to be expected: the algorithm discussed here was designed to explore topological sample space, not to mimic real polyhedral networks found in nature.

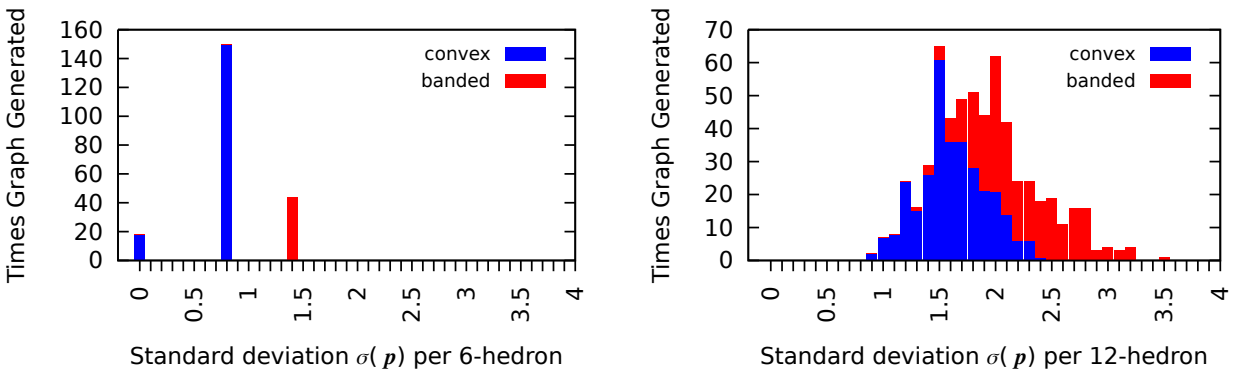


**Figure 3:** Number of times polyhedral graphs of given $\sigma$, including duplicates, have been generated by our algorithm to date. Regular polyhedra, such as the cube or regular dodecahedron, are generated considerably less frequently than are graphs with $\sigma > 0$.

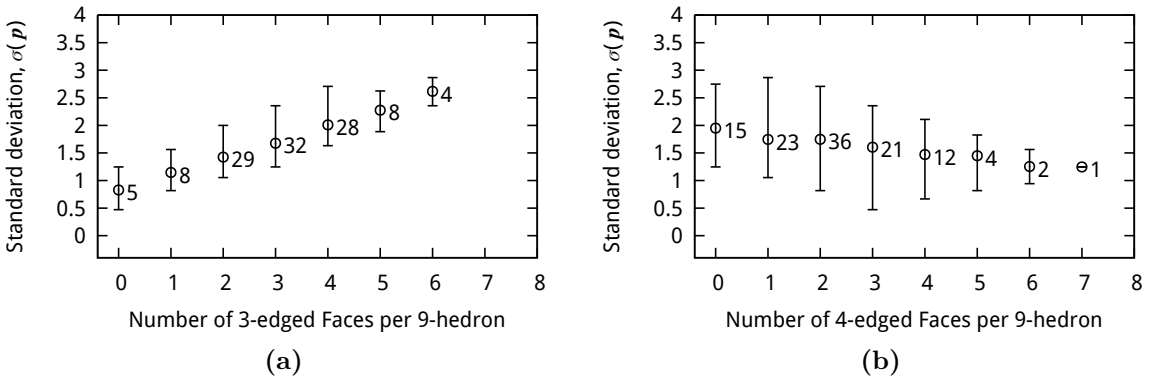


**(a)** **(b)**

**Figure 4:** Dispersion in the number of edges per face $p$ of the 50 convex nonahedra plus 64 nonahedra with band or 2-edged faces. Bars indicate the range of $\sigma$, rings the average; the number of nonahedra per category are noted.

Discussion of Polyhedra

Bearing the intent of our algorithm in mind, we begin to analyze graphs having the largest number of faces for which every graph has been generated: the nonahedra, $f = 9$ and $\bar{p} \approx 4.67$ edges per face. We section this data for study by choosing a face topology of interest and determining how many times it shows up; e.g., how many 3-edged faces there are in each 9-hedral graph. We perform the dispersion analysis discussed above to yield a set of plots for these graphs, comparing the dispersion in $p$ to the number of faces with a selected geometry; a couple are represented in Figure 4. The minimal value of dispersion corresponds to the nonahedron having three faces with $p = 4$ and six with $p = 5$ edges per face. The upward trend in Figure 4a is the result of our tri-valency constraint and Euler's characteristic:

$$3n = 2e \tag{3}$$

$$\chi = n - e + f, \tag{4}$$

so that polyhedra with $f = 9$ and an increasing number of 3-edged faces must also have increasing numbers of faces with $p > \bar{p}$ to conserve $\chi$. This is increasing dispersion, by definition.

Assuming that 3- and 4-edged faces are curved in such a way that they are generally shrinking in area, we expect grains with graphs located at the upper-right of Figure 4a, for example, to exit the $f = 9$ class more quickly than those at the lower-left. Similarly, grains from higher $f$-classes are expected to enter lower ones as these highly-curved faces collapse. Based on the number of 3- and 4-edged faces, $\sigma$, and other topological properties of the grain, it may be possible to estimate residence time upon entry to an $f$-class. As we begin to index grain growth experiments according to our enumeration of polyhedral graphs, we plan to chart the trajectory of grains as they traverse topological space to characterize the topological dependence of residence time in the polycrystalline structure.

## Conclusions and Future Work

From this study we conclude:

1. The total number of polyhedra beyond $f = 15$ is still unknown, and the number of topological variants for a given number of faces remains incomplete beyond $f = 9$. We have partially enumerated the topological variants for $9 < f < 16$, but many more exist.

2. The frequency of occurrence of particular topological elements can be analyzed using a dispersion formula referenced to the generalized $N$-hedron as the ideal.

3. The algorithm used to enumerate the topological variants likely introduces a bias that causes polyhedra with higher dispersion (compared to all possible topological variants) to be generated more frequently. Therefore care should be taken when drawing conclusions based on the partially complete enumerations.

4. In the future we anticipate the set of topological variants to play a central role in understanding topological distributions and residence time of particular grain topologies in dynamic calculations, and in the analysis of experimental grain growth data.

## References


[1] P. J. Federico, "The number of polyhedra," *Philips Research Reports*, 30 (1975) 220–231.

[2] A. J. W. Duijvestijn and P. J. Federico, "The number of polyhedral (3-connected planar) graphs," *Mathematics of Computation*, 37 (1981) 523–532.

[3] P. Engel, "On the enumeration of the simple 3-polyhedra," *Acta Crystallographica Section A*, 59 (2003) 14–17.

[4] C. S. Smith, "Grain shapes and other metallurgical applications of topology," in "Metal Interfaces," pages 65–118, 1952.

[5] W. M. Williams and C. S. Smith, "A study of grain shape in an aluminum alloy and other applications of stereoscopic microradiography," *Transactions of the American Institute of Mining and Metallurgical Engineers*, 194 (1952) 755–765.

[6] W. Thomson, "On the division of space with minimum partitional area," *Philosophical Magazine*, 24 (1887) 503.

[7] M. E. Glicksman, "Analysis of 3-D network structures," *Philosophical Magazine*, 85 (2005) 3–31.

[8] D. J. Rowenhorst, A. C. Lewis, and G. Spanos, "Three-dimensional analysis of grain topology and interface curvature in a $\beta$-titanium alloy," *Acta Materialia*, 58 (2010) 5511–5519.

[9] Y. Suwa, Y. Saito, and H. Onodera, "Parallel computer simulation of three-dimensional grain growth using the multi-phase-field model," *Materials Transactions*, 49 (2008) 704–709.

[10] M. Elsey, S. Esedoḡlu, and P. Smereka, "Large-scale simulation of normal grain growth via diffusion-generated motion," *Proceedings of the Royal Society A: Mathematical, Physical and Engineering Science*, 467 (2011) 381–401.

[11] E. A. Lazar, J. K. Mason, R. D. MacPherson, and D. J. Srolovitz, "A more accurate three-dimensional grain growth algorithm," *Acta Materialia*, 59 (2011) 6837–6847.

[12] A. J. W. Duijvestijn, "List of 3-connected planar graphs with 6 to 22 edges," 1979, unpublished computer tape, Twente University of Technology, Enschede, The Netherlands.

[13] Y. L. Voytekhovsky and D. G. Stepenshchikov, "On the symmetry of simple 14- and 15-hedra," *Acta Crystallographica Section A*, 59 (2003) 367–370.

[14] Y. L. Voytekhovsky and D. G. Stepenshchikov, "On the symmetry of simple 16-hedra," *Acta Crystallographica Section A*, 62 (2006) 230–232.

[15] J. A. F. Plateau, *Statique Expérimentale et Théorique des Liquides Soumis aux Seules Forces Molécularies*, Paris: Gauthier-Villars, 1873.

[16] E. A. Lazar, *The Evolution of Cellular Structures via Curvature Flow*, Ph.D. thesis, Princeton University, 2011.

1st International Conference on 3D Materials Science
*Edited by: Marc De Graef, Henning Friis Poulsen, Alexis Lewis, Jeff Simmons, George Spanos*
***TMS (The Minerals, Metals & Materials Society), 2012***

# Distribution of carbide particles and its influence on grain growth of ferrite in Fe-C alloys containing B and V

Takafumi Oikawa[1], Masato Enomoto[2]

[1]Graduate Student, Faculty of Engineering, Ibaraki University
4-12-1 Nakanarusawa, Hitachi, 316-8511 Japan
[2]Department of Materials Science and Engineering, Ibaraki University

Keywords: Grain growth, Pinning effect, Carbide, Iron alloy

## Abstract

The pinning effects of carbide particles on the grain growth of ferrite were studied in Fe-0.1C-0.0005B and Fe-0.1C-0.09V alloys. The number and size distribution of carbide particles were determined from the number of consecutive sections cutting a particle or the observed largest size in distinction of grain faces, edges and corners by means of serial sectioning. The particle numbers in contact with each type of grain boundary site were considerably greater than those calculated assuming random distribution. Theories that all particles pin grain boundaries predicted the final grain size in fair agreement with measured ones.

## Introduction

Grain growth is impeded in the presence of 2nd phase particles. This phenomenon, known as the Zener pinning effects, is utilized industrially to suppress grain coarsening in steel and steel weld. In order to predict the final grain size it is crucial to evaluate correctly the proportion of particles actually pinning the boundary. A number of theoretical and computational studies have been conducted to propose the $f^{-1/n}$ ($n>1$) dependence of grain size where f is the volume fraction of particle [1-5]. Since f is usually of the order of a few percent or less, the final grain size is very sensitive to the n value which depends on the pinning sites.

Experimental studies along this line are rather scarce. We have conducted serial sectioning to observe the spatial and size distributions of pinning carbide particles in distinction of grain faces, edges and corners in cold-rolled and annealed Fe-0.1C-0.0005B [6] and Fe-0.1C-0.09V alloys. In the former alloy only cementite particles were formed while two carbide phases were formed and the particle size was not uniform in the latter alloy. In this report, the influence of non-uniform distribution of particles, both in size and space, on the grain growth of ferrite is discussed on the basis of modified Zener theories of boundary pinning.

## Experimental Procedure

High purity Fe-C alloys containing B and V were vacuum-induction melted. The chemical compositions of alloys are shown in Table 1. After hot-rolling and homogenization at 1250°C for 48 hr hot-rolled plates were 80% cold rolled and cut into square specimens 10 mm in side and 0.6 mm in thickness. Specimens were vacuum-sealed in silica tube and annealed at 700°C for up

Table 1 Chemical composition of alloys studied in mass%.

| Fe | C | Mn | Si | Al | V | P | S | B | N |
|---|---|---|---|---|---|---|---|---|---|
| Bal. | 0.11 | 0.01 | 0.02 | <0.002 | — | <0.002 | <0.001 | 0.0005 | — |
| Bal. | 0.108 | <0.01 | <0.02 | <0.002 | 0.092 | <0.002 | <0.0001 | — | <0.004 |

to 96 hr. Thermodynamic calculations revealed that only cementite was formed in the former alloy, while cementite and vanadium carbide were formed in the latter alloy. The V concentration in cementite was very small whereas the Fe concentration in vanadium carbide was substantial, see Table 2. In order to cover a large number of matrix grains serial sectioning was conducted with the removal thickness $\delta$=0.25 ~0.28 μm for the specimen annealed for 48 hr. The size distribution was measured over 17 out of 90 sections which covered the largest particle size (~4 μm). The procedure of sectioning has been described elsewhere [6].

Table 2 Composition of 2nd phase particles in ferrite in mass fraction

| | Carbide | | Volume fraction | |
|---|---|---|---|---|
| Fe-C-B | Cementite | $Fe_3(CB)$* | 0.015 | |
| Fe-C-V | Cementite | $(Fe_{0.995}V_{0.005})_3C$ | 0.011 | 0.013 |
| | Vanadium carbide | $(Fe_{0.23}V_{0.77})_7C_6$ | 0.0018 | |

* The ratio of carbon to boron concentrations is 99.45:0.55.

## Results and discussion

Identification of pinning sites and size distribution of carbide particles

Fig. 1a shows the 3D-reconstructed image of carbide particles on the surface of a grain in the B alloy annealed for 48 hr. The particle number and size distributions were measured separately at grain faces, edges and corners. Grain corner can be discriminated from grain edge either by triangular annihilation or recombination of grain boundaries as illustrated in Figs. 1b and 1c. The numbers of edges and corners in the sample volume and those of carbide particles in contact with them are shown in Table 3.

In the B alloy particles were relatively coarse. The particle size was measured by the number of consecutive sections cutting one particle. This procedure is not sufficient to measure the distribution of real particle size because if one particle is cut by i sections, the real particle diameter lies between (i-1)$\delta$ and (i+1)$\delta$. Hence, a computer program was developed to calculate the probability of one particle of diameter i$\delta$ being cut by (i-1) and (i+1) sections to obtain the real size distributions.

Table 3 Number of edges and corners in the sample volume and carbide particles in contact with them.

| Alloy | Sample volume, $\mu m^3$ | edge | | corner | |
|---|---|---|---|---|---|
| | | Total number | Number occupied | Total number | Number occupied |
| Fe-C-B | $7.1x10^4$ | 380 | 80 | 79 | 39 |
| Fe-C-V | $6.4x10^4$ | 440 | 114 | 119 | 68 |

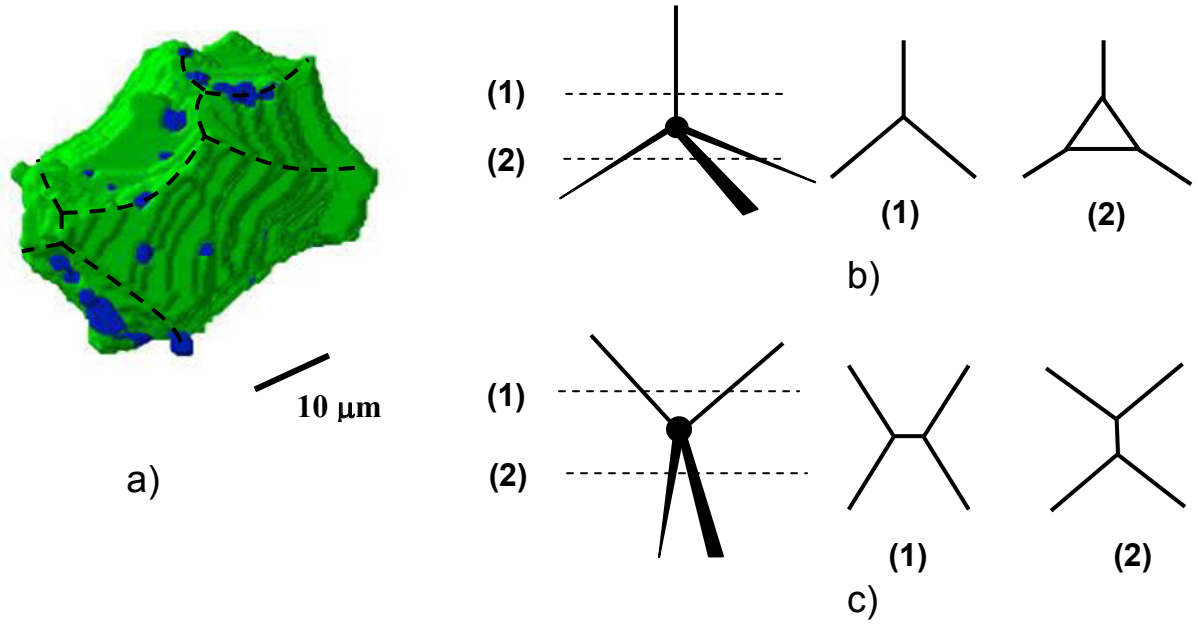


Fig. 1 Optical micrograph of a) 3D-reconstructed image of carbide on the surface of a grain in an Fe-C-B alloy annealed at 700°C for 48 hr, and b) triangular annihilation and c) recombination of grain boundaries for identification of a grain corner.

In the V alloy the particle size was highly non-uniform; SEM-EDX analysis revealed that the majority of smaller particles observed in the matrix were vanadium carbide. Thus, the largest diameter observed in consecutive sections associated with each particle was recorded. Even by doing so, a significant amount of error is expected for smaller particles because they may not be sectioned through the center of the particle. Accordingly, another computer program was developed to calculate the probability of particles enrolled in a smaller size group and corrections were made to the distribution of measured largest particle diameters.

The distributions of real diameters for particles at grain faces, edges and corners are shown in Figs. 2 and 3 for the B and V alloys, respectively. In these figures the numbers of particles in

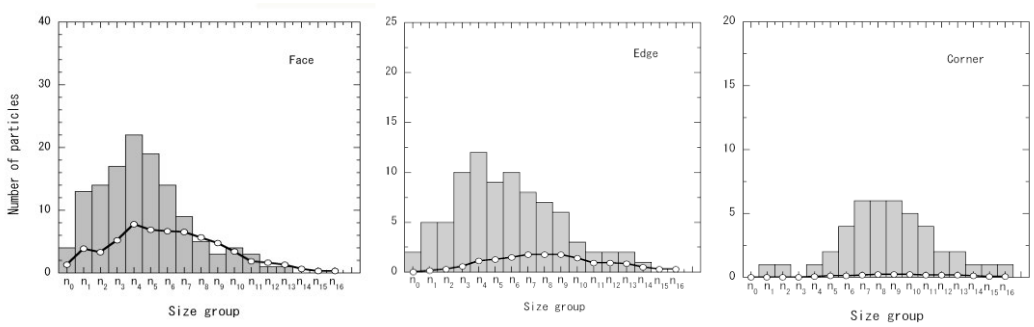


Fig. 2 Comparison of real size distribution of particles a) at grain faces, b) at grain edges and c) at grain corners with the numbers of particles calculated assuming random distribution (white circle) in the Fe-C-B alloy.

contact with each grain boundary site were calculated assuming that particles were distributed *at random* by the following equations,

$$n_f = 2rn_V SV\,, \qquad n_e = \pi r^2 n_V LV\,, \quad \text{and} \qquad n_f = \frac{4\pi}{3} r^3 n_V MV$$

for grain faces, edges and corners, respectively. Here, r is particle radius, $n_V$ is the particle density and V is the sample volume. S=3.35/D, L=8.5/$D^2$ and M=12/$D^3$ are the area of grain faces, the length of grain edges and the number of grain corners per unit volume, where all grains are assumed to be a tetrakaidecahedron of diameter D [8]. $n_V$ was taken to be the sum of particle numbers at all sites, including grain matrix, in each group. It is immediately seen that the observed particle numbers are much greater than those of random distribution at all grain boundary sites. Moreover, the ratio of the observed to the calculated numbers increased in the order of grain faces, edges and corners and it appears to be a few tens times greater at corners.

Grain size calculated from modified Zener theories

A number of modified Zener theories have been proposed to improve the capability of predicting the grain size. One of the most crucial points is the proportion of particles actually pinning grain boundaries. Anand and Gurland [9] and Haroun [10] proposed the $f^{-1/2}$ dependence of the final grain size assuming that all particles are in contact with grain boundaries. An $f^{-1/3}$ dependence was proposed assuming all particles are pinning grain corners [2]. Hunderi and Ryum (H-R) [11] developed a theory which incorporates pinning at all grain boundary sites. Since the H-R theory assumed random distribution of particles, the grain size depends on $f^{-1}$ as in the original Zener theory. Finally, Nishizawa et al [12] assumed that particles lying in a region within half the inter-particle spacing from the grain boundary contribute to the pinning and proposed the $f^{-2/3}$ dependence.

It should be noted that in the V alloy the final grain size is calculated to be very small compared to the measured grain size in all these theories if the mean radius of *all* particles is incorporated. This is probably because the mean size of all particles does not represent the total particle number actually present in the alloy. Although not explicitly included in the equations, the number of particles may play a key role for the total pinning force. As an alternative, the mean radius of particles in contact with grain boundaries was employed to calculate the grain size. On the other hand, the mean radius of all particles were used in the B alloy. The grain sizes calculated from the above theories are shown in Table 4.

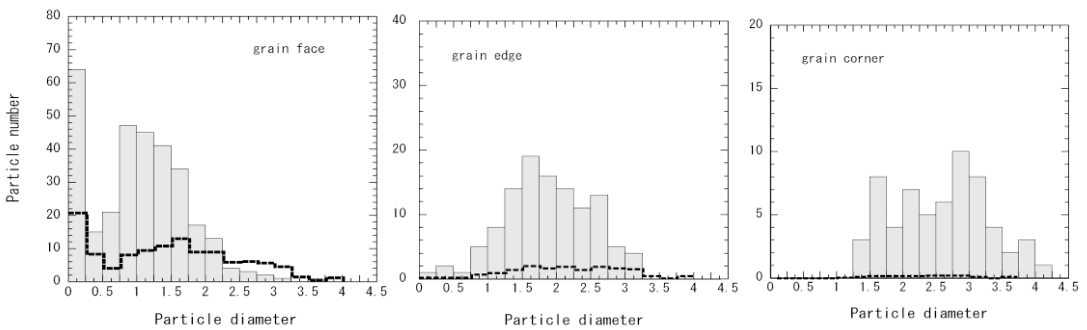


a) b) c)

Fig. 3 Comparison of real size distribution of particles a) at grain faces, b) at grain edges and c) at grain corners with the numbers of particles calculated assuming random distribution (dashed line) in the Fe-C-V alloy.

Table 4 Comparison of measured grain size calculated from modified Zener theories

| Model | Dependence of grain size with volume fraction f | Grain radius, μm | |
|---|---|---|---|
| | | Fe-C-B | Fe-C-V |
| Measured | — | 9.8±0.7 | 6.8±0.5 |
| Zener | $R=\frac{4r}{3f}$ | 65.3 | 73.1 |
| Grain boundary pinning | $R=(0.95\sim 2)\frac{r}{f^{1/2}}$ | 5.7~11.9 | 5.9~12.5 |
| Grain corner pinning | $R=(1.26\sim 1.82)\frac{r}{f^{1/3}}$ | 3.7~5.4 | 3.8~5.5 |
| Correlation model [12] | $R=\frac{4r}{3f^{2/3}}$ | 16.0 | 17.3 |
| Hunderi-Ryum [11] | $\frac{R_1}{r}=\frac{8}{9f}\left\{2\alpha f+0.25+\sqrt{(2\alpha f+0.25)^2+15f^2\beta}\right\}$ | 21.8~24.6 | 24.3~27.0 |

In both alloys the original Zener and Hunderi-Ryum theories yielded a grain size considerably greater than the measured ones. Conversely, the theory of grain corner pinning yielded a grain size smaller than the experiment. The grain sizes predicted from the grain boundary pinning and the correlation model are in fair agreement with experiment.

## Summary

The spatial and size distributions of carbide particles were measured by multiple sectioning in cold-rolled and annealed Fe-C alloys containing B and V, and the real size distributions of particles at grain faces, edges and corners were determined with the aid of computer simulation. In both alloys the proportions of particles in contact with grain boundaries were all greater than they would be if particles were distributed at random throughout the sample volume. As a result, theories which assume random distribution and lead to the $f^{-1}$ dependence of grain size predicted grain sizes considerably greater than the measured ones. The theories that all particles are trapped in grain boundaries yielded grain sizes in fair agreement with experiment, while the grain size is predicted to be too small if all particles were assumed to be at grain corners. In the V alloy in which the particle size was highly non-uniform the mean size of particles in contact with grain boundaries was more relevant to the prediction of grain size than the mean size of all particles.

## Acknowledgements

This research was funded by Grant-in-Aid of the Ministry of Education, Culture and Sports (no. 22560655) and Steel Research Promotion Fund of The Iron and Steel Institute of Japan (2009-2011).

## References


1.P.A. Manohar, M. Ferry and T. Chandra, "Five Decades of the Zener Equation", *ISIJ International*, 38(1998), 913-924

2. M. Hillert, "Inhibition of Grain Growth by Second-Phase Particles", *Acta Metallurgica* 36(1988), 3177-3181

3. D.J. Srolovitz, M.P. Anderson. G.S. Grest and P.S. Sahni, "Computer Simulation of Grain Growth –III Influence of Particle Dispersion", *Acta Metallurgica*, 32(1984), 1429-1438

4.G. Gouturier, R. Doherty, C. Maurice and R. fortunier, "3D Finite Element Simulation of the Inhibition of Normal Grain Growth by Particels", *Acta Materialia*, 53(2005), 977-989

5.Y. Suwa, Y. Saito, and H. Onodera, "Phase Field Simulation of Grain Growth in Three Dimensional System Containing Finely Dispersed Second-Phase Particles", *Scripta Materialia*, 55(2006), 407-410

6.T. Oikawa and M. Enomoto, "Pinning Effects on Grain Growth of Ferrite in an Fe-C-B Alloy", *Tetsu-to-Hagane*, 97(2011), 584-591

7.E.E. Underwood, *Quantitative Stereology*, (Reading, MA: Addison Wesley, 1970), 109-145

8.J.W. Cahn, "The Kinetics of Grain Boundary Nucleated Reactions", *Acta Metallurgica*, 4(1956), 449-459

9.L. Anand and J. Gurland, "The Relationship Between the Size of Cementite Particles and the Subgrain Size in Quenched-and-Tempered Steels", *Metallurgical Transactions A*, 6A(1975), 928-931

10.N.A. Haroun, "Theory of Inclusion Controlled Grain Growth", *Journal of Materials Science*, 15(1980), 2816-2822

11.O. Hunderi and N. Ryum, "The Interaction Between Spherical Particles and Triple Lines and Quadruple Points", *Acta metallurgica et materialia*, 40(1992), 543-549

12.T.Nishizawa, I. Ohnuma and K. Ishida, "Examination of the Zener Relationship between Grain Size and Particle Dispersion", *Materials Transactions, JIM*, 38(1997), 950-956

1st International Conference on 3D Materials Science
*Edited by: Marc De Graef, Henning Friis Poulsen, Alexis Lewis, Jeff Simmons, George Spanos*
***TMS (The Minerals, Metals & Materials Society), 2012***

# MODELING GRAIN BOUNDARY INTERFACES IN PURE NICKEL

T.J. Turner, P.A. Shade, J.C. Schuren, M.A. Groeber

Air Force Research Laboratory, Materials and Manufacturing Directorate, AFRL/RXLMP,
2230 Tenth Street, Wright-Patterson, AFB, OH 45433-7817, USA

Keywords: Crystal-Plasticity, Finite Elements, Grain Boundary Deformation

## Abstract

This work presents a three tiered modeling approach to examine grain boundary interfaces in a pure Nickel foil material utilizing a crystal plasticity based finite element model (CPFEM). The goal of this work is to calibrate a modeling approach through comparison to experimental data, and then use the models to gain insight into deformation at grain boundaries in Nickel and Nickel-base superalloy polycrystals. The first study utilizes a multi-crystal micro-tension specimen and simulations to calibrate the CPFEM model and examine the development of "hot-spots" or localized plasticity near the grain boundaries. Some orientation combinations exhibit localized plasticity along the boundary (bad-actor boundaries) while others do not. Insight from the deformation of this model is then used to instantiate simulations of Nickel bi-crystals which exhibit localized plasticity near the boundary. The third study embeds the grain boundary interfaces of interest, as determined from the bi-crystal simulations, into a larger polycrystalline simulation utilizing the same CPFEM framework. Using these interfaces we study deformation at these "characteristic" interfaces when subjected to the generalized loading conditions present in a polycrystalline microstructure.

## 1. Introduction

In this work, we make direct comparisons of simulation results with experimental measurements in an attempt to calibrate a Crystal Plasticity Finite Element Model (CPFEM) for use in investigating complex deformation phenomena. In particular, we calibrate our model through comparison with experimental results and then use the model to examine the nature of deformation at grain boundary interfaces. We hope this work will lead to an enhanced understanding of the onset and evolution of non-uniform deformation, and eventually provide a basis for prediction of crack initiation and failure in Nickel-base alloys.

Comparison of simulation results with experiments is a critical component in the development of computational tools which predict the plastic deformation response of polycrystalline ensembles. Previous studies have compared bulk crystallographic texture changes with deformation, while others examined local lattice orientation changes and the development of intra-granular misorientation and deformation [1-4]. While those studies are useful in setting the groundwork for the present study, they often stop after validating their particular model and methodology. For this work we go beyond a simple model calibration and validation, and apply our model to study aspects of the deformation that cannot be experimentally measured. In particular, this study builds upon the techniques presented in [5], where microstructural features at the relevant length-scales were experimentally characterized and used to instantiate a CPFEM model. From this we hope to gain insight into the mechanics of deformation, as well as to understand where experimental techniques may fall short in order to develop new relevant experiments for the future.

## 2. Materials and Experimental Procedures

### 2.1 Material

For this work we examined a commercially purchases 99.0% pure nickel foil material with a thickness of 50 μm. Although not shown, Electron Back-Scatter Diffraction (EBSD) measurements revealed a random crystallographic texture and an approximate average equiaxed grain size of 20 μm.

### 2.2 Micro-Tension Test

To calibrate our CPFEM model, a micro-tensile specimen was fabricated from the nickel foil by implementing a stencil mask technique. The final sample geometry was defined using focused ion beam (FIB) milling, creating a specimen with a rectangular cross section and a gage width of 21μm, a thickness of 38μm, and a gage length of 80μm. The FIB was also used to machine a grid of points onto the top surface of the sample to be used as fiducial markers for digital image correlation (DIC) tracking of surface displacements. An image of the sample prior to testing is shown in Figure 1 (a). A custom in-situ mechanical testing device [6-7] was used to deform the specimen in tension to an axial true strain of 2.4%. Throughout deformation, the location of the fiducial markers on the specimen surface was tracked through automated SEM imaging to derive the surface strain distribution.

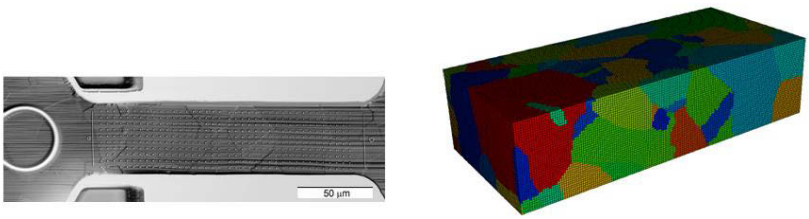


**Figure 1. (a) Pure nickel micro-tension test specimen (b) CPFEM model representing tensile specimen**

### 2.3 Serial Sectioning

After the tensile test, the full 3D microstructure and internal crystallographic lattice rotations of the deformed sample were characterized through destructive 3D-electron backscatter diffraction (EBSD) serial sectioning. Cross-sections were repeatedly milled with a section thickness of 250 nm, while crystallographic orientation data was captured on each section with a pixel size of 250 nm. The 3D-EBSD dataset consisted of approximately 400 sections and the full 3D post-deformation microstructure was subsequently re-constructed using DREAM 3-D software (http://dream3d.bluequartz.net/).

## 3. Modeling Approach

### 3.1 Polycrystal Model

The crystal-plasticity model employed for this work approximates the micro-mechanics of plastic flow in crystalline solids using restricted slip assumed to only occur on the octahedral family of {111}<110>. A brief overview of the single crystal constitutive model is presented here; a more detailed development may be found in [3-4]. The salient features of the crystal plasticity model for this paper include the constitutive formulation and the hardening equation. The rate of shearing on each slip system is determined from a rate-dependent constitutive formulation relating the shearing rate to the resolved shear stress:

$$\dot{\gamma}^{\alpha} = \Phi\left(\tau^{\alpha}, g^{\alpha}\right) = \dot{\gamma}_{o}\left|\frac{\tau^{\alpha}}{g^{\alpha}}\right|^{1/m} \operatorname{sgn}\left(\tau^{\alpha}\right) \qquad (1)$$

in which $\dot{\gamma}^{\alpha}$ denotes the rate of shearing on the $\alpha^{th}$ slip system , $\tau^{\alpha}$ and $g^{\alpha}$ are the resolved shear stress and slip-system strength of the $\alpha^{th}$ slip system, respectively, $m$ is the rate-sensitivity, and $\dot{\gamma}_o$ is a model parameter. The slip-system strengths are evolved through a Voce-type saturation law [8-9] of the following form:

$$\dot{g}^{\alpha} = \theta(\dot{\gamma}, g) = h_0 \left( \frac{g_{so} - g^{\alpha}}{g_{so} - h_s} \right) \dot{\gamma} \qquad (2)$$

Here, $\dot{\gamma}$ is the net rate of slip on all the slip systems within the crystal, and $h_o, g_{s0}$, and $h_s$ are material parameters.

3.2 Model Calibration Using the Micro-Tension Virtual Specimen

The constitutive response of the material was calibrated using the single-crystal model discussed above, coupled with the Arbitrary Lagrangian/Eulerian 3D (ALE3D) finite-element code developed at Lawrence Livermore National Laboratory [10]. We employed an individual crystal orientation for each finite element, and unique grains in the model were then defined by a collection of elements with the same orientation. This technique has been used in other efforts to produce virtual microstructures for CPFEM simulations [4-5]. The serial section data were reconstructed and used as input for the model, creating the virtual microstructure shown in Figure 1b. The model parameters ($h_o, g_{s0}, h_s, g^{\alpha}_{initial}, \dot{\gamma}_0$, and $m$) were initialized such that the macroscopic stress-strain response from the CPFEM simulations matched that of the experiments. In addition, the standard anisotropic elastic moduli ($c_{11}$= 247GPa, $c_{12}$ = 147GPa, $c_{44}$ =125GPa) were chosen to match the elastic response of the experiments. The finite element mesh was created with 448,000 hexehedral finite elements (Figure 1b). Figure 2 shows the results of the surface strain distributions in the experimental specimen (Figure 2a) as measured with DIC, and in the simulation (Figure 2b) after a uni-axial tensile deformation to 2.5% axial true strain. Although the experimental surface strain was measured on a coarser grid than the finite element mesh, the general trends in both magnitude and patterning of the surface strain were captured, further indicating that the model calibration was qualitatively reasonable.

**Table I. Material Parameters for the Simulation of the micro-tension test**

| $h_o$ | $g_{so}$ | $h_s$ | $g^{\alpha}_{initial}$ | $\dot{\gamma}_0$ | $m$ |
|---|---|---|---|---|---|
| (MPa) | (MPa) | (MPa) | (MPa) | ($s^{-1}$) | - |
| 500 | 103 | 43 | 43 | $1e^{-5}$ | 0.06 |

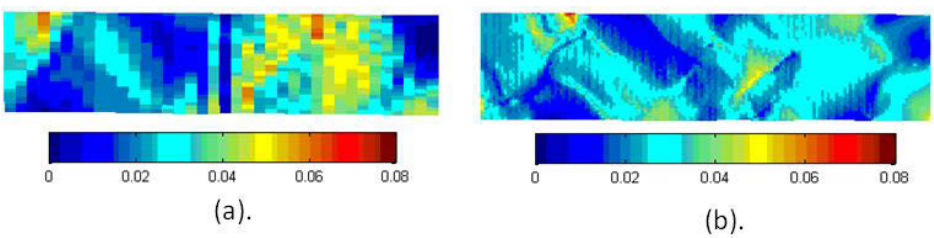


**Figure 2. Axial surface strain plots for the (a) experimental micro-tension specimen, and (b) the CPFEM simulation of the micro-tension specimen**

3.3 Bi-Crystal Simulations

Examination of the results from the micro-tension specimen revealed that significant heterogeneity existed in the deformation. In particular, the concentration of localized plasticity or "hot-spots" appeared to form at or near grain boundaries. Therefore we decided to further

explore the issue of deformation at the grain boundary interfaces through bi-crystal simulations of particular grain boundaries. We chose the particular sets of orientations in the bi-crystal simulations through intuition of which orientation pairs might generate large plastic flow localizations (Figure 3a) [11]. To that end we developed the finite element mesh shown in Figure 3b utilizing 470,000 finite elements which included a refined region near the grain boundary. We instantiated the mesh with two different crystallographic orientations, creating a bi-crystal simulation, and then ran two different simulations—the first with orientations aligned for multi-slip (Figure 3c) and the second with crystallographic orientations aligned for single-slip (Figure 3d). The virtual specimens were deformed under uni-axial tension to 2.5% axial true strain.

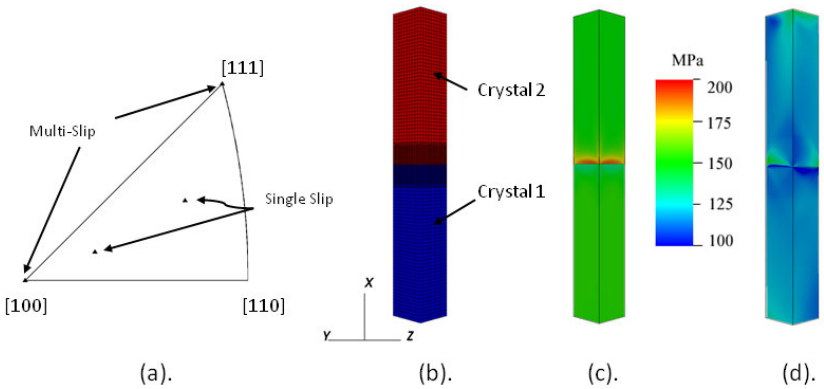


**Figure 3. (a) The orientations selected for the bi-crystal simulation are labeled in the Inverse Pole Figure (b) the Finite Element mesh used for the simulations (c) Von Mises effective stress in the Multi-slip and (d) in the Single Slip cases**

## 3.4 Embedded Polycrystal Simulations

After examining the bi-crystal simulations in Figure 3, we took the same crystallographic orientations from those simulations and embedded them into a larger polycrystal aggregate with a random crystallographic texture to examine the response of the same boundaries when subjected to the more arbitrary deformation state they might experience as part of a deforming polycrystal. In addition, we ran several simulations where we inclined the grain boundary at different angles (0, 45, and 90 degrees) relative to the tensile axis. Figure 4 shows the basic setup of the virtual polycrystals, as well as slices of the interior with the embedded bi-crystal at the center of the model. The colors in this figure are shaded to show the surrounding microstructure and the two crystals of interest at the center. Figure 5 shows the CPFEM results, plotting the Von Mises effective stress on a slice through the interior of the 3D microstructure.

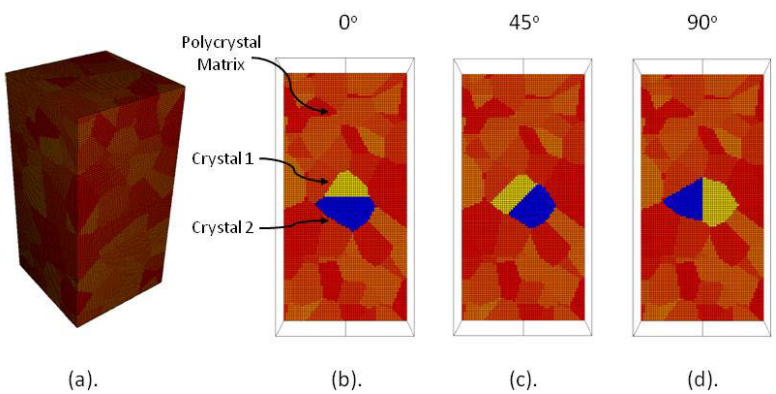


**Figure 4. (a) CPFEM model of the embedded microstructure (b) 0 degree simulation (c) 45 degree simulation (d) 90 degree simulation**

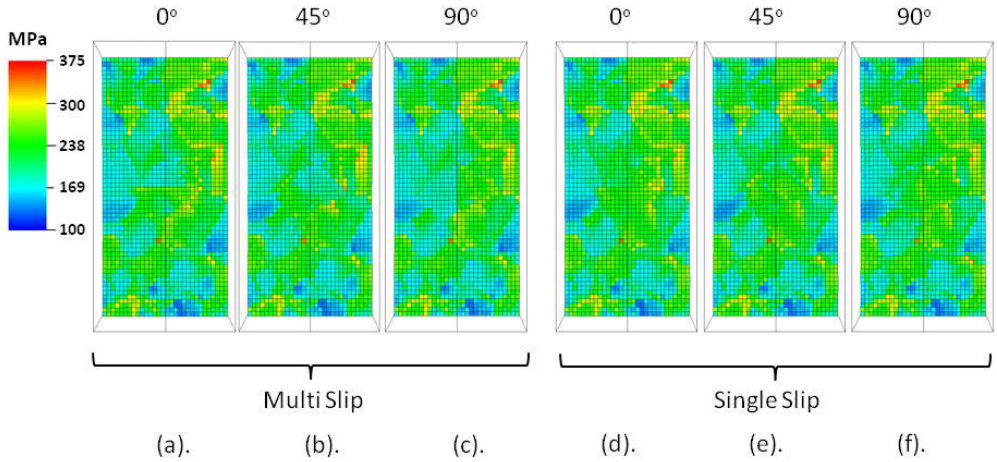


**Figure 5. (a) Von Mises effective stress in the CPFEM model of the embedded microstructure (a-c) embedded grains aligned for multi-slip (d-f) embedded grains aligned for single-slip**

## 4. Discussion

For this study we calibrated our CPFEM model and methodology through a micro-tensile test with a pure Nickel polycrystal. We found that the CPFEM model qualitatively captured the surface strain gradients seen in the experiment, even though the fiducial markers utilized for the DIC were on a coarser scale than the simulation results. However, both the experiment and simulation showed significant heterogeneity in the deformation field at the surface of the specimen. Closer examination of Figure 2 reveals that localized plasticity or "hot spots" appear to form at or near grain boundaries. This provided the motivation to use our calibrated CPFEM model to explore the development of this heterogeneity.

To this end, we developed bi-crystal simulations with two sets of crystallographic orientations. The bi-crystal model allowed us to examine only one grain boundary at a time, thereby reducing the complexity of the loading conditions inherently present in a polycrystalline sample. We chose to examine two sets of crystals that based on our intuition and knowledge of deformation in single crystals [11] we believed would provide extremes in behavior along the grain boundary. The first set was chosen with their crystallographic orientations aligned for multi-slip. These orientations are plotted in the inverse pole figure maps of Figure 3a, which shows the tensile axis in the crystal coordinate system. The multi-slip crystal orientations have the tensile axis aligned with the [100] and [111] crystal directions, respectively, where we assumed the multiplicity of slip systems involved would provide a more homogeneous deformation at the grain boundary. In a similar fashion, we chose a pair of single-slip oriented crystals thereby setting up a condition we believed would be less accommodating of the macroscopic deformation, forcing a larger amount of heterogeneity in the plastic response near the grain boundary. By examining Figure 3, it does appear that the single-slip case deformed less homogenously, although both sets of crystals develop localized stress concentrations near the grain boundary.

It is important to note that both bi-crystal simulations deformed in a non-intuitive manner based on our knowledge of single crystal deformation, where both combinations may be seen as so called "bad-actor" grain boundaries—areas where stress concentrations develop under load. This occurs because the act of combining them into a bi-crystal inherently changes the boundary conditions, particularly at the grain boundary, and thus changes the local stress state. Therefore, to evaluate these grain boundaries under a more arbitrary deformation state, we carried out a suite of simulations where we embedded the bi-crystals into a larger polycrystalline aggregate.

Once again, this larger polycrystal was deformed in uni-axial tension to 2.5% axial true strain, and the bi-crystal combinations were placed at the center of the aggregate. In addition, for each bi-crystal combination we performed three simulations where the grain boundary between the two crystals was configured in different orientations relative to the axial loading. Figure 4 shows the configuration of those simulations, while Figure 5 displays the Von Mises effective stress on a cross section through the middle of the aggregate and the embedded bi-crystal grains. In both the multi-slip and single-slip cases, and in all three angular orientations of the grain boundary, no appreciable stress concentration develops at the boundary. This varies significantly from the results shown in Figure 3 of the standalone bi-crystal simulations, and indicates that the polycrystalline aggregate applies a very different deformation state to the embedded bi-crystal grains than is seen under the idealized loading in the pure bi-crystal simulations. Therefore, in order to predict localized plasticity and develop meaningful criteria for the onset of failure, it is extremely important to understand not only the character of the grain boundaries, but also the local stress state at the grain level. In turn, this local stress state is influenced by the nature of the externally applied loading, as well as the neighborhood of grains in the polycrystalline material. In addition, it is important for the larger materials community to continue to develop micro-mechanical models, such as the CPFEM method presented here, coupled with critical experimental validation of these models, if we hope to use them as design tool to predict the development of deformation heterogeneity and the onset of failure in engineering materials.

## 5. References


1. Becker R and Panchanadeeswaran S 1995 Effects of Grain Interactions on Deformation and Local Texture in Polycrystals *Acta Metall. Mater.* **43** 2701-19
2. Bhattacharyya A, El-Danaf E, Kalidindi S R, Doherty R D, 2001 Evolution of grain-scale microstructure during large strain simple compression of polycrystalline aluminum with quasi-columnar grains *International Journal of Plasticity* **17** 861-883
3. Marin E and Dawson P R 1998 Elastoplastic finite element analysis of metal deformation using polycrystal constitutive models *Comp. Methods in Appl. Mech. and Eng* 1998 **165** 1-21
4. Turner T J, and Miller M P 2007 Modeling the influence of material structure on deformation induced surface roughening in AA7050 thick plate *ASME Journal of Engineering Materials and Technology* **129** 367-79
5. Turner T J, and Semiatin, S L 2011 Modeling large-strain deformation behaviour and neighborhood effects during hot working of a coarse-grain nickel-base superalloy *Modeling and Simulation in Materials Science and Engineering*, **19**, 1-25
6. Shade P A, Wheeler R, Choi Y S, Uchic M D, Dimiduk D M, Fraser H L 2009 A combined experimental and simulation study to examine lateral constraint effects on microcompression of single-slip oriented single crystals *Acta Mater.* **57** 4580-87
7. Wheeler R, Shade P A, and Uchic M D 2012 Insights gained through image analysis during in-situ micromechanical experiments *JOM* In press
8. Kocks U F 1976 Laws for work-hardening and low-temperature creep *ASME J. Eng. Mater. Tech* **98** 76–85
9. Mathur K, and Dawson P R 1989 On modeling the development of crystallographic texture in bulk forming processes *Inter. J. Plasticity* **5** 67-94
10. Anderson A, Cooper R, Neely R, Nichols A, Sharp R, Wallin B 2003 Users manual for ALE3D—an arbitrary Lagrange/Eulerian 3D code system *Technical Report UCRL-MA-152204, Lawrence Livermore National Laboratory*
11. Hosford WF, *The Mechanics of Crystals and Textured Polycrystals* (New York, NY, Oxford University Press, 1993)

1st International Conference on 3D Materials Science
*Edited by: Marc De Graef, Henning Friis Poulsen, Alexis Lewis, Jeff Simmons, George Spanos*
***TMS (The Minerals, Metals & Materials Society), 2012***

# A Toolbox for Geometric Grain Boundary Characterization

Krzysztof Glowinski[1], Adam Morawiec[1]

[1]Institute of Metallurgy and Materials Science, Polish Academy of Sciences, Reymonta 25, 30-059 Krakow, Poland

Keywords: Grain boundary, interface, geometric characterization, macroscopic boundary parameters

## Abstract

Properties of polycrystalline materials are affected by grain boundary networks. The most basic aspect of boundary analysis is boundary geometry. This paper describes a package of computer programs for geometric boundary characterization based on macroscopic boundary parameters. The program allows for determination whether a boundary can be classified as near-tilt, -twist, -symmetric et cetera. Since calculations on experimental, i.e., error affected data are assumed, the program also provides distances to the nearest geometrically characteristic boundaries. The software has a number of other functions helpful in grain boundary analysis. One of them is the determination of planes of all characteristic boundaries for a given misorientation. The resulting diagrams of geometrically characteristic boundaries can be linked to experimentally determined grain boundary distributions. In computations, all symmetrically equivalent representations of boundaries are taken into account. Cubic and hexagonal holohedral crystal symmetries are allowed.

## Introduction

Solid state materials frequently occur as polycrystalline agglomerates. Such aggregates contain complex three-dimensional (3D) networks of boundaries separating adjacent grains. The boundaries have an impact on properties of polycrystals. The most basic feature of a boundary is its geometry. Although geometric attributes themselves are insufficient for a complete boundary characterization, they are a foundation for more extensive investigations of grain boundaries. Recent progress in development of 3D experimental techniques (in particular, in precise serial sectioning techniques [1]) gives the opportunity to determine macroscopic parameters [2] for significant numbers of boundaries. Large data sets containing grain misorientations and boundary planes are being collected [3, 4]. In order to explore these sets in an efficient and automated way, dedicated computer programs are needed.

There exist numerous software solutions for boundary detection and for processing of boundary data obtained via electron backscatter diffraction (EBSD) experiments (e.g., *OIM Analysis* of EDAX-TSL, *DREAM.3D* [5], *MTEX* [6]). Other programs are designed to reconstruct geometric surfaces of boundaries; see, e.g., [7]. Some calculations related to crystal misorientations and orientation relationships can be performed using crystallographic tools (e.g., *SP2* [8]). However, we are not aware of any software which would be capable of a complete geometric characterization of boundaries. By this we

mean the issue of resolving whether a boundary can be classified as twist, tilt, symmetric et cetera, or providing numerical values of the deviations of a given boundary from the nearest geometrically characteristic boundaries (like pure-tilt, pure-twist, pure-symmetric et cetera). This paper presents a new software package intended to fill this gap. The purpose of the package is to make geometric analysis of boundaries easy and efficient. The algorithms used in the program are based on analytical solutions as well as on purely numerical searches. Several most common parameterizations can be used to input data of planar boundary segments. The cubic $m\bar{3}m$ and the hexagonal $6/mmm$ crystallographic point groups are allowed. Internally, all calculations are performed in Cartesian coordinate systems. Since the package has been developed in Java technology (SE 7), it is expected to run on numerous platforms equipped with Java Runtime Environment. It has been tested on Windows (XP and 7) and Linux (Ubuntu) operating systems.

## Preliminaries

Macroscopic boundary parameters: Comprehensive studies of interface geometry demand incorporating all five macroscopic degrees of freedom [2]. Assuming the presence of inversion center, a planar boundary in a bi-crystal can be specified by the relative misorientation between semi-crystals and the boundary plane. Following [9], a boundary can be represented by the $4 \times 4$ interface matrix

$$\mathbf{B} = \begin{bmatrix} 0 & \mathbf{m}_2^T \\ \mathbf{m}_1 & M \end{bmatrix} \quad , \tag{1}$$

where $M$ is the misorientation matrix, and $\mathbf{m}_1$ ($\mathbf{m}_2$) is the unit vector normal to the boundary plane expressed in the Cartesian reference frame attached to the first (second) crystallite. Furthermore, the condition $\mathbf{m}_2 = -M^T\mathbf{m}_1$ is satisfied. To extract complete information about a given physical boundary, all its symmetrically equivalent representations must be processed. The equivalent representations can be easily obtained using interface matrices: the representation $\mathbf{B}$ given by eq.(1) is equivalent to $\mathbf{B}^-$ and $\mathbf{C}_1\mathbf{B}\mathbf{C}_2^T$, where

$$\mathbf{B}^- = \begin{bmatrix} 0 & -\mathbf{m}_2^T \\ -\mathbf{m}_1 & M \end{bmatrix} \quad , \qquad \mathbf{C}_i = \begin{bmatrix} 1 & 0 \\ 0 & C_i \end{bmatrix} \tag{2}$$

and $C_i$ $(i = 1, 2)$ are proper orthogonal matrices of symmetry operations of the crystals. Additionally, in the case of homophase interfaces, if an interchange of grains is allowed, the representation $\mathbf{B}$ is equivalent to $\mathbf{B}^T$.

Geometrically characteristic boundaries: Several types of boundaries are distinguished using purely geometric criteria. The concepts of tilt and twist boundaries are widely known. A boundary is a *twist* boundary if its plane is perpendicular to the misorientation axis, while a *tilt* boundary has the axis in its plane. Since there is some confusion with the notions of symmetric and quasi-symmetric boundaries [10], they need to be described in more detail. We adhere to the established definition of a *symmetric* boundary: its plane is a mirror between crystal structures separated by the boundary. A boundary is called *properly* (*improperly*) *quasi-symmetric* if it has a representation given by eq.(1) with the

vectors $\mathbf{m}_1$ and $\mathbf{m}_2$ related via $\mathbf{m}_1 = -C_2\mathbf{m}_2$ ($\mathbf{m}_1 = +C_2\mathbf{m}_2$). There are a number of relationships between various boundary types. With the assumed crystal symmetries, every symmetric boundary is a tilt boundary. A properly quasi-symmetric boundary is also a twist boundary, and vice versa, a twist boundary is properly quasi-symmetric. In the same sense, improperly quasi-symmetric boundaries are equivalent to 180°–tilt boundaries, and symmetric boundaries are equivalent to 180°–twist boundaries. Proofs of these statements can be found in [10].

## Capabilities of the package

Recognition of a boundary type: One of the main functions of the package is its ability to classify a given boundary, i.e., to determine whether it belongs to any of the groups of geometrically characteristic boundaries. Since the program is meant to be applicable to experimental (i.e., error affected) data, it is necessary to look for boundaries satisfying the type-defining conditions with certain tolerances limited by user-specified thresholds.

The classification of a boundary can be done in a number of ways. The simplest method is based on a decomposition of the boundary into tilt and twist components. With an algorithm proposed by Fortes [11], one obtains the angles corresponding to each of these components, and a boundary is classified as near-tilt (near-twist) if the angle of the twist (tilt) component is below a given threshold; if none of the conditions is satisfied, it is a mixed boundary.

The next technique is analogous to that used in [12, 13]: a given boundary is classified as near-tilt (near-twist) if it is sufficiently close to a pure-tilt (pure-twist) boundary. Closeness between two boundaries is determined by a predefined distance function (cf. [9, 14, 15]). For instance, the distance can be given by $\min(\|\mathbf{B} - \mathbf{B}'\|/2)$, where $\|.\|$ denotes the Frobenius norm, $\mathbf{B}$ ($\mathbf{B}'$) is a representation of the first (second) boundary, and the minimization is over equivalent representations of the boundaries. For a given boundary, the nearest pure-tilt and pure-twist boundaries are calculated via numerical minimization of the distance function. These procedures have been extended, and they allow for computing the nearest symmetric and quasi-symmetric boundaries; the computations are based on the fact that the symmetric and quasi-symmetric boundaries can be also characterized as specific twist and tilt boundaries.

The program has some other useful capabilities like verification whether a given boundary has a CSL character, conversion between boundary parameterizations, or generation of data sets with the random distribution of boundaries.

Searches for all characteristic boundaries: The algorithms implemented in the program can be combined in many ways. Combining them opens new opportunities for more comprehensive boundary analyzes. For instance, one can pursue the concept of cataloging geometrically characteristic boundaries [13]. In order to deal with significant amount of data (caused by the large number of degrees of freedom), the catalogs are presented in the form of stereographic projections of boundary plane normals corresponding to geometrically characteristic boundaries for fixed misorientations. For brevity, the projections are called *maps*. With this representation, our diagrams can be directly linked to maps of experimental grain boundary distributions like those described in [4].

Tilt and twist boundaries are determined by, respectively, four and three independent parameters. Therefore, in maps, tilt and twist boundaries are represented, respectively, by points and lines (or spots and bands if a tolerance is allowed). Symmetric (quasi-symmetric) boundaries, as particular cases of twist (tilt) boundaries restricted by extra conditions occur only for some misorientations.

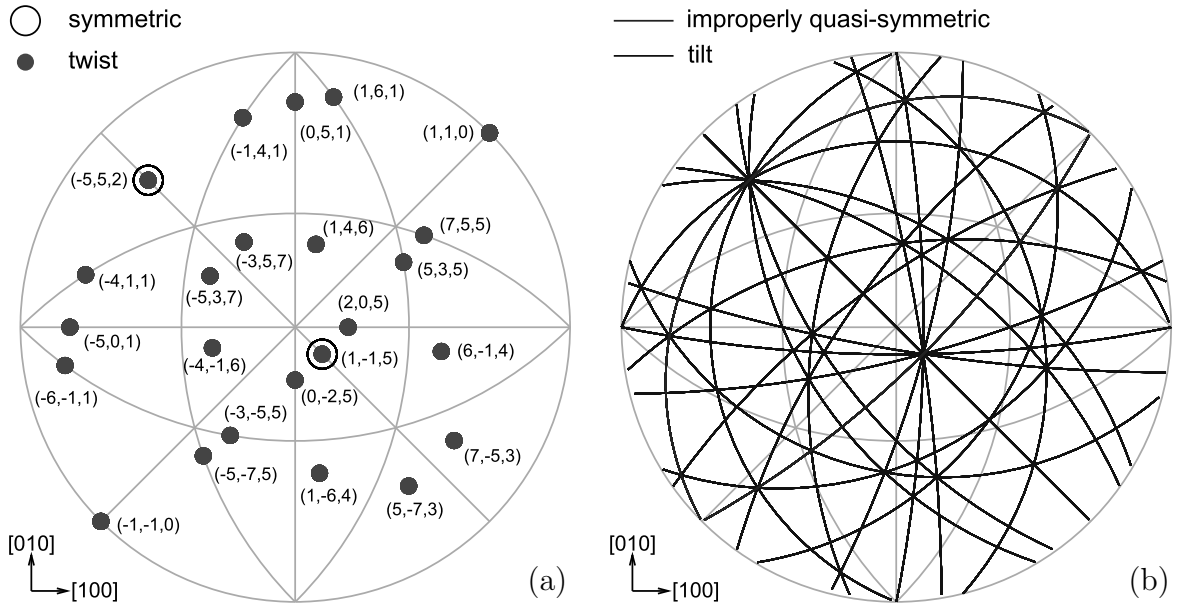


Figure 1: Maps with geometrically characteristic boundaries for the $\Sigma 27a$ misorientation. Points representing all pure-twist boundaries are shown in (a). Miller indices of the boundary planes of the first grain are given. Additionally, planes of symmetric boundaries are marked with extra circles. Lines corresponding to all pure-tilt boundaries are shown in (b). Improperly quasi-symmetric boundaries are drawn with thick lines.

The simplest and most effective algorithms for determining positions of characteristic boundaries in the maps are based on analytical expressions. With misorientations fixed, formulas for planes of such characteristic boundaries can be derived directly from their definitions. Example maps obtained using analytical solutions for the $\Sigma 27a$ misorientation[1] between crystals of cubic symmetry are shown in Fig. 1. Based on figures of this type, one can easily identify boundaries which are in a sense more "special" than other boundaries. For instance, the boundaries with multiple tilt axes must be two-dimensionally periodic. Some of them have also the twist character. For the example misorientation $\Sigma 27a$ (Fig. 1), the most particular are the boundaries with the planes $(1\bar{1}5)$ and $(\bar{5}52)$; they can be simultaneously qualified as tilt, twist, symmetric and quasi-symmetric. Such boundaries with distinctive geometries may have special structures and – consequently – special properties.

Similar maps can be obtained using the Fortes decomposition or the distance minimization method. The figures are constructed by testing all boundaries with a fixed misorientation and boundary normals forming a dense grid of directions; if a boundary

[1]Here, $\Sigma 27a$ is the 31.59° *right-hand* rotation about [110]. This convention agrees with that of [4]. The opposite handedness was used in [13].

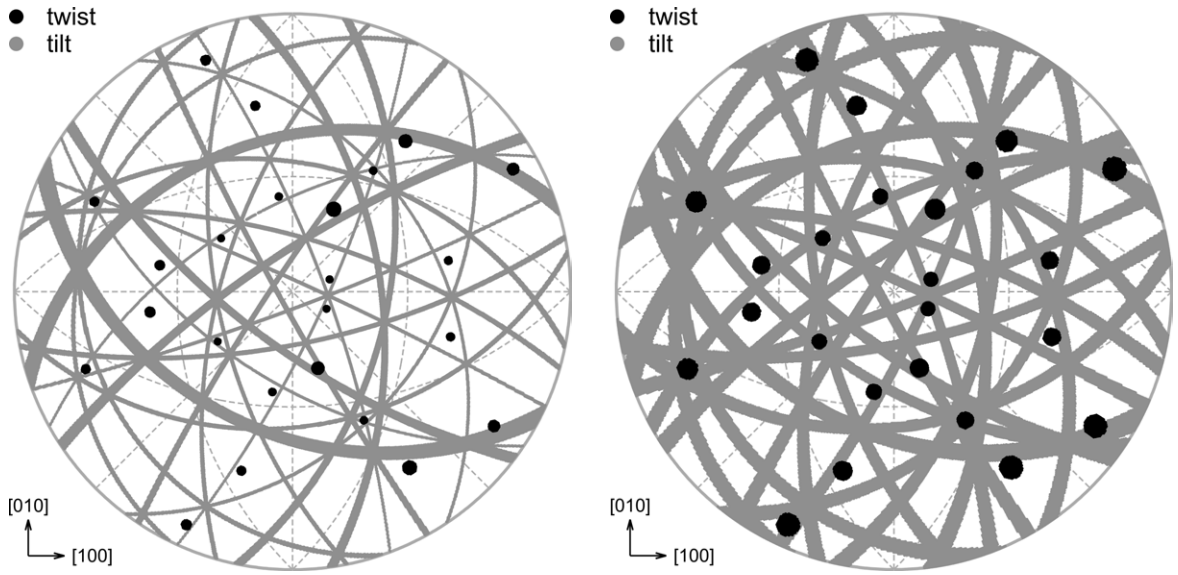


Figure 2: Stereographic projections of normals to tilt and twist boundaries for Σ39 misorientation (50.13° rotation about [123]). The diagram obtained via the Fortes decomposition is shown in (a). Boundaries with angles of tilt components below 2.5° are classified as near-twist, and those having angles of twist components below 1.5° are near-tilt boundaries. The grid of plane normals with the step 0.2° in spherical angles was used. Results obtained by the distance minimization method are shown in (b). A boundary was classified as near-twist (near-tilt) if its distance to the nearest pure-twist (pure-tilt) boundary was smaller than 2.5° (1.5°). The step of the grid was 0.33°.

turns out to be geometrically characteristic, the corresponding direction is marked on the map. These methods of getting the maps are not as effective as the method based on analytical calculations, but they allow for a direct introduction of tolerances, they characterize boundaries from different points of view, and they are useful for cross-checking various results.

It is interesting to compare directly the maps obtained by the Fortes decomposition and the distance minimization for the same levels of tolerance. Fig. 2 presents such images calculated using these two approaches for the Σ39 misorientation between crystals of cubic symmetry. One should keep in mind that the interpretation of the tolerance thresholds in these two cases is different: with the minimization method, the tolerance concerns both misorientation and boundary plane parameters, whereas with the decomposition technique, the misorientation is fixed. Therefore, the distance minimization method classifies more boundaries as tilt or twist. Consequently, the bands of near-tilt boundaries (spots of near-twist boundaries) resulting from the distance minimization method are generally wider (larger) than those generated by the Fortes decomposition. It is interesting to note that the distributions of spot diameters and band widths in the maps obtained by the two methods are different. In the case of the decomposition, the widths of bands (near-tilt boundaries) and diameters of spots (near-twist boundaries) differ significantly, whereas with the minimization method, the differences are much smaller. Smaller spread of sizes of the objects representing tilt and twist boundaries in the case of the minimization method shows that this approach is less dependent on

particular geometric configurations. All these differences diminish with the reduction of the tolerance thresholds.

## Final remarks

A software package for geometric characterization of homophase interfaces has been presented. It is useful for classification of individual boundaries into various geometric types, and it is capable of creating maps of geometrically characteristic boundaries using several methods. The package is a step towards creation of a larger framework for grain boundary characterization. There are a number of possible extensions of its capabilities. The most basic one is to incorporate other crystal symmetries. Moreover, the software is planned to be applied to large sets of experimental boundary data in order to estimate the frequencies of occurrence of geometrically characteristic grain boundaries.

## Acknowledgments

Work of K.G. was supported by the European Union under the European Social Fund within Project No. POKL.04.01.00-00-004/10.

## References

[1] Viewpoint set 41: 3D Characterization and Analysis of Materials, *Scripta Mater.* **55** (2006).

[2] C. Goux, *Can. Metall. Quart.* **13**, 9-31 (1974).

[3] G.S. Rohrer, J. Li, S. Lee, A. D. Rollett, M. Groeber, M.D. Uchic, *Mater. Sci. Technol.* **26**, 661-669 (2010).

[4] G.S. Rohrer, *JOM* **59**, 38-42 (2007).

[5] `http://dream3d.bluequartz.net`

[6] F. Bachmann, R. Hielscher, H. Schaeben, *Ultramicroscopy* **111**, 1720-1733 (2011).

[7] R.H. Moore, G.S. Rohrer, S. Saigal, *Eng. Comput.* **25**, 221-235 (2009).

[8] H. Liu, J. Liu, *J. Appl. Cryst.* **45**, 130-134 (2012).

[9] A. Morawiec, *J. Appl. Cryst.* **42**, 783-792 (2009).

[10] A. Morawiec, *Z. Kristallogr.* **227**, 199-206 (2012).

[11] M. A. Fortes, *Acta Cryst.* A **29**, 68-70 (1973).

[12] A. Morawiec, *Scripta Mater.* **61**, 438-440 (2009).

[13] A. Morawiec, *J. Appl. Cryst.* **44**, 1152-1156 (2011).

[14] J.W. Cahn, J.E. Taylor, *J. Mater. Sci.* **41**, 7669-7674 (2006).

[15] D.L. Olmsted, *Acta Mater.* **57**, 2793-2799 (2009).

1st International Conference on 3D Materials Science
*Edited by: Marc De Graef, Henning Friis Poulsen, Alexis Lewis, Jeff Simmons, George Spanos*
***TMS (The Minerals, Metals & Materials Society), 2012***

# 3D MICROSTRUCTURES OF $Sb_2Te_3$ PRECIPITATES IN PbTe MATRIX WITH PREDICTION BY A WEAK COMPATIBILITY CONDITION

Xian Chen[1], Shanshan Cao[2], Teruyuki Ikeda[3], Vijay Srivastava[1], G. Jeffrey Snyder[3], Dominique Schryvers[2], Richard D. James[1]

[1]Department of Aerospace Engineering and Mechanics, 107 Akerman Hall, University of Minnesota, Minneapolis, MN 55414, USA
[2]Electron Microscopy of Materials Science (EMAT), University of Antwerp, Antwerp, Belgium
Materials Science, California Institute of Technology, 1200 E California Blvd., Pasadena, CA 91125, USA

Keywords: Compatibility, Slice-and-view, Widmanstätten, Precipitates, Focused-ion-beam

## Abstract

We propose that a weak compatibility condition predicts the elongated directions for Widmanstätten type precipitates. The distribution of the elongated directions of precipitates lies on a family of crystallographically equivalent cones in 3D determined by a certain transformation stretch matrix obtained independently. A 3D visualization and digitization method is developed to show how the cone variants control the preferred growth directions during precipitation of $Sb_2Te_3$ in a $(5\ \mu\text{m})^3$ PbTe matrix. A series of two-dimensional secondary electron images are acquired along the direction perpendicular to the imaging plane. By pixelating all the images and calculating the position vectors on the surface of each precipitate, the elongation directions are calculated using a 3-dimensional ellipsoidal fitting for 182 precipitates. The 3D plot of the elongation directions shows that their spacial orientations are close to four predicted cones with a standard deviation of 5.6°. The length along the elongation directions reveals an asymmetric distribution with a mean value of about 240 nm. The total volume fraction of the precipitates is 8.3 %. The average area of the precipitates per volume is 0.68 $\mu m^{-1}$ by one point statistical calculation. These results build on our study presented in [1] by analyzing a significantly bigger data set and by including the length distribution and 1-point statistics.

## Introduction

In martensitic phase transformations, elastic compatibility plays an important role in the hysteresis and reversibility of the transformation [2–4]. The condition $\lambda_2 = 1$, where $\lambda_2$ is the middle eigenvalue of the transformation stretch matrix, correlates with low hysteresis and a high degree of reversibility during the transition [2, 4]. The low hysteresis and improved reversibility, in turn, has been linked to many useful properties of materials, such as an improved shape memory effect [5], improved thermal stability and fatigue properties [6] and efficient energy conversion [7, 8]. In coherent martensitic transformations, the lattice distortion can be represented by a linear transformation $\mathbf{F}$ [9]. The eigenvalues of $\mathbf{U} = \sqrt{\mathbf{F}^T\mathbf{F}}$, physically, represent the three principle stretches. The middle eigenvalue $\lambda_2 = 1$ is a necessary and sufficient condition for the existence of an undistorted plane across which the lattice of austenite perfectly fits with the lattice of martensite. According to the

geometrically nonlinear theory of martensite [10], the symmetry relations between austenite and martensite reveal all variants of $\mathbf{U}$ that contribute to predict the microstructures and interface configurations of the two phases. In other words, when the compositions of the alloys $Ti_{50}Ni_{50-x}Pd_x$ are systematically tuned to satisfy $\lambda_2 = 1$, HRTEM images show highly compatible austenite/martensite interfaces [11]. The measured interface normal vector is parallel to the calculated one given by the predicted perfect interface between austenite and one variant of martensite [11].

However, for materials that undergo diffusional phase transformations, especially those showing dislocations at the phase boundaries, the condition of elastic compatibility is not expected to govern behavior and properties of the interfaces. In our recent paper regarding the Widmanstätten microstructure of $Sb_2Te_3$ precipitates, we postulated a weak compatibility condition governing the growth of the precipitates in the matrix phase [1]. We assumed that there still exists a transformation stretch matrix that maps a unit cell of matrix phase to the corresponding unit cell of the precipitate for a semi-coherent interface, but we did not use the condition $\lambda_2 = 1$ to determine the interface. Rather, our postulate implies that precipitates grow in the unstretched directions, but that otherwise there can be discontinuities in the deformation in other directions. The unstretched directions lie on a cone where the half-cone angle depends on the eigenvalues of the transformation stretch matrix. Analogous to the martensitic phase transformation, the symmetry relations between the lattices of precipitates and matrix phase imply the existence of crystallographically equivalent cone variants. In the $(5\mu m)^3$ sample box revealed by the slice-and-view method [1, 12], the large precipitates are seen to have a ribbon-like shape with certain elongated directions as shown in Figure 1. Among these, we selected 27 precipitates for comparison. The measured elongation direc-

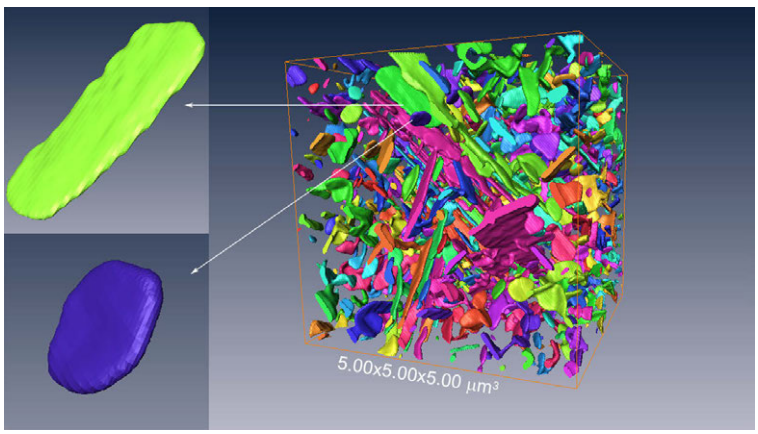


Figure 1: 3D microstructures of $Sb_2Te_3$ precipitates in a $(5\mu m)^3$ sample box [1]

tions fit very well with the theoretically predicted cones in reference [1]. From a statistical point of view, the histogram of angles between measured elongation directions and the cone axis given by the theory were fitted with a Gaussian distribution with standard deviation 2.94° and average half-angle 47.20° compared with 49.30° calculated by the theory [1]. In fact, the number of precipitates is much more than 27, and the shapes vary from ribbon-like to disk-like as they become smaller as shown in Figure 1. Therefore, a comprehensive sample collection is desirable to understand the applicability of the weak compatibility condition which is the purpose of this paper.

In this paper, the position vectors of all precipitates in Figure 1 were systematically digitalized and computed. As a result, the volume fraction and area per volume for the precipitates were precisely evaluated by one-point statistics. A histogram of the lengths of

all precipitates reveals an asymmetric distribution peaked at 240 nm. Among all collected data, we filtered out those having the longest axis less than twice of the second one, leaving 182 precipitates. These are plotted together with four crystallographically equivalent cones predicted by the theory. Since the orientation relationships between the physical basis of the sample box and the crystallographic basis of the matrix phase were only roughly determined, the alignment of the cones, but not their half-angles, were adjusted to fit the measured elongation directions consistent with symmetry. The histogram of the angles between the elongation directions and their nearest cone axes are fitted quite well by a Gaussian distribution. The average angle is 48.13° and the standard deviation is 5.6°. From the plot of normalized elongation directions in 3D, most of them tend to lie on one of the four cone variants consistent with our result in [1] for 27 precipitates. This consistency is striking because it shows how elastic fields affect the growth of precipitates during the aging process, even though there is clearly some loss of coherence. Since the cones are influenced by the transformation stretch matrix, the weak compatibility condition then gives a potential way to control the alignment of precipitates using, for example, heat treatment under stress.

## Review of The Weak Compatibility Condition

For a precipitation process with an almost coherent phase boundary, a positive definite symmetric stretch tensor $\mathbf{U}$ is used to relate the lattices of the precipitates and matrix phase. Let $\mathcal{M}(\mathbf{x}_{\mathrm{Te}}; \mathbf{e}_1^m, \mathbf{e}_2^m, \mathbf{e}_3^m) = \{\mathbf{x}_{\mathrm{Te}} + \nu_i^j \mathbf{e}_j^m : \ \nu_i^j \in \text{integers}\}$ be the tellurium sublattice of PbTe matrix phase and $\mathcal{P}(\mathbf{x}_{\mathrm{Te}}; \mathbf{e}_1^p, \mathbf{e}_2^p, \mathbf{e}_3^p) = \{\mathbf{x}_{\mathrm{Te}} + \mu_i^j \mathbf{e}_j^p : \mu_i^j \in \text{integers}\}$ be the tellurium sublattice of $Sb_2Te_3$ with the same base position $\mathbf{x}_{\mathrm{Te}} \in \mathbb{R}^3$. In principle, the transformation stretch matrix is calculated by $\mathbf{U} = \sqrt{\mathbf{F}^T\mathbf{F}}$ with the linear transformation $\mathbf{F}$ which minimizes the lattice distortion. Based on the orientation relationships that $(0001)_{\mathrm{Sb_2Te_3}} || \ \{111\}_{\mathrm{PbTe}}$ and $< 11\bar{2}0 >_{\mathrm{Sb_2Te_3}} \ || < 110 >_{\mathrm{PbTe}}$, we derive the transformation stretch matrix

$$\mathbf{U} = \frac{1}{3}\begin{bmatrix} 2\lambda_1 + \lambda_3 & \lambda_3 - \lambda_1 & \lambda_3 - \lambda_1 \\ \lambda_3 - \lambda_1 & 2\lambda_1 + \lambda_3 & \lambda_3 - \lambda_1 \\ \lambda_3 - \lambda_1 & \lambda_3 - \lambda_1 & 2\lambda_1 + \lambda_3 \end{bmatrix}, \tag{1}$$

with eigenvalues $\lambda_1 = \lambda_2 = 0.938269, \lambda_3 = 1.07786$ [1] which have been verified to result in the smallest volume change during the transition by our algorithm [13]. The necessary and sufficient condition for the existence of an unstretched direction is that the stretch tensor $\mathbf{U}$ has the smallest eigenvalue less than 1 and the largest eigenvalue greater than 1 [1]. Mathematically, this condition is $\lambda_1 \leq 1 \leq \lambda_3$ where $\lambda_1$ and $\lambda_3$ are the smallest and largest eigenvalues of $\mathbf{U}$, and the middle eigenvalue need not be 1. If $\lambda_1 \leq 1 \leq \lambda_3$ the deformation gradients differ by a rank-two matrix across the phase boundary,

$$\mathbf{RU} - \mathbf{I} = \mathbf{a}_1 \otimes \mathbf{n}_1 + \mathbf{a}_2 \otimes \mathbf{n}_2 \tag{2}$$

for some vectors $\mathbf{a}_1,\ \mathbf{n}_1,\ \mathbf{a}_2,\ \mathbf{n}_2$ and a certain rotation tensor $\mathbf{R}$. The unstretched direction is the direction perpendicular to both $\mathbf{n}_1$ and $\mathbf{n}_2$. The solution for it is not unique, but can be obtained from

$$\hat{\mathbf{e}} \cdot \mathbf{U}\hat{\mathbf{e}} = 1, \tag{3}$$

where $\hat{\mathbf{e}},\ |\hat{\mathbf{e}}| = 1$ is the unstretched direction. Geometrically, the solutions of (3) form a lateral surface of a cone, the base of which is determined by the intersection of the concentric unit sphere and an ellipsoid whose semi-principal axes of length $\frac{1}{\lambda_1},\ \frac{1}{\lambda_2},\ \frac{1}{\lambda_3}$ where $\lambda_1,\ \lambda_2,\ \lambda_3$ are ordered eigenvalues of $\mathbf{U}$. In the case of the $Sb_2Te_3$ precipitates in PbTe matrix, the solutions

of $\hat{\mathbf{e}}$ lie on a cone with a circular base because $\mathbf{U}$ has two equal eigenvalues $\lambda_1 = \lambda_2$. The half angle of the cone is calculated by (4),

$$\psi = \arccos(\pm\sqrt{\frac{1-\lambda_1^2}{\lambda_3^2-1}}) = 49.30^\circ. \tag{4}$$

The ratio of the number of elements in the symmetry group of parent phase to that of the produced phase implies crystallographically equivalent variants contributing the same strain status as $\mathbf{U}$ [2, 10]. For example, there are 24 symmetry elements in cubic PbTe matrix phase while 6 symmetry elements in hexagonal $Sb_2Te_3$, thus there exist $24/6 = 4$ cone variants with the same half cone angle $\psi$ but different cone axes $[111], [\bar{1}11], [1\bar{1}1], [11\bar{1}]$.

## Statistics Results

A $(5\mu\text{m})^3$ sample box was sliced by focused $Ga^+$ ion beam and viewed by scanning electron beam[1, 12], then a series of SE images were pixelated and reconstructed in 3D. We can identify the volume fraction as the ratio of the total number of points occupied by precipitates and that of all points in the sample box, which is 8.3%. Another characterization factor for this thermoelectric composite - Widmanstätten $Sb_2Te_3$/PbTe matrix is the area per volume in unit of $\mu m^{-1}$. We directly calculate it by the reconstructed 3D data. Compare with the area per volume from 0.5 to $1.8\mu m^{-1}$ calculated by stereological relations converted from a set of 2D SE images by [14], our direct calculation gives $0.68\mu\text{m}^{-1}$. We use position

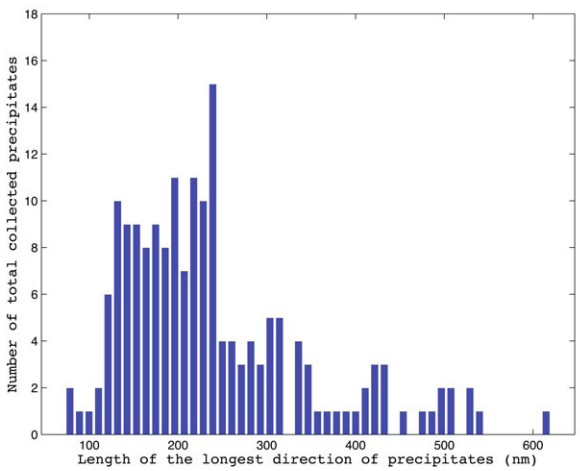


Figure 2: The distribution of the length along the elongation direction for all collected precipitates

vectors $\mathbf{x}_i^J$ to express the surface points of the $J^{\text{th}}$ precipitate in $(5\mu\text{m})^3$ sample box, where $i = 1, 2, ..., \nu^J$. $\nu^J$ is the total number of the surface points for $J^{\text{th}}$ precipitate with the average position given by $\bar{\mathbf{x}}^J = \frac{1}{\nu^J}\sum \mathbf{x}_i^J$. The ellipsoidal equation

$$(\mathbf{x} - \bar{\mathbf{x}}^J) \cdot (\mathbf{B}^J)^{-1}(\mathbf{x} - \bar{\mathbf{x}}^J) = 1, \tag{5}$$

in which, $\mathbf{B}^J$ is defined by Chen [1] is used to fit the $J^{\text{th}}$ precipitate. Thus the unit eigenvector $\mathbf{v}^J$ associated with the largest eigenvalue of $\mathbf{B}^J$ is considered to be the elongation direction. The histogram of the length along elongation directions of precipitates all over the sample

box is shown in Figure 2. The length distribution is asymmetric and concentrated at 240 nm. It is of more interest whether the distribution of the elongation directions agrees with the prediction by the weak compatibility condition after extending the statistical sampling.

Among all collected data, we rule out those whose longest axis is shorter than twice of its second longest one. Nearly 180 precipitates are used to compare with the cones that have been calculated by the method above. Figure 3(a) shows the elongation directions and their comparison with predicted cones with the half-cone angle 49.30°. As expected, more elongation directions appear lying on the lateral surfaces of other cones, however, Figure 3(a) also reveals that there exists a main cone which attracts most of the precipitates. This distribution partition might be due to the interactions between the stress fields generated by nearby precipitates. Otherwise, temperature gradients, gravity fields or residual stresses from previous water quenching are possible influences that may force the precipitates to be aligned in a certain spatial range. The histogram of angles between the elongation directions of measured precipitates and their nearest cone axes is shown in Figure 3(b). In the whole sample space, there are no precipitates found lower than 35° or greater than 70°. Without omitting any precipitates, this histogram is fitted by a Gaussian distribution. The standard deviation is 5.6° and the mean value is 48.13° while the theoretical predicted half-cone angle $\psi = 49.30°$, which shows better agreement than what we did previously for only 27 precipitates [1]. This statistical result convinces that the elastic compatibility, still, plays an important role in diffusional phase transformations, but in a weaker way.

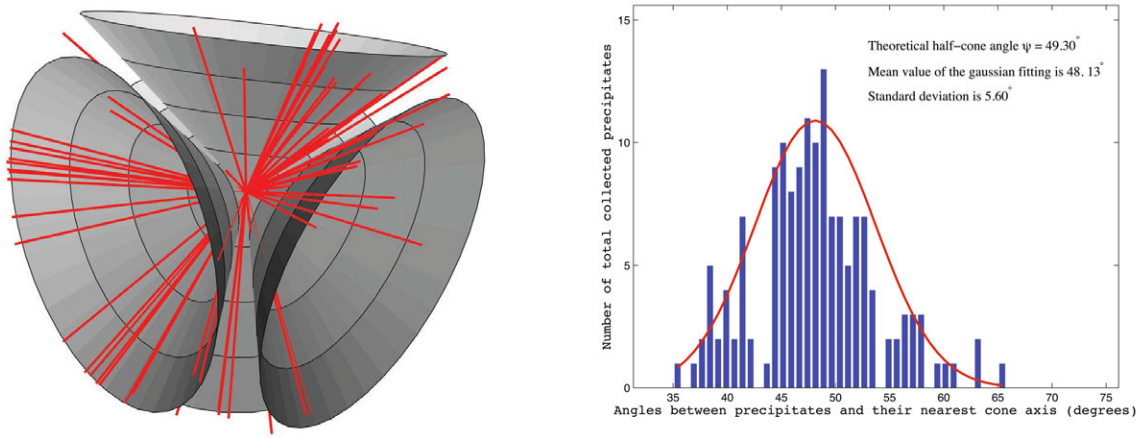


(a) (b)

Figure 3: (a) The four crystallographically equivalent cones together with elongation directions for the 182 precipitates in the sample box. (b) Histogram of angles that deviates from the half-cone angle $\psi$ for all collected precipitates.

## Conclusion

In summary, we systematically measured and calculated elongation directions, and the longest length of a large collection of $Sb_2Te_3$ precipitates spread out all over the sample box. The volume fraction of precipitates and the area per volume were precisely calculated by one point statistics. The length distribution is asymmetric and concentrated at 240 nm. The orientations of those elongated precipitates lie on the four cones predicted by the eigenvalues of the transformation strain matrix and governed by a weak compatibility condition

established in our previous paper [1]. The histogram of angles between the elongation directions and their nearest cone axis shows even better agreement with the theory. The strong orientation dependences on elastic compatibility lead us to seek a proper way to do heat treatment under stresses. The partition of elongation directions indicates the influences of external elastic fields that can be used to align the precipitates against heat flow, which is preferred for most thermoelectric materials.

## References


[1] Chen, Xian et al. "A weak compatibility condition for precipitation with application to the microstructure of PbTe-$Sb_2Te_3$ thermoelectrics." *Acta Materialia* 59 (2011), 6124–6132.

[2] Ball, J. M. and R. D. James. "Fine phase mixtures as minimizers of energy." *Archive for Rational Mechanics and Analysis* 100 (1987), 13–52.

[3] Jian, Li and Richard D. James. "Prediction of microstructure in monoclinic $LaNbO_4$ by energy minimization." *Acta Materialia* 45 (1997), 4271–4281.

[4] Zhang, Zhiyong, R.D. James, and S. Müller. "Energy barriers and hysteresis in martensitic phase transformations." *Acta Materialia* 57 (2009), 4332–4352.

[5] Cui, Jun et al. "Combinatorial search of thermoelastic shape-memory alloys with extremely small hysteresis width." *Nature materials* 5 (2006), 286–90.

[6] Zarnetta, Robert et al. "Identification of Quaternary Shape Memory Alloys with Near-Zero Thermal Hysteresis and Unprecedented Functional Stability." *Advanced Functional Materials* 20 (2010), 1917–1923.

[7] Srivastava, Vijay et al. "Hysteresis and unusual magnetic properties in the singular Heusler alloy $Ni_45Co_5Mn_40Sn_10$." *Applied Physics Letters* 97 (2010), 014101.

[8] Srivastava, Vijay et al. "The Direct Conversion of Heat to Electricity Using Multiferroic Alloys." *Advanced Energy Materials* 1 (2011), 97–104.

[9] Lieberman, D. S., T. A. Read, and M. S. Wechsler. "Graphical Analysis of Diffusionless Phase Changesthe Cubic to Twinned Orthorhombic Transformation." *Journal of Applied Physics* 28 (1957), 532.

[10] Bhattacharya, Kaushik. *microstructure of martensite*. Oxford University, 2003.

[11] Delville, Rémi et al. "Transmission electron microscopy study of phase compatibility in low hysteresis shape memory alloys." *Philosophical Magazine* 90 (2010), 177–195.

[12] Cao, S et al. "Optimization of a FIB/SEM slice-and-view study of the 3D distribution of $Ni_4Ti_3$ precipitates in Ni-Ti." *Journal of microscopy* 233 (2009), 61–8.

[13] Chen, Xian and Richard D James. A generalized algorithm to determine transformation strain matrix. In preparation, 2012.

[14] Ikeda, Teruyuki et al. "Size control of Sb2Te3 Widmanstätten precipitates in thermoelectric PbTe." *Acta Materialia* 59 (2011), 2679–2692.

1st International Conference on 3D Materials Science
*Edited by: Marc De Graef, Henning Friis Poulsen, Alexis Lewis, Jeff Simmons, George Spanos*
***TMS (The Minerals, Metals & Materials Society), 2012***

# IN SITU CHARACTERISATION OF ENTRAINMENT DEFECTS IN LIQUID Al-Si-Mg ALLOY

Y. Yue[1], W. D. Griffiths[1], J. L. Fife[2], N. R. Green[1]

[1]School of Metallurgy and Materials, University of Birmingham, Edgbaston, B15 2TT, UK
[2]Laboratory for Synchrotron Radiation, Swiss Light Source, Paul Scherrer Institut, CH-5232 Villigen, Switzerland

Keywords: Entrainment defects, X-ray tomographic microscopy, Al alloys.

## Abstract

Entrainment defects occur frequently in aluminium alloy castings during mould filling, and are very detrimental to both mechanical properties and reliability. The formation mechanisms and influences of these defects have been discussed previously, but the behaviour of the defects in the liquid metal and their evolution during solidification has not been studied in detail. In this research, samples of Al-Si-Mg alloy A356 that contained entrainment defects were scanned using ultra-fast synchrotron-based X-ray tomographic microscopy at the TOMCAT beamline of the Paul Scherrer Institut. The samples were directly viewed at both room temperature and in a fully liquid state. The reconstructed images showed three different entrainment defect morphologies, namely, entrained pores, tangled double oxide films and closed cracks. The evolution of the morphology of the entrainment defects was studied to better understand morphological changes of the defects, and the relationship between entrainment defects and microporosity.

## Introduction

Entrainment defects in light alloy castings, including double oxide films and bubble trails, have been identified as major defects and the origin of other significant defects, such as microporosity [1]. Oxide films form readily on the surface of the liquid alloy and can easily be broken up and folded into the fluid due to the surface turbulence of the liquid during the mould filling process, entrapping local atmosphere between the layers. These defects initialize cracks and may introduce heterogeneous growth sites for microporosity during solidification. Previous studies of the influence of entrainment defects on the mechanical properties of castings have demonstrated that the higher contents of entrainment defects in the castings resulted in both lower mechanical properties and lower reliability [2~4].

Raiszadeh and Griffiths carried out an experiment to mimic the behaviour of a double oxide film defect by deliberately trapping an air bubble in liquid Al and monitoring the volume change of the bubble by real-time X-ray imaging. The results showed that the trapped air reacted with the surrounding liquid metal, reducing the volume of the bubble [5]. It was also shown that double oxide films could be initiators of hydrogen porosity [6]. However, the morphology of these entrainment defects in three dimensions and their morphological behaviour in the liquid state and during solidification require further study. In this research, synchrotron X-ray tomographic microscopy was employed to study the morphological evolution and behaviour of entrainment defects in aluminium alloy both in the liquid state and during solidification in real time, to try to obtain some insight into the behaviour of entrainment defects during casting.

## Experimental Procedure

Sample preparation

Castings were made in resin-bonded silica sand moulds using Al-7Si-0.4Mg alloy (A356). A specially designed running system was used to generate a high level of surface turbulence in the liquid metal during filling the mould; this also contained a 20 ppi ceramic filter to remove inclusions and oxides formed during alloy preparation. The alloy was heated to 730 °C and cast at 710 ± 5 °C. The filling process was recorded by real-time X-ray radiography and the video footage confirmed that surface turbulence and entrainment had occurred in the running system.

Test bars were then cut off from the running system and examined using film X-ray radiography to locate the entrainment defects. Cylindrical samples containing the defects were then cut from the test bars by electrical discharge machining (EDM) and ground to the dimensions of 3 mm diameter and 6 mm height. The samples were viewed by a desktop-based X-ray micro-tomography machine to establish the approximately size and position of defects in the samples.

Synchrotron-based X-ray tomographic microscopy and image processing

Synchrotron-based X-ray tomographic microscopy observations of the entrainment defects were conducted at the TOMCAT (TOmographic Microscopy and Coherent rAdiology experimenT), beamline of the Swiss Light Source (SLS) at the Paul Scherrer Institut (Villigen, Switzerland). The sample was placed in the centre of a pyrex glass tube (3 mm inner diameter, 6 mm outer diameter) and scanned using the ultra-fast end station [7], which incorporates a PCO.Dimax camera that acquires and reads-out data orders of magnitude faster than traditional CCD technology. Couple this with the use of polychromatic radiation, and a full 3D data set can be acquired in a fraction of a second. The adjustable magnification microscope, specifically designed for high numerical aperture and polychromatic radiation, provided a 3.15 μm pixel size. Controlled heating and cooling of the sample was obtained by a general-use laser-based heating system [8]. Each sample was scanned initially at room temperature, then heated up to 727 °C (1000 K) and scanned in the fully liquid state, and subsequently 6-8 additional times in a 200 s interval. Finally, the sample was scanned during solidification and at room temperature after the sample had solidified. The 0.9 s scanning time of each scan offered opportunities to observe the evolution of the entrainment defects in real time. The image analysis and segmentation of the tomograms collected at TOMCAT were completed in Fiji and ITK-SNAP respectively [9, 10]. The volume of the defect was measured based on the quantity of voxels it occupied in the segmented images.

## Results and Discussion

Classification of entrainment defects

Generally the entrainment defects observed in the solidified samples can be classified into three types, according to their morphology. They were *a).* entrained pores, *b).* closed cracks and *c).* tangled double oxide films, as illustrated in Figure 1. The entrained pores found in the experiment were usually larger than the other two types in both size and volume, with a diameter in the range of 0.1 to 1 mm. They had nearly spherical shapes, trapping a pocket of gas inside the void. The closed cracks were much more angular voids, appearing as long and narrow shapes in some sections. The tangled double oxide films had very complex geometries in three dimensions, and sometimes would be seen as discontinuous pores or cracks in polished sections in the castings. All three types of entrainment defects existed as voids and may contain differing

amounts of gases depending on their morphology. Such voids might easily be opened up under external forces, contributing to low mechanical properties of castings. However, it should be noted that the morphology of each entrainment defect would be dependent on two factors. It may be due to the formation mechanism, e.g., a captured bubble, or a convoluted double oxide film may have been entrained in this form, or it may be due to the subsequent development of the defect, e.g., a captured bubble may collapse to become a closed crack.

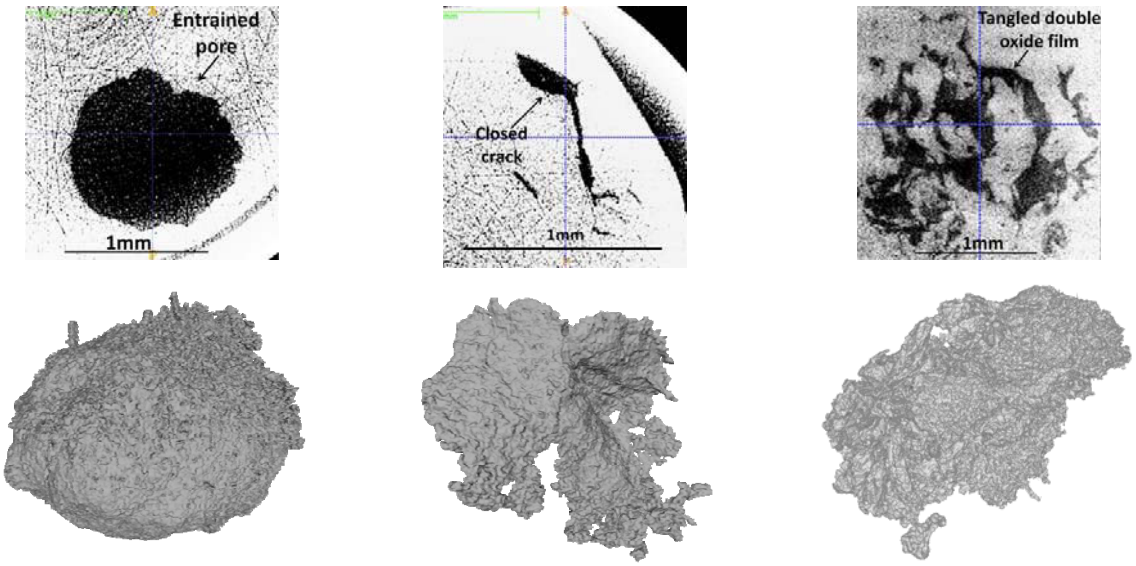


(a) (b) (c)

Figure 1. Three types of entrainment defects, *a)*. an entrained pore, *b)*. a closed crack and *c)*. a tangled double oxide film. (Top: axial view; Bottom: 3D view).

The evolution of the morphology of entrainment defects

The morphological evolution of entrainment defects may be driven by a combination of two factors: the reaction between any interior gases with the surrounding liquid metal, and hydrogen diffusion into the defects, as suggested by Raiszadeh and Griffiths [5]. In general, when the samples were melted, the defects contracted, changing in both shape and volume. Observation then showed that the morphology of the entrainment defects changed little with time in the liquid state. During subsequent solidification the defects expanded slightly, probably due to solidification contraction. The volume and shape of the defects did not return to their initial state when the samples solidified. Figures 2 to 4 show the morphological evolution of the three typical entrainment defects. During melting and holding, their volumes reduced to approximately 20%, 90% and 60% of their initial volumes, respectively. Figures 2(a) and (b) show that the entrained pore collapsed and became an irregular shape, illustrating that the large pore, which contained most gas, experienced the greatest change in both volume and shape. Figures 3 and 4 show how defects that had complex geometries and less trapped gas maintained their general shape in the liquid state and after solidification.

The unfurling of entrainment defects proposed by Campbell [1], i.e., the reopening of a convoluted double oxide film in the liquid, was not observed in this experiment. Possible reasons for this could be: *a)*. the unfurling of entrainment defects requires longer holding times, *b)*. the strength of oxide films hinders shape changes of the defects, and *c)*. the viscosity of the liquid metal obstructs the movement or deformation of the defects.

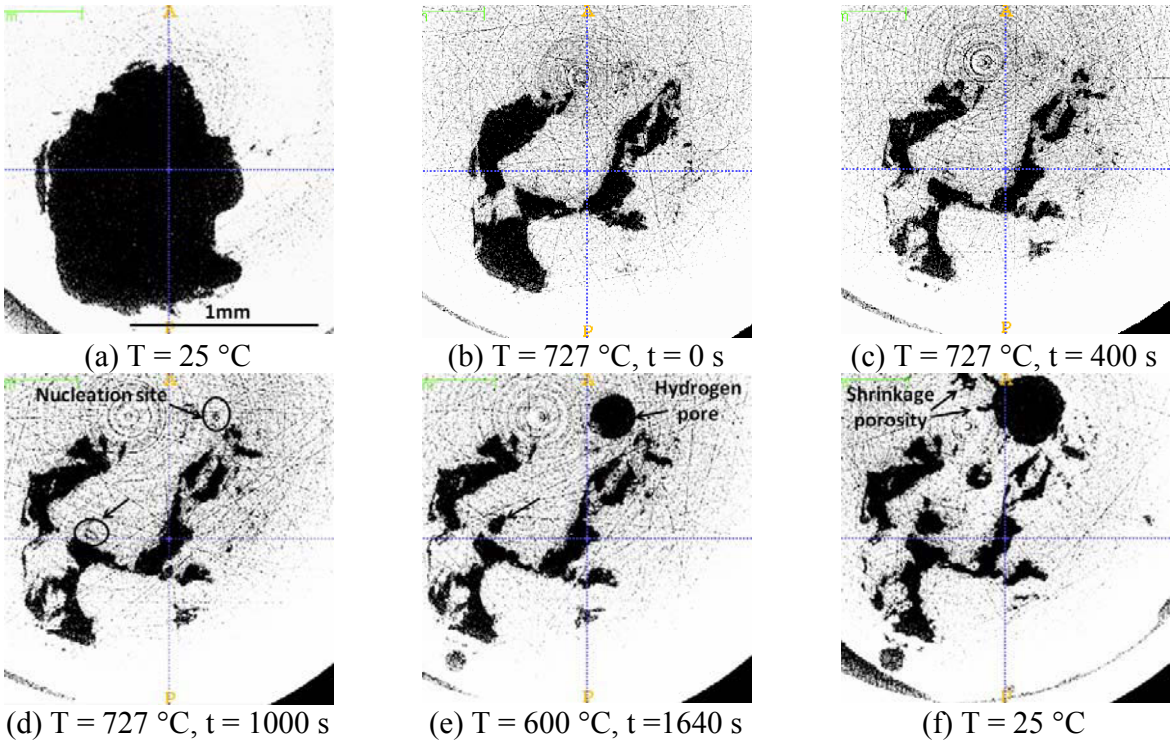


(a) T = 25 °C (b) T = 727 °C, t = 0 s (c) T = 727 °C, t = 400 s

(d) T = 727 °C, t = 1000 s (e) T = 600 °C, t =1640 s (f) T = 25 °C

Figure 2. Morphological evolution of an entrained pore. The time, t, was measured from the time the sample temperature reached 727 °C.

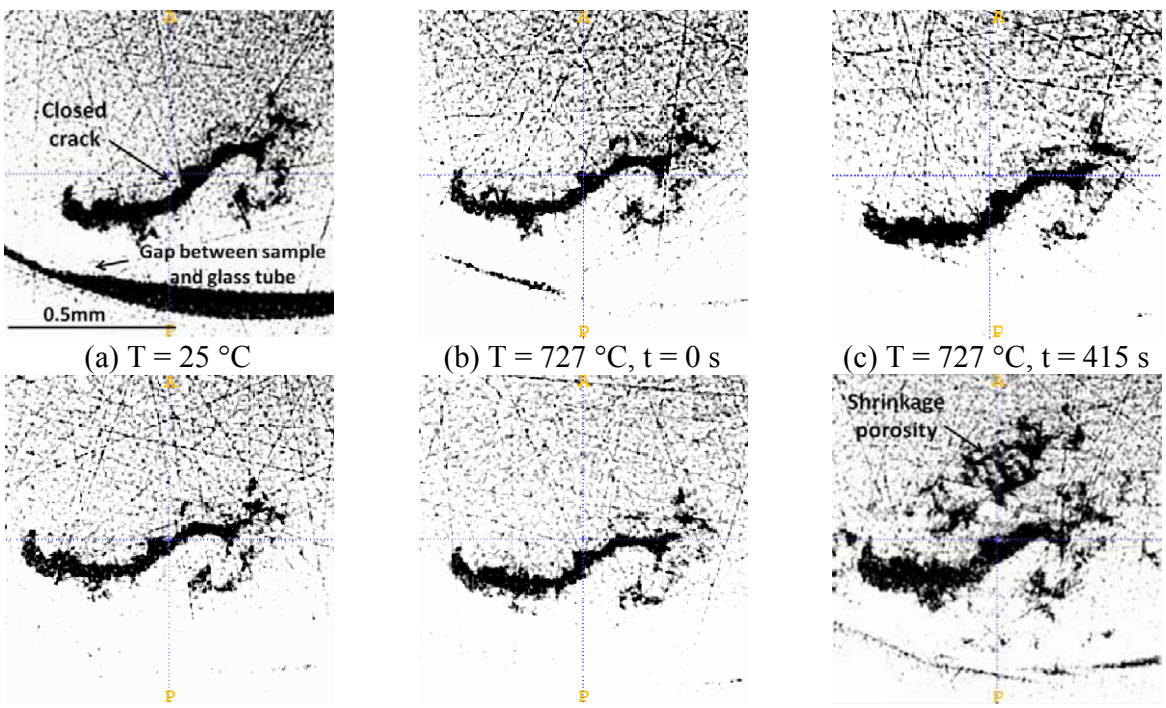


(a) T = 25 °C (b) T = 727 °C, t = 0 s (c) T = 727 °C, t = 415 s

(d) T = 727 °C, t = 1015 s (e) T = 500 °C, t = 1415 s (f) T = 25 °C

Figure 3. Morphological evolution of a closed crack. The time, t, was measured from the time the sample temperature reached 727 °C.

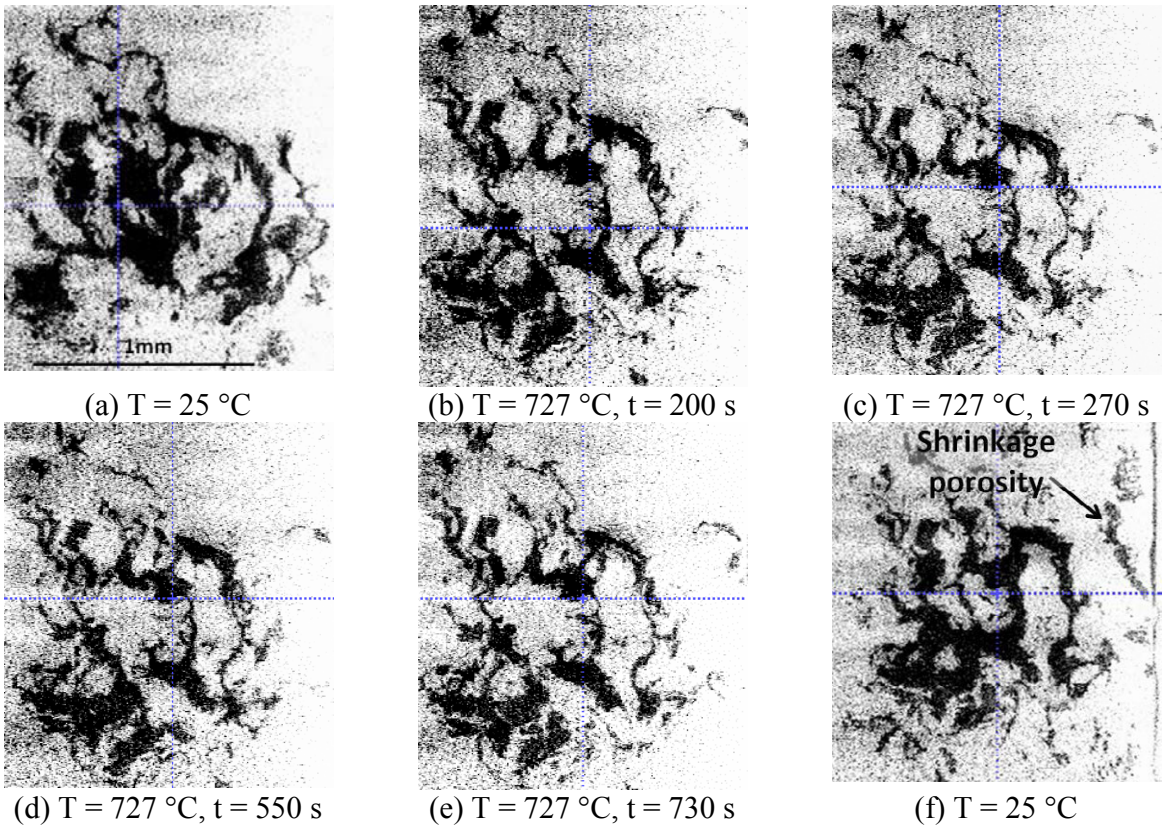


(a) T = 25 °C (b) T = 727 °C, t = 200 s (c) T = 727 °C, t = 270 s

(d) T = 727 °C, t = 550 s (e) T = 727 °C, t = 730 s (f) T = 25 °C

Figure 4. Morphological evolution of a tangled double oxide films. The time, t, was measured from the time the sample temperature reached 727 °C.

The behaviour of entrainment defects in liquid metal

The experiments showed that entrainment defects, regardless of their size, geometry and their volume of entrained gas, could maintain their position in a tranquil liquid metal. This may imply that entrainment defects generally have a similar density to that of the liquid metal around them. Morphological changes of the defects from simple pores to tangled networks might result in greater drag forces on the defects with complex geometries, reducing their mobility further. This suggests that the movement of entrainment defects in the liquid metal relies on the external momentum. Therefore, the distribution of entrainment defects is determined by the turbulent flow of the liquid metal, rather than their buoyancy. Since the oxide film entrainment defects are expected to be brittle, turbulent flow during processing may break up the defects and affect their behaviour further.

The relationship between entrainment defects and microporosity

As mentioned previous, the entrainment defects maintained their general morphology during solidification, but that morphology was affected by microporosity and solidification shrinkage, to some extent. Figure 2(d ~ f) shows that a spherical hydrogen pore nucleated near the entrainment defect and that shrinkage porosity originated near and on these voids (double oxide films and hydrogen pores). This shows that the entrainment defects could provide heterogeneous sites for shrinkage porosity growth, possibly because the presence of the voids retarded heat transfer and changed the local solidification rate, as suggested by Lee and Gokhale [11]. However, the

relationship between the entrainment defects and hydrogen porosity is still not clear. As shown in Figure 2(e), hydrogen porosity did not originate within the large entrainment defect, as has been suggested should be the case [1]. Instead, this occurred in an area where very small defects were present which were difficult to see clearly in the images (circled in Figure 2(d)). Compared with the large defect, these small defects might be oxide films formed in the later stage of mould filling, which had less chance to react with their internal atmosphere, and hence, might be thinner and weaker, and might have already ruptured. Since the oxide layer formed on the surface of large defects could provide a barrier preventing hydrogen from penetrating into the void, as suggested by Griffiths and Raiszadeh [6], these small defects might be the preferred sites for nucleation and growth of hydrogen porosity.

## Conclusions

The evolution of entrainment defects in liquid state was observed directly by synchrotron-based X-ray tomographic microscopy. This characterisation showed variation in the morphology of entrainment defects and their subsequent volume and shape changes in a liquid Al alloy. The results suggested that entrainment defects could maintain their position in a tranquil liquid flow and could be growth sites for shrinkage porosity. But the relationship with entrainment defects and hydrogen porosity requires further research.

## Acknowledgements

One of the authors (YY) acknowledges the financial support of the School of Metallurgy and Materials, University of Birmingham for his PhD.

## References

[1] J. Campbell, “Entrainment defects,” *Materials Science and Technology*, vol. 22, no. 2, pp. 127-145, 2006.

[2] N. R. Green and J. Campbell, “Statistical distributions of fracture strengths of cast Al-7Si-Mg alloy,” *Materials Science and Engineering: A*, vol. 173, pp. 261-266, 1993.

[3] C. Nyahumwa, N. R. Green, and J. Campbell, “Effect of mold-filling turbulence on fatigue properties of cast aluminum alloys,” *AFS Transactions*, no. 106, pp. 215-224, 1998.

[4] J. Mi, R. . Harding, and J. Campbell, “Effects of the entrained surface film on the reliability of castings,” *Metallurgical and Materials Transactions A*, vol. 35, no. 9, pp. 2893-2902, Sep. 2004.

[5] R. Raiszadeh and W. D. Griffiths, “A method to study the history of a double oxide film defect in liquid aluminum alloys,” *Metallurgical and Materials Transactions B*, vol. 37, no. 6, pp. 865-871, Dec. 2006.

[6] W. D. Griffiths and R. Raiszadeh, “Hydrogen , porosity and oxide film defects in liquid Al,” *Journal of Materials Science*, vol. 44, no. November, pp. 3402-3407, 2009.

[7] R. Mokso et al., “Real Time Tomography at the Swiss Light Source,” in *AIP Conference Proceedings*, vol. 87, no. 1, pp. 87-90, 2010.

[8] J. L. Fife, M. Rappaz, M. Pistone, T. Celcer, G. Mikuljan, and M. Stampanoni, “Development of a laser-based heating system for in-situ synchrotron-based X-ray tomograpic microscopy.,” *Journal of Synchrotron Radiation*, 2012, in press.

[9] J. Schindelin, “Fiji is just ImageJ-Batteries included,” in *ImageJ User and Developer Conference*, 2008.

[10] P. A. Yushkevich et al., “User-guided 3D active contour segmentation of anatomical structures: significantly improved efficiency and reliability.,” *NeuroImage*, vol. 31, no. 3, pp. 1116-28, Jul. 2006.

[11] S. G. Lee and A. M. Gokhale, “Formation of gas induced shrinkage porosity in Mg-alloy high-pressure die-castings,” *Scripta Materialia*, vol. 55, no. 4, pp. 387-390, Aug. 2006.

1st International Conference on 3D Materials Science
*Edited by: Marc De Graef, Henning Friis Poulsen, Alexis Lewis, Jeff Simmons, George Spanos*
***TMS (The Minerals, Metals & Materials Society), 2012***

# SHAPE ANALYSIS AND THE CLASSIFICATION OF OBJECTS

F. Brent Neal[1], John C. Russ[2]

[1]Milliken & Company, Research Division
920 Milliken Rd., M-405, Spartanburg, SC 29303
[2]Dept. of Materials Science and Engineering, North Carolina State University
911 Partner's Way, EB I, Room 3002, Raleigh, NC 27695

Keywords: shape classification, shape descriptors, invariant moments, harmonic analysis, machine vision

## Abstract

Quantification of shape remains an area of active study in the field of image analysis and machine vision. We present a comparative survey of three approaches to shape measurement: classical dimensionless ratios, harmonic analysis, and invariant moments, showing their suitability for classification of objects and other statistical analyses, including quantitative structure-property relationships. We show that for topologically simple shapes and well controlled imaging conditions, all three methods can provide robust classification of objects.

## Introduction

There is a growing demand for measures and methods that allow objects to be automatically classified. From medical imaging to manufacturing, many processes of immense economic value rely on the ability of man or machine to quickly, precisely, and accurately distinguish one class of objects from another. Shape descriptors are also important for correlation with processing or performance. Consequently finding a few numbers that robustly describe the shape of objects is an important goal for computer vision. [1] While software that can match numbers or apply statistical tests to find similarities between numerical descriptors is efficient and widely used, selecting the best set of descriptors to resolve differences between the objects measured and at the same time provide some relationship to the cues that human vision uses to distinguish shape remains a complex task.

Desirable attributes for a shape descriptor include being robust (stable to minor variations), insensitivity to rotation, translation, and scaling, and to image resolution within reasonable limits, as well as enabling classification of partially occluded objects. Other traits that are often desired are compactness (i.e., a small set of numbers), suitability for statistical analysis, and completeness (i.e., containing enough information to reconstruct the original shape.) Obviously, these criteria cannot all be met simultaneously.

In this paper we compare three shape measurement techniques in conjunction with linear discriminant analysis (LDA) and neural networks to show that each technique can yield robust classification of real-world objects. The descriptors that we will compare are classical shape descriptors (dimensionless ratios as defined below in Equation 1), invariant moments [2–5], and harmonic analysis [6–9].

It is important to note many measurements of shape are not normally distributed, particularly dimensionless ratios. Classifiers based on non-normal data may be less accurate unless the non-

normality is taken into account. This can be accomplished by using rank statistics and nonparametric statistics [10]. It is also understood that careful selection of measurements is required in order to achieve satisfactory results. This selection cannot be made without some knowledge of the objects to be classified.

Although this paper primarily focuses on 2D datasets, there are 3D analogues of all the measurement types compared here. Harmonic analysis of 3D data is often accomplished by means of expansion in terms of spherical harmonics, which form a complete basis set for describing an object's shape [11]. The calculation of a 3D moment is a straightforward extension of Equation 2 below and invariants have been determined for this case [12]. Dimensionless ratios can be easily constructed in analogy to those defined in Equation 1 below, but are used less frequently than their 2D counterparts. One potential reason for this is the anisotropic resolution of many 3D imaging techniques. This makes the computation of surface area and length more complex and directionally biased. For this reason and a relative lack of available general-purpose 3D measurement software the primary use of 3D imaging outside of academia is visualization [12,13].

## Description of Objects and Methods

Several data sets were used to compare the various shape measurements. These test samples were chosen as proxies for classes of imaging problems of interest to researchers in diverse fields. The first data set consists of 654 animal crackers (Trader Joe's). These crackers are produced using a rotary die process and production variables or shipping damage can create small defects and variations in the outline of the object. These objects were imaged by first sorting manually, relying on syntactical characteristics, into 13 categories, while rejecting broken and structurally incomplete objects. All objects of each class were scanned on a flatbed scanner at 600 ppi and the resulting images thresholded. This data set serves as a proxy for a wide range of manufactured goods and classification problems where there is limited control of variability in the object.

The second data set consists of 146 images of tree leaves from 9 different species of trees native to North Carolina. The leaf images were acquired by scanning on a flatbed scanner at 600 ppi. The leaves were selected to be complete objects; thus, no partial or damaged objects were included in the set. This data set is a proxy for a wide variety of problems in measuring objects with complex shapes with detail at multiple scales.

Another data set consists of 28 images of single snowflakes (images courtesy of Dr. Kenneth Libbrecht, California Institute of Technology). The acquisition of these images is covered in Ref. [15]. This data set is a proxy for a wide variety of problems in measuring structure-property relationships in materials where the crystallization of a material drives final properties, such as the structure of graphite in cast irons. In these cases, the morphology may not be precisely Boolean, but rather a continuous variation between classes (e.g. dendritic and plate-like). This structure is not known a priori for each flake, and the task is to perform a cluster analysis by unsupervised training, typically to correlate with a set of performance data in a quantitative structure-property relationship (QSPR). While each of the objects is unique, there exist many structural parameters by which the data set can be quantitatively subdivided.

Lastly, we have used a data set consisting of 38 images of Native American arrow points (images courtesy of Dr. Billy Oliver, North Carolina Office of State Archaeology Research Center.)

These high-resolution images were thresholded and measured. Only substantially intact points were used, representing five recognized styles of point. These objects are proxies for objects that are substantially similar on a gross scale, but exhibit large variations due to non-uniform processes such as hand-tooling, weathering, or aging.

Statistical analysis, including neural network training and application, was completed using JMP® 9 (SAS Institute, Cary, NC). Custom code was written implementing methods for calculating invariant moments and the Fourier shape descriptors for the given objects. Dimensionless ratios were measured using Fovea Pro® (Reindeer Graphics, Asheville, NC).

Definitions of Measured Parameters

For clarity, the dimensionless ratios used here are defined below:

$$Formfactor = 4\pi \frac{Area}{Perimeter^2} \qquad Extent2 = \frac{Area}{Area\ of\ Circumscribed\ Circle} \quad (1)$$

$$Roundness = \frac{4 \cdot Area}{\pi \cdot (Maximum\ Dimension)^2} \qquad Solidity = \frac{Area}{Convex\ Hull\ Area}$$

$$Aspect\ Ratio = \frac{Maximum\ Dimension}{Minimum\ Dimension} \qquad Convexity = \frac{Perimeter}{Convex\ Hull\ Perimeter}$$

$$Curl = \frac{Maximum\ Dimension}{Fiber\ Length} \qquad Eccentricity = \frac{\sqrt{a^2 - b^2}}{a}$$

$$Elongation = \frac{Fiber\ Length}{Fiber\ Width} \qquad Area\ Fraction = \frac{Net\ Area}{Filled\ Area}$$

$$Extent1 = \frac{Area}{Bounding\ Box\ Area} \qquad Radius\ Ratio = \frac{Inscribed\ Radius}{Circumscribed\ Radius}$$

In the relationships in Equation 1, maximum and minimum dimension by convention refer to the maximum and minimum caliper dimension of an object. Fiber length is the length of the skeleton of an object, corrected to account for the fact that the skeleton does not quite reach the ends of a feature. Fiber width is computed from the Euclidean distance map of the object and is the average of the dimension perpendicular to the fiber axis. In the relationship for eccentricity, the *a* and *b* parameters refer to semi-major and semi-minor axes respectively, and are measured as the maximum caliper dimension and the dimension perpendicular to the maximum caliper dimension. Area fraction as defined here is the ratio between the object's area and its area including internal gaps and voids.

The moments of a feature composed of pixels are calculated as

$$\mu_{ij} = \sum_{x,y} x^i y^j \cdot v \quad (2)$$

where $v$ is the measured pixel value at location $(x,y)$, if the pixel values have meaning. Usually, the moments are normalized by calculating

$$\eta_{ij} = \frac{\mu_{ij}}{\mu_{00}^{\left(\frac{i+j+2}{2}\right)}} \tag{3}$$

After Equation 3, we can express seven invariant moments as derived by Hu [3].

$$m_1 = \eta_{20} + \eta_{02} \tag{4}$$

$$m_2 = (\eta_{20} - \eta_{02})^2 + 4\eta_{11}^2$$

$$m_3 = (\eta_{30} - \eta_{12})^2 + (3\eta_{21} - \eta_{03})^2$$

$$m_4 = (\eta_{30} + \eta_{12})^2 + (\eta_{21} + \eta_{03})^2$$

$$m_5 = (\eta_{30} - 3\eta_{12})(\eta_{30} + \eta_{12})[(\eta_{30} + \eta_{12})^2 - 3(\eta_{21} + \eta_{03})^2] + (3\eta_{21} - \eta_{03})(\eta_{21} + \eta_{03})[3(\eta_{30} + \eta_{12})^2 - (\eta_{21} + \eta_{03})^2]$$

$$m_6 = (\eta_{20} - \eta_{02})[(\eta_{30} + \eta_{12})^2 - (\eta_{21} + \eta_{03})^2] + 4\eta_{11}(\eta_{30} + \eta_{12})(\eta_{21} + \eta_{03})$$

$$m_7 = (3\eta_{21} - \eta_{03})(\eta_{30} + \eta_{12})[(\eta_{30} + \eta_{12})^2 - 3(\eta_{21} + \eta_{03})^2] - (\eta_{30} - 3\eta_{12})(\eta_{21} + \eta_{03})[3(\eta_{30} + \eta_{12})^2 - (\eta_{21} + \eta_{03})^2]$$

More recent work by Flusser[5] has shown that Hu's original moments are not independent and incomplete. Due to their relative ubiquity, the earlier set of invariant moments was used in this analysis. The use of Flusser's independent invariants in some cases may result in better classification of objects. Harmonic analysis is performed by elliptic Fourier descriptors[16], taking the boundary points (*x*,*y*) of the object and expressing them as a complex number $x^* = x + iy$ suitable for Fourier analysis.

$$F(x^*) = \sum_k c_k \sin(2\pi k x^* - \delta_k) \tag{5}$$

where the amplitudes $c_k$ are used as shape descriptors in the analysis.

## Results and Discussion

Full Comparison: Measurement Type and Analysis Methods

The cookie data set was measured using dimensionless ratios, invariant moments, and harmonic analysis. The measurements were then analyzed by both linear discriminant analysis and a neural network. The neural network used consisted of a single layer, with each input representing one individual measurement and one node per input. The neural network was trained on two thirds of cookies and validated with the remaining one third. The analysis using dimensionless ratios was performed with all twelve ratios and with a selected subset of four ratios (formfactor, roundness, solidity, and convexity). The harmonic analysis used terms $k$ = 2-7. All seven invariant moments $m_1$-$m_7$ were analyzed. Table I shows the relative error rates of each measurement and analysis method.

The data indicate that without resort to more complex neural network architectures, there is no clear advantage to one method of analysis over the other. Further, it is possible to get to a reasonably high level of accuracy using all three measurement types. While the four ratios that were selected were insufficient, the full set of twelve ratios provided roughly equivalent accuracy to the harmonic coefficients when analyzed by linear discriminants. The highest accuracy was achieved by neural network analysis of the harmonic coefficients. Linear discriminant analysis of invariant moments provided lower accuracy.

**Table I: Summary of results for classification of cookies**

| Measurements | Analysis Method | Misclassified (N=654) |
|---|---|---|
| Four dimensionless ratios | Linear discriminant | 16 (2.4%) |
| | Neural network | 18 (2.8%) |
| Twelve dimensionless ratios | Linear discriminant | 5 (0.8%) |
| | Neural network | 9 (1.4%) |
| Harmonic coefficients 2-7 | Linear discriminant | 6 (0.8%) |
| | Neural network | 2 (0.3%) |
| Invariant moments | Linear discriminant | 13 (2.0%) |
| | Neural network | 8 (1.2%) |

The leaf data set was measured using each of the three measurement types and analyzed with linear discriminants and a neural network constructed similarly to the one used in the previous example. In this analysis, three dimensionless ratios (formfactor, solidity, and radius ratio), a set of harmonic coefficients, and all seven invariant moments (Equation 4) were used. The ratios used with linear discriminant analysis were selected based on significance analysis of the larger full set of ratios; similarly, the choice of Fourier coefficients was made by significance analysis. For the neural network analysis of the harmonic coefficients, the subset determined to be statistically significant performed poorly (11 misclassifications). Using a larger set of coefficients yielded results comparable to LDA. Table II contains a summary of the results of this analysis.

**Table II: Summary of results for classification of leaves**

| Measurements | Analysis Method | Misclassified (N=146) |
|---|---|---|
| Three dimensionless ratios | Linear discriminant | 3 (2.1%) |
| | Neural network | 1 (0.7%) |
| Harmonic coefficients (2,4,5,7,10,14) | Linear discriminant | 2 (1.4%) |
| Harmonic coefficients (2-14) | Neural network | 3 (2.1%) |
| Invariant moments | Linear discriminant | 3 (2.1%) |
| | Neural network | 3 (2.1%) |

In the case of the leaves, each measurement type performs reasonably well considering the smaller population size. Table III contains the actual vs. predicted classifications for invariant moments. While the results are similar, the misclassifications provide some insight. Moments have the greatest difficulty distinguishing compact shapes (e.g., cherry vs. dogwood), while harmonic analysis problems arise for smooth bordered leaves (e.g. hickory vs. dogwood). Some of the ratios are more sensitive to one or the other difference (e.g. formfactor for border smoothness, radius ratio for compactness. In the cookie data set, all of the shapes were relatively compact due to the limitations of the production process. It is thus reasonable to expect invariant moments to perform less well for the cookies.

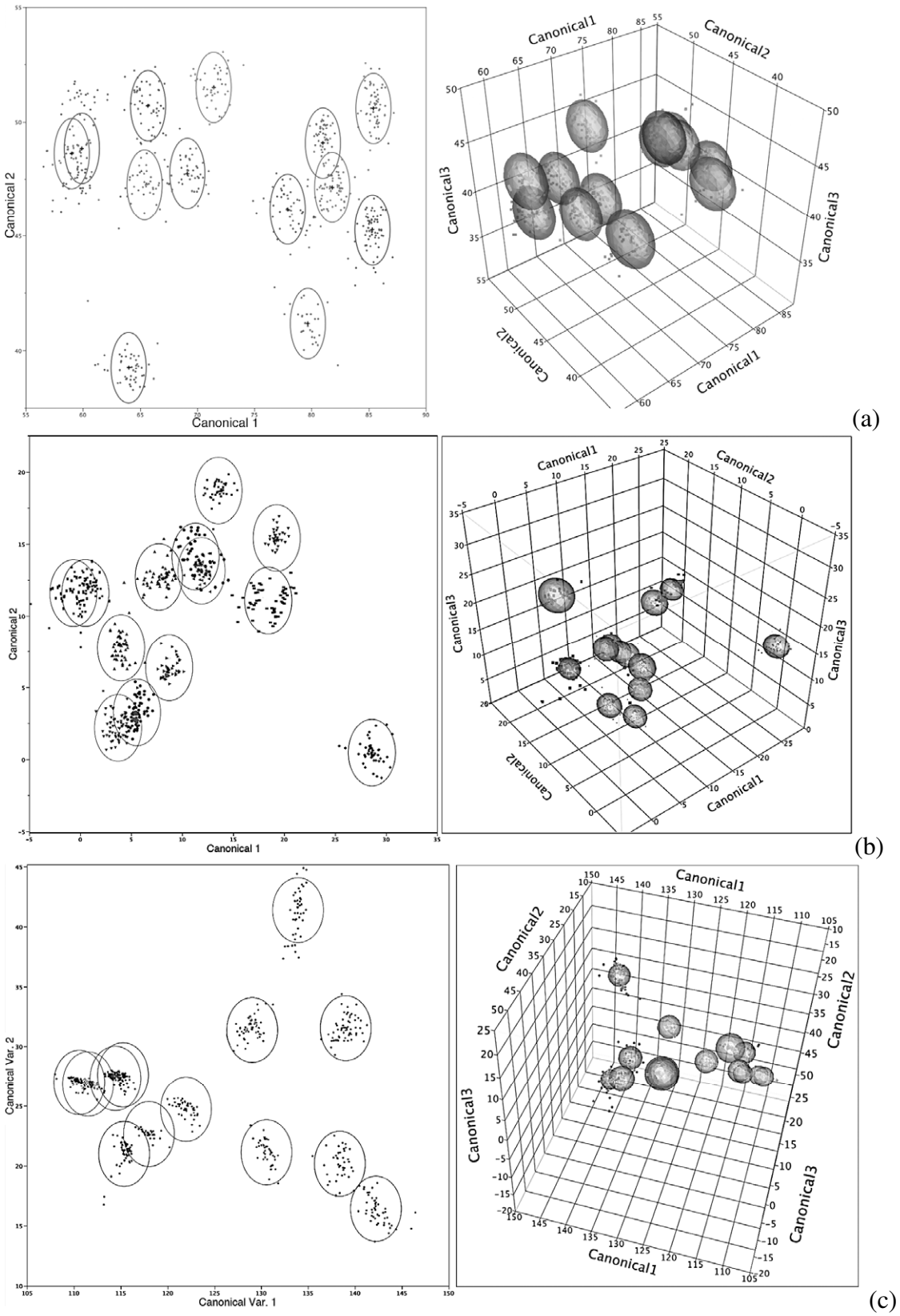


Figure 1: 2D & 3D plots of most significant canonical axes from LDA results for the cookie data set: (a) dimensionless ratios, (b) harmonic coefficients, (c) invariant moments

**Table III: Actual (rows) vs. predicted (columns) classification for leaves using invariant moments.**

| | cherry | dogwood | hickory | mulberry | red maple | red oak | silver maple | Sweetgum | white oak |
|---|---|---|---|---|---|---|---|---|---|
| cherry | 16 | 1 | 0 | 1 | 0 | 0 | 0 | 0 | 0 |
| dogwood | 0 | 14 | 0 | 0 | 0 | 0 | 0 | 0 | 0 |
| hickory | 0 | 0 | 16 | 0 | 0 | 0 | 0 | 0 | 0 |
| mulberry | 0 | 1 | 0 | 16 | 0 | 0 | 0 | 0 | 0 |
| redmaple | 0 | 0 | 0 | 0 | 19 | 0 | 0 | 0 | 0 |
| redoak | 0 | 0 | 0 | 0 | 0 | 12 | 0 | 0 | 0 |
| silvermaple | 0 | 0 | 0 | 0 | 0 | 0 | 18 | 0 | 0 |
| sweetgum | 0 | 0 | 0 | 0 | 0 | 0 | 0 | 16 | 0 |
| whiteoak | 0 | 0 | 0 | 0 | 0 | 0 | 0 | 0 | 16 |

The arrow points (shown in Figure 2) were also well-classified by the three measurement types. Of note is the compactness of the harmonic coefficients relative to the dimensionless ratios, requiring just 3 terms. While the dimensionless ratios used (formfactor, roundness, aspect ratio, solidity, convexity, radius ratio, and elongation) resulted in no misclassifications on this relatively small data set, the ratios do not separate the classes as well as the harmonic coefficients, indicating the high probability of misclassification on a larger data set. As in the leaf data set, the reduced set of harmonic coefficients resulted in a poor neural net classifier, but the addition of a larger number of terms gave satisfactory results. The inclusion of more harmonic coefficients reduced the scatter in the LDA analysis as well. Figure 2 shows the two most significant canonical axes from the LDA of the arrow points, with 95% confidence ellipses shown. Table IV gives the summary of the classification results for the arrow points.

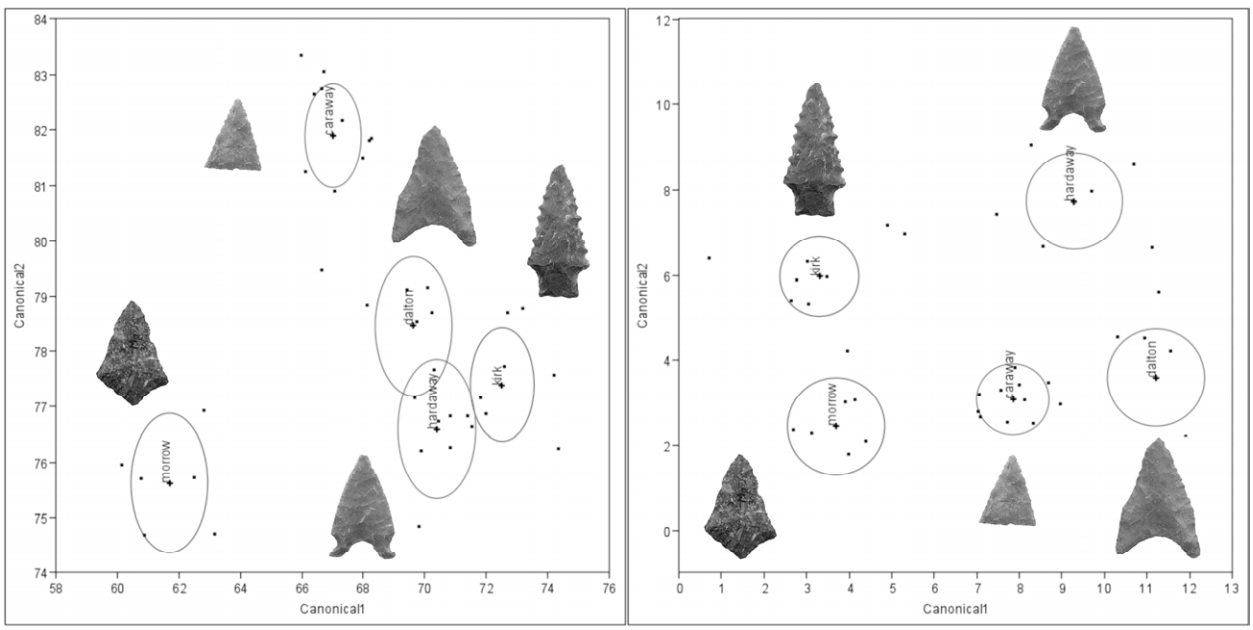


Figure 2: LDA results for dimensionless ratios (left) and 3 harmonic coefficients (right). Only the two most significant canonical axes are shown.

**Table IV: Summary of results for classification of points**

| Measurements | Analysis Method | Misclassified (N=38) |
|---|---|---|
| Seven dimensionless ratios | Linear discriminant | 0 (0%) |
| | Neural network | 0 (0%) |
| Harmonic coefficients (4,6,10) | Linear discriminant | 1 (2.6%) |
| Harmonic coefficients (2-6) | Neural network | 1 (2.6%) |
| Invariant moments | Linear discriminant | 1 (2.6%) |
| | Neural network | 0 (0%) |

Construction of dendrograms based on shape measures

The snowflake data set exemplifies a different type of problem than the previous three sets. In the prior data sets, there were a set of *a priori* groups into which each object was sorted. In contrast, all of the objects in the snowflake set belong to a single heuristic group ("snowflakes") and the goal is to discover classifications on the basis of measurement. Dendrograms provide a convenient tool by which to display these classifications. Using two dimensionless ratios and a topological measure (number of skeleton end points), it is possible to construct a dendrogram that meaningfully sorts the snowflakes (illustrated in Figure 4). In the dendrogram, items or groups are joined at the point along the horizontal axis representing the difference in value of the first principal component. The threshold selected divides the population into two groups.

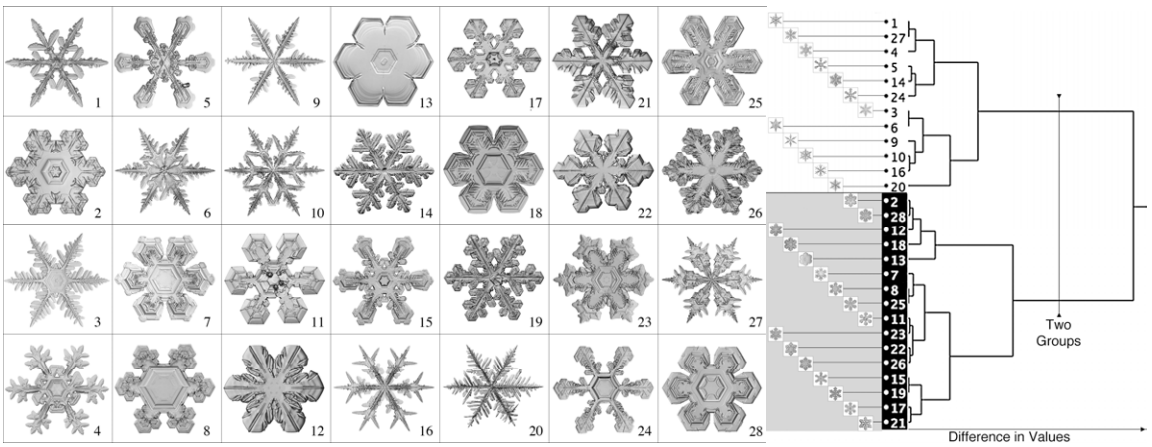


Figure 4. Images of 28 snowflakes (left) and dendrogram (right) of the snowflakes classified by first principal component.

Ward's method, as implemented by JMP® 9, was used to create the hierarchical clustering based on the most significant of the principal components. Ward's method is a variance minimization algorithm; thus, each successive refinement (moving from right to left) reduces the variance in each child set. The dendrogram as constructed in Figure 4 shades the snowflakes on the basis of membership in the two highest level groups. From visual inspection, the white (top) group appears to be more dendritic in nature while the black (bottom) group appears more platelike.

While dimensionless shape descriptors were used in the construction of this dendrogram, it is possible to use either moments or harmonic coefficients to construct a dendrogram. The drawback to doing so is that there may not be a clear visual grouping of the objects. This consideration can be ignored if there are correlated properties that can be used in lieu of visual heuristics.

## Conclusions

Shape measurements performed using image capture and computer analysis are capable of isolating characteristics that can distinguish classes of objects and structures. Dimensionless ratios, harmonic (Fourier) coefficients, and invariant moments, are representative of the types of measurements available. While these are not capable of fully reconstructing the original shapes, they select characteristics that are important for identification, sorting, correlation with processing or properties, and many more industrial and research applications. The selection of the best measurement set to use in any particular case can be evaluated using standard statistical techniques such as principal components analysis, stepwise regression, discriminant analysis, and neural nets.

## References


[1] S. Loncaric, "A survey of shape analysis techniques," *Pattern Recognition*, 31 (8) (1998), 983-1001.

[2] M. R. Teague, "Image analysis via the general theory of moments," *Journal of the Optical Society of America*, 70 (8) (1980), 920-930.

[3] M. K. Hu, "Visual pattern recognition by moment invariants," *IEEE Transactions on Information Theory*, 8 (2) (1962), 179-187.

[4] J. Flusser and T. Suk, "Pattern recognition by affine moment invariants," *Pattern Recognition*, 26 (1) (1993), 167-174.

[5] J. Flusser, "On the independence of rotation moment invariants," *Pattern Recognition*, 33 (9) (2000), 1405-1410.

[6] H. P. Schwartz and K. C. Shane, "Measurement of particle shape by Fourier analysis," *Sedimentology*, 13 (3-4) (1969), 213-231.

[7] R. Ehrlich and B. Weinberg, "An Exact Method for Characterization of Grain Shape," *SEPM Journal of Sedimentary Research*, 40 (1) (1970), 205-212.

[8] A. J. Haines and J. S. Crampton, "Improvements To The Method Of Fourier Shape Analysis As Applied In Morphometric Studies," *Palaeontology*, 43 (4) (2000), 765-783.

[9] P. E. Lestrel, Ed., *Fourier Descriptors and Their Applications in Biology* (Cambridge, UK: Cambridge University Press, 1997.)

[10] F. B. Neal and J. C. Russ, *Measuring Shape* (Boca Raton, FL: CRC Press, 2012), 337-347.

[11] C. Brechbühler, "Parametrization of Closed Surfaces for 3-D Shape Description," *Computer Vision and Image Understanding*, 61 (2) (1995), 154-170.

[12] N. Canterakis, "3D Zernike moments and Zernike affine invariants for 3D image analysis and recognition," (Paper presented at the 11th Scandinavian Conference on Image Analysis, 1999.)

[13] B. Ruthensteiner, N. Baeumler, and D. G. Barnes, "Interactive 3D volume rendering in biomedical publications.," *Micron ,* 41 (7) (2010), 886.e1-886.e17.

[14] A. Ziegler, M. Ogurreck, T. Steinke, F. Beckmann, S. Prohaska, and A. Ziegler, "Opportunities and challenges for digital morphology.," *Biology direct*, 5 (2010), 45.

[15] K. Libbrecht, *Field Guide to Snowflakes* (St. Paul, MN: Voyageur Press, 2006), 102-107.

[16] F. Kuhl and C. Giardina, "Elliptic Fourier features of a closed contour," *Computer Graphics and Image Processing*, 18 (3) (1982), 236-258.

1st International Conference on 3D Materials Science
*Edited by: Marc De Graef, Henning Friis Poulsen, Alexis Lewis, Jeff Simmons, George Spanos*
***TMS (The Minerals, Metals & Materials Society), 2012***

# Graph Cut Approaches for Materials Segmentation Preserving Shape, Appearance, and Topology

Jarrell W. Waggoner[1], Jeff Simmons[2], Marc De Graef[3], Song Wang[1]

[1]University of South Carolina, Department of Engineering and Computing,
315 Main St.; Columbia, SC, 29208, USA
[2]Materials and Manufacturing Directorate, Air Force Research Labs;
Dayton, OH, 45433, USA
[3]Carnegie Mellon University, Department of Materials Science and Engineering,
5000 Forbes Avenue; Pittsburgh, PA, 15213, USA

Keywords: segmentation, propagation, shape, appearance, topology, graph cut

## Abstract

Segmenting material images into underlying objects is an important but challenging problem given object complexity and image noise. Consistency of shape, appearance, and topology among the underlying objects are critical properties of materials images and can be considered as criteria to improve segmentation. For example, some materials may have objects with a specific shape or appearance in each serial section slice, which only changes minimally from slice to slice; and some materials may exhibit specific inter-object topology which constrains their neighboring relations. In this paper, we develop new graph-cut based approaches for materials science image segmentation. Specifically, these approaches segment image volumes by repeatedly propagating a 2D segmentation from one slice to another. We introduce different terms into the graph-cut cost function to enforce desirable shape, appearance, and topology consistency. We justify the effectiveness of the proposed approaches by using them to segment sequences of serial-section images of different materials.

## Segmentation via Labeling

In this paper we use the multi-labeling framework outlined in [1, 2, 3, 4] to *propagate* a 2D segmentation from one segmented slice $S_i$ to another $S_{i+1}$. A labeling algorithm simply assigns an integer (label) to each pixel in $S_{i+1}$, in which we use labels to represent the phases in a material (e.g. specific crystal structures, or different material states). A label function in this framework $f$ is formulated as

$$E(f) = \sum_{p \in \mathcal{P}} D_p(f_p) + \sum_{\{p,q\} \in \mathcal{N}} V_{pq}(f_p, f_q), \tag{1}$$

where $\mathcal{P}$ is the set of image pixels in $S_{i+1}$, $f_p$ is the label (phase) of pixel $p \in \mathcal{P}$, and $\mathcal{N}$ is the set of pixel pairs that are neighbors in $S_{i+1}$. In this paper, pixels directly above, below, left, or right of a pixel are considered neighbors.

The *phase term*, $D_p(f_p)$, represents a cost for assigning a particular phase (label $f_p$) to a particular pixel $p$; it is propagated from the available segmentation of $S_i$ [4]. In

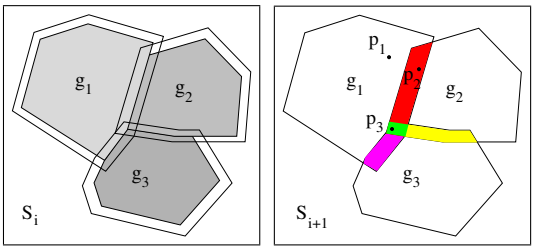


(a) (b)

| $D$ | $g_1$ | $g_2$ | $g_3$ |
|---|---|---|---|
| $p_1$ | 0 | $\infty$ | $\infty$ |
| $p_2$ | 0 | 0 | $\infty$ |
| $p_3$ | 0 | 0 | 0 |

(c)

Figure 1: An example of the phase term $D_p(f_p)$. **(a)** Objects $g_1$, $g_2$, and $g_3$ in slice $S_i$ and the regions near the phase boundaries (dashed lines). **(b)** Phases propagated to slice $S_{i+1}$, where the colored regions are near phase boundaries. **(c)** Phase term $D_p$ defined for three pixels in (b) in terms of three phase labels, $g_1$, $g_2$, and $g_3$.

particular, to reflect the phase continuity between $S_i$ and $S_{i+1}$, we can set all the pixels in $S_{i+1}$ to be the same phase as $S_i$ (e.g. pixel $p_1$ in Fig. 1(b)), except for pixels near the phase boundaries (e.g. pixels $p_2$ and $p_3$ in Fig. 1(b)), where the pixels have non-infinity cost for all nearby phases, as shown in Fig. 1(b-c).

The *interface term*, $V_{pq}(f_p, f_q)$, represents the interfacial energy between phases (analogous to the Potts model for multiphase mixtures). If $f_p = f_q$ at two neighboring pixels $p$ and $q$, then the interfacial energy is zero; otherwise there will be a penalty representing the energy between the different phases. In [4], if $f_p \neq f_q$, we define this penalty as

$$V_{pq}(f_p, f_q) = \begin{cases} \infty, & f_p \not\Leftrightarrow f_q \\ \frac{255}{\max(S_{i+1}(p), S_{i+1}(q))}, & f_p \Leftrightarrow f_q \end{cases} . \tag{2}$$

where $S_{i+1}(p)$ and $S_{i+1}(q)$ are the image intensities of pixels $p$ and $q$ in $S_{i+1}$, respectively. There is an infinity energy if the phases of $p$ and $q$ are different and these phases were not adjacent in $S_i$ ($f_p \not\Leftrightarrow f_q$). This prevents non-adjacent phases from being labeled as adjacent. There is a non-zero finite energy related to image information if the phases of $p$ and $q$ are different and these phases are adjacent in $S_i$ ($f_p \Leftrightarrow f_q$). As detailed in [4], this drives phase boundaries toward desired image edges.

In [5], it is shown that finding a globally optimal labeling that minimizes Eq. (1) is an NP-hard problem, but a locally-optimal labeling can be efficiently found with the minimum graph-cut algorithm. In this algorithm, a graph model is constructed to represent pixels, and the phase terms and interface terms are encoded into the edge weights of the graph. Finding the local optimal labeling is reduced to the problem of partitioning the graph into two disjoint subgraphs by removing edges with minimum total edge weight. Furthermore, this problem can be solved by the well-known max-flow min-cut algorithm [6].

## Preserving Shape

According to normal practice, the spacing between serial sections of a material are made frequently enough that at least roughly 10 slices are made through each object of interest (e.g. grain, precipitate, etc.). With this high density sampling, successive slices of the same object usually exhibit consistent shapes, at least through several sections, as shown in Fig. 2(a-b).

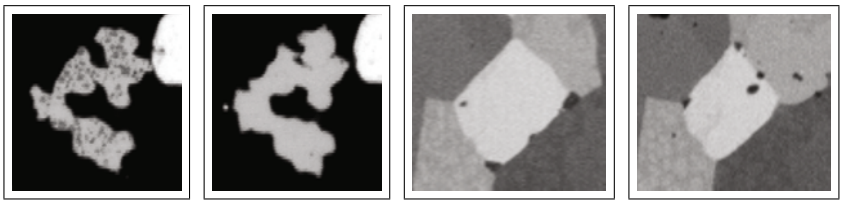

(a) (b) (c) (d)

Figure 2: **(a-b)** Gamma′ precipitates in Rene88DT [7]. **(c-d)** Grains in IN100 superalloy [8], courtesy of Mike Groeber. **(a)** Slice $S_i$. **(b)** Slice $S_{i+1}$, where the object shows similar shape to the object in $S_i$. **(c)** Slice $S_i$. **(d)** Slice $S_{i+1}$, where the objects show similar intensity distribution to the objects in $S_i$.

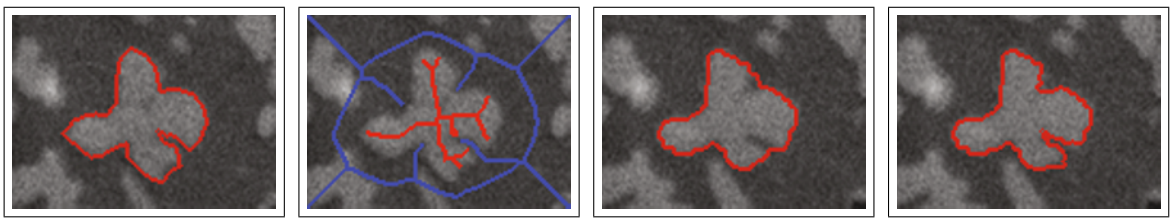

(a) (b) (c) (d)

Figure 3: Dendritic gamma′ precipitates in Rene88DT. **(a)** Segmentation of slice $S_i$, created manually. **(b)** Skeletonizaton of the segmented object in slice $S_i$ (morphologically eroded slightly), showing the shape of the object (red) and background (blue). **(c)** Segmentation results on slice $S_{i+1}$ using our baseline method in [4]. **(d)** Segmentation result on slice $S_{i+1}$ preserving shape between slices by assigning a desired phase to the skeleton pixels.

For the phase term in Eq. (1) we can define a Dirac delta function

$$D_p(f_p) = \begin{cases} 0, & f_p = d_p \\ \infty, & f_p \neq d_p \end{cases} . \tag{3}$$

if $d_p$ is the desired phase for pixel $p$, and all other phases are known to be undesired. In the following, we use this approach to preserve an object shape when propagating a segmentation from $S_i$ to $S_{i+1}$.

Specifically, we perform a skeletonization [9] of each object of interest in $S_i$, as shown in Fig. 3(b), and assign a desired phase to the skeleton pixels in $S_{i+1}$. The desired phase of a skeleton pixel in $S_{i+1}$ is defined to be the phase of the same pixel in $S_i$. This helps preserve the shape of each object of interest when propagating the segmentation from $S_i$ to $S_{i+1}$. The skeleton is morphologically eroded slightly to account for changes in the object's size. Note that for the pixels in $S_{i+1}$ without desired phases, we still determine their phases by minimizing Eq. (1). Figure 3 shows a comparison between our baseline approach using the phase term as in [4] vs. the method outlined in this section to propagate a manually created segmentation in $S_i$ to a new slice $S_{i+1}$.

## Preserving Appearance

The intensity within an object can be another important property which may be desirable to preserve when propagating a segmentation. As shown in Fig. 2(c-d), an object might undergo changes in size or shape from one slice to the next while retaining a consistent intensity, aside from image noise. While the interface term $V_{pq}(f_p, f_q)$ in [4] incorporates

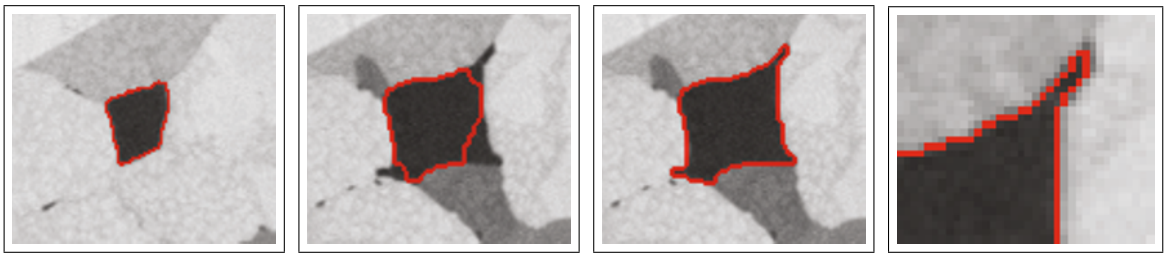

(a) (b) (c) (d)

Figure 4: Grain structure of IN100 superalloy [8]. Image courtesy of Mike Groeber, AFRL. **(a)** Segmentation of slice $S_i$, created manually. **(b)** Segmentation result on slice $S_{i+1}$ using our baseline method in [4]. **(c)** Segmentation result on slice $S_{i+1}$ considering object intensity consistency between $S_i$ and $S_{i+1}$. **(d)** Zoomed view of upper-right corner of (c).

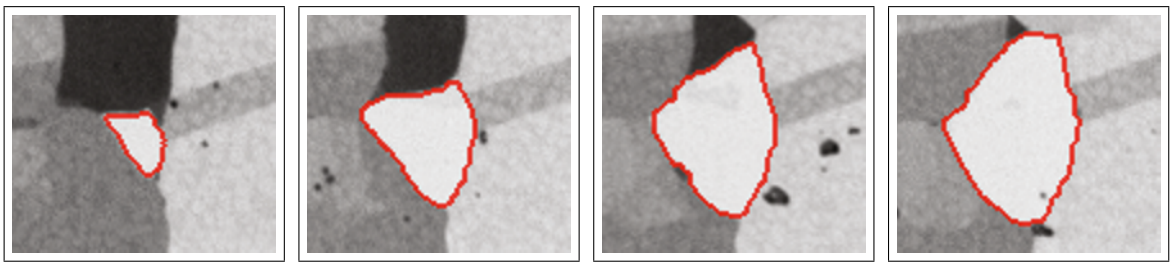

(a) (b) (c) (d)

Figure 5: Same IN100 [8] as in Fig. 4. **(a)** Segmentation of slice $S_i$, created manually. **(b-d)** Segmentation results of iteratively propagating the segmentation in (a) to subsequent slices by using the intensity-preserving technique.

pairwise intensity difference between neighboring pixels to determine whether they have the same phase or different phases, it does not capture the *overall* intensity of a specific object. As such, we present a method to incorporate the intensity of an object into the phase term $D_p(f_p)$ in Eq. (1).

Our key observation is that the overall intensity of many objects can be modeled as a simple Gaussian distribution $\mathcal{N}(\mu, \sigma^2)$ to account for image noise. By computing such a Gaussian for every phase in $S_i$, we can determine the probability of a pixel in slice $S_{i+1}$ belonging to a specific object. For each phase $f$ from slice $S_i$ and corresponding Gaussian $\mathcal{N}(\mu_f, \sigma_f^2)$, the phase term $D_p(f_p)$ can be defined by evaluating all the pixels in slice $S_{i+1}$ against this distribution by using a Dirac delta function

$$D_p(f_p) = \begin{cases} 0, & (\mu_f + \lambda\sigma_f) > S_{i+1}(p) > (\mu_f - \lambda\sigma_f) \\ \infty, & otherwise \end{cases} \tag{4}$$

where $S_{i+1}(p)$ is the intensity of pixel $p$ in slice $S_{i+1}$ and $\lambda > 0$ is a sensitivity parameter. As in [4], we add an additional constraint that only pixels within a certain distance of the original object in $S_i$ are considered. Figure 4 shows a comparison between our baseline approach using the phase term as in [4] vs. the method outlined in this section to propagate a manually created segmentation in $S_i$ to a new slice $S_{i+1}$. Figure 5 shows a sample segmentation result after iteratively propagating for several slices.

It is possible to combine the techniques discussed in this paper by first applying the intensity-based technique in this section, followed by the shape-based technique presented in the previous section. A sample result is shown in Fig. 6.

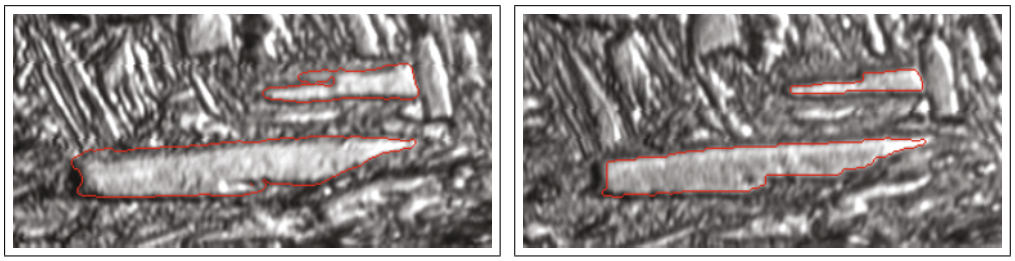

(a) (b)

Figure 6: Martensite lath structure in steel [10]. Image courtesy Dave Rowenhorst, NRL. **(a)** Rough segmentation of slice $S_i$ created by hand. Notice the boundaries do not correspond well to object boundaries. **(b)** Segmentation result on slice $S_{i+1}$ by using both shape-preserving and appearance-preserving techniques.

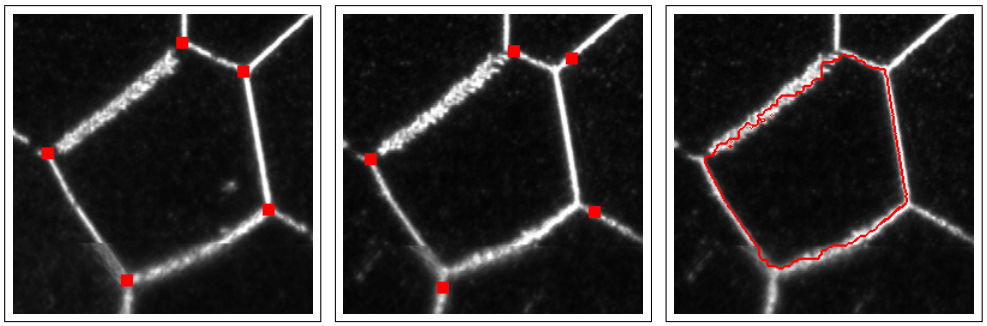

(a) (b) (c)

Figure 7: $\beta$-Ti grains in Ti-21S [12], courtesy of Dave Rowenhorst, NRL. **(a)** Slice $S_i$, where the triple junctions shown as red dots (manually selected). **(b)** Slice $S_{i+1}$, where the triple junctions have been propagated from the previous slice. **(c)** Segmentation result of applying our baseline method in [4] to the region bounded by the points in (b).

## Preserving Junction Topology

In addition to propagating a segmentation by minimizing an energy (such as Eq. (1)), it is possible to instead propagate key topological points in some materials objects. For example, polycrystalline metals have triple junctions where three objects (grains) meet. The relationship between triple junctions in two slices is determined by the dihedral angle that models the interfacial energy between the grains [11]. In some cases, we may have prior knowledge about this dihedral angle which can help us determine the location of triple junctions in the new slice $S_{i+1}$. For example, we can select a number of candidate points for each triple junction in slice $S_{i+1}$, and choose the candidate that leads to dihedral angles that closely conform to the known prior knowledge.

We conducted a simple experiment on a subset of an electron microscopy titanium volume provided by Dave Rowenhorst, which is shown in Fig. 7. For such material, the dihedral angles at triple junctions are always close to 120°. For each triple junction point in $S_i$, we find a set of candidate corresponding triple junction points in $S_{i+1}$ by examining the image intensity gradient in $S_{i+1}$. We select the candidate that leads to dihedral angles that are closest to 120° for each triple junction. Results are shown in Fig. 7(b). Based on the identified triple junctions, the multi-labeling techniques described above can be used to refine the boundaries, as shown in Fig. 7(c).

## Conclusion

In this paper, we have shown how to incorporate both shape and appearance consistency to improve material science image segmentation by propagating a 2D segmentation from one slice to another, based on a graph-cut energy minimization framework. For incorporating shape, we preserve the topology consistency of the object skeleton between slices. For incorporating appearance, we model the intensity distribution of the object of interest, and use this model to segment the same object in the new slice. Finally, we proposed an approach to incorporate prior knowledge of the dihedral angles to improve localization of triple junctions, and use this approach to improve segmentation. We have presented sample results for each approach.

**Acknowledgments** We would like to thank Dave Rowenhorst from the Navy Research Lab for providing the titanium serial section images and Mike Groeber for the IN100 images. This work was funded, in part, by AFOSR FA9550-11-1-0327, NSF-1017199, NSF-0951754, and ARL W911NF-10-2-0060. The views and conclusions contained in this document are those of the authors and should not be interpreted as representing the official policies, either express or implied, of AFOSR, NSF, ARL or the U.S. Government. The U.S. Government is authorized to reproduce and distribute reprints for Government purposes, notwithstanding any copyright notation herein.

## References

[1] Y. Boykov and V. Kolmogorov. *IEEE Transactions on Pattern Analysis and Machine Intelligence*, 26 (9) (2004), pp. 1124–1137.

[2] Y. Boykov, O. Veksler, and R. Zabih. *IEEE Transactions on Pattern Analysis and Machine Intelligence*, 23 (11) (2001), pp. 1222–1239.

[3] V. Kolmogorov and R. Zabih. *IEEE Transactions on Pattern Analysis and Machine Intelligence*, 26 (2) (2004), pp. 147–159.

[4] J. Waggoner, J. Simmons, and S. Wang. *Proceedings of SPIE (Computational Imaging X)*, vol. 8296 (Burlingame, CA, 2012).

[5] O. Veksler. *Efficient graph-based energy minimization methods in computer vision*. Ph.D. thesis, Cornell University, Ithaca, NY, USA, 1999.

[6] R. K. Ahuja, T. L. Magnanti, and J. B. Orlin. *Network Flows: Theory, Algorithms, & Applications* (Englewood Cliffs: Prentice Hall).

[7] J. MacSleyne, M. Uchic, J. Simmons, and M. D. Graef. *Acta Materialia*, 57 (2009), pp. 6251–6267.

[8] M. Groeber, S. Ghosh, M. D. Uchic, and D. M. Dimiduk. *JOM Journal of the Minerals, Metals and Materials Society*, 59 (2007), pp. 32–36.

[9] L. Lam, S.-W. Lee, and C. Y. Suen. *IEEE Transactions on Pattern Analysis and Machine Intelligence*, 14 (9) (1992), pp. 869–885.

[10] D. Rowenhorst, A. Gupta, C. Feng, and G. Spanos. *Scripta Materialia*, 55 (1) (2006), pp. 11–16.

[11] C. H. P. Lupis. *Chemical Thermodynamics of Materials* (Elsevier, 1983).

[12] D. Rowenhorst, A. Lewis, and G. Spanos. *Acta Materialia*, 58 (2010), pp. 5511–5519.

1st International Conference on 3D Materials Science
*Edited by: Marc De Graef, Henning Friis Poulsen, Alexis Lewis, Jeff Simmons, George Spanos*
***TMS (The Minerals, Metals & Materials Society), 2012***

# Fitting Laguerre Tessellations to the Microstructure of Cellular Materials

Irene Vecchio[1], Katja Schladitz[1], Claudia Redenbach[2]

[1]Fraunhofer Institut für Techno- und Wirtschaftsmathematik (ITWM), Fraunhofer-Platz 1, 67663 Kaiserslautern, Germany
[2]Technische Universität Kaiserslautern, Erwin-Schrödinger-Straße, 67653 Kaiserslautern, Germany

Keywords: weighted Voronoi tessellation, geometric model, 3D image analysis, random closed set, sphere packing, polymer foam

## Abstract

Cellular materials are employed in many fields, ranging from medical technologies to aerospace industry. In applications, understanding the influence of the microstructures on the physical properties of materials is of crucial importance. Stochastic models are a powerful tool to investigate this link. In particular, random Laguerre tessellations (weighted generalizations of the well-known Voronoi model) generated by systems of non-overlapping balls have proven to be a promising model for rigid foams. Model fitting is based on geometric characteristics estimated from micro-computed tomographic images of the microstructures. More precisely, the model is chosen to minimize a distance measure composed of several geometric characteristics of the typical cell. However, with this approach, inference on the model parameters is time consuming and needs expert knowledge. In this talk, we investigate strategies leading to an automatic model fitting. Finally, this model fitting approach is applied to polymethacrylimide (PMI) foam samples.

## Introduction

Rigid foams, ceramic and biological structures are only a few examples in the class of cellular materials. Here, we focus on modeling polymethacrylimide (PMI), a polymer closed-cells rigid foam employed in many application fields. This material features a variety of interesting properties, most pronounced are high stiffness and low specific weight, making it particularly interesting for light weight construction applications. A model reproducing the geometric features of the microstructures is a powerful tool to investigate the link between microscopic and macroscopic properties.

Micro computed tomography ($\mu$CT) succeeds to capture the complex three-dimensional cell structure of PMI foams. Processing the resulting images yields the geometric properties of the material that can be used to fit a model. The randomness embedded in stochastic models matches the microscopic heterogeneity of the structures. In particular, the system of cells can be modeled by random tessellations, i. e. space-filling systems of non-overlapping polytopes.

In the following, we will focus on Laguerre tessellations, presenting the main properties of this model. Subsequently, a technique to select the model parameters (semi)-automatically is outlined. The approach is applied to a PMI foam in the last section.

## Laguerre tessellations

We first provide definitions of the model in the $d$-dimensional real space $\mathbb{R}^d$.

A tessellation is a partition of the Euclidean space in convex cells. Namely, a *tessellation* $T$ is a countable set $T = \{C_i \subset \mathbb{R}^d, i \in \mathbb{N}\}$ such that each cell $C_i$ is full dimensional, non empty, bounded and convex; pairs of cells intersect only in their boundaries; the union of all cells is equal to $\mathbb{R}^d$; if $B$ is a bounded Borel set, then the number of cells in $T \cap B$ is finite.

We define *$k$-faces*, $k < d$, of the tessellation $T$ the $k$-dimensional intersections of adjacent cells. For $x \in \mathbb{R}^d$, define

$$F(x) = \bigcap_{C \in T, x \in C} C,$$

the intersection of cells containing $x$. Then for $k = 0, 1, .., d$, $F(x)$ is a $k$-dimensional polytope. The set of the $k$-faces of T is

$$\mathcal{F}^k(T) := \{F(x) : \dim F(x) = k, x \in \mathbb{R}^d\}. \tag{1}$$

In three dimensions, there are four types of faces: cells ($k = 3$), facets ($k = 2$), edges ($k = 1$) and nodes ($k = 0$).

A tessellation is called *face-to-face* if the faces of the tessellation coincide with faces of the cells. Moreover, a face-to-face tessellation is said to be *normal* if every $k$-face belongs almost surely to $d - k + 1$ cells. In 3D, this means that nodes are shared by four cells, edges by three and facets by two.

Most rigid foams are face-to-face and normal, thus we will restrict to tessellation with these properties in the following. Besides, we only deal with tessellations generated by random point processes.

Let $S$ be a locally finite set of points in $\mathbb{R}^d$, then the *Voronoi tessellation* generated by $S$ is the collection of cells

$$C_V(x, S) = \{y \in \mathbb{R}^d : \|y - x\|^2 \leq \|y - x'\|^2, \ \forall x' \in S\}, \ x \in S.$$

Each point $x$ in $S$ generates a cell containing all the points that have $x$ as their nearest neighbor in $S$. A generalization is possible by assigning a weight to each point. This can be seen as a sphere with arbitrary radius centered in $x$. Formally, let $S$ be a locally finite set of spheres $s(x, r)$ with $r \geq 0$, then the *Laguerre tessellation* generated by $S$ is the collection of cells

$$C_L(s(x, r), S) = \{y \in \mathbb{R}^d : \|y - x\|^2 - r^2 \leq \|y - x'\|^2 - r'^2, \ \forall s(x', r') \in S\}, \ s(x, r) \in S.$$

If the radii of the generating spheres are equal, the Laguerre tessellation corresponds to a Voronoi. However, in the Laguerre case, not all spheres generate a cell in the tessellation and not all centers are included in the cell they generate. By definition, the cells are all convex $d$-dimensional polytopes. Two examples of Laguerre tessellations with the corresponding sphere systems are displayed in Figure 1. The set $S$ of spheres can be seen as a realization of a marked point process, i. e. a random variable which takes values in $\mathbb{R}^d \times [0, \infty)$, locally finite and for which a random weight is assigned to each point, cf. [9]. The properties of the tessellation are closely related to those of the underlying marked point process. Under mild assumptions of regularity of the random point process, Laguerre tessellations are face-to-face and normal. Moreover, each normal tessellation with convex cells in $\mathbb{R}^d$ with $d \geq 3$ can be realized as a Laguerre tessellation, see [6]. For a thorough analysis of random Laguerre tessellations, refer to [4].

Geometric characteristics

A first approach to describe a tessellation is by the mean number of $k$-dimensional faces per unit volume ($\gamma_k$, $k = 0, .., d$). Another set of characteristics are those describing the geometry of the faces. We call *typical $k$-face* a random $k$-dimensional polytope which has the same distribution as a uniformly randomly chosen $k$-face of the tessellation, cf. [9]. In 3D, geometric features are

$N_{kl}$ mean number of $l$-faces adjacent to a $k$-face for $k, l = 0, .., 3$,
$L_1$ mean length of an edge,
$L_2$ mean perimeter of a facet,
$A_2$ mean area of a facet,
$B_3$ mean width of a cell, i. e. mean of Feret diameters
$L_3$ mean total edge length of a cell
$S_3$ mean surface area of a cell,
$V_3$ mean volume of a cell.

Further characteristics for tessellations can be found in [9, 10].

As discussed in [5], a set of features advantageous for modeling consists of the following mean values of the typical cell: the mean volume $V_3$, the mean surface area $S_3$, the mean width $\bar{\bar{b}} = B_3$ and mean number of facets per cell $F_C = N_{32}$. However, mean values do not carry enough information about the distribution of these characteristics. Thus also empirical variances have to be estimated.

Geometric features can not be measured correctly on cells intersecting the boundaries. However, considering only the cells completely contained in the image yields a bias (large cells are more likely to overlap the boundaries). To avoid this effect, edge corrections are included in our analysis, see [7, p. 164–166].

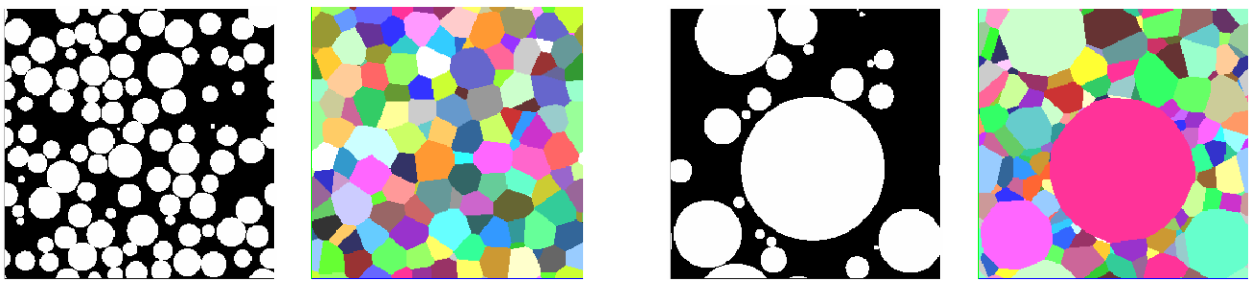

(a) $V_V = 50\%$, $c = 0.2$. (b) Laguerre tessellation. (c) $V_V = 50\%$, $c = 2$. (d) Laguerre tessellation.

Figure 1: Sections of 3D sphere packing with different coefficients of variation and corresponding Laguerre tessellations. Note that the tessellation in one slice is influenced by spheres in other not visible layers, too.

## Model fitting

Compared to open foams, in closed-cell structures a higher variability in the cell volumes occurs. We will generate a Laguerre tessellation from a system of non overlapping spheres. In this case, the cell size distribution depends on the distribution of the volumes of the spheres, see [2].

Random spheres packing

A way to generate dense systems of non overlapping spheres is the force biased method, see e. g. [1]. In the initial configuration all the random spheres are inserted and intersection is allowed. A collective rearrangement begins: spheres are shifted and radii are decreased in

order to reduce, eventually avoid, overlapping. Up to a scaling factor, the size distribution is preserved in the final configuration. Dense packing of spheres with arbitrary radii can be obtained. The parameters of this algorithm are: the intensity, i. e. the number of spheres to be included, the sphere size distribution, the desired volume fraction to be filled $V_V$ and $c$, the coefficient of variation of the volume distribution.

Size distribution

Typically, cells size distributions in cellular materials follow gamma or log-normal distributions, cf. [2]. The gamma distribution depends on a shape parameter $a > 0$ and a scale parameter $s < 0$ and has the following density

$$f(x) = \frac{x^{a-1}\mathrm{e}^{-\frac{x}{s}}}{s^a\Gamma(a)}, \quad x \geq 0. \tag{2}$$

The mean is $as$ and the variance is $as^2$. The density of a log-normal distribution is

$$g(x) = \frac{\mathrm{e}^{-\frac{(\log x-\mu)^2}{2\sigma^2}}}{\sqrt{2\pi}\sigma x}, \quad x \geq 0, \tag{3}$$

with mean $\mu \in \mathbb{R}$ and standard deviation $\sigma \geq 0$.

The distribution parameters can be estimated from the observed cell size via the maximum likelihood method. The output of a goodness-of-fit test, e. g. Kolmogorov-Smirnov, tells which distribution fits the data better.

Model parameters

We now assume to have estimated the geometric characteristics of the material from the three-dimensional image data. The merit of a model is evaluated on how well it reproduces the features of the original structures. Hence the approach proposed in [5] is to measure the distance between material and model on the basis of some significative geometric features. Let $\hat{m} = (\hat{m}_1, .., \hat{m}_n)$ be the vector of $n$ features estimated from the material and $m = (m_1, .., m_n)$ the corresponding characteristics of the model. Then the distance is

$$d_e(\hat{m}, m) = \sqrt{\sum_{i=1}^{n} \left(\frac{\hat{m}_i - m_i}{\hat{m}_i}\right)^2}. \tag{4}$$

In particular, the characteristics used are the first and second moments of volume, surface area, mean width and mean number of facets per cell.

In [8], it was demonstrated that the moments of characteristics can be expressed as cubic polynomials in $c$ depending on the volume fraction $p_{V_V,i}(c)$, $i = 1, .., 8$. Coefficients also depend on the size distribution of spheres in the sphere packing. Thence two sets of polynomials are estimated, one for the gamma and one for the log-normal distribution with parameters depending on $V_V$ and $c$. The distance function can be reformulated as

$$d_e(\hat{m}, p_{V_V,i}(c)) = \sqrt{\sum_{i=1}^{n} \left(\frac{\hat{m}_i - p_{V_V,i}(c)}{\hat{m}_i}\right)^2}. \tag{5}$$

For each size distribution, the values of the pair $(V_V, c)$ that minimize the distance function are the parameters of the best fitting model.

It is now possible to simulate sphere packings with the estimated parameters. Centers and radii can then be used to construct a Laguerre tessellation.

Simulating sphere packings with the given parameters, we have a collection of spheres to feed the algorithm for the Laguerre tessellation generation. The algorithm to construct a Laguerre tessellation given a collection of spheres is based on [11]. The idea is to construct a four-dimensional convex hull, where the fourth coordinate depends on the sphere radius. The projection in 3D is a Delaunay tessellation, which is dual to Laguerre tessellation. Some examples of realizations of the sphere packing and the corresponding Laguerre tessellation can be seen in Figure 1.

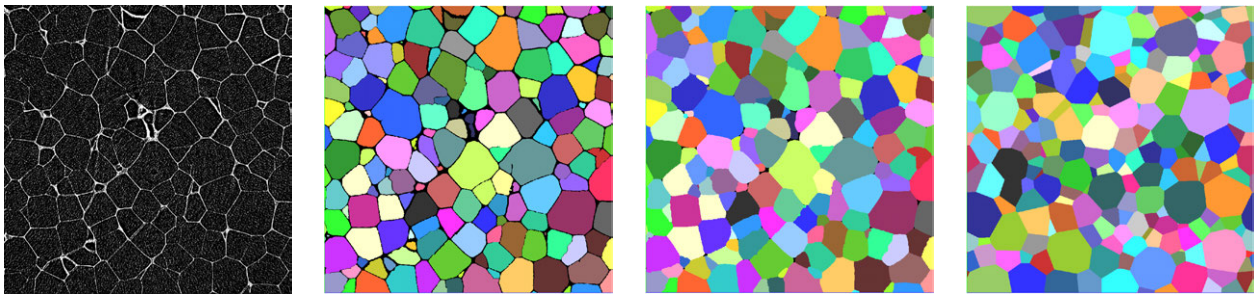

(a) (b) (c) (d)

Figure 2: (a) Section of the reconstructed 3D $\mu$CT image, pixel size = 2.73$\mu$m, sample of ROHACELL® RIST RC71 foam, Evonik Industries AG. (b) Reconstructed cells. (c) Dilated cells. (d) Model: Laguerre tessellation generated by a force biased sphere packing with gamma distributed size and parameters $V_V = 50\%$ and $c = 0.6$.

## Application to a PMI hard foam

In this section, we apply the procedure to a ROHACELL® RIST RC71 foam sample by Evonik Industries AG. The sample size is 3.28 x 3.93 x 3.82 mm, that is an image of 1200 x 1440 x 1400 pixels with isotropic pixel size of 2.73 $\mu$m. A section is displayed in Fig. 2(a).

After smoothing, the cell reconstruction requires many processing steps, refer to [5] for details. The result is shown in Fig. 2(b). The wall system constitutes the 8.84% of the whole volume. However, it is not modeled by Laguerre tessellation, which is space-filling. Thus to allow feature comparison, the reconstructed cells are dilated, Fig. 2(c).

Excluding the cells intersecting the border, we have 2507 cells. The cell size distribution matches well a gamma distribution. The distance function (5) is minimized w. r. t. the characteristics estimated from the image. The optimal parameters are $V_V = 50\%$ and $c = 0.6$. A realization of the tessellation obtained with these values is shown in Fig. 2(d). To validate the model, one should compare several tessellation features uncorrelated to those used to minimize the distance function.

The shape of the cells is not explicitely fitted with our method. However, shape descriptors such as the isoperimetric shape factors [7] depend on the characteristics used to minimize the distance function. For instance, the first isoperimetric shape factor, also called *sphericity*, depends on volume and surface area only. An alternative shape index is the ratio between the smallest and the largest diameter of a cell. This is independent of the features used in the fitting precodure, thus can be exploited for model validation.

The current results are promising. Nevertheless, some optimizations in the parameters estimate still have to be included in the method. This research is in progress.

## Acknowledgments

This work has been supported by the German Federal Ministry of Economics and Technology via the German Federation of Industrial Research Associations, project number 16912 N "MAFoaM" and by the German Federal Ministry of Education and Research, project number 03MS603D "AMiNa". Irene Vecchio acknowledges support by the Deutsch-Französische Hochschule (DFH). All images are visualized and processed with the support of the software MAVI and the MAVIlib developed in the Image Processing department of the Fraunhofer ITWM, Kaiserslautern, [3].

## References

[1] A. Bezrukov, M. Bargiel and D. Stoyan, "Statistical analysis of simulated random packings of spheres," *Part. Part. Syst. Charact.*, 19 (2001), 111–118.

[2] Z. Fan et al., "Simulation of polycrystalline structure with Voronoi diagram in Laguerre geometry based on random closed packing of spheres," *Comp. Mater. Sci.*, 29 (2004), 301–308.

[3] Fraunhofer ITWM, Department of Image Processing, *MAVI – Modular Algorithms for Volume Images*, www.mavi-3d.de, (2005).

[4] C. Lautensack. *Random Laguerre Tessellations* (Ph.D. thesis, Universität Karlsruhe, 2007).

[5] C. Lautensack, "Fitting three-dimensional Laguerre tessellations to foam structures," *Journal of Applied Statistics*, 35(9) (2008), S. 985-995.

[6] C. Lautensack and S. Zuyev, "Random Laguerre tessellations," *Adv. in Appl. Probab.*, 40 no.3 (2008), 630–650.

[7] Joachim Ohser and Katja Schladitz, *3d Images of Materials Structures – Processing and Analysis* (Wiley VCH, Weinheim, 2009).

[8] C. Redenbach, "Microstructure Models for Cellular Materials," *Comp. Mater. Sci.*, 44(4) (2009), 1397–1407.

[9] Rolf Schneider and Wolfgang Weil, *Stochastic and Integral Geometry, Probability and Its Applications* (Springer, Heideleberg, 2008).

[10] Dietrich Stoyan, Wilfrid S. Kendall and Joseph Mecke, *Stochastic Geometry and its Applications* (second edition, Wiley, Chichester, 1995).

[11] K. Sugihara, "Three-dimensional Convex Hull as a Fruitful Source of Diagrams," *Theor. Comput. Sci.* 235 (2000) 325–337.

1st International Conference on 3D Materials Science
*Edited by: Marc De Graef, Henning Friis Poulsen, Alexis Lewis, Jeff Simmons, George Spanos*
***TMS (The Minerals, Metals & Materials Society), 2012***

# Simulation of FIB-SEM Images for Segmentation of Porous Microstructures

Torben Prill[1], Katja Schladitz[1],Christian Wieser[2]

[1]Fraunhofer ITWM (Institute for Industrial Mathematics),
Fraunhofer Platz 1, Kaiserslautern, 67663, Germany,[2] Adam Opel AG GM Alternative Propulsion Center Europe, 65423 Rüsselsheim, Germany

Keywords: scanning electron microscopy, materials microstructures, Boolean model, FIB tomography, quantitative analysis, Monte-Carlo simulation

## Abstract

FIB tomography yields high quality 3D images materials microstructures at the nanometer scale combining serial sectioning using a focused ion beam with scanning electron microscopy (SEM). However, SEM images represent the projection of a slice of unknown thickness. In FIB tomography of highly porous media this leads to shine-through-artifacts preventing automatic segmentation of the solid component. To overcome these difficulties, we simulate the SEM process. Monte-Carlo techniques yield accurate results, but are too slow for FIB-SEM requiring hundreds of SEM images for one dataset. Nevertheless, a quasi analytic description of the specimen and acceleration techniques cut down the computing time by orders of magnitude, allowing the simulation of FIB-SEM data. Based on simulated FIB-SEM image data, segmentation methods for the 3D microstructure of highly porous media from the FIB-SEM data can be developed and evaluated. Finally successful segementation enables quantitative analysis and numerical simulations of macroscopic properties.

## Introduction

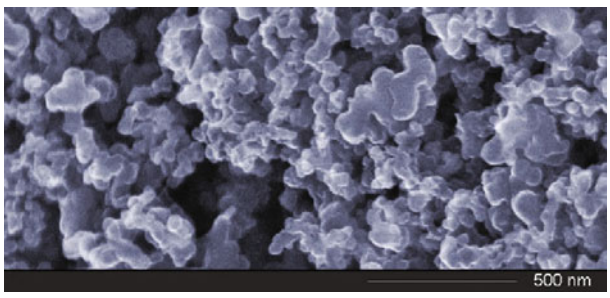


Figure 1: Single FIB/SEM image of typical fuel cell MPL from image stack obtained by serial slicing applying FIB/SEM [1]

Advanced automotive engineering in the last two decades moved more and more towards electrified vehicles and electric traction systems in order to provide sustainable mobility with reduced or zero tailpipe emissions. Particularly hydrogen-consuming fuel cells and lithium ion batteries have been demonstrated to be electrochemical energy converters of choice for efficient and environmentally sound vehicles that meet customer expectations such as performance and range [2]. The simulation-based virtual vehicle development process consequently needs to consider powertrain electrification including the electrochemical energy converter. Recent technology trends aim at connecting the individual building blocks of the fuel cell or battery system through multiscale simulation approaches from the materials scale of the electrochemical cell up to the entire system. With regard to the former, both fuel cells and batteries comprise mostly carbon-based porous materials such as porous electrodes or porous transport layers (e.g. fuel cell diffusion media or

battery separators). In order to predict macroscopic efficient material properties, such as effective diffusivity, or even the electrochemical performance, such as battery charge/discharge behavior, so-called $\mu$-simulation approaches have been developed [3, 4, 5]. By nature, these approaches require computational domains that resolve the solid/pore structure of the porous material in order to solve the transport equations in the different phases separately. Ideally, computational domains derived from material imaging data sets which have been image-processed adequately should be applied. Doing this has been demonstrated successfully with x-ray tomographical imaging data sets of fuel cell carbon fiber papers [6]. In other areas, providing processed imaging data sets to the -simulation effort is still challenging. In order to calculate the properties of so-called microporous layer coatings (MPL) of the above mentioned carbon fiber papers, for instance, virtual model representations had to be used so far [3]. Due to the length scales of pores and solid carbon particles which form the complex pore system of an MPL, focused ion beam nanotomography (FIB-SEM) has been identified as method of choice to resolve the structure sufficiently as typical pore and particle sizes are well below 100 nm of diameter, and FIB-SEM imaging for these materials has been demonstrated successfully (Fig. 1). However, specific artifacts caused by the imaging technique applied to highly porous media prevent efficient and objective identification of the solid/void boundary. Hence, new methods and processes are desired to adequately and efficiently image-process the raw SEM images.

## FIB tomography

The fact that the SEM image is a parallel projection of the structure onto the image plane makes it impossible to extract any three-dimensional structural information. Also, stereology is hampered by the unknown thickness of the imaged slice. FIB tomography was developed to gain 3D images at the lateral resolution provided by the SEM technique. Usual SEM imaging is combined with a slicing technique where a focused ion beam mills slices of a block of material. An SEM image is taken after each slicing step, generating a stack of SEM images depicting the 3D microstructure of the material.

Unfortunately, for porous media, the reconstruction is hampered by 'shine through' artifacts, stemming from the fact that material from deeper slices is visible through pores. To develop segmentation algorithms that can cope with these difficulties, a simulation of the FIB-SEM imaging process is needed. In this report we present a simulation method for FIB-SEM images of highly porous media, which is able to generate hundreds of SEM images of the highly complex geometries of porous materials in a reasonable amount of time, while maintaining a great deal of physical accuracy. Available programs for SEM simulation include CASINO [7], MCSEM [8] and the MONSEL series [9, 10]. However, all these programs exceed the needed runtime by far. To remedy this, we build our simulation on MONSEL2 [9] as a physical model combined with efficient geometric structure generation and several acceleration techniques.

## FIB-SEM simulation

We use a Monte Carlo technique to simulate the electron diffusion, since it is physically accurate while using little memory. The diffusion of the electrons is simulated one electron at a time. The simulation starts at the focus point of the beam, where the primary electron (PE) enters the specimen and begins to scatter in the material. To simulate a finite width of the beam, the starting points are sampled from a 2D Gaussian distribution in the XY-plane.

From the starting point, the electron travels a random distance through the material, the free path. Then it scatters with an atom/molecule at a random angle, again traveling a random distance and so on (see Fig. 2, left). This generates an electron track through the material. The scattering angles and free paths are sampled from a distribution provided by the underlying physical model, both distributions depending on the energy of the electron, which decreases during the process. Eventually, the electron is either absorbed by the material or reaches the surface and escapes (back scattered electron (BSE), see Fig. 2, right).

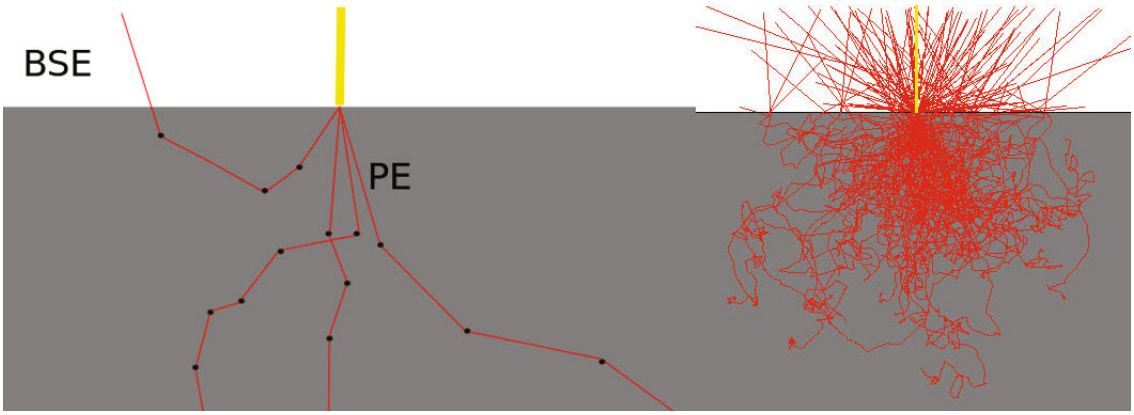


Figure 2: Electrons diffusing through a specimen, schematic (left) and simulated (right)

Physical model

MONSEL2 by [9] is physically well motivated through the use of the Mott cross section for elastic scattering, which is of special importance for modeling large angle scattering. A second advantage of the model is, that it also provides a good description for the electron scattering at low energies by accounting for collective phenomena such as plasmons. This is of particular significance for the modeling of the generation of secondary electrons (SE). The energy loss is modeled by a modified version of the continuous slowing down approximation (CSDA) by Joy and Lou [11]. A distinction from the original MONSEL2 model arises through the pre-computation technique described later. Since the pre-computed SE are binned with respect to the energy of their production, the production cross section is approximated by a piecewise constant function.

Geometric model

We use a Boolean model [12], with spherical or cylindrical grains (see fig. 3, for examples) to model the solid component of the microstructure. The geometry is described quasi-analytically, i.e. as a list of vectors, directions, radii etc.. This saves a lot of memory compared to e.g. a lattice based description and it allows to simulate geometries with thousands of grains. Moreover, it enables to simulate effects on very different length scales, such as SE emission (nanometer scale) and specimen sized of hundreds of micrometers. In vacuum, the electrons, irrespective of their energy, travel along straight lines, neglecting electrical fields within the specimen as well as charging effects.

Acceleration

In a full simulation MONSEL can calculate several hundred tracks per second. This is much too slow for our application, thus the simulation needs to be accelerated. A powerful

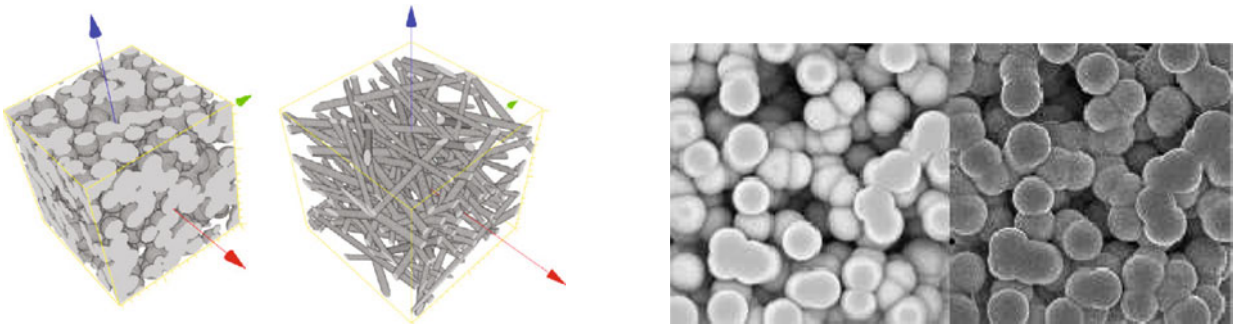

Figure 3: Examples of geometries from boolean models with spheres and cylinders; Simulated SEM images of a Boolean model of spheres BSE signal(left) SE signal (right)

technique developed by Seeger[13] is based on the pre-computation of electron tracks in an infinite medium. A large number (e.g. $10^4$) of tracks is precomputed and for the imaging a smaller number (e.g. $10^3$) is sampled randomly for each pixel. If an electron leaves the specimen no scattering occurs and a straight line segment is inserted into the trajectory until it enters the material again, then the simulation continues with the pre-computed track. The pre-computation is done with a modified version of the program MONSEL2.

The SE can only be detected if they are produced within a thin layer below the specimen surface, hence pre-computing the SE tracks for the whole trajectory is superfluous. Therefore the primary electron PE and SE are decoupled during pre-computation. For the PE the complete track is pre-computed and stored, while for the SE only the scattering angle and free path of every step is stored, together with the energy of the generating PE. The pre-computed SE tracks are stored in bins, according to the energy of their creation. For a good approximation with even a low number of bins, we chose non-uniform bins each containing a given number of SE tracks. This improves approximation of the creation cross section and prevents bins from having an insufficient number of electron tracks.

Reducing the number of segments can reduce the runtime of the simulation considerably, since every simulated segment requires a test whether it lies inside the material. Therefore a compressed version of the pre-computed track is created consisting of segments of a given length, which is of the order of the escape depth of the SE. It is however necessary to simulate the parts of the tracks where SE are created very accurately, since the number of SE created depends on the path length covered by the PE. Hence simulation accuracy is chosen according to the depth of the simulated electron within the specimen. If an electron moves deep enough below the surface such that no produced SE can escape to the detector, the compressed track is used for the simulation. Since the primitives used for the modeling of the specimen are all convex, the depth test can be performed of the primitives without loss of accuracy or speed. The depth is even available as a by-product of the test whether a point is inside the material.

For further acceleration we use a binning technique developed for raytracing. When an electron leaves the specimen, a straight line segment is inserted into the track. Consequently, an intersection test has to be performed between the segment and the generated structure. For complex geometries, this means that thousands of primitives have to be tested each time. To accelerate these tests we use the uniform spacial subdivision technique [14, 15]. The structure is divided into cubic bins and for each bin the primitives intersecting the bin are pre-computed and stored. During the simulation only those primitives are tested for intersection, that lie within the bins intersected by the segment. We chose the algorithm [16] by Amanatides & Woo for the bin traversing, because it finds the closest intersection without

extra techniques, such as mailboxing. The speedup factor provided by this technique can be up to 100 for a complex geometry.

Finally, the speed-up gained from parallelization scales nearly linear with the number of kernels as every track can be computed independently from the others in a Monte-Carlo simulation. The simulation runs parallel on multicore CPUs as well as on clusters. Applying all these techniques, the time needed for the simulation of a FIB scan reduces to the order of hours or even minutes on a cluster.

## Results

The simulation developed for the project allows for the generation of simulated SEM images of complex geometries in a short time. Examples of results can be seen in fig. 3 with spherical grains. Both images show a gold sample. Fig. 4 (left) shows a simulated SE image of a carbon microstructure, and for comparison, a real SEM image of a similar structure. As can be seen, the material simulated has a great effect on the image, showing the physical exactness of the simulation. Also the edge effects and overall appearance of the real image can be replicated very accurately. The simulation took about 2 hours.

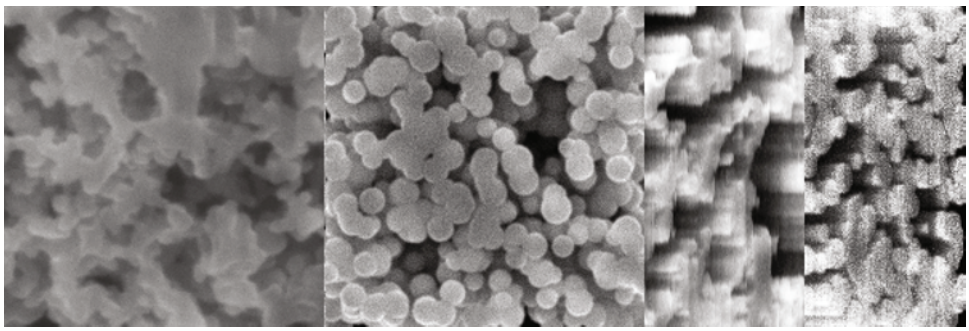

Figure 4: left to right: real FIB-SEM slice of carbon structure; simulated image of carbon structure with same parameters; side view with enhanced contrast of real FIB-SEM stack; simulated FIB-SEM stack

Fig. 4 (right) shows a side view of a simulated stack of FIB-SEM images and a stack taken from real FIB-SEM tomography. It can be seen, that the simulated images replicate the shine through artifacts, which present a major obstacle for image segmentation. The simulation took 15 minutes per image.

## Discussion

We have demonstrated for the first time that simulation of FIB-SEM imaging of porous media in reasonable computation time is feasible. This enables further research avenues in image analysis, as methods developed to analyze and segment FIB-SEM data can be tested and validated on the ground truth of the simulated synthetic data now available. We thus provide a new tool for analysis and simulation of porous materials as needed e.g. in the field of electromobility, where new porous materials are developed for the use in fuel cells and batteries.

## Acknowledgement

This work was partly funded by the German Federal Ministry of Education and Research, project AMiNa (03MS603D).

## References


[1] Ch. Wieser. Nanoporous and microporous materials in fuel cell applications. In *New Congress Materials Science and Engineering*, Nuremberg, September 4, 2008.

[2] R. v. Helmolt U. Eberle. Fuel cell electric vehicles, battery electric vehicles, and their impact on energy storage technologies: An overview. *Electric and Hybrid Vehicles*, Chapter 9:227–245, 2010.

[3] J. Becker, Ch. Wieser, S. Fell, and K. Steiner. A multi-scale approach to material modeling of fuel cell diffusion media. *International Journal of Heat and Mass Transfer*, 54:1360–1368, 2011.

[4] G.B. Less, J.H. Seo, S. Han, A.M. Sastry, J. Zausch, A. Latz, S. Schmidt, Ch. Wieser, D. Kehrwald, and S. Fell. Micro-scale modeling of li-ion batteries: Parameterization and validation. *publication in progress.*

[5] A. Latz J. Zausch J. Becker G.B. Less J.H. Seo S. Han A. M. Sastry S. Fell, K. Steiner. Porous materials of electrochemical cells in the cae design process. *SIMVEC*, 2010.

[6] J. Becker, R. Flueckinger, M. Reum, F. Buechi, F. Marone, and M. Stampanoni. Determination of material properties of gas diffusion layers: Experiments and simulations using phase contrast tomographic microscopy. *Journal of The Electrochemical Society*, 156 (10):B1175–B1181, 2009.

[7] Couture A. R. Joly D. Tastet X. Aimez V. Drouin, D. and R. Gauvin. Casino v2.42a fast and easy-to-use modeling tool for scanning electron microscopy and microanalysis users. *Scanning*, 29:92–101, 2007.

[8] D. Gnieser, C. G. Frase, H. Bosse, and R. Tutsch. Mcsem- a modular monte carlo simulation program for various applications in sem metrology and sem photogrammetry. In Martina Luysberg, Karsten Tillmann, and Thomas Weirich, editors, *EMC 2008 14th European Microscopy Congress 15 September 2008, Aachen, Germany*, pages 549–550. Springer Berlin Heidelberg, 2008.

[9] Lowney J. Monsel-ii: Monte carlo simulation of sem signals for linewidth metrology. *Microbeam Analysis*, 4:131–136, 1995.

[10] A. Karabekov, O. Zoran, Z. Rosenberg, and G. Eytan. Using monte carlo simulation for accurate critical dimension metrology of super small isolated poly-lines. *Scanning*, 25(6):291–296, 2003.

[11] D. C. Joy and S. Luo. An empirical stopping power relationship for low-energy electrons. *Scanning*, 11(4):176–180, 1989.

[12] D. Stoyan, W. S. Kendall, and J. Mecke. *Stochastic Geometry and Its Applications.* Wiley, Chichester, 2nd edition, 1995.

[13] A. Seeger, C. Fretzagias, and R. Taylor. Software acceleration techniques for the simulation of scanning electron microscope images. *Scanning*, 25(5):264–273, 2003.

[14] A S Glassner. Space subdivision for fast ray tracing. *IEEE Computer Graphics and Applications*, 4:15–22, 1984.

[15] K. Iwata A. Fujimoto. Accelerated ray tracing. In *Proc. CG Tokyo 85*, 1985.

[16] J. Amanatides and A. Woo. A fast voxel traversal algorithm for ray tracing. In *In Eurographics 87*, pages 3–10, 1987.

1st International Conference on 3D Materials Science
*Edited by: Marc De Graef, Henning Friis Poulsen, Alexis Lewis, Jeff Simmons, George Spanos*
***TMS (The Minerals, Metals & Materials Society), 2012***

# Handling Misalignment and Drift in 3D EBSD Data Sets

Yuchi Huang, Brandon Laflen, Andrew Deal, Ian Spinelli, Anthony Barbuto, Timothy Hanlon

GE Global Research; 1 Research Circle; Niskayuna, NY 12309

## Abstract

GE Global Research is exploring the 3D reconstruction of high temperature materials to understand material behavior in lifing applications. Large volumes of material are required to generate the appropriate statistical understanding of grain morphologies, grain boundary types and distributions, and residual plastic strain. Consequently, GE has adopted mechanical sectioning coupled with EBSD analysis as the methodology for investigating regions of interest. Among the major factors that affect the accuracy of such a reconstruction are thermal or mechanical drift during EBSD measurements and the precision and accuracy of sample alignment. To correct for these unavoidable issues when reconstructing the final volume, an algorithm based on grain center-of-mass and various shape factors has been developed and applied to a data set. Results show a significant improvement in slice-to-slice registration.

## Introduction

It is well-known that thermal and mechanical drift play a role in the accuracy of electron beam steering in scanning electron microscopy applications, including electron back-scatter diffraction (EBSD). A result of this drift is a misalignment between the physical coordinate and the recorded coordinate of each scanned point. While standard procedures can reduce misalignment, accuracy suffers in quantitative studies and is further exacerbated in successive slice analysis (e.g., 3D volumetric analysis) because the misalignment varies independently between slices.

At GE Global Research, we have developed a methodology to reduce misalignment error in our ongoing 3D analytical studies. This method is comprised of three components. First, a second-order polynomial transformation is used to correct misalignment. Second, the first EBSD slice is compared with a companion optical slice to pin the EBSD transformation for that slice to the physical coordinate system of the optical slice. Third, successive EBSD slices are corrected iteratively and automatically with a two-step process: (1) shape and orientation information are used to identify grain correspondences between successive slices and then (2) the centers-of-mass of each corresponding pair are used to compute the transformation between slices. At the end of the process, all EBSD slices have been transformed back to the original physical coordinate system of the first optical slice.

## Misalignment Correction

We correct EBSD misalignment due to mechanical and thermal drift with a 2nd-degree polynomial coordinate transformation of the following form:

$$x = a_1 x_0^2 + a_2 y_0^2 + a_3 x_0 y_0 + a_4 x_0 + a_5 y_0 + a_6$$
$$y = b_1 x_0^2 + b_2 y_0^2 + b_3 x_0 y_0 + b_4 x_0 + b_5 y_0 + b_6$$

where $a_n$ and $b_n$ represent 12 unknown transformation parameters, $(x_0, y_0)$ is a point in the physical coordinate system, and $(x, y)$ is the resulting point in the EBSD coordinate frame. This formulation allows for independent drift and also accommodates a linear rate of change in drift, all varying with spatial location. Because it is a linear system, as few as six point correspondences between two slices determine the transformation, and additional correspondences yield an over-determined transform estimate, which reduces noise in the automatic alignment process.

## Automatic Misalignment Correction

Given the above definition of the polynomial transformation used to correct misalignment, it is possible to automatically correct misalignment across the full stack of EBSD slices. To accomplish automatic correction, it is necessary to estimate enough point correspondences between successive EBSD slices to permit accurate estimation of the underlying transformation between each slice. While the minimum number of required correspondences is six, in practice we identify one or two orders of magnitude more (e.g., 100 correspondences) in order to damp estimation noise. The volumetric correction is then clamped to physical coordinates by manually picking correspondences between a single EBSD slice and an optical image of the same slice. (Because the human operator can manually choose impactful correspondences, far fewer are required at this stage.) The transformation of a given slice to physical coordinates is the aggregate of all preceding slice-to-slice transformations back to this clamped slice.

Point correspondences are automatically estimated between successive slices by first identifying pairs of grains with high similarity, and then using the centers-of-mass of each grain in a pair to establish a single correspondence for each pair. Because this process relies on accurate selection of grain pairs, several features are used in combination to assess similarity: shape, size, shape orientation, and crystal orientation (from EBSD). Following this assessment, grain pairs with highest similarity are selected for misalignment correction estimation. The following sub-sections describe this process in more detail.

### *Shape Descriptors*

Shape descriptors such as Shape Context [1] and Histogram of Oriented Gradients (HOG) [2] have been successfully applied to various problems in shape matching and object recognition. However, computing a grain-to-grain similarity based on Shape Context is too time-consuming for images containing hundreds or thousands of grains. Histogram of Oriented Gradients is defined in the Cartesian coordinate system of the image, and is therefore not translation-, rotation-, or scale-invariant. For this work, we used a polar-coordinate based shape descriptor based on both Shape Context and HOG, as illustrated in Figure 1. This descriptor is invariant to translation, rotation, and scale.

The first step in computing the shape descriptor is aligning the shape with the axis of least inertia (ALI). The ALI is defined as the line for which the integral of the square of the distances to points on the shape boundary is a minimum [3].

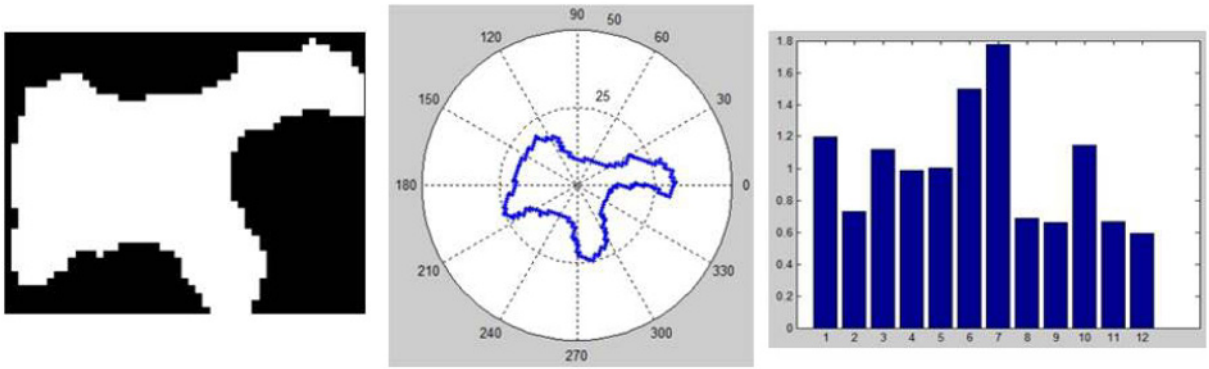


Figure 1: Polar-coordinate-based Shape Descriptor. Left: an original closed shape. Middle: the same shape in a polar coordinate system. Right: the generated histogram.

Next, the grain boundary points are extracted with a basic morphological operation. As illustrated in Figure 1 (middle), the region is divided into twelve 30° bins. Each boundary point can be represented in the polar-coordinate system by a ($\theta$,$\rho$) pair, where $\theta$ denotes angle and $\rho$ is the distance. To form a histogram of all boundary points, each point is projected into its corresponding bin, according to the following formula:

$$H = \frac{1}{\sum_{\forall j} B(j)} \sum_{\forall \theta \in B(i)} \log\left(1 + \frac{1}{\rho}\right),$$

where $B$(i) denotes a degree interval of the $i^{\text{th}}$ bin. By this definition, our shape descriptor is translation-, rotation-, and scale-invariant.

The $\chi^2$ distance function is a standard method used to measure the shape-to-shape distance between two histograms $H_1$ and $H_2$:

$$D_{\text{shape}}(H_1, H_2) = \frac{1}{2} \sum_{\forall k} \frac{[H_1(k) - H_2(k)]^2}{H_1(k) + H_2(k)}$$

The $\chi^2$ distance function is used in conjunction with the exponential function to score shape similarity:

$$S_{\text{shape}}(H_1, H_2) = \exp\left(-\frac{D_{\text{shape}}(H_1, H_2)}{\overline{D_{\text{shape}}}}\right)$$

where $\overline{D_{\text{shape}}}$ is the mean value of all computed shape-to-shape distances.

*Size and Shape Orientation Descriptors*

The size and shape orientation (ALI) are also considered in the matching process. These quantities are scalars and are directly injected into the exponential function as above, using a scalar difference metric like absolute difference.

*Crystal Orientation Descriptors*

EBSD data contain crystal orientation estimates for each scan point. We compute the minimum angle and axis pair, under symmetry, which relate two lattice orientations. For match

assessment, we retain only the absolute angle as a measure of the degree of lattice mismatch and compute a normalized exponential score for this mismatch, as above.

*Combined Grain-to-Grain Similarity Score*
We define grain-to-grain similarity by the weighted sum of each of the above similarity scores:

$$S(G_1, G_2) = \lambda_{\text{shape}} S_{\text{shape}}(G_1, G_2) + \lambda_{\text{size}} S_{\text{size}}(G_1, G_2) + \lambda_{\text{ALI}} S_{\text{ALI}}(G_1, G_2) + \lambda_{\text{EBSD}} S_{\text{EBSD}}(G_1, G_2)$$

with $0<\lambda<1$ and the sum of all $\lambda$ normalized to unity. This score is used in the following matching phase of the algorithm to select the best grain-pair candidates between slices.

*Candidate Grain Selection and Matching*
Several potential issues arise when matching grains between successive slices. These include grains that are missing from one slice due to drift or sample translation, rapidly changing grains, grains with special boundary planes that move appreciably between slices, and grains that lack distinguishing features. We attempt to mitigate these issues with a heuristic selection of initial candidates from the total grain pool.

Candidate selection begins by discarding the bottom 50% of grains based solely on size. This step is based on the observation that smaller grains have a greater likelihood of vanishing or growing rapidly between slices. Total translation (distance) is also considered. When similarities are assessed, grains are only compared with other grains within a neighborhood of some radial distance $r < R$, where $R$ is specified by the user as a maximum displacement between slices (see Figure 2). Finally, candidates are selected based on the desire to use grains that have a distinct similarity to only one corresponding grain. We exhaustively compute the combined similarity between all remaining grains (between slices), building a similarity matrix. Then we compute for each grain the ratio of the highest similarity score to the next highest similarity score. This ratio is highest when a grain matches well to only one grain. Final candidates are the top 20%, ordered by this ratio.

Matching and pair selection proceeds with a simple greedy selection strategy. The grain pair with the highest similarity is selected, added to the pair list, and removed from the candidate pool. This process continues iteratively until the desired number of pairs (e.g., 100) is selected. Figure 3 illustrates an example of matching results. These pairs are then reduced to point correspondences using the center-of-mass of each grain, and a slice-to-slice correction transformation is estimated from these correspondences.

## Matching and Registration Results

To validate our procedure, we examined the matching and registration algorithm with six sequential EBSD slices. Although in application the slices would be manually registered to an optical slice, we assume for this study that the first EBSD image is already in the physical coordinate system and we proceed with correcting the misalignment in the subsequent five slices, iteratively as described above. Figure 4 illustrates the top 30 matching grains between two EBSD slices. Figure 5 illustrates the cropped region from Figure 4 (yellow boxes), with a comparison of the second slice before and after registration. In figure 5, the automatic transformation matrix was

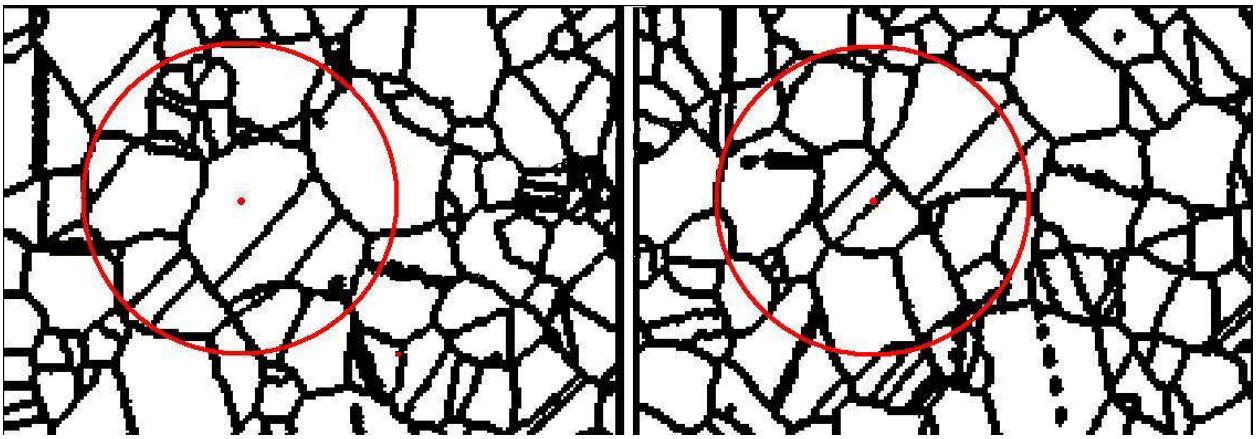

Figure 2: A center of mass of a grain in the left image and its corresponding location in the right image. When the centers of grains in the right image do not fall into the red circle ($r$=$R$), the similarities between these grain and the grain in the left image will be set to 0.

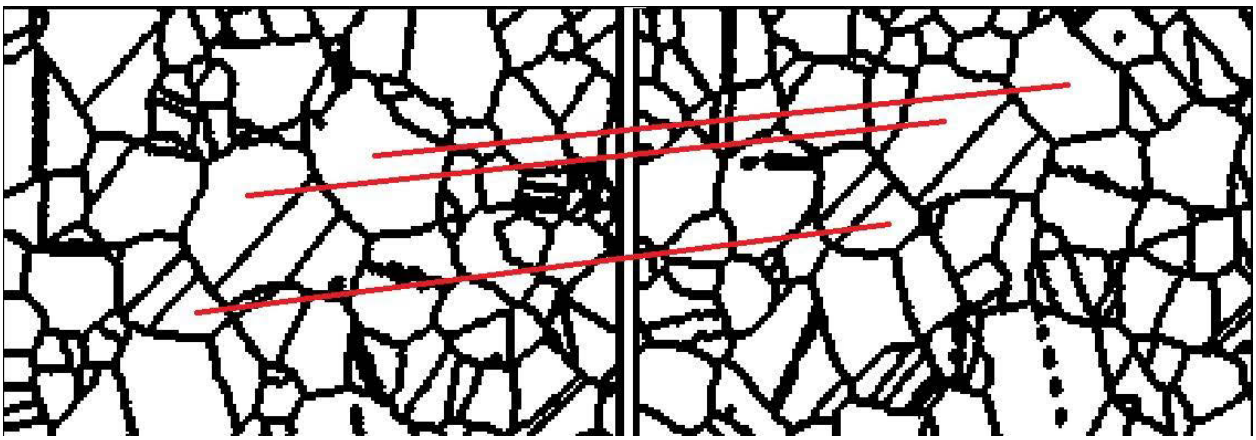

Figure 3: An example to show local matching result. Only three matches are illustrated.

$$x = -1.5 \cdot 10^{-6}x_0^2 - 1.4 \cdot 10^{-6}y_0^2 + 4.6 \cdot 10^{-7}x_0y_0 + 0.9995x_0 + 0.0006y_0 + 16.5$$
$$y = -4.4 \cdot 10^{-7}x_0^2 + 1.5 \cdot 10^{-6}y_0^2 + 2.9 \cdot 10^{-6}x_0y_0 + 0.0028x_0 + 1.0013y_0 - 31.5$$

which is a small affine rotation and distortion, with translation of 16.5 pixels in X and -31.5 pixels in Y.

## Conclusion

We have developed a method for automatically correcting misalignment between subsequent EBSD slices. This method can be adapted to different crystal lattices and grain structures, and allows the user flexibility in balancing trade-offs between computational complexity and performance. We have demonstrated the successful application of the automatic process to the alignment of real, successive EBSD slices. This method can be used to reconstruct a three-dimensional volume of material crystal lattice structures, enabling deeper inquiry into three-dimensional microstructures in material science.

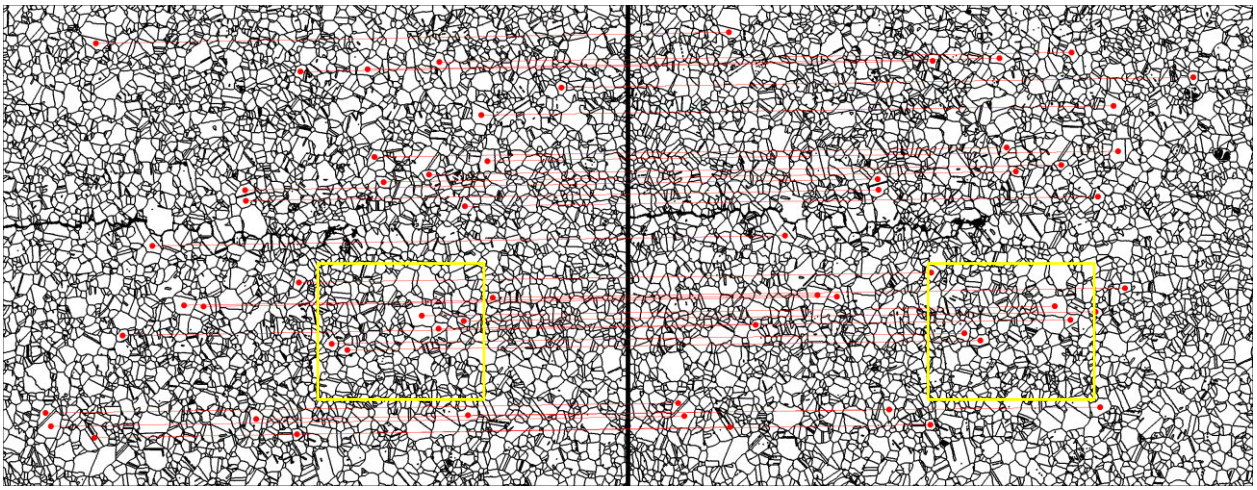

Figure 4: Example result from automatic matching process. Top 30 pairs of grains are shown in two adjacent slices.

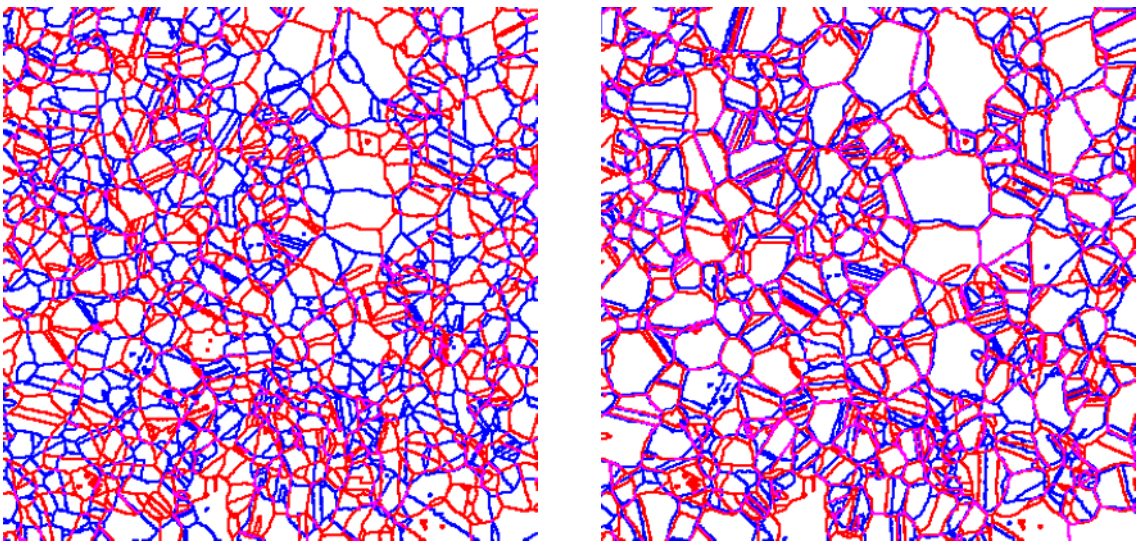

Figure 5: Zoom-in examples from the cropped region in Figure 4 (yellow box), with the second slice shown super-imposed on the first before and after registration. Left: comparison of the first slice (red) and the second slice (blue) without registration. Right: same comparison, but after registration.

## References


1. G. Mori, S. Belongie, and J. Malik, "Efficient shape matching using shape contexts," *IEEE Transactions on Pattern Analysis and Machine Intelligence*, 27(11) (2005), 1832-1837.

N. Dalal and B. Triggs, "Histograms of oriented gradients for human detection," *In Proc. of the IEEE Computer Society Conf. on Computer Vision and Pattern Recognition*, 1 (2005), 886-893.

Mingqiang Yang, Kidiyo Kpalma and Joseph Ronsin, "A survey of shape feature extraction techniques," *Pattern Recognition*, 2008, 43-90.

1st International Conference on 3D Materials Science
*Edited by: Marc De Graef, Henning Friis Poulsen, Alexis Lewis, Jeff Simmons, George Spanos*
***TMS (The Minerals, Metals & Materials Society), 2012***

# OPTIMIZING STOCHASTIC PROCESS FOR EFFICIENT MICROSTRUCTURE RECONSTRUCTION

Seun Ryu, Dongsheng Li

Fundamental and Computational Sciences Division, Pacific Northwest National Laboratory, 902 Battelle Blvd, Richland, WA 99354, USA

Keywords: correlation, microstructure reconstruction, simulated annealing, cooling schedule, stochastic process

## Abstract

To improve the efficiency in microstructure reconstruction is critical to build a high resolution statistical stable representative volume element practically. Using correlation function to reconstruct image using simulated annealing is revisited in this study. Different cooling schedules in simulated annealing were utilized and compared. Dramatic increase of computation efficiency has been achieved by optimizing cooling schedule, making it feasible for future computation intensive study on upscaling prediction.

## Introduction

Microstructure reconstruction is important in establishing a statistical representative volume element (RVE) for effective property prediction. Spatial and statistical structural information needed in characterization and performance prediction is a large data set with high resolution due to the inherent complexity and heterogeneity. However, in most studies the structure information are usually captured from difference views at various positions with multiple length scales, either using imaging instrumentation such as scanning electron microscope, atomic force microscope, electron back-scattering diffraction, or scattering facility such as X-ray diffraction, nuclear magnetic resonance, neutron scattering. Microstructure reconstruction generates microstructure realizations using statistical descriptors measured from target microstructures. The reconstruction process is important because it provides a two-dimensional or three-dimensional signature microstructure for further property prediction from limited microstructure information. Moreover, microstructure reconstruction provides insight into which statistical descriptors best represent the target microstructure. Once the most relevant statistical descriptors are revealed, computational models may use these descriptors and their evolution as a function of processing or deformation to improve material property predictions.

Statistical analysis and pattern recognition were implemented to represent structure information of high strength steel, a complex heterogeneous materials system. Fig. 1 demonstrated the microstructure of a heterogeneous steel sample[1] characterized from different locations and directions to thoroughly understand the anisotropic microstructure of steel. Furthermore, 3D reconstruction is necessary to characterize the structure information as future input into hierarchical upscaling with multiscale modeling. In this paper, we introduced an efficient 3D microstructure reconstruction method by using statistical analysis function and improved dramatically the computation speed by using different cooling schedules in simulated annealing. In this way, it will be practical for future image information fusion and reconstruction of images with high resolution and large domain. In this paper we utilized two point correlation function (TPCF) in reconstruction. We optimized the calculating of two point correlation

functions and dramatically reduced the computation time during stochastic reconstruction. Through these improvements in algorithms, 3D microstructure is generated in reasonable time.

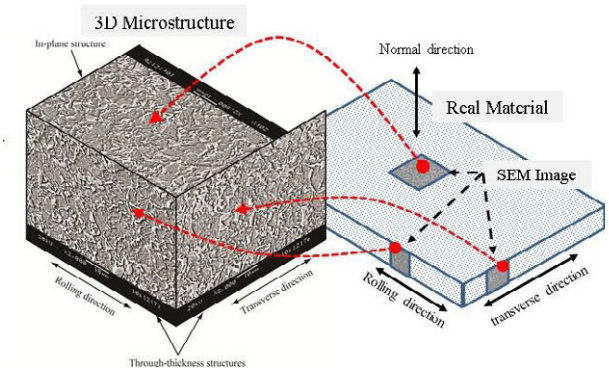


Figure 1: Statistical microstructure 3D Reconstruction from the multiple images [1]

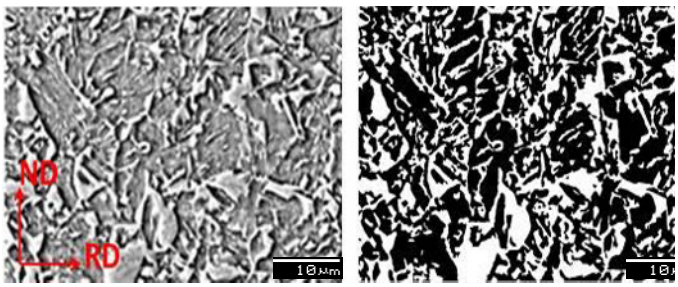


(a) SEM Image (b) Binary Image

Figure 2: SEM image and segmented binary image of dual phase stainless steel used in microstructure reconstruction [1]

Much progress has been made in microstructure reconstruction. Generally two kinds of methods have been used: stochastic method [2-13] and direct computation methods, such as Gaussian filter method, fast Fourier transformation inverse method [8], phase recovery algorithm [9] and genetic algorithm [14]. Optimization methods have all been applied to expedite the regression. Different sets of statistical descriptors have been applied to reconstruct microstructure. It is still a challenge to generate a large 3D image which enough features for microstructure characterization and modeling. This paper is not to propose a new microstructure reconstruction approach, but to optimize computational efficiency to make large 3D image reconstruction practical in the future.

Preprocessing of images is required before image reconstruction. Segmentation, island removal, boundary smooth and k-nearest neighbor classification are utilized to reach binary image for a two phase material system. Figure 2 (a) is a scanning electronic micrograph (SEM) of dual phase high strength steel. Due to the different resistance to the etchant, the bright phase in Fig. 2(a) is martensite and the gray phase is ferrite. Figure 2 (b) is binary image after the preprocessing and noise reduction.

## Two Point Correlation Function

To represent a random heterogeneous medium, we partition the space $V$ occupied by each digitized realization into $i$ (number of phases or components) disjointed subspaces $V_i$. For a given realization, the indicator function for phase i at position $x$ ( $x \in V_i$ ) is defined as

$$\mathrm{I}^{(i)}(x) = \begin{cases} 1, & \text{if } x \in V_i \\ 0, & \text{otherwise} \end{cases} \tag{1}$$

Information concerning the spatial arrangement of a variety of elements in microstructures can be provided from n-point correlation functions. Increase of order n provides more detailed microstructure representations [15]. Due to high computation expense, the n-point function most commonly used in microstructure reconstruction is the two-point correlation function (TPCF). The standard TPCF [15-16] is defined as

$$S_2^{(i,j)}(\vec{x}_1, \vec{x}_2) \equiv \left\langle I^{(i)}(\vec{x}_1) I^{(j)}(\vec{x}_2) \right\rangle \tag{2}$$

where the angle brackets denote an ensemble average. This function is the probability that 2 points $\vec{x}_1$ and $\vec{x}_2$ are found in phase $i$ and $j$ respectively. Traditionally, the TPCF is used to

calculate the probability that two points separated by a vector $r \equiv |\vec{x}_1 - \vec{x}_2|$, a function of distance , azimuthal angle $\theta$ and polar angle $\phi$. Henceforth, the TPCF $S_2^{(i,i)}(\vec{x}_1, \vec{x}_2)$ for the phase of interest ($i$) is indicated by $S_2(r, \theta, \phi)$ for a three-dimensional microstructure.

Other statistical descriptor functions were also used in microstructure reconstruction to supplement TPCF. The two-point cluster function, proposed by Torquato et al.[17], was added in microstructure reconstruction approach by Capek et al. [18] to reconstruct porous microstructure in order to improve the prediction of pore connectivity. Jiao and colleagues have shown the cluster function's utility for accurately reconstructing textures [19]. Lineal path functions have also been used for reconstructing anisotropic microstructures [20].

## Microstructure Reconstruction

TPCF have been previously used to study multi-phase composite materials, porous materials, and polycrystalline materials. Moreover, these statistical correlation functions are not limited to two-dimensional (2D) reconstructions, but can also be applied in three-dimensions (3D). In this study of efficiency and accuracy, we investigate a simple material system with two phases in a 2D system. The algorithms developed and conclusions observed may be generalized into 3D multiple phase materials.

The reconstruction algorithm in this approach is as follows. First, a target microstructure is identified and the relevant statistical descriptors are calculated. Second, a random microstructure is generated with the same volume fraction of components as target microstructure. Third, a Monte Carlo-based technique is used to switch pairs of vertices of different phases to enhance the agreement between the reconstructed microstructure and the original microstructure. An energy function, $E$, is defined to quantify the agreement between microstructures and is given by the sum of square of the difference between statistical descriptors for the reconstructed and target microstructures.

$$E = \sum_{t=1}^{T} \sum_{i=1}^{n} \sum_{j=1}^{m} \sum_{k=0}^{l_0} w_{tjk} \left( S_t^r(u_i, \theta_j, \phi_k) - S_t^t(u_i, \theta_j, \varphi_k) \right)^2 \quad (3)$$

Here $T$=2, when only two types of statistical descriptor functions, two point functions is used. $S_{2r}$ and $S_{2t}$ represent the statistical descriptor functions for the reconstructed and target microstructures, respectively. These statistical descriptors are functions of both vector magnitude $r$ and vector orientations ($\theta$, $\varphi$). The weight tensor, w, controls the relative importance of different statistical descriptor functions and is used here to balance the weighting of different descriptor functions along different directions, so that the initial contribution of each statistical descriptor is equivalent. In other words, in this formulation, the weighting function is only applied over the vector orientations, such that the squared difference between the reconstructed and target functions at larger distances is given the same weighting as those at smaller distances for a particular vector orientation. However, the sum of squares difference over all distances for a particular orientation is weighted such that it contributes equally to the total energy function as any other orientation. The initial energy for a purely random image is normalized to a value of 1.

The overall process for the reconstruction is shown in Figure 4 in which the Monte Carlo simulation. First, three orthogonal target images are used to calculate TPCF. Second, multiple random initial images are obtained by slicing from generated initial random 3D data structure. Third, differential energy (or error) from TPCF are calculated and minimized through stochastic process. Fourth, reconstruction data is selected when threshold reached. Various algorithms have been adopted to find the minimum of the Eq. (3). The objective function defined here is characterized by many local optima, making it difficult to minimizing energy using traditional

mathematical techniques. In these situations, modified heuristic methods like very fast SA with image enhancement algorithms offer a power tool to researchers.

## Simulated Annealing (SA) based Optimization

The basic idea of SA originates from thermodynamics and metallurgy: when molten iron is cooled slowly enough it tends to solidify in a structure of minimal energy. The idea of applying the annealing principle to optimization problems is due to [21-22]. In both works SA was applied to the traveling salesman problem.

The procedure involves finding a state of minimum "energy" among a set of many local minima by manipulating the phase of pixels in the digitized system. The energy of the system is defined by Eq. (3). The reconstruction procedure has a number of useful features; it is simple to implement, and generally applicable to multi-dimensional, multi-phase, and anisotropic structures. Moreover, it is expandable to include any type and number of correlation functions as micro-structural information, and therefore can be used to construct unknown structures from specified correlation functions even those with physically unrealizable properties [2]. The pixels of the digitized medium are manipulated appropriately in order to lead the minimizing $E$. After each pixel manipulation the energy $E'$ and the energy difference $\Delta E = E' - E$ between two successive states of the system are calculated. The new configuration is then accepted with probability $P(\Delta E)$ applying the Metropolis method [23] as:

$$P(\Delta E) = \begin{cases} 1 & if\ \Delta E \le 0 \\ \exp(-\Delta E / T) & otherwise \end{cases} \tag{4}$$

where $T$ is temperature. The cooling schedule, which governs the value and the rate of change of T, is chosen to allow the system to evolve to the desired state as quickly as possible, without getting trapped in any local energy minima. The starting $T$ should have a value such that the initial acceptance rate is 0.5. The algorithm terminates when the energy E given by Eq. (4) is less than some small tolerance value or when the number of consecutive unsuccessful phase interchanges is greater than a large number.

$$T_t = \begin{cases} T \times \lambda & if\ t = nk \\ T & otherwise \end{cases} (n = 1,2,\cdots,\infty) \tag{5}$$

And we can control the various cooling condition (CS). The various cooling schedules are cascade, ad hoc and exponential decrease cooling schedule. The cascade CS is decrease $T$ at each $k$ iteration cycle. The temperature $T_t$ is defined by Eq. (5). The $t$ is time property and $\lambda$ is a constant with a value of less than 1. Although the ad hoc CS is similar with cascade CS, if the $\Delta E$ didn't reach the tolerance value $E_t$, it increases $T$ by using $\lambda$ with a value of more than 1 and repeat cooling schedule.

## Results and Discussion

In this experiment, we developed the visual 3D microstructure reconstruction by using Visual C++ and OpenGL API on a desktop with Xeon dual core 2.40GHz CPU and 12GB RAM. The reconstructed microstructure is then generated using the aforementioned methodology. In the Figure 3, we can obtain fast results by using various cooling schedule simulated annealing method. The target image is 64×64 pixel, while all the reconstructed images are 128×28 pixels. Using optimized cooling schedule, the computation time is decreased from 600 seconds to 10 seconds with energy minimized to 0.02.

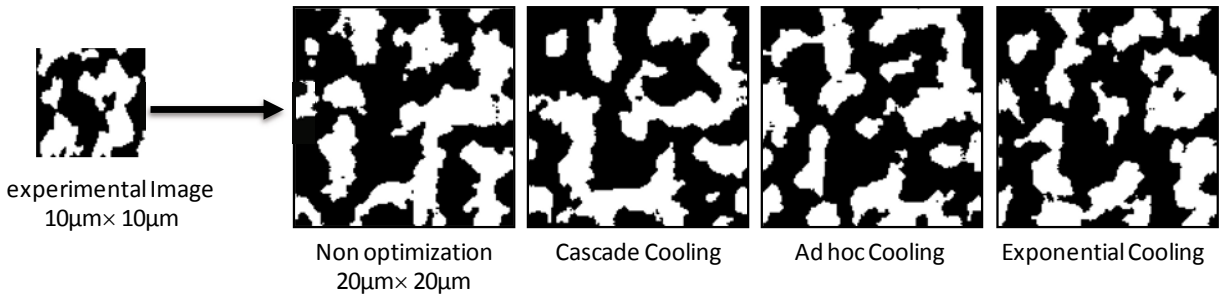


Figure 3: The processing speed comparison between non-optimized method and various simulated annealing (SA) method

Figure 4 shows 3D microstructure reconstruction result. Figure 4 (a) is a 2D porous reconstruction image on the cubic surface, Figure 4(b) shows 3D volume shape with opaque visualization and Figure 4(c) with transparent volume.

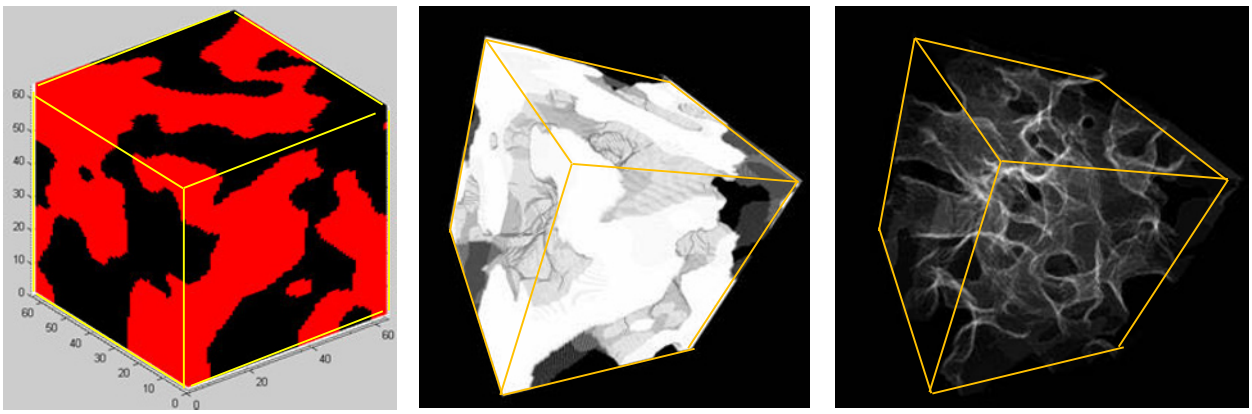

10μm× 10μm× 10μm

(a) 3D reconstruction surface (b) 3D opaque volume (c) 3D transparent volume

Figure 4: 3D microstructure reconstruction result.

## Conclusion

We applied optimization on stochastic reconstruction, correlation function recomputation to expedite the regression of microstructure reconstruction. The computation time is decreased from $O(n^2)$ to $O(n)$ for 2D microstructure reconstruction and from $O(n^3)$ to $O(n)$ for 3D reconstruction. This efficient and accurate method makes large 3D microstructure reconstruction practical. It is critical to structure information representation, fusion, reconstruction and hierarchical upscaling.

## Acknowledgements

This work was funded by PNNL LDRD Chemical Imaging Initiative project. PNNL is operated by Battelle Memorial Institute for the U.S. Department of Energy under contract No. DE-AC05-76RL01830.

## References

[1] K.S. Choi, Soulami, A., Li, D., Sun, X., Khaleel, M. A., Xu, L. and Barlat, F., submitted for SAE 2012 World Congress, 12M-0156 (2012).
[2] C. Yeong, S. Torquato, Physical Review E, 57 (1998) 495.

[3] Y. Jiao, F. Stillinger, S. Torquato, Physical Review E, 77 (2008) 031135.
[4] D. Cule, S. Torquato, Journal of applied physics, 86 (1999) 3428.
[5] C. Manwart, R. Hilfer, Physical Review E, 59 (1999) 5596.
[6] M.G. Rozman, M. Utz, Physical Review E, 63 (2001) 066701.
[7] Y. Mao, A. Gokhale, J. Harris, Computational materials science, 37 (2006) 543-556.
[8] D. Fullwood, S. Kalidindi, S. Niezgoda, A. Fast, N. Hampson, Materials Science and Engineering: A, 494 (2008) 68-72.
[9] D.T. Fullwood, S.R. Niezgoda, S.R. Kalidindi, Acta Materialia, 56 (2008) 942-948.
[10] H. Garmestani, M. Baniassadi, D. Li, M. Fathi, International Journal of Theoretical and Applied Multiscale Mechanics, 1 (2009) 134-149.
[11] M. Baniassadi, H. Garmestani, D. Li, S. Ahzi, M. Khaleel, X. Sun, Acta Materialia, 59 (2011) 30-43.
[12] D. Li, M. Baniassadi, H. Garmestani, S. Ahzi, M. Reda Taha, D. Ruch, Journal of Computational and Theoretical Nanoscience, 7 (2010) 1462-1468.
[13] R. Piasecki, Proceedings of the Royal Society A: Mathematical, Physical and Engineering Science, 467 (2011) 806.
[14] N.C. Kumar, K. Matouš, P.H. Geubelle, Computational materials science, 42 (2008) 352-367.
[15] S. Torquato, H. Haslach Jr, Applied Mechanics Reviews, 55 (2002) B62.
[16] D. Li, M. Khaleel, X. Sun, H. Garmestani, Computational materials science, 48 (2010) 133-139.
[17] S. Torquato, J. Beasley, Y. Chiew, The Journal of chemical physics, 88 (1988) 6540.
[18] P. Čapek, V. Hejtmánek, L. Brabec, A. Zikánová, M. Kočiřík, Transport in porous media, 76 (2009) 179-198.
[19] Y. Jiao, F. Stillinger, S. Torquato, Proceedings of the National Academy of Sciences, 106 (2009) 17634-17639.
[20] C. Manwart, S. Torquato, R. Hilfer, Physical Review E, 62 (2000) 893.
[21] V. Černý, Journal of optimization theory and applications, 45 (1985) 41-51.
[22] S. Kirkpatrick, C.D. Gelatt, M.P. Vecchi, science, 220 (1983) 671.
[23] N. Metropolis, A.W. Rosenbluth, M.N. Rosenbluth, A.H. Teller, E. Teller, The Journal of chemical physics, 21 (1953) 1087.

1st International Conference on 3D Materials Science
*Edited by: Marc De Graef, Henning Friis Poulsen, Alexis Lewis, Jeff Simmons, George Spanos*
***TMS (The Minerals, Metals & Materials Society), 2012***

# CHARACTERIZATION OF PORES AND CRACKS IN UNDERWATER WELDS BY μCT AND DIGITAL OPTICAL MICROSCOPY

Sidnei Paciornik[1]; Timo Bernthaler[2]; Valter dos Santos[1]; Mauricio Monteiro[1]; Marcos Henrique Mauricio[1], Alexandre Bracarense[3]; Ezequiel Pessoa[4]

[1]DEMa PUC-Rio, Rua Marquês de São Vicente 225, Rio de Janeiro, RJ, 22451-900, Brazil
[2]Aalen University Materials Research Institute, Beethovenstraße 1, D-73430 Aalen, Germany
[3]Mechanical Engineering Department, Universidade Federal de Minas Gerais, Av. Antônio Carlos 6627, Belo Horizonte, MG, 31270-901, Brazil
[4]Instituto Federal de Educação, Ciência e Tecnologia de Minas Gerais, R. Dr. Silvio Lobo 171, Betim, 32630-130, Brazil

Keywords: underwater weld, μCT, porosity, cracks

## Abstract

Underwater shielded metal arc wet welding with coated electrodes is a common procedure for in situ repair of structural parts of offshore oil production units. However, there are serious difficulties in obtaining sound welds similar to the ones achieved under atmospheric conditions. The water environment surrounding the weld pool is usually responsible for very high cooling rates and high hydrogen content in the weld metal. These factors may lead to the formation of porosity and cracks in the weld metal which are not precisely analyzed by the conventional 2D techniques. The 3D visualization and measurement of these defects can contribute significantly to a better characterization and prediction of weld metal properties. In the present work wet welded steel samples were analyzed by μCT, with the aim of analyzing the presence of pores and cracks, their concentration, spatial distribution, and orientation.

## Introduction

Underwater wet welding suffers from harsh conditions that, in spite of extensive efforts in research and development, still make it hard to obtain welded joints with full structural quality similar to that obtained under atmospheric conditions [1-5]. The AWS standard D3.6M:2010 "Underwater Welding Code" [6] classifies welds according to requirements of toughness, strength, ductility, hardness and bending. Research in wet welding aims at reaching properties similar to welds performed under atmospheric conditions. However, defects such as pores and cracks are detrimental to the weld mechanical properties.

The presence of water during welding creates high cooling speeds and hydrogen absorption by the weld pool. In turn, the presence of hydrogen leads to the formation of pores and cracks in the weld metal. Moreover the concentration of these defects depends on the welding depth. Specifically, the porosity increases with welding depth. On the other hand, crack presence has a more complex relationship to depth, which is not a topic of the present paper.

Additionally, very few studies about cold cracks in the weld metal are available. The occurrence and measurement of micro-cracks in the weld metal is rarely reported because usual tests required for welding procedure qualification only require macrographic analysis of the cross section at 5x. Under these conditions the transversal weld metal cracks are usually not revealed, independent of the electrode and equivalent water depth. However, in the longitudinal section, cracks have been commonly observed under the optical microscope, depending on the diffusible hydrogen content (7-9). The same authors correlate the presence of these small transversal cracks with low weld metal ductility.

In the present paper x-ray microtomography (μCT) was evaluated as a tool to image and quantify pores and cracks in underwater welds. Samples and image acquisition conditions were selected to allow separating the contribution of the two types of defects. The visibility of these defects under different experimental conditions was evaluated and image processing procedures were established to segment and measure 3D parameters.

## Experimental

Welding and Samples

Multipass butt welds were performed on a 19 mm thick A36 steel plate with a 3.25 mm rutillic electrode in the flat position. The V preparation had a root opening of 3 mm and 45$^{o}$ angle.
Two types of samples were cut from the original welded plates:

- Blocks (5S1) – 15x15x19 mm$^3$ blocks containing both base metal (A36 steel) and weld metal – these samples were more representative of the material due to their larger volume, but also posed resolution limitations to μCT, as discussed below. The welds were performed with a mechanized gravity system in a hyperbaric chamber to simulate an equivalent welding depth of 20 m. They were mainly used to reveal pores.
- Slabs (1N1) - 2 mm thick slabs containing just weld metal machined from a larger block – due to their smaller volumes these samples were less representative but allowed achieving finer resolution. The welds were performed with a mechanized gravity system in a small tank at 0.5 m depth. They were mainly used to reveal cracks, as porosity is essentially nil at this depth.

Details of the samples and their welding conditions are listed in Table 1.

Table 1 - Welding conditions

| | **Samples** | |
|---|---|---|
| **Conditions** | 5S1 | 1N1 |
| Electrode type | Rutillic | Rutillic |
| Depth (m) | 20 | 0.5 |
| Diffusible hydrogen measured in samples welded at 0.5 m (ml/100g) | 85.4 | 88.7 |

Microtomography

A GE v|tome|x s with a dual tube configuration (microfocus/nanofocus) operating at up to 240kV/300W – this equipment was used to image both thick and thin samples. Its high energy allowed imaging the thick blocks, albeit at a coarser 30 μm voxel size. It was also used for the slabs and tensile samples, down to 5 μm voxel size. No further preparation of the samples was necessary Image acquisition conditions are listed in the Table 2.

Table 2 - μCT acquisition conditions

| | **Samples** | |
|---|---|---|
| **Conditions** | 5S1 | 1N1 |
| Tomograph | VTome\|X | VTome\|X |
| Source Settings (kV/μA) | 240/120 | 120/60 |
| Pixel Size (μm) | 30 | 5 |
| Acquisition. Time (s) | 0.75 | 0.50 |
| Views/Angular Step (#/$^{o}$) | 600/0.6 | 800/0.45 |

## Results and Discussion

Visualization and Quantification of Pores

Sample 5S1 was welded at 20 m depth and should present high porosity. Moreover, due to its high diffusible hydrogen, it should also present cracks. However, when using the welded block the resolution was limited to 30 μm, what precludes the visualization of cracks.

Figure 1 shows a reconstructed slice of the 5S1 sample. The bottom left of the image corresponds to the base metal and is free of pores, which are concentrated in the weld metal. The left part of Figure 2 is a rendered 3D image obtained after suitably processing the image stack to segment pores and the metal matrix (see next paragraph for details). Using the Marching Cubes algorithm the 3D models for metal and pores were rendered and superimposed, and the opacity of the metal was reduced to allow visualization of the pores. Another view of the same model is shown in the right part of Figure 2. In this image certain relevant characteristics of the pore distribution are visible, e.g. the alignment between pores, with their main axes pointing towards the welded surface with an inclination due to the welding direction. A large elongated melting defect is also visible at the bottom of the weld, at the interface with the base metal.

To evaluate the porosity in the weld the image stack was processed with the following sequence. A polygonal region of interest (ROI) was manually drawn to select just the weld metal. This ROI was tested in a few a images and extrapolated to the whole stack to create a volume of interest (VOI) that was totally included in the weld metal. The pores were segmented with a simple threshold and their total volume obtained. The estimated volume fraction of pores was 3.4%. In comparison, an area fraction of 2.2% was measured by traditional metallography of cross sections of another part of the same weld. These results are hard to compare due the lack of homogeneity in the welds and to the difficulty of defining the VOI, but are nevertheless of the same order of magnitude. Considering that μCT resolution, in this case, was much coarser than for optical microscopy, and thus many small pores were not imaged, the larger volume fraction indicates that the sampling used in traditional metallography strongly underestimated the true porosity.

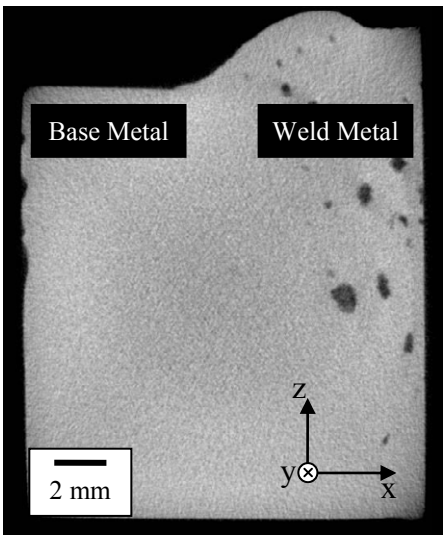


Figure 1 – μCT of sample 5S1. A single reconstructed slice revealing pores.

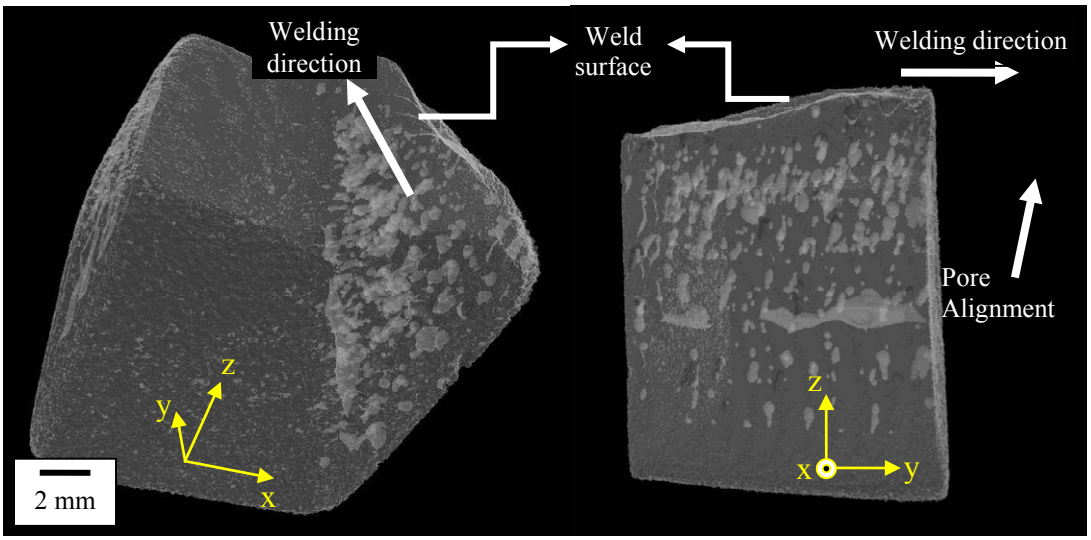

Figure 2 – µCT of sample 5S1 revealing pore concentration in the weld metal (left) and pore alignment (right).

Visualization and Quantification of Cracks

Sample 1N1 was welded at 0.5 m depth and should present very low porosity. Still, due to its high diffusible hydrogen, it should present extensive cracking. In this case thin slabs were machined out of the weld metal to allow reaching 5 µm resolution in µCT and visualization of cracks. Because cracks are very thin they are strongly affected by noise and by the threshold level used in their segmentation. Thus, a pre-processing step with the Kuwahara filter [10] (edge-preserving low-pass) was applied to reduce noise. Figure 3 shows a before and after view of an image slice. Cracks can then be accurately segmented without excessive noise.

Figure 4 shows the resulting 3D model composed of the solid metal, semi-transparent grey, and the cracks, shown in light grey. As expected, cracks are roughly parallel to each other and normal to the welding direction.

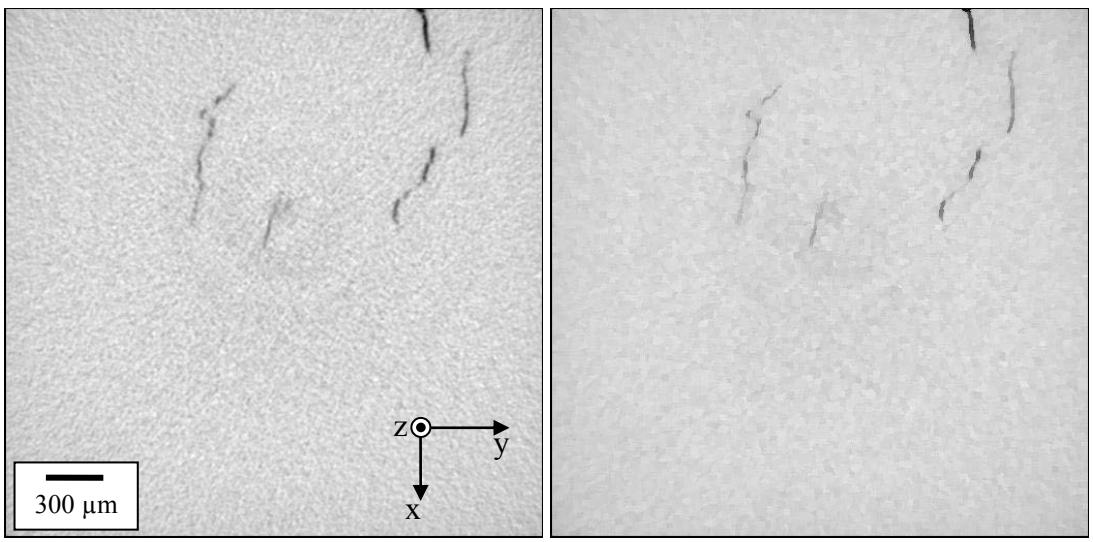

Figure 3 – Sample 1N1. Image slice, with cracks, before and after application of Kuwahara filter.

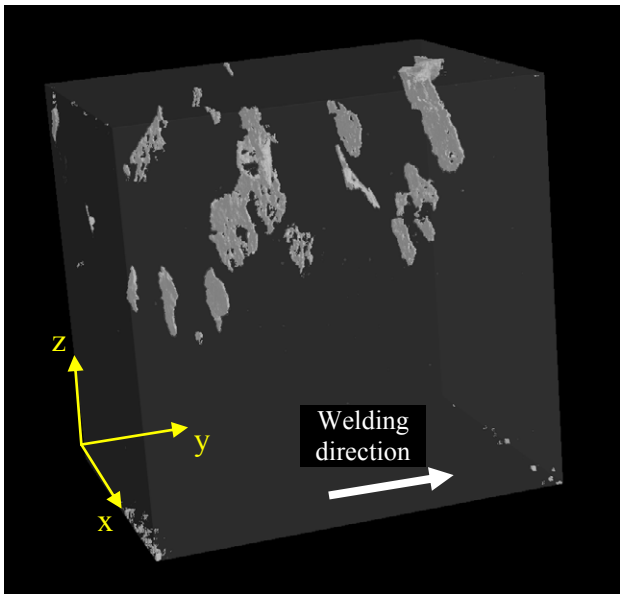

Figure 4 – Sample 1N1. 3D model showing cracks.

Crack quantification, either in 2D or 3D, is not straightforward due to their small thickness and mutual alignment. An inadequate selection of cross-section for 2D analysis (e.g. a xz plane in Figure 4) may lead to no cracks detected. In a previous work with optical microscopy, Mauricio et al. [9], employed careful specimen preparation, large mosaic images, and extensive image processing to measure the number of cracks and their total length in different welds. Cross sections were selected in the xy plane (Figure 4) to guarantee intercepting cracks. It was shown that both parameters correlated well with diffusible hydrogen content.

In 3D, besides simple measurements such as number of cracks, their volume and surface area, it would also be interesting to quantify their alignment orientation relative to the welding direction. Other parameters, such as tortuosity, which could correlate to mechanical properties can also be useful. This quantification is under development and will be shown elsewhere.

## Conclusions

In this initial μCT evaluation of underwater wet welded samples it was shown that it is possible to visualize pores and cracks, their spatial distribution and orientation. The results are consistent with the known behavior of these defects, but substantially extend the traditional 2D analysis performed in cross-sections. When the goal is to foresee mechanical properties and the qualification of underwater welds under strict requirements, the 3D visualization and quantification of the defects is a very powerful tool.

The main limitations of μCT are the power of the tomograph, necessary to traverse large and representative samples of a dense material such as steel, and the compromise between sample size and resolution, to allow visualization of small defects. Initial results (not shown) with an XRadia MicroXCT tomograph with special x-ray optics reached 2.17 μm resolution in 2 mm thick slabs, allowing an even finer visualization of cracks.

## Acknowledgments

The authors are grateful to Markus Schwenger and Thomas Samtleben, from Aalen University, Germany, for their support in tomography and image file organization. The support of Allen Gu and S. H. Lau, from XRadia, USA, with high resolution μCT, is also acknowledged.

## References

1. T. G. GOOCH, "Properties of Underwater Welds. Part 1. Procedures Trials," *Metal Construction*, 8 (1983), 164-167.

2. S. LIU et al., "Electrode Formulation to Reduce Weld Metal Hydrogen and Porosity" (Paper presented at the 13th Offshore Mechanics and Arctic Engineering Conference, Copenhagen, 1994), 291-298.

3. S. LIU et al., "Welding Consumables and Weldability" (Paper presented at the International Workshop on Underwater Welding of Marine Structures, Louisiana, 1994), 321-350.

4. Y. Suga, and A. Hasui, "On formation of porosity in underwater weld metal" (Paper presented at the IX Meeting of the International Institute of Welding, 1983), 1388.

5. SSC-370, Ship Structure Committee, "Underwater Repair Procedures for Ship Hulls (Fatigue and Ductility of Underwater Wet Welds)", 1994.

6. AMERICAN WELDING SOCIETY. Specification for Underwater Welding, ANSI/AWS D3.6M:1999.

7. A. Q. BRACARENSE et al., "Comparative study of commercial electrodes for underwater wet welding", (Paper presented at the International Congress of the International Institute of Welding - 2nd Latin American Welding Congress, São Paulo, 2008).

8. V. R. SANTOS et al., "Recent Evaluation and Development of Electrodes for Wet Welding of Structural Ship Steels" (Paper presented at the 29th International Conference on Ocean, Offshore and Arctic Engineering, Shangai, 2010).

9. M. H. P. MAURICIO et al., "Quantitative Hydrogen Cracking Evaluation by Digital Optical Microscopy", (Paper presented at the International Microscopy Congress – IMC17, Rio de Janeiro, 2010).

10. M. KUWAHARA et al. "Processing of RI-angiocardiographic images", *Digital Processing of Biomedical Images*, ed. K. Preston and M. Onoe (New York, NY: Plenum Press, 1976), 187-203.

1st International Conference on 3D Materials Science
*Edited by: Marc De Graef, Henning Friis Poulsen, Alexis Lewis, Jeff Simmons, George Spanos*
***TMS (The Minerals, Metals & Materials Society), 2012***

# CHARACTERIZATION OF CARBONATE ROCKS THROUGH X-RAY MICROTOMOGRAPHY

Débora Pilotto[1], Sergio Fontoura[2], Sidnei Paciornik[3], Marcos Henrique de Pinho Mauricio[3]

[1]GTEP, [2] Department of Civil Engineering, [3]Department of Materials Engineering
PUC-Rio; Av. Marquês de São Vicente, 225; Rio de Janeiro, RJ, 22451-900, Brazil.

Keywords: x-ray microtomography, carbonate rocks, porosity, digital microscopy

## Abstract

Image characterization of rocks is generally carried out by optical and scanning electron microscopy techniques. In this paper, the non-destructive technique of X-Ray micro tomography (μCT) was used in order to obtain microstructural parameters. The experimental program consisted in obtaining these properties from three different carbonate rocks: the Roman, Turkish and Itaboraí Travertines. The rocks were selected since they possess similar properties to the Brazilian oil-bearing pre-salt rocks. The results have shown that μCT is very useful in a) determining the porosity and pore size distribution, as compared to traditional porosimetry methods, b) establishing the pore arrangement within the rock matrix and c) detecting pore connectivity. Additionally, the generation of 3-D models allowed a faithful representation of the samples and allowed the selection of regions for thin section preparation of their most representative features, which were then analyzed by Digital Optical Microscopy.

## Introduction

Hydrocarbon reservoirs in carbonate rocks represent circa 50% of worldwide oil & gas production. These reservoirs are very complex since they are quite heterogeneous. A striking example of these reservoirs is the Ghawar oil field in Saudi Arabia where circa 5 million barrels of oil are extracted per day from the Arab D carbonate reservoirs [1]. In Brazil, carbonate rocks gained great importance with the discovery of the pre-salt reservoirs.

In order to understand and characterize microstructural parameters of these reservoirs major efforts will be required in research and development. In order to contribute to this goal, the non-destructive technique of X-Ray micro tomography (μCT) was employed to obtain microstructural parameters. This technique has been widely used in the petroleum industry for the analysis of reservoir rocks because it provides important microstructural parameters, such as porosity, permeability, and pore size distribution [2].

This paper aims to contribute in this regard, through the characterization of microstructural parameters of carbonate rocks with a focus on drilling optimization.

## Materials and Methods

Three different carbonate rocks, the Roman, Turkish and Itaboraí Travertines were selected as possible analogues to the pre-salt rocks. Figure 1 shows samples from these rocks.

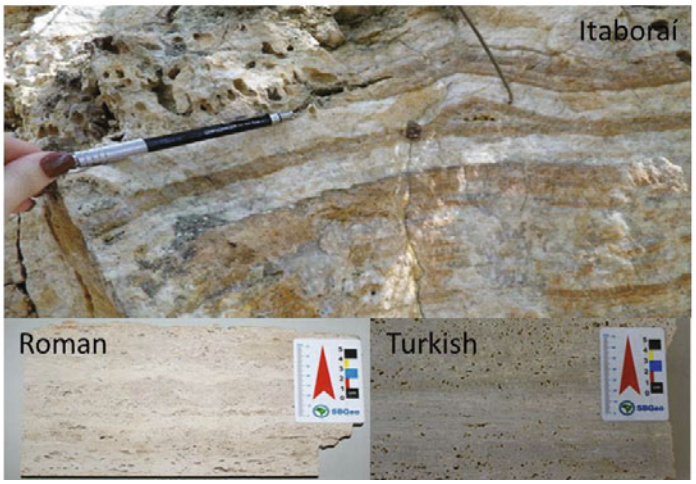

Figure 1 – Travertines studied in this research.

The Roman travertine was chosen since it presents similar texture and porosity to the pre-salt carbonate reservoir facies. The Turkish travertine was chosen since it has similar characteristics to the Roman travertine. The Itaboraí travertine was selected due to the presence of quartz in its composition and its apparent strength, which occurs in the pre-salt reservoir facies.
The experimental program consisted in digital imaging analysis [3,4] from optical micrographs of thin sections and X-Ray microtomography (μCT).

X-Ray Microtomography (μCT)

Microtomographic data of the samples were collected using a Skyscan μCT scanner, model 1173. The tests were performed in Lagesed (IGEO/UFRJ). This equipment has a X-ray tube with a maximum power of 8W. Tests employed 80kV and 100μA in the acquisition of the images, and were performed in the samples shown in Figure 2. The samples were cut with a saw frame, then with a band saw and finally ground to create smooth surfaces.

Figure 2 – Samples analyzed in Skyscan μCT scanner. From left to right: Itaboraí Travertine, Turkish Travertine and Roman Travertine.

A 1 mm thick aluminum filter was used for data acquisition with the aim of reducing the effect of beam hardening. Spatial resolution was 34 μm for the Itaboraí sample, and 26 μm for Turkish and Roman samples.

Acquired images were processed with the sequence depicted in Figure 3, developed under the CTAn program by Skyscan [3]. After an initial segmentation [3,4] of the rock matrix, with pores, a Region/Volume of Interest (ROI/VOI) was adapted to the boundaries of the irregular shape samples. Morphological operations [4,5] were applied to the binary image with the goal of reducing edge problems and eliminating small objects. Porosity was then measured followed by the generation of a 3D Model of the solid rock with pores. The pores were independently segmented and a separate 3D model was also created. This allowed the superimposition of the two models for more flexible visualization of the result.

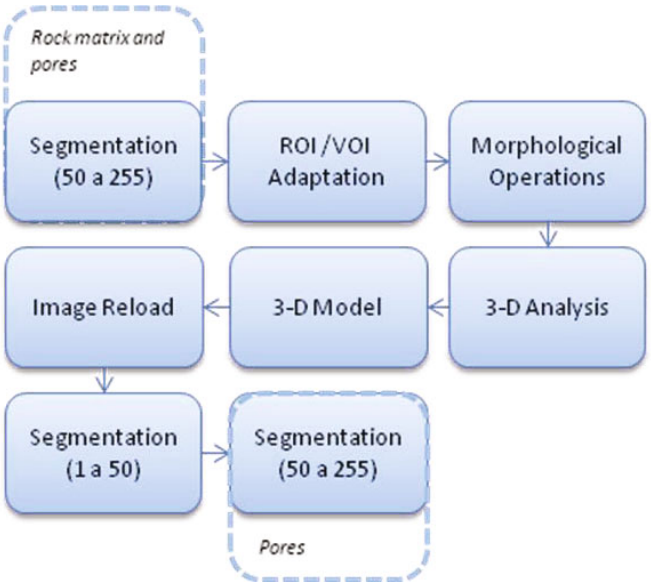


Figure 3 – Methodology of µCT test.

Digital Optical Microscopy - DOM

Thin sections were prepared in slides and dyed with methylene blue to reveal the pores. The digitization of the slides consisted of capturing images in mosaics. For this purpose a Zeiss optical microscope, model AxioImager.M2m, with XY motorized stage and automatic focus (motorized Z axis), and an AxioCam MRc 5 camera (1292x968 pixels resolution) was used. To allow covering full slides while keeping image memory manageable, a 5X objective (2.11 µm/pixel) was chosen.
The AxioVision software was used to control the microscope and camera. An image processing and analysis procedure was developed to process the large mosaic images and measure the porosity [6]. Pores were marked by tinting the thin sections with blue methylene and detected by RGB threshold segmentation [4].

## Results

µCT

Table 1 shows the total, connected and unconnected porosity computed from the 3-D analysis of the samples.

Table 1 – Results of µCT.

| Sample | Total Porosity (%) | Open Porosity (%) | Closed Porosity (%) | Open/Closed Ratio |
|---|---|---|---|---|
| Itaboraí Travertine | 0.24 | 0.16 | 0.08 | 2 |
| Roman Travertine | 6.49 | 5.38 | 1.11 | 4,9 |
| Turkish Travertine | 4.26 | 2.33 | 1.93 | 1,2 |

It can be seen in Table 1 that the Itaboraí travertine sample has lower porosity than the other two rocks. The Roman travertine sample showed the highest porosity, and also the largest ratio between open and closed pores (~5x). The Turkish travertine presented total porosity between the Roman and Itaboraí and a similar amount of open and closed pores.
A 3-D distribution of pore diameters in the samples was also carried out. Figure 4 shows the results for the Roman travertine sample.

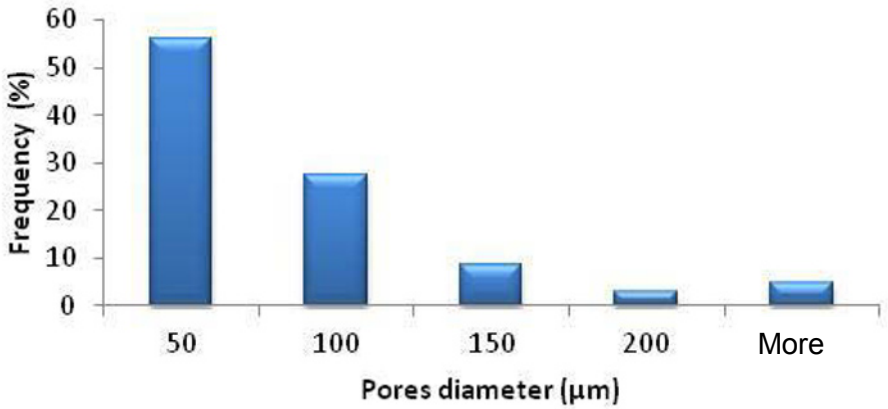


Figure 4 – Histogram distribution of pore diameter in the sample of Roman travertine

Figure 5 shows the distribution of porosity throughout the 2-D µCT sections of the Roman travertine sample. Note that the graph shows a distribution of porosity ranging from 1 to 13%,. The average 2-D porosity was found to be 7.04%, showing a good agreement with the results derived from the 3-D analysis (6.49%).

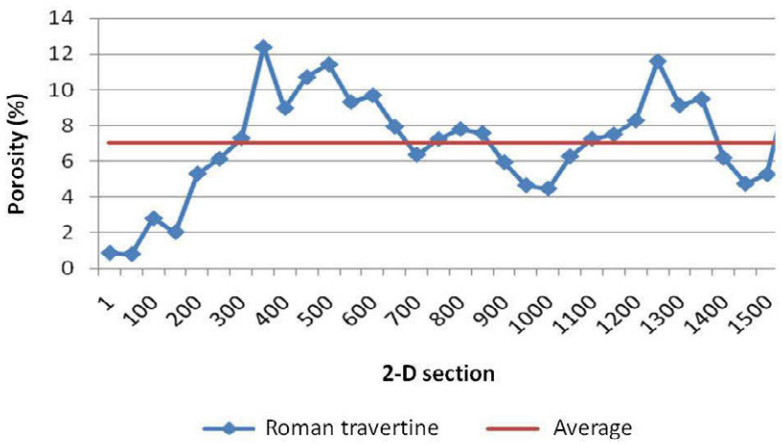


Figure 5 – Profile of porosity of 1550 2-D sections of the Roman travertine sample.

Figure 6 shows the 3-D reconstructed image of the Roman travertine sample. It is noted that the sample is a complex network of connected pores.

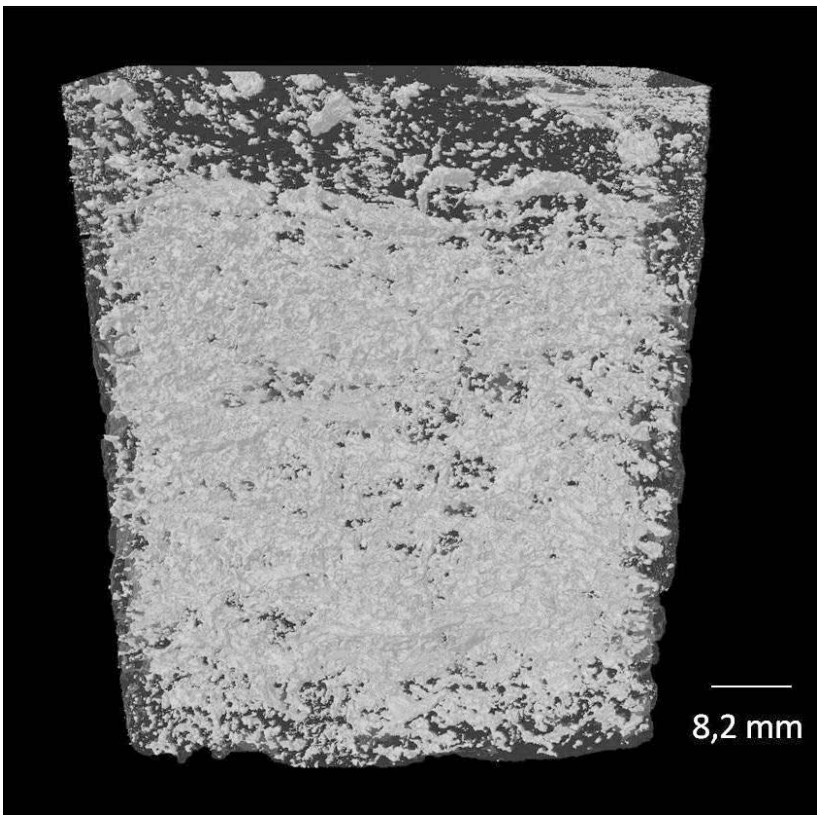


Figure 6 – 3-D reconstructed image of the Roman travertine sample.

DOM

Table 2 shows the porosity results obtained from the thin sections analyzed by digital optical microscopy.

**Table 2 – Results of DOM – Porosity (%)**

| | Itaboraí | Roman | Turkish |
|---|---|---|---|
| Thin section 1 | 0.02 | 5.80 | 0.27 |
| Thin Section 2 | 0.21 | 6.60 | 0.13 |
| Thin section 3 | 0.57 | – | – |
| Average | 0.27 | 6.20 | 0.20 |

Comparing Tables 1 and 2, it is noted that the porosity of Itaboraí and Roman travertine samples measured by μCT and DOM are similar – 0.24% versus 0.27% for Itaboraí, 6.49% versus 6.20% for Roman, respectively. For the Turkish travertine samples porosity obtained by DOM is much lower than by μCT. This difference could be explained by the fact that some of the pores were not completely filled with the methylene blue dye, what could underestimate the value of porosity in the thin sections.

## Conclusions

The non-destructive technique μCT proved to be useful in the analysis of porosity, pore size distribution and observation of the pore arrangement within the rock matrix. μCT also allowed detecting the connectivity between pores within the rock matrix. The rendered 3D models accurately represented the samples analyzed.
The total porosity determination by digital imaging processing from thin sections is simple and fast. The results are quite similar to the ones from the 3-D analyses performed in Roman and Itaboraí travertines.
The optical resolution (2.11 μm) is much finer than for μCT (34 or 26 μm) what should lead to higher porosity values. However, given the wide variation along cross sections, as shown in the μCT analysis (Figure 5) it is evident that sampling is a relevant issue that can substantially bias the results.
When comparing μCT results to traditional Hg or BET porosimetry methods (shown elsewhere), the open/closed pores ratio is a relevant parameter, as these traditional techniques cannot access closed pores. Even though, again, μCT resolution is still much coarser than for porosimetry, it can provide unique information that the other techniques cannot.
Thus, whenever available full 3D μCT analysis should be the technique of choice for porosity evaluation in oil-bearing rock samples.

## Acknowledgements

We acknowledge the support of Professor Leonardo Borghi (Lagesed/UFRJ) in μCT data acquisition.

## References

1. M. S. AMEEM et al. “Predicting rock mechanical properties of carbonates from wireline logs (A case study: Arab-D reservoir, Ghawar field, Saudi Arabia)”, *Marine and Petroleum Geology*, 26 (2009), 430-444.

2. J. S. FERNANDES, C. R. APPOLONI, C. P. FERNANDES. “Microstructural Parameters Determination and 3D Imaging Reconstruction from Reservoir Rocks by X-Ray Microtomography (in portuguese). *Revista Ciências Exatas e Naturais*, 11(1) (2009), 35-47.

3. J. C. RUSS, *The Image Processing Handbook* (New York, NY: CRC, 2006).

4. CT Analyzer, Version 1.11.0.0, Copyright 2003-2011 Skyscan, www.skyscan.be.

5. S. PACIORNIK and M. H. P. MAURICIO, “Digital Imaging” *ASM Handbook*, vol. 9, ed. G. F. Vander-Voort, (Materials Park, OH: American Society of Materials International, 2004) 368-402.

6. S. PACIORNIK and J.R.M D’ALMEIDA, “Measurement of Void Content and Distribution in Composite Materials through Digital Microscopy,” *J. Comp. Mater.*, 43(2) (2009), 101-112.

1st International Conference on 3D Materials Science
*Edited by: Marc De Graef, Henning Friis Poulsen, Alexis Lewis, Jeff Simmons, George Spanos*
***TMS (The Minerals, Metals & Materials Society), 2012***

# SUBGRAIN BOUNDARY IDENTIFICATION IN 3D EBSD DATA THROUGH FAST MULTISCALE CLUSTERING

Brian Soe[1], Cullen McMahon[1], David Golay[1],
Md. Zakaria Quadir[2], Michael Ferry[2], Lori Bassman[1]

[1]Department of Engineering, Harvey Mudd College;
301 Platt Blvd., Claremont, CA 91711 USA
[2]School of Materials Science and Engineering, University of New South Wales;
Sydney NSW 2052, Australia

Keywords: Electron Backscatter Diffraction, Segmentation, 3D EBSD,
Fast Multiscale Clustering, Microbands, Low Angle Boundaries

## Abstract

Complete and accurate characterization of subgrain microstructural features permits study of the relationships among loading, microstructure and properties in plastically deformed metals. 3D electron backscatter diffraction data can produce reconstructed crystallographic volumes, however low angle subgrain boundaries cannot be determined simply with point-to-point misorientation thresholding because many are gradual transitions in orientation. We demonstrate a novel 3D implementation of the data segmentation technique Fast Multiscale Clustering, which uses a quaternion representation of orientation and a corresponding distance metric. Examples of the 3D segmentation of microbands and morphological analysis from the results are presented for die-compressed nickel single crystal and uniaxially loaded commercially pure aluminum.

## Introduction

Subgrain microstructural features in deformed metals play important roles in dictating mechanical and physical properties of the materials and their use in a wide range of applications. There is ample evidence that two-dimensional analysis of microstructural features is insufficient for characterizing true geometries and crystallographic relationships (for example [1,2]). An understanding of these features calls for three-dimensional crystallographic investigation.

Three-dimensional electron backscatter diffraction (EBSD) is a technique that uses a focused ion beam (FIB) as a serial sectioning tool together with EBSD to map each section and generate crystallographic volumes of material at submicron resolution. The resulting 3D dataset can be processed to generate the shapes and distributions of features of a microstructure. While preliminary reconstruction may be done using commercial software tools, they do not allow the accuracy in low angle boundary identification, skew correction, fitting of surfaces or local surface analysis needed for this particular problem. Methods in this paper address all of these issues, with a focus on a novel algorithm for repeatable identification of subgrain boundaries. Although the misorientation thresholding capabilities of commercial software can be used to determine grain boundaries, subgrain features may have gradual boundaries with pixel-to-pixel misorientations of a few degrees or less. As demonstrated in Figure 1, there may be no single threshold value that is effective for boundary identification [3]. The presence of noise further diminishes the effectiveness of thresholding. The method presented here uses a Fast Multiscale Clustering (FMC) algorithm that incorporates regional information from multiple length scales, rather than relying on pixel-to-pixel misorientation, to segment the data.


Figure 1: Inverse pole figure (IPF) color maps showing misorientation thresholding of an EBSD data set containing microbands in a cold rolled Al sample. Black boundaries indicate pixel-to-pixel misorientations of a) 1 degree, which produces boundaries dominated by noise, and b) 2 degrees, which does not capture important boundaries.

## Fast Multiscale Clustering

Clustering algorithms are tools for determining the structure of a data set using regional information. Fast Multiscale Clustering (FMC) is an established image segmentation method introduced by Sharon et al. [4], inspired by algebraic multigrid solvers. FMC uses a graph representation of the data, which begins with each pixel as its own node at the finest resolution. The adjacent nodes of the graph are related to one another by weights representing the similarity between the two nodes. The graph is recursively simplified, in a process known as coarsening, by combining nodes based on a similarity metric to create lower and lower resolution representations of the data. At each level of resolution, each coarse node represents a potential segmentation of the original graph. The quality of a particular segmentation is indicated by a saliency value, defined as the ratio between the similarities relating a node and its neighboring nodes (external weights) and the similarities among data points within a node (internal weights). At the end of the recursive process, the nodes with the lowest saliency are selected as the segmentation solution.

Use of FMC with EBSD orientation data is more complex than for image processing, because of the nonlinear nature of orientation data. For this work, FMC has been generalized with a similarity metric based on misorientation computed from a quaternion representation of orientation [3]. This version of FMC incorporates two aggregative properties to assist in segmentation. Aggregative properties are scale-dependent features of coarsened nodes, in this case the quaternion mean of points within a node and the variance in orientation or points within a node. A generalization of Mahalonobis distance $D_{\text{Maha\_gen}}$ is computed from these properties and is used to adjust the graph weights after each coarsening step (Equation 1).

$$D_{\text{Maha\_gen}}(X_i, X_j) = \sqrt{\frac{d_{\text{misorien}}(\bar{X}_i, \bar{X}_j)^2}{\min(\sigma_i^2, \sigma_j^2)}} \tag{1}$$

Where the distance function $d_{\text{misorien}}$ is the misorientation between node mean orientations and $\sigma^2$ is the distance function variance. The segmentation results for a single slice of 3D-EBSD data within a single grain of cold-rolled aluminum sample containing microbands with gradual orientation variations is shown in Figure 2.

Figure 2: The data set segmented by FMC with a novel distance function metric.

Three-dimensional reconstructions of microbands have been created by stacking 2D segmentation of EBSD data slices [5]. However, FMC can be generalized to perform a true 3D segmentation. Three-dimensional analysis offers the significant advantage of consistent analysis slice to slice, with all segmentation done in a single process. All spatial directions are equivalent, meaning that clustering equally takes into account regional information in slices above and below a point and within the 2D slice. FMC clusters and their boundaries therefore encapsulate a continuous and smooth volume of crystallographic data. However, treatment of the data as a single complete point cloud requires additional pre-processing prior to FMC analysis. First, the 3D data must be reconstructed with corrections for instrument drift and skew within each slice. Second, the nearest neighbors to each point must be known for creation of the initial graph.

## Formation of Initial Graph from 3D Data

The volumes studied contain no grain boundaries, so have no internal markers such as triple points that can be used to guide slice alignment. As shown in Figure 3a, a rectangular pillar created with FIB provides an external reference. In processing the data, a bilinear transformation of the data in each slice corrects for skew and offset that come from inexact stage positioning during EBSD data collection. The transformation uses four features, in most cases the corner points of the pillar as shown in Figure 3b, that form a general convex quadrilateral. This is then transformed to a biunit square with corners at $(\pm1,\pm1)$ and then scaled to the physical dimensions of the pillar measured using ion beam imaging (Figure 3c). Fiducial marks (Figure 3a) that produce non-indexed points in each data slice are used to confirm alignment when the data set is reconstructed (Figures 3d and 3e).

The result of this transformation is that data points are no longer on a uniform rectangular grid. Construction of the initial graph for FMC requires knowledge of the nearest neighbors for each point. This is accomplished with a lookup table for the full 3D data set, which provides the indices of all neighboring points within a fixed radius of each point. To find these neighbors, each point is first mapped to the nearest node of the original uniform rectangular grid. The grid organization allows immediate identification of all points in a local region from the adjacent graph nodes. For each point, the distance between itself and the local regional points is easily compared. For this analysis, the radius criterion was chosen to give an average of six neighbors, the same number that would be used in the case of a rectangular grid.

## Results

The FMC algorithm has been applied to a 18 (RD) × 19 (TD) × 3 (ND) micron volume of a 3D EBSD data set taken with 0.1 micron resolution from a channel die-compressed nickel single crystal sample. The volume is built from 30 slices and contains just over one million points [6,7]. Results are shown in Figure 4, with clusters given random colors for differentiation. Unlike the

aluminum shown in Figure 1, almost no variation in orientation can be discerned from the IPF colormap. Center to center microband misorientations vary in the range of 2.5 to 7 degrees [6].

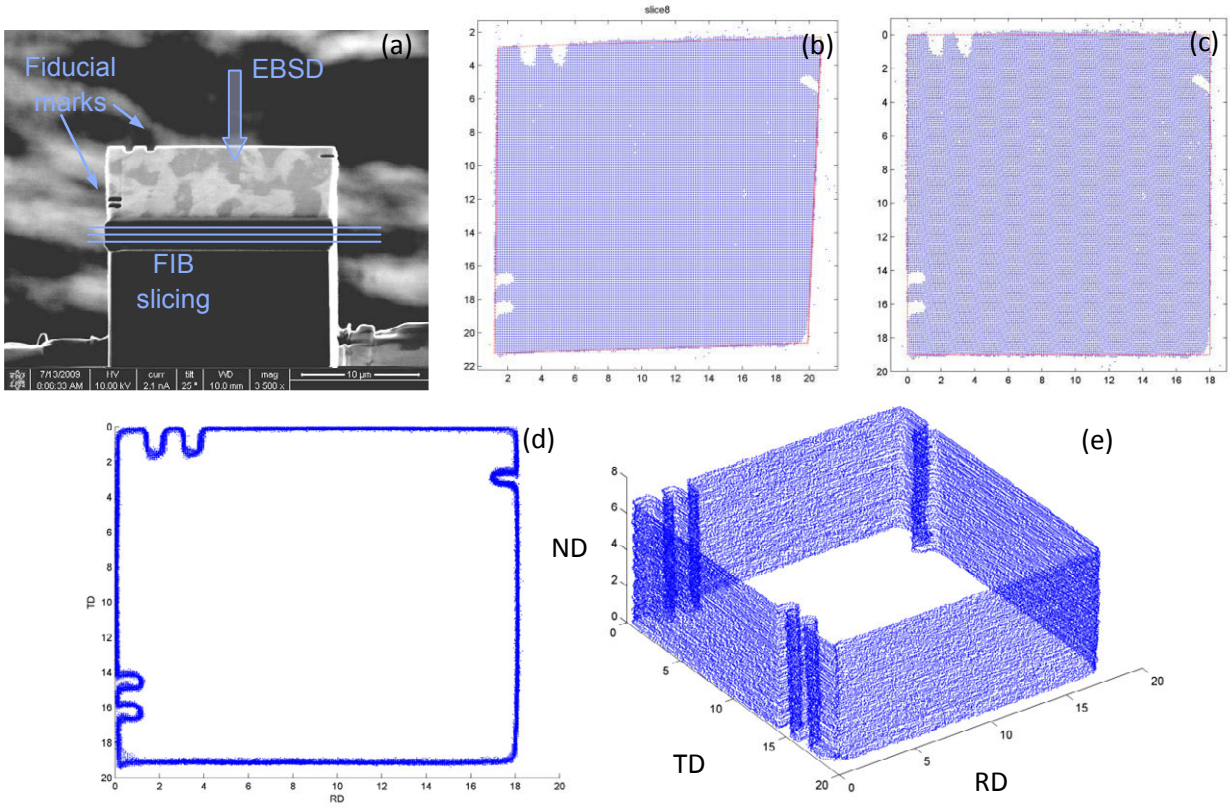


Figure 3: a) Pillar formed by FIB in a Ni single crystal die-compressed sample with area 18 x 19 microns. b,c) Pillar corner points are identified and skew and offset are corrected by a bilinear transformation. d,e) Corrections are verified by alignment of fiducial marks through the data set, which has a depth of 6.7 microns.

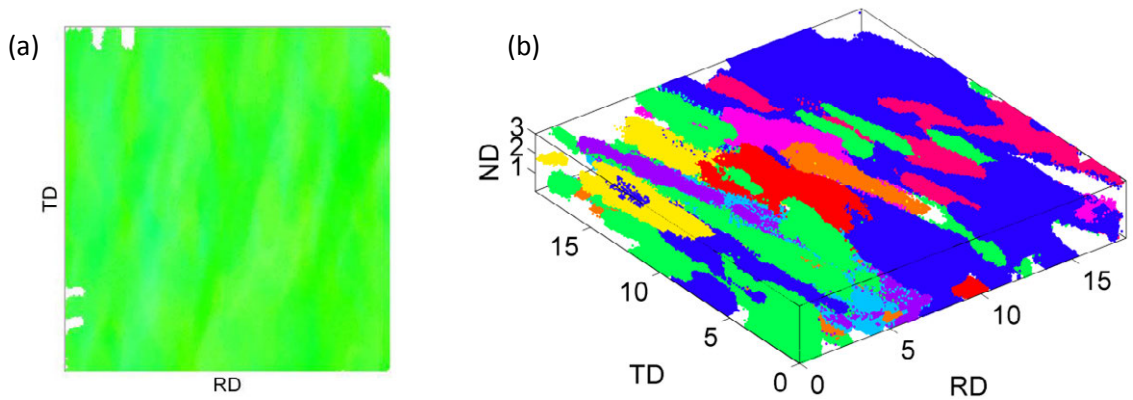


Figure 4: a) IPF color map of one slice in an EBSD data set containing microbands in a channel die-compressed Ni single crystal sample. b) Segmentation of a volume of the 3D EBSD data set. Note that while the distinct clusters appear similar to grain identification performed in commercial software, the method is very different. The boundaries are low angle and many are gradual.

The 3D segmentation algorithm was also applied to a 12 (RD) × 5 (TD) × 2 (ND) micron volume of the cold-rolled aluminum sample of Figure 1, which was built from 20 data slice and contains roughly 120,000 points (Figure 5a). The boundary points encapsulating a cluster are easily determined. Microband surfaces can be reconstructed from the bordering boundary points between two clusters, shown in Figure 5b.

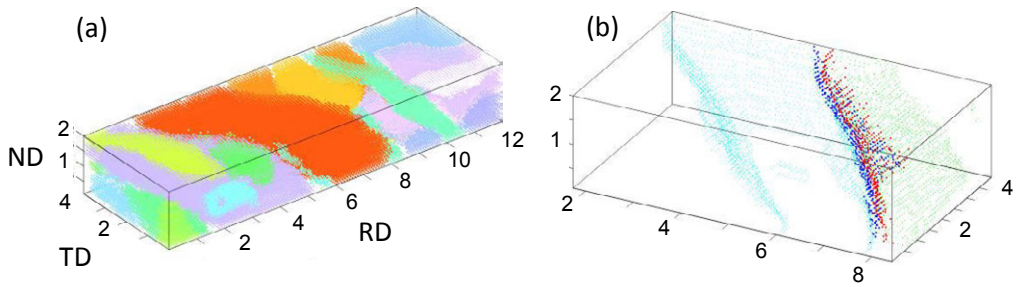


Figure 5: a) Segmentation of a volume of 3D EBSD Al data set. b) Isolation of points in adjacent clusters for analysis of local boundary properties.

These continuous boundaries and surfaces allow quantitative analysis of microstructural features. Applications include determination of point-to-point misorientation across the boundary, local boundary curvature and width, local orientation with respect to crystallographic planes, and overall cluster to cluster misorientation. As an example, local curvature of the isolated microband surface on Figure 5b is shown in Figure 6. These studies can provide insight into microstructural features and their formation.

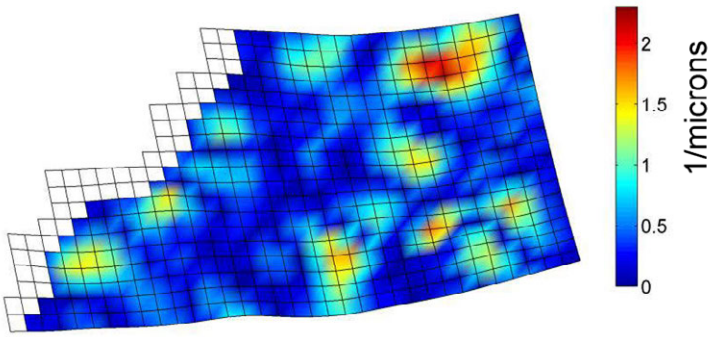


Figure 6. A microband surface isolated from the rolled aluminum sample, showing local curvature which is accented by color.

## Discussion

FMC is a novel approach to determine low angle boundaries, for which traditional thresholding is insufficient. In order to validate the results of the method a 3D EBSD data set from a multi-grain data set is being used. The grains in this 3D data set may be found by thresholding in commercial software and their boundaries compared to those produced by FMC, which can detect these clear boundaries as well as more subtle ones. In more challenging subgrain data sets tuning of several well-understood algorithm specific parameters is required, for example to specify the level of segmentation.

Implementation of FMC on large data sets is currently limited by memory consumption and run time. A million point data set requires over sixteen gigabytes of RAM and over a day to run on an 8 core processor. FMC is theoretically an O(N) algorithm, but the implementation is slowed by large memory processes. Future work includes modification of the algorithm's coarsening steps to reduce the growth of the graph in the first few recursive runs.

## Acknowledgements

This work was supported by grants from the National Science Foundation (DMR-0907240), the Australian Research Council Centre of Excellence for Design in Light Metals (CE 05611574), and the Harvey Mudd College Department of Engineering. We thank the Harvey Mudd College and University of New South Wales students working on related projects: Cassie George, Ayyappa Vemulkar, Andrew Loeb and Nasima Afrin, and Scott Sitzman at Oxford Instruments for collaboration on validation of methods with commercial software.

## References

[1] A.D. Rollett et al., "Three-dimensional characterization of microstructure by electron back-scatter diffraction," *Annual Review of Materials Research* 37 (2007), 627-658.

[2] G. Rohrer et al., "Deriving grain boundary character distributions and relative grain boundary energies from three-dimensional EBSD data," *Materials Science and Technology,* 26 (2010), 661-669.

[3] C. McMahon et al., "Segmentation of three-dimensional EBSD data through fast multiscale clustering," Proceedings of The Minerals, Metals & Materials Society 140th Annual Meeting, (2011).

[4] E. Sharon et al., "Hierarchy and adaptivity in segmenting visual scenes," *Nature,* 442 (2006), 810-813.

[5] L. Bassman et al., "Study of the true nature of microband boundaries in aluminum with 3D EBSD," Proceedings of the 16th International Conference on Textures of Microstructures. In *Materials Science Forum* 702-703 (2012), 558-561.

[6] N. Afrin et al., "The three-dimensional nature of microbands in a channel die compressed Goss-oriented Ni single crystal," Scripta Materialia 64 (2011) 221-224.

[7] N. Afrin et al., "On the bumps and curves in the microband boundaries in a channel-die compressed Goss-oriented Ni single crystal," Proceedings of the 16th International Conference on Textures of Microstructures. In *Materials Science Forum* 702-703 (2012), 101-104.

1st International Conference on 3D Materials Science
*Edited by: Marc De Graef, Henning Friis Poulsen, Alexis Lewis, Jeff Simmons, George Spanos*
***TMS (The Minerals, Metals & Materials Society), 2012***

# An Automated Multi-Modal Serial Sectioning System for Characterization of Grain-Scale Microstructures in Engineering Materials

Michael Uchic[1], Michael Groeber[1], Megna Shah[2], Patrick Callahan[1,3], Adam Shiveley[4], Michael Scott[2], Michael Chapman[4], and Jonathan Spowart[1]

[1]Air Force Research Laboratory, Materials & Manufacturing Directorate, Wright-Patterson AFB, OH 45433
[2] UES, Inc, Dayton, OH 45432
[3]Carnegie Mellon University, Department of Materials Science and Engineering, Pittsburgh, PA 15213
[4] SOCHE, Dayton, OH 45433

Keywords: serial sectioning, 3D microscopy, EBSD, EDS

## Abstract

This paper describes the development of a new serial sectioning system that has been designed to collect microstructural, crystallographic, and chemical information from volumes in excess of 1 $mm^3$. The system integrates a robotic multi-platen mechanical polishing system with a modern SEM that enables the acquisition of multi-modal data—scanning electron images, EBSD and hyperspectral EDS map—at each section. Selected details of the system construction as well as an initial demonstration of the system capabilities are presented.

## Introduction

For the past two decades the materials research community has sustained research and development of hardware and software to enable 3D characterization of microstructural features across the wide range of length scales that are observed in many engineering materials. The list of dedicated laboratory-scale instrumentation for structural materials includes serial sectioning devices such as those based on micromilling [1], mechanical polishing [2,3], and femtosecond laser ablation [4], the 3D Atom Probe [5], x-ray microtomography systems, as well as instruments that have been adapted for this purpose like dual-beam Focused Ion Beam Scanning Electron Microscopes (FIB-SEM) [6] and Transmission Electron Microscopes outfitted with specialty tomographic sample holders.

Nonetheless, there remain capability gaps with regards to the type of data and the spatial coverage/resolution that can be achieved with the aforementioned list of current instrumentation. The 3D characterization system described in this paper attempts to fill one of these gaps through the collection of multi-modal information (local crystallographic, chemical, and image data) over a key range of length scales with regards to optimizing structural material performance, i.e., from micrometer-to-centimeter scale volumes.

The development of the system described herein was motivated by the success of FIB-SEM microscopes to rapidly characterize complex engineering alloy microstructures. These versatile microscopes have been used to perform serial sectioning experiments on a host of disparate material types: metals, ceramics, polymers, electronic materials, and biological materials. One of the key capabilities of FIB-SEM microscopes is the ability to incorporate advanced analytical

methods such as Electron BackScatter Diffraction (EBSD) and Energy Dispersive Spectrometers (EDS) systems. These methods provide more information regarding the local material state, and importantly, allow for segmentation of grains or second phases from complex microstructures using physically-meaningful parameters, such using a misorientation threshold to aggregate neighboring voxels into grains [7]. However, the limited material removal rate of liquid-metal ion sources has restricted the role of FIB-SEM microscopes to the study of nano- and micrometer-scale features in volumes that have dimensions on the order of tens-of-micrometers.

The multi-modal serial sectioning device described in this paper addresses the issue of volumetric coverage by replacing ion-beam sectioning with automated mechanical lapping and polishing. Mechanical polishing methods have been the traditional pathway for preparing the surface of materials for quantitative 2D microstructural analysis, and such methods have also been commonly employed for manual 'macro-scale' serial sectioning experiments [8], including those that incorporate multi-modal data [9]. Note that for the intended application there is the critical issue of preparing samples with minimal subsurface damage because of the stringent surface finish requirements of EBSD-based analysis. Unlike other automated serial sectioning instruments that employ mechanical polishing and optical microscopes [2,3], the device described in this paper has the ability to use multiple polishing platens to sequentially remove material using successively finer polishing media, thus enabling the use of EBSD. Although the system is still under development and full integration of the individual sub-systems is still in-progress, the basic layout of the device and a demonstration of its capabilities are presented in the following sections.

## System Design and Capabilities

The initial system configuration consists of a three primary subsystems that reside within a 15' x 12' safety enclosure: a Mitsubishi transfer robot, a RoboMet.3D serial mechanical polishing instrument, and a Tescan SEM outfitted with EBSD and EDS detectors and a motorized load lock. An image taken from outside of the enclosure that shows the relative position of the three subsystems is shown in Figure 1.

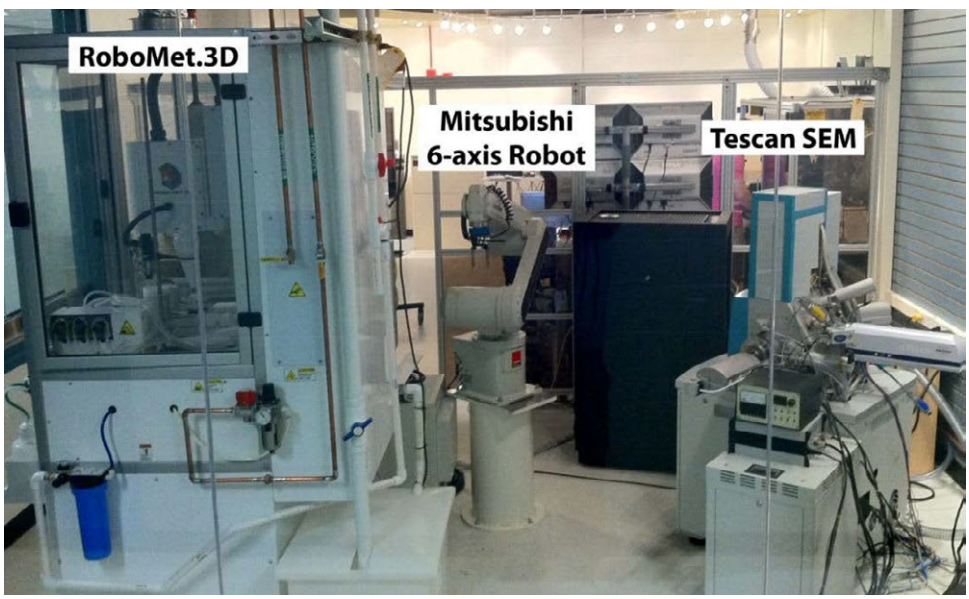


Figure 1. Image that shows the arrangement of the three main sub-systems that comprise the serial sectioning instrument.

These subsystems are controlled by a master computer that dictates the sequence of operations for the various sub-systems, which will also be eventually responsible for storing the multi-modal information and all other metadata into a single 3D data file in HDF5 format [10]. The following sections describe the key features for each of the three main sub-systems.

The Mitsubishi RV12SVL 6-axis robot arm has a 54'' reach, which allows it to readily move a 2" diameter stainless steel sample holder, Figure 2A, between sample exchange points on the Robo-Met.3D, the Tescan SEM, and an additional sample transfer stand that enables the robot to switch between two gripping configurations, as shown in Figures 2B and 2C. Custom end-of-arm-tooling enables two gripping modes. The top-gripping mode is used to place the holder in the SEM load lock with the sample surface facing up, while the side-gripping mode is used to insert the holder in the RoboMet.3D with the sample surface facing down. Half-cylindrical locating features on the top and bottom surfaces of the sample holders are used with mating features at the sample transfer positions ensure that the sample orientation and position is roughly maintained during hand-offs. In addition, the Mitsubishi robot will also be used to completely immerse the sample holder into beakers containing ethanol for ultrasonic cleaning, followed by articulating the sample in front of a nitrogen gas nozzle to dry the sample prior to SEM analysis. Robot arm movements are controlled remotely using executable scripts written in a manufacturer-supplied programming language (RTToolbox2). The flexibility for re-programming the motion of the 6-axis robot allows for easy reconfiguration of the characterization system in the future, such as adding additional sample preparation or analysis stations.

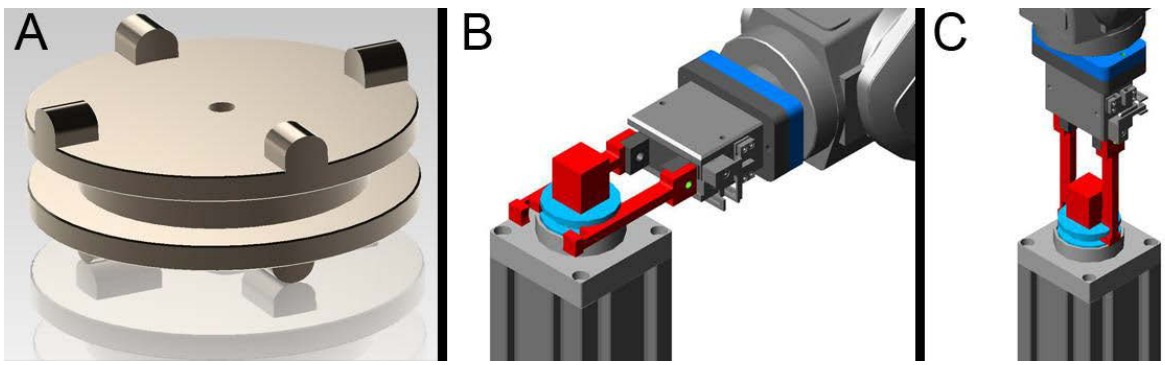


Figure 2. A) Schematic of the sample holder, B) Side-gripping mode for the Mitsubishi robot and end-of-arm-tooling, C) Top-gripping mode.

RoboMet.3D (www.ues.com/content/robomet3d), shown in Figure 3, is used to automatically perform the serial mechanical polishing step, removing a notionally planar section of material while obtaining a high-quality surface finish that is suitable for both imaging and EBSD characterization in the SEM. Note that surface planarity is not currently monitored, although planned expansion of the system will include a non-contact surface profiling capability to track the full 3D shape of the as-polished surface. The RoboMet.3D installed on this system has been customized with a multi-platen exchange arm, which allows the use of up to eight 12-inch diameter platens in the polishing cycle. At present, at least two platens are used for EBSD-inclusive experiments, where typically a 1 micron diamond media (Allied High-Tech 1µm Polycrystalline Diamond Suspension) along with a low-nap cloth (Buehler Texmet C) is used to minimize differential polishing during the majority of material removal (for ~ 1 micrometer

sections). This step is followed by nm-scale polishing media on a high-nap cloth, either colloidal silica (Allied High-Tech 40 nm Non-Stick/Rinsable Colloidal Silica Suspension), or a two-step combination of alumina (Buehler 50nm alpha-Alumina Micropolish) followed by colloidal silica, to minimize subsurface deformation. Figure 4 shows the difference in BSE images and representative backscatter Kikuchi patterns between the 1 μm removal step (Figure 3a) and sub-50 nm polishing steps. Good quality indexable patterns are observed after the sub-50nm polishing step, illustrating the need for a multi-step polishing sequence. Water-soluble polishing media and additional lubrication (distilled water) are automatically dispensed, and the application rates of all fluids as well as other polishing parameters such as wheel speed and sample oscillation are user-defined. Between polishing steps, current experiments use additional platens with high-nap cloths (Buehler Chemomet) and distilled water to mechanically clean abrasives from the surface prior to ultrasonic immersion in an ethanol bath. Just before this cleaning step, the sample surface is dipped into a chemical well on the RoboMet.3D that is originally-intended to be used for selective etching of the sample surface for optical microscopy. Rather than an etchant, the well is filled with diluted micro-organic soap to aid the cleaning process.

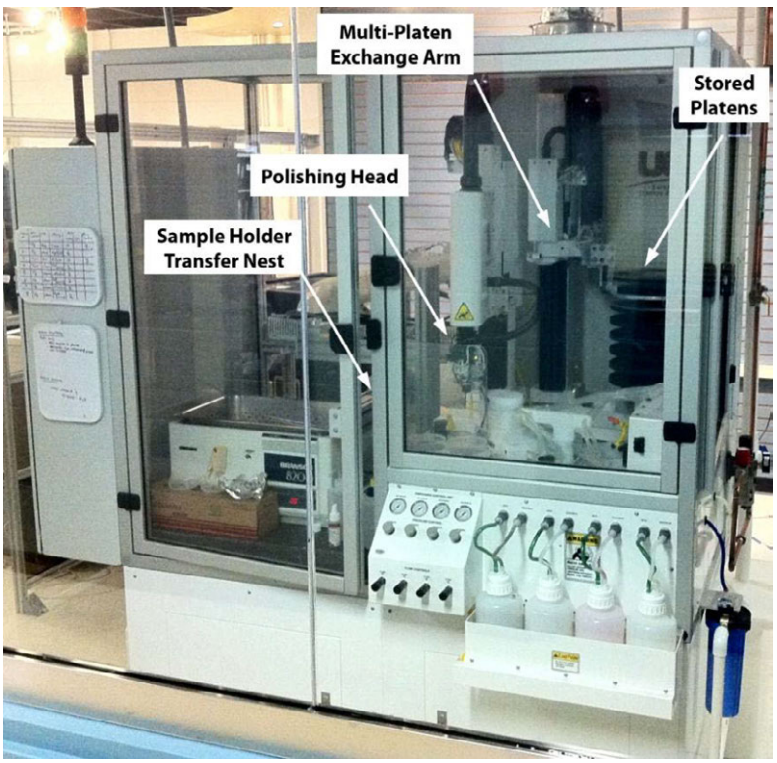


Figure 3. View of the front of the RoboMet.3D mechanical polishing system.

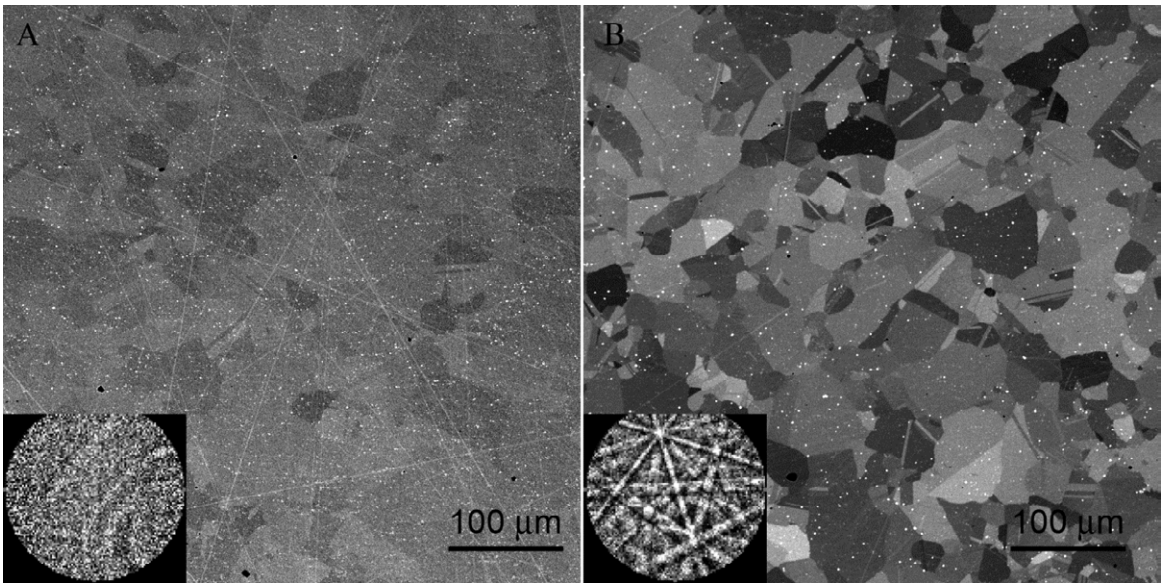


Figure 4. A) BSE image of a polycrystalline Ni superalloy (LSHR) after mechanical polishing for 2 minutes with 1 µm diamond slurry. The inset in the figure shows a representative EBSD pattern from the sample using the following conditions: 20 kV, 5 nA probe current, acquisition time of 2 ms, and pattern size of 128 x 96 pixels. B) BSE image and EBSD pattern from the same sample after additional polishing for 2 minutes with 50 nm alumina, followed by 1 minute of polishing with a 40 nm colloidal silica.

After mechanical polishing, a Tescan Vega 3 XMH microscope outfitted with a Bruker e-Flash 1000 EBSD and a X-Flash Quad 5040 EDS is used for characterization of the section surface. An OEM-constructed motorized load lock assembly is used to quickly transfer the sample holder into and out of the SEM chamber within approximately one minute. This process—as well as all other aspects of stage movement, detector insertion, beam optimization, image optimization, image collection, EDS and EBSD analysis—are controlled through the use of custom-developed Python scripts that use OEM-supplied application programming interfaces for the Tescan microscope (SharkSEM API) and the Bruker detectors (ESPRIT API).

To illustrate the type of algorithms that are used to control the operation of the microscope, the optimization of imaging conditions is performed using two scripts that determine the best focus and brightness/contrast values. At present, best focus is obtained by calculating the edge content within selected images over a user-defined range in focus settings:

$$\sum_{i=0}^{M}\sum_{j=0}^{N}\sqrt{S_x\left|I(i,j)\right|^2+S_Y\left|I(i,j)\right|^2} \tag{1}$$

$$S_x=\begin{bmatrix}-1 & 0 & 1\\ -2 & 0 & 2\\ -1 & 0 & 1\end{bmatrix}\quad S_y=\begin{bmatrix}-1 & -2 & -1\\ 0 & 0 & 0\\ 1 & 2 & 1\end{bmatrix} \tag{2}$$

where $S_x$ and $S_y$ are the Sobel kernels. A Gaussian curve is fit to the edge-content data as a function of focus/working distance, and the peak value from the fit corresponds to the best focus and the actual specimen-to-column working distance. The sample stage is raised or lowered to bring the sample surface to the desired working distance (e.g., 10 mm), and the focus is re-

checked to confirm both accurate vertical positioning of the sample and optimal focus. The brightness and contrast of images are optimized using an ad-hoc algorithm that compares the mean and standard deviation of the current image histogram to a user-defined reference image. The microscope brightness and contrast values are iteratively adjusted until the mean and standard deviation of the current image closely match those of a user defined reference image. At present, most of the algorithms used for automated instrument control are similar to the latter example and are somewhat basic in design. Nonetheless, the images and data maps returned by the microscope are quite suitable for post-processing and analysis, although further advancement of these methods is desired. Figure 5 shows a representative backscattered electron (BSE) image that has been collected without human intervention, which highlights the image quality that has been achieved to date.

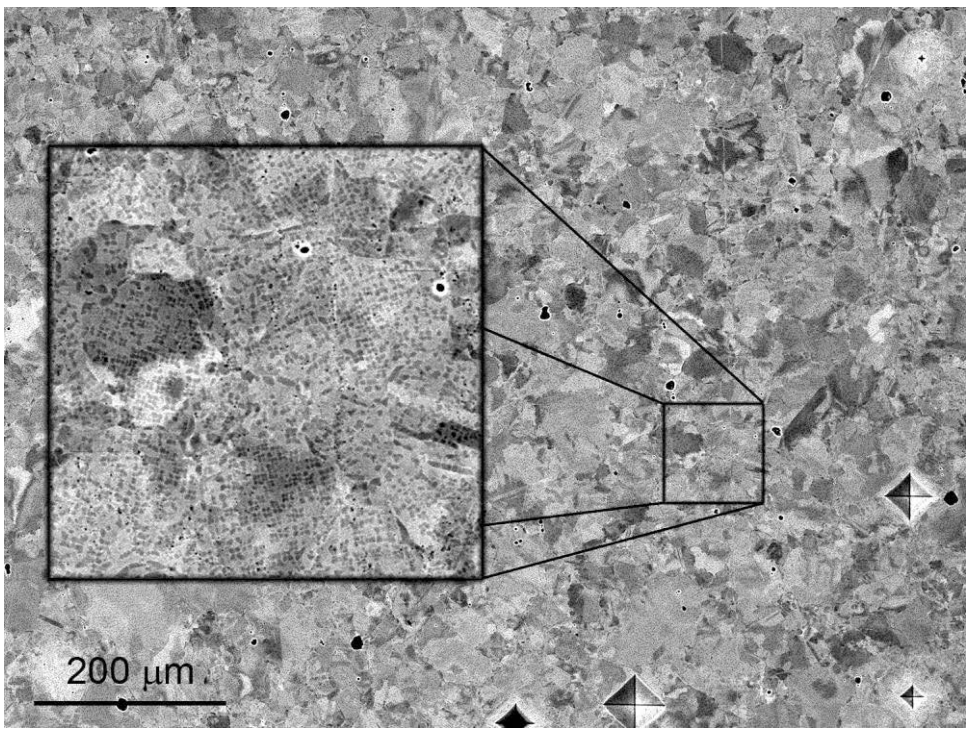


Figure 5. A representative BSE collected by the Tescan SEM using automation scripts. Field of view is 1 mm x 0.75 mm with pixel dimensions of 250 nm. Microscope operating conditions are an accelerating voltage of 30 kV, probe current of ~ 1 nA, and a pixel dwell time of 100 μs. Material is an IN100 superalloy that has undergone a supersolvus heat treatment.

Table 1 provides a summary list of current capabilities for the multi-modal serial sectioning system. Desired improvements for the future include obtaining finer sectioning processes to directly overlap with meso-scale FIB-SEM experiments, and faster cycle times to improve data throughput. Reductions in the cycle time will come through both evolutionary improvements in instrument operation, for example, faster optimization of the electron imaging/analysis environment or minimizing the number of polishing pad operations, as well as by more radical methods, such as the use of real-time analysis to guide the efficient collection of EBSD and EDS data via sparse sampling. The volume of material that can be interrogated by the system can be easily in excess of 1 $mm^3$, and the main restriction on size is that the sample must clear the load-lock opening, which corresponds to a cylindrical-shaped maximum volume of 38 mm diameter x 25 mm in length.

| CAPABILITY | INITIAL | GOAL |
|---|---|---|
| SECTION THICKNESS | 1 µm | 200 nm |
| MIN. CYCLE TIME | > 20min | Faster |
| MATERIALS SYSTEMS | Ni, Ti Alloys | Most Alloys, Composites |
| IMAGING | SEI, BSE | Same |
| ORIENTATION INFO | Automated Collection | 'Intelligent' Scans |
| CHEMICAL INFO | Automated Collection | 'Intelligent' Scans |

Table 1: Demonstrated and goal capabilities for the novel multi-modal serial sectioning system.

## Example Application

As mentioned previously, the serial sectioning system is still in development and is not fully operational. However, each of the individual sub-systems can be operated in an automated fashion, and preliminary experiments have been conducted to help identify issues that need to be addressed during the final phase of development. These experiments have primarily consisted of performing semi-automated serial sectioning studies where the polishing and imaging sub-systems have been run without human intervention, while sample cleaning and microhardness indentation have been performed manually. Microhardness indents are used to 'frame' the area for microstructural analysis, and a few indents can be observed in the lower right portion of Figure 5. These features are useful as temporary reference marks that enable section-to-section registration that is unbiased by the morphology of internal microstructural features [11], as well as provide a measure of the local material removal rate [8].

Figure 6 shows a 3D reconstruction from a preliminary serial sectioning experiment of an IN100 superalloy that was previously described in Figure 4. The limited data set contains only 15 sections that have an average spacing of approximately 1 micrometer. Both BEI and EBSD maps have been collected at each section, and the total cycle time per section from polishing through SEM imaging and analysis was a little over two hours. Note that only the EBSD maps have been used to create the 3D reconstruction shown in Figure 5, which was generated using the DREAM.3D software environment (http://dream3d.bluequartz.net). This data set is too small to perform an unbiased analysis of the grain structure, as almost all of the grains touch one of the bounding surfaces of the data volume. However, once development of the automated serial sectioning system is completed, such analysis should become commonplace as suitable volumes could be collected within a few weeks, and the system will be capable of processing multiple samples at the same time.

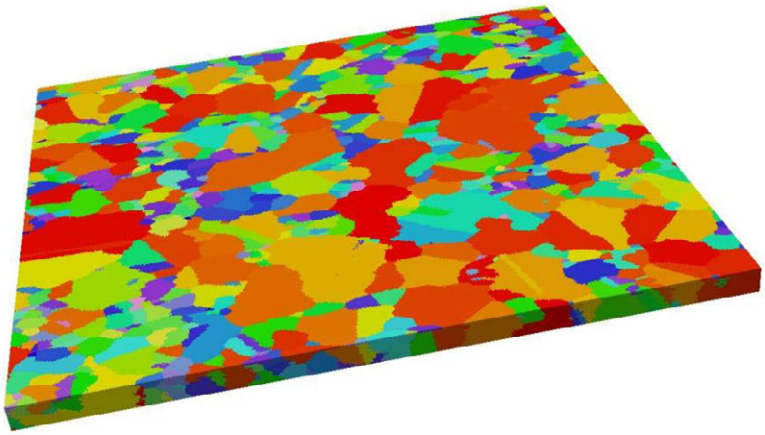

Figure 6. 3D reconstruction of an IN100 superalloy microstructure that was interrogated by the multi-modal 3D characterization system. Volume is 500 x 500 x 15 micrometers in size, and grain coloring corresponds to a unique grain ID.


## Acknowledgements

The authors would like to acknowledge the following people that have contributed to the development of this system: Luke Creachbaum, Petr Tichopádek, Filip Lopour, Tony Owens, Kent Walker, Allen Poe, and Scott Schoessow. Funding was provided by the Air Force Research Laboratory Venture Fund Program and the Materials & Manufacturing Directorate.


## References


[1] Alkemper J, Voorhees PW (2001) Quantitative serial sectioning analysis. J Microscopy 201:388-394

[2] Spowart JE, Mullens HM, Puchala BT (2003) Collecting and Analyzing Microstructures in Three Dimensions: A Fully Automated Approach. JOM 55:35-37

[3] Adachi Y, et al. (2012) 3D image-based stereology. Materials Science Forum 706-709:2687-2692

[4] Echlin MP, et al. (2012) A new TriBeam system for three-dimensional multimodal materials analysis. Rev Sci Instr 83:023701

[5] Miller M (2000) *Atom Probe Tomography: Analysis at the Atomic Level*. Kluwer Academic/Plenum Publishers

[6] Uchic MD, et al. (2006) 3D microstructural characterization of nickel superalloys via serial-sectioning using a dual beam FIB-SEM. Scripta Materialia 55:23-28

[7] Groeber MA, et al. (2008) A framework for automated analysis and simulation of 3D polycrystalline microstructures. Part I: Statistical characterization. Acta Materialia 56:1257-1273

[8] Kral M, Spanos G (1999) Three-dimensional analysis of proeutectoid cementite precipitates. Acta Materialia 47:711-724

[9] Rowenhorst DJ, et al. (2006) Crystallographic and morphological analysis of coarse martensite: Combining EBSD and serial sectioning. Scripta Materialia 55:11-16

[10] Jackson M, Simmons JP, De Graef M (2010) MXA: a Customizable Data Format for Multi-Dimensional Data Sets. Mod Sim Mater Sci Eng 18:06500

[11] Russ J (2002) *The Image Processing Handbook, 4th Ed*. CRC Press

1st International Conference on 3D Materials Science
*Edited by: Marc De Graef, Henning Friis Poulsen, Alexis Lewis, Jeff Simmons, George Spanos*
***TMS (The Minerals, Metals & Materials Society), 2012***

# Ultra Fast Tomography: New Developments for 4D Studies in Material Science

Pierre Lhuissier[1], Mario Scheel[2], Marco Di Michiel[2], Elodie Boller[2], Jerome Adrien[3], Eric Maire[3], Luc Salvo[1], Jean-Jacques Blandin[1], Michel Suery[1]

[1]SIMaP - Grenoble University, BP 46, 101 rue de la Physique, 38402 Saint Martin d'Hères, France
[2]ESRF, 6 rue Jules Horowitz, BP 220, 38043 Grenoble Cedex 9, France
[3]MATEIS - Lyon University, 7 Avenue Jean Capelle, 69621 Villeurbanne, France

Keywords: In situ, Continuous tomography, Damage evolution

## Abstract

X-ray tomography has become a widely used 3D characterization technique in materials science using either laboratory tomographs or large X-ray facilities. The two main improvements in the last decade are the decrease of the spatial resolution down to tens of nanometers and also the decrease in acquisition time of a complete scan down to 1 second with 2 $\mu m$ spatial resolution. The aim of this presentation is to focus on the second point. We will present the technical problems arising due to ultra fast acquisition (development of specific sample environment) and its application in material science. We will show, that thanks to ultra fast tomography, it is now possible to investigate material science problems in 4D (crack propagation in metals and high temperature deformation).

## Introduction

In situ experiments carried out inside a tomograph have shown their unique potential to collect non destructive observation of the internal 3D structure of materials. With this technique, damage evolution can be precisely described as a function of the local strain field in bulk materials [1]; local deformation and damage mechanisms can be observed and thus better understood in architectured materials such as foams [2, 3] or fibrous materials [4]; fatigue crack propagation can be measured and related with the local grain orientation thanks to complementary 3D-XRD techniques [5]. Most of these studies can also now be carried out inside any laboratory tomograph, provided that the test can be interrupted during the scan without any perturbation of the phenomena at play. But, if these phenomena are time dependant, it becomes difficult to pause the test without inducing any artefact. For example, in the case of solidification of aluminum alloys, [6] showed that quenching induces some perturbation into the system and that the quenched microstructure is not the same as the one at high temperature. In the case of high temperature deformation of magnesium alloys, interruption of strain loading during the scan can lead to an enhanced ultimate strain due to restauration mechanisms having a first order influence simply because of the extra time required for X-ray observation. In order to avoid all these artefacts, an ideal method would be to use *continuous tomography*. In a continuous mode, the tests are no longer paused for scanning. This requires that the acquisition time is reduced so that the microstructure do not to evolve "too much" during the scan. On the contrary, the term *interrupted tomography* is used when the test is paused during the acquisition. For a tomographic scan with a voxel size of 1 or 2 $\mu m$ and a final volume size of the order of $1024^3$ voxels, we will refer to *classical tomography* if a scan is recorded with a set of parameters that give a 3D image (one scan) in

more than 600 seconds. *Fast tomography* will refer to a scan acquired in 10 to 600 seconds. Below this limit of 10 seconds per scan we will refer to *Ultra-fast tomography*. Continuous tomography is not necessarily associated with ultra-fast tomography. Nevertheless in the field of materials sciences, if we consider either phase transformation or mechanical testing, the domains of interest involve short characteristic times. In the case of phase transformation, the interesting domain of thermal cooling or heating rate ranges from 0.1 to $10°C/s$. It is admitted that for an exploitable 3D image, temperature should not change more than $1°C$ during the time required for a scan. Thus each scan should be acquired in 0.1 to 10 s. [7]. In the case of mechanical loading, an interesting strain rate domain ranges between $10^{-4}$ and $10^{-1}s^{-1}$. If a test is carried out at room temperature and if the material is very ductile, one can consider using interrupted tomography [8, 9]. Nevertheless the testing device must be stiff enough to avoid any relaxation. This condition is often not fulfilled in actual in situ devices. If tests are carried out at high temperature, or if the matrerial to test is fragile and breaks very fast, continuous tomography must be considered and one scan must be acquired in 0.01 to 10 $s$ in order to limit the displacement of the sample to less than 1 voxel during the scan (*i.e.* less than about 1 $\mu m$). Thus for phase transformation, for high temperature deformation and for fragile samples, in situ continuous tomography requires ultra-fast conditions. The aim of this paper is to present ultra-fast microtomography and a selection of applications in material science.

## Ultra-fast tomography

### Acquisition

Optimization of all the acquisition parameters is required to reduce the acquisition time.
The first element of the acquisition chain is the X-ray source and its brightness. A synchrotron pink beam (*i.e. not completely monochromated*) or even a white beam (*i.e. fully monochromated*) delivers a very high flux. Specific scintillators, adapted to the high energy range and more efficient, give a better ratio of transformation of X-rays to visible light. Optics aperture also has to be maximized.
The second element is the camera. On the one hand, standard CCD cameras usually exhibit a very good signal dynamic range, but they require a shutter and downloading the acquired image from the CCD to a computer can be rather slow. On the other hand new CMOS cameras can be operated without the use of a shutter and can achieve acquisition time for a single image as short as $1/40000s$. They are usually equipped with an on board memory of several tens of gigabytes so that the recorded images can be quickly stored in this memory during the test and transferred to the computer at the end of the total acquisition. If the on board memory is not large enough to store all the scans, downloading rates have to be reduced as much as possible to limit the time between scans.
One should also consider the mechanical limitations. The rotating stage must be fast and stable enough to ensure that the sample performs half a turn at constant speed during the time for one scan. Acquisition times of 4 scans per second require a minimum rotation velocity of $720°/s$. Classical methods that consists in accelerating, acquiring, decelerating and rotating back to the initial position cannot be used in such conditions. Continuous rotation of the rotating stage should rather be prefered. The rotating stage is often a key element, because of the stability of the velocity and of induced vibrations that arise when the upper bound of the velocity is reached.

Sample environment

Because of the continuous rotation, classical in situ devices for mechanical loading at high temperature such as the one previously used for fast tomography and described in [10] are no more usable. Devices must be designed to allow an unlimited number of turns. Such a constrain has a large impact on the design of in situ devices that can impose thermomechanical loading to a sample within controlled conditions.

## Applications

We will present three applications in the field of damage studies in materials were ultra-fast tomography has been applied showing the great potential of this technique. The experimental conditions for the tests are :

- *damage at low temperature during mechanical testing of reinforced and unreinforced aluminium alloy* : experiments were performed in situ on ID15A beamline at the ESRF in white beam conditions on an $Al/Al_2O_3$ composite (provided by A. Mortensen, EPFL) and on an Al-Mn alloy 3103. The strain rate imposed to the sample was about $10^{-3}s^{-1}$. The camera used was a PCO Dimax with a field of view of 864x488 and an optic leading to a pixel size of 2.2 $\mu m$. During each scan 600 projections have been acquired. The acquisition rate was of one scan every 0.15 second.

- *damage at high temperature during mechanical testing of magnesium alloys* : experiments have been performed on a commercial Magnesium alloy AZ31 at $400°C$ with a strain rate of $5.10^{-4}s^{-1}$. The imaging camera was a DALSA with a field of view of $1024^2$, and an optic leading to a pixel size of 1.2 $\mu m$. During each scan, 300 projections were acquired. The irradiation time for one scan was about 5 seconds [11] and 2 scans were acquired every minute.

Room temperature damage of reinforced aluminium matrix composites

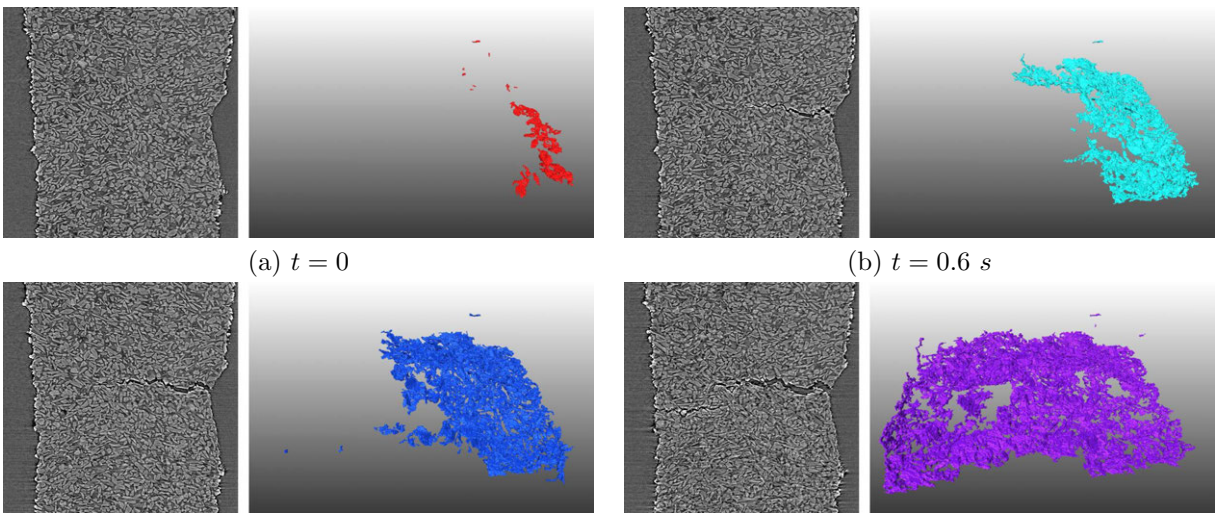

(a) $t = 0$ (b) $t = 0.6\ s$

(c) $t = 0.75\ s$ (d) $t = 0.9\ s$

Figure 1: Evolution of a longitudinal cross section with time and evolution of a 3D view of the crack with time.

$Al/Al_2O_3$ composites presents a very low ductility at room temperature. When submitted to tension, a crack initiates and propagates through the sample. The crack path can be

observed post mortem, but informations on the crack velocity can only be obtained thanks to in situ observations. The high velocity of the crack tip requires the use of ultra-fast tomography. Figure 1 presents the evolution of a longitudinal cross section of the sample and of a 3D view of the crack. All the phenomena presented in the series of images appended in less than 1 second.

From the sequence of 3D images the crack tip velocity could be estimated. Figure 2 presents the evolution of the crack tip velocity with time. The front velocity is stable around 40 $\mu m/s$ and accelerates when the cracks becomes longer leading to the rupture of the sample.

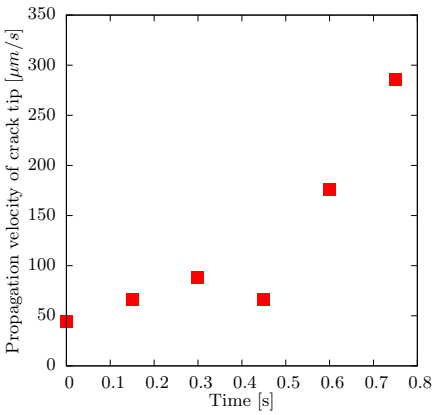


Figure 2: Crack tip velocity as a function of time

Room temperature damage evolutin in the unreinforced aluminium alloy

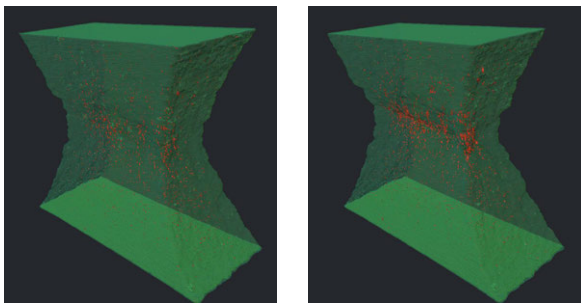

(a) $t = 0$



(b) $t = 1.2\ s$

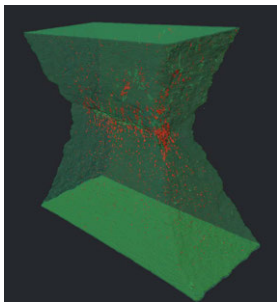

(c) $t = 1.5\ s$

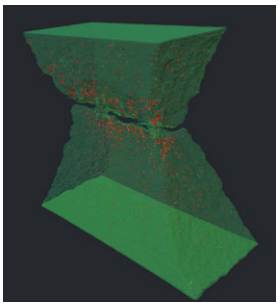

(d) $t = 1.95\ s$

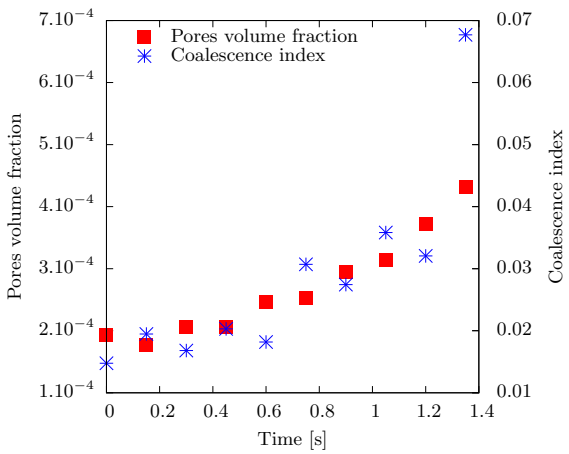


(e)

Figure 3: **(a-d)** Evolution of the sample shape (green) and of pores (red) with time. **(e)** Pores volume fraction (red square) and Coalescence index (blue cross) as function of time.

Al-Mn alloys generally present a very goo ductility at room temperature. When submitted to strain, damage appears and evolve. Pores nucleate, grow and coalesce. The volume

fraction of pores and the size of the largest pores are important informations for the quantification of damage. The evolution of these parameters with strain could be used as a useful validation tool to refine the prediction of standard damage models.
Figures 3.a-d present 3D views of the shape of the sample (green) and of the presence of internal pores (red, closed porosity). The pores concentrate in the necked region. The volume fraction of these cavities increase with time (strain) up to the separation between the upper and lower parts of the sample (between image b and image c). The pore volume fraction and the coalescence index, defined as the ratio between the volume of the largest cavity and the total volume of porosity inside the sample, ware calculated for each strain step and are plotted in figure 3.e as a function of time.

Damage is mainly induced by growth and local coalescence of the cavities leading to final rupture. The low value of the coalescence index indicates that only growth and local coalescence are involved up to $t = 1.2\ s$. The change of increasing rate for the coalescence index after $t = 1.2s$ is a signature of global coalescence of cavities leading to the rapid fracture of the sample in less than $1\ s$ .

High temperature damage in magnesium alloy

Depending on the strain rate and the temperature, Magnesium alloys can present a superplastic behavior. During such a large plastic deformation, both growth and coalescence of cavities occur. There should also be some interaction between cavities and intermetallic particles that are present in the bulk material. Global quantities would hardly allow us to clarify the respective proportion of growth and coalescence on the global pores volume fraction evolution. Moreover the interaction with particles cannot be globally measured. Thus some pores (about 60) have been tracked during the deformation. Figure 4 presents the evolution of some cavities with strain. Among the varied mechanisms, one can observe

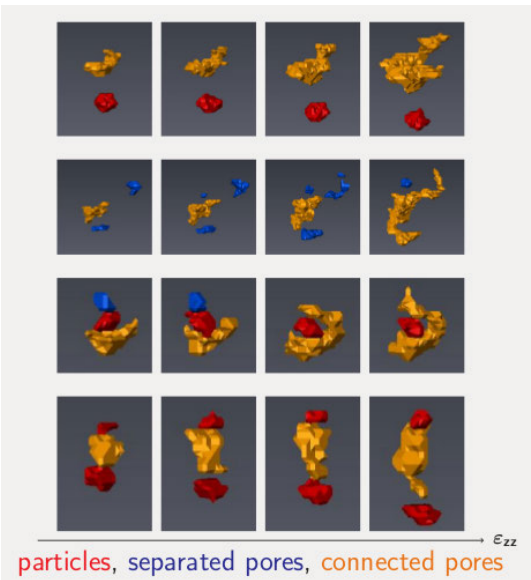


Figure 4: Evolution of cavities with strain. The main cavity (yellow), isolated cavities (blue) and particles (red) are presented.

growth of cavities with complex shape, coalescence of cavities and interaction between pores and cavities growth.
Such high temperature experiments show that coalescence mechanisms are active even at

relatively low strain and that the shape of the cavities is often far to be elliptic as assumed in most of the models. In situ experiments could now be conducted at higher strain rates, and would thus allow to investigate the superplastic transition.

## Conclusion and outgoings

Ultra fast tomography extends the field of observable phenomena during in situ experiments. The short time required for acquisition allows us to perform tests without any interruption. The technique allows to follow the evolution of important parameters of the structure.
We have presented some technical points, mostly based on devices and hardware, that permits to reduce the acquisition time. A simple way to reduce the time for one scan is to reduce the number of projections. Up to some extends, classical filtered back projection reconstruction is effective. An order of magnitude on the acquisition time would be achievable with new reconstruction algorithms : either discrete tomography and its extension to multimaterials [12], or bayesian iterative techniques [13]. Another way to observe phenomena with short characteristic times is to accept some evolution of the microstructure during the time for one scan. Depending on the evolution of the microstructure, interpolation of the projections based on strain fields obtained by digital image correlation allow to correct large motions (such a technique have been used for the reconstruction of two of the examples presented).

## References


[1] C. Landron, E. Maire, O. Bouaziz, J. Adrien, L. Lecarme, A. Bareggi. Acta Mater., 59 (2011) : 7564-7573.

[2] O. Caty, E. Maire, S. Youssef, R. Bouchet. Acta Mater., 56 (2008) : 5524-5534.

[3] A. Fallet, P. Lhuissier, L. Salvo, Y. Brechet. Adv. Eng. Mater., 10 (2008), 858-862.

[4] A.E. Scot, M. Mavrogordato, P. Wright, I. Sinclair, S.M. Spearing. Compos. Sci. Technol., 71 (2011) : 1471-1477.

[5] W. Ludwig, A. King, P. Reischig, M. Herbig, E.M. Lauridsen, S. Schmidt, H. Proudhon, S. Forest, P. Cloetens, P., S. Rolland Du Roscoat. Mater. Sci. Eng. A, 524 (2009) : 69-76.

[6] O. Pompe, M. Rettenmayr. J Cryst Growth, 192 (1998) : 300-306.

[7] L. Salvo, M. DiMichiel, M. Scheel, P. Lhuissier, B. Mireux, M. Suéry. Materials Science Forum, 706 (2012) : 1713-1718.

[8] M. Suéry, J. Adrien, C. Landron et al. Int. J. Mater. Res., 101 (2010) : 1080-1088.

[9] E. Maire, V. Carmona, J. Courbon, W. Ludwig. Acta mater., 55 (2007) : 6806-6815.

[10] J.-Y. Buffiere, E. Maire, J. Adrien, J.-P. Masse, E. Boller. Exp. Mech., 50 (2010): 289-305.

[11] P. Lhuissier, A. Villanueva Fernandez, L. Salvo, J.J. Blandin. Materials Science Forum, 706 (2012) : 1128-1133.

[12] K.J. Batenburg, J. Math. Imaging Vis. 30 (2008) : 231-248.

[13] N. Gac, A. Vabre, A. Mohammad Djafari, A. Rabanal, F. Buyens. The First International Conference on Image Formation in X-Ray Computed Tomography, Salt Lake City, United States (2010).

1st International Conference on 3D Materials Science
*Edited by: Marc De Graef, Henning Friis Poulsen, Alexis Lewis, Jeff Simmons, George Spanos*
***TMS (The Minerals, Metals & Materials Society), 2012***

# THREE-DIMENSIONAL CHARACTERIZATION OF DISLOCATION-DEFECT INTERACTIONS

Josh Kacher, Grace Liu, IM Robertson

University of Illinois at Urbana-Champaign; Urbana, IL 61801, USA

Keywords: Dislocations, Transmission electron microscopy, Electron tomography

## Abstract

Transmission electron microscopes play a critical role in building our knowledge base of the atomic structure and composition as well as the electronic and magnetic state of materials. This information is a two-dimensional snapshot of the material state and requires *a posteriori* analysis to reveal the reaction or processing pathway, or to correlate with a macroscopic property. However, using electron tomography it is feasible to recover the information lost in the electron beam direction and obtain a three-dimensional view of the internal structure in an electron transparent foil. In this paper, example applications of diffraction-contrast electron tomography to understand various dislocation-obstacle interactions are presented and discussed.

## Introduction

Traditional transmission electron microscopy (TEM) techniques allow direct imaging of defects, but present the information as a two-dimensional projection, thus losing information on the spatial relations of the defects within a material. Electron tomography, developed initially for application in the life sciences [1], seeks to overcome this problem by combining a number of images collected at a single location in a material but over a wide angular range into a three-dimensional (3D) representation of the probed volume. The tomogram resolution depends on the number of images collected and the angular range over which they are acquired - ideally an image should be acquired every degree over an angular range of 120 - 140 degrees with the variation in intensity across and between images varying uniformly. Consequently, most applications have used scanning transmission electron microscopy modes to acquire the input data [2].

Recent efforts have extended the application of electron tomography to defect studies in crystalline materials using diffraction contrast imaging conditions, including two-beam bright field as well as weak-beam dark-field imaging conditions [3-9]. These imaging conditions introduce additional challenges as the image contrast can vary during the sample tilting operation, e.g., thickness fringes, elastic strain centers and bend contours. Nevertheless, acquiring some 120 images while maintaining constant diffraction contrast imaging conditions represents an experimental challenge. To overcome the need to capture 120 or more images, Liu, Kacher and Robertson developed a method whereby a lower resolution tomogram served as the basis for constructing via tracing three-dimensionally the defect structure. In creating the model, prior knowledge about defect image theory and about dislocation properties was used to improve the fidelity of the model. An added advantage of this approach is that two such models, based on tomograms reconstructed using images acquired with different diffraction vectors, can be combined to resolve the defect invisibility issue.

This paper will illustrate the development of diffraction contrast electron tomography for studies of defects, illustrating the fidelity of the model with respect to the tomogram and the consequent reduction of the number of images and the angular range. The enhanced interpretability of dislocation-defect interactions enabled by having the tomogram or dislocation model will be achieved by presenting examples of recent applications: characterization of dislocation interactions with twin boundaries in austenitic stainless steel [5], the dislocation structure produced in channels from which the irradiation produced defects have been annihilated [4], and dislocation/precipitate interactions in an aluminum-copper alloy [10].

## Experimental Methods

In the following analysis, all samples were prepared using standard TEM sample preparation techniques of grinding to an appropriate thickness and jet-polishing to electron transparency. A JEOL 2010 $LaB_6$ transmission electron microscope operating at 200 keV was used for the electron microscopy. The tomography techniques used for reconstruction of a tomogram as well as construction of a high fidelity 3D model from it have been explained elsewhere [6].

## Results and Discussion

The first example considers the interaction of dislocations with twin boundaries in 304 stainless steel. The sample was deformed *ex situ* and interactions of interest identified. In the example shown, three sets of perfect dislocations interacted with a twin boundary, each interaction resulted in a different transfer product being ejected into the twinned area, and these new product dislocations crossed the twinned region and intersected the other twinned boundary, which resulted in slip being transferred across it. The resultant interactions are shown with different diffraction vectors for two different bean directions; the different views each provide information obscured in the other (Fig. 1). Diffraction analysis was used to characterize the twin boundary and the Burgers vectors of the dislocations. A tilt series of the interaction was collected by maintaining the tilt axis parallel to the plane normal of the twin boundaries and collecting an image every 2° in bright-field mode over an angular range of 74°. Once collected, the images were aligned and used to reconstruct of tomogram from which a 3D model was created. Snapshots taken from the model as viewed from different vantage directions and with the dislocations colored with respect to the Burgers vector are presented in Figure 2. The real space coordinate systems, in the form of Thompson tetrahedra, are included for the matrix and twinned regions. The final model can be used for simple identification of the line direction of the slip planes, as well as the plane on which they reside. In the following analysis, the subscripts *in* and *out* are used to identify the frame of reference and refer to the grains containing the incoming and outgoing dislocations, respectively.

System labels, the number distinguishes between the three interactions and the letter specifies elements within an interaction, are given in Figure 1. The twin boundaries reside on $(\bar{1}1\bar{1})_{in}$. The incoming dislocations reside on the slip system $\pm\ {}^{a}/_{2}[\bar{1}10]_{in}(\bar{1}\bar{1}1)_{in}$ and have a line direction parallel to the $[112]_{in}$, making them pure edge dislocations. Each of the three incoming slip systems leads to a unique transmission event. System 1 results in two sets of dislocations being emitted into the twinned region on the $\pm\ {}^{a}/_{2}[101]_{out}$ $(\bar{1}\bar{1}1)_{out}$ slip system (1a), but with line directions of $[1\bar{2}\,\bar{1}]_{out}$ and near $[1\bar{3}\,\bar{2}\,]_{out}$, making them pure edge and mixed character dislocations, respectively. A partial dislocation emerges from the boundary back into the grain of

the incoming dislocations, but its character could not be determined due to its near proximity to the boundary. Similarly, System 2 results in the emission of perfect dislocations into the twinned region on the slip system $\pm\ {}^{a}/_{2}[101]_{out}(\overline{1}\overline{1}1)_{out}$ (2a), but in this case the dislocations have a line direction parallel to the $[1\overline{2}\ \overline{1}]_{out}$ direction, making them pure edge dislocations. Also similar to System 1, there is back emission of Shockley partial dislocations (2c). These partial dislocations are fully emitted and reside on $(1\overline{1}\overline{1})_{in}$. There is a second dislocation system emitted into the twinned region (2b); both Shockley partial and perfect dislocations are emitted in about equal numbers; they reside on the $\pm\ {}^{a}/_{2}[110]_{out}(\overline{1}11)_{out}$ system. The third system is more complex than the first two, resulting in the emission of multiple systems into the twinned region (3a, 3b) as well as two separate dislocation systems back emitted into the original grain (3c, 3d). Due to overlapping dislocations, the dislocations in the twinned region could not be characterized. Apart from the three visible systems in the image, a large number of dislocations are mobile in the twin boundary; these migrated from interactions elsewhere on the boundary.

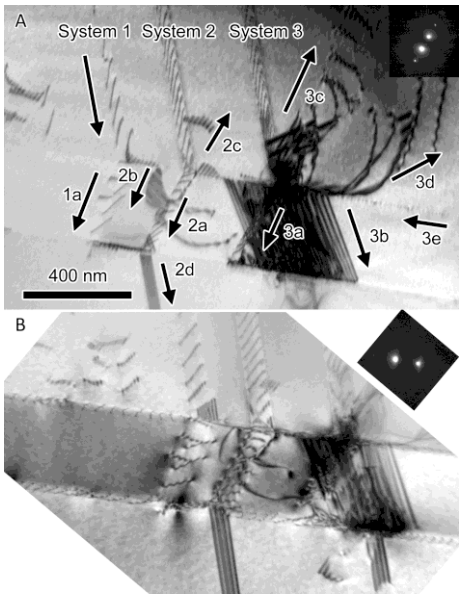

Figure 1. Bright-field TEM micrograph with associated diffraction pattern of dislocations interacting with twin boundaries. Arrows show direction of dislocation motion.

The full system characterization allows for comparison with the slip transfer criteria put forth by Lee *et al*. [11]. These state that the emitted dislocation system from a grain boundary, instigated by an incoming dislocation system, can be predicted by considering the Burgers vector of the residual dislocation left in the system after the interaction, the local resolved shear stress acting on the emitted system, and the angle made by the incoming and outgoing slip planes on the boundary plane. Burgers vector characterization can be used to determine the residual dislocation, but the local resolved shear stress has been more difficult to estimate. The full characterization of the dislocation system, including the line directions of the dislocations, can be used to calculate the stress fields surrounding the dislocations, and thus estimate the stress state in the neighboring grain. Here the presence of extrinsic grain boundary dislocations from an outside source complicates the analysis, but analysis of the interactions suggests that the observed emitted dislocations minimize the magnitude of the Burgers vector of the residual grain boundary dislocation.

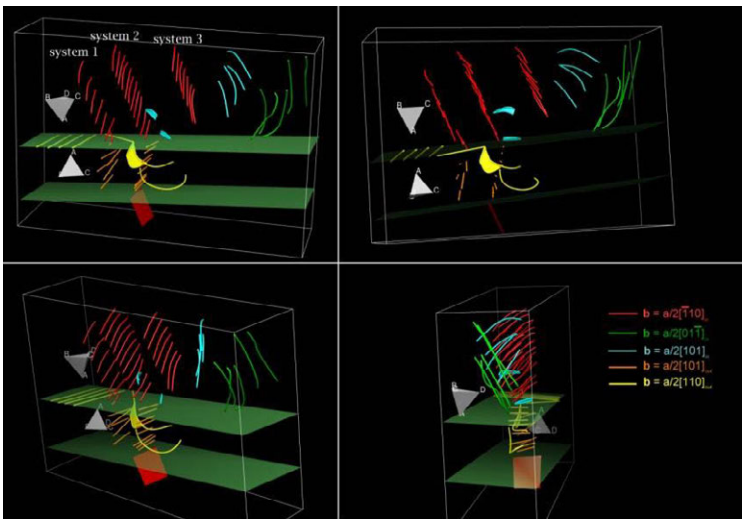

Figure 2. Three-dimensional model of interaction shown in Fig. 1. Dislocations are color-coded according to the Burgers vector.

The second example considers the microstructure of deformed irradiated metals that are typified by channels from which the irradiation-produced defects have been annihilated. These channels are envisioned as being created by mobile dislocations interacting with and annihilating the defects. Understanding their formation has important consequences for understanding the degradation of the properties of materials due to irradiation environments. *In situ* irradiation and straining in the TEM has shown that channel formation is complex and evolves with increasing strain. Initially, dislocations move in a stochastic and uncoordinated manner as they annihilate the defects. With increasing strain the processes become more complex with dislocation cross-slip becoming more common and with long dislocations extending along the channel forming a boundary between the unslipped and slipped volumes [12]. An example of such a microstructure forming in stainless steel that had been bombarded with 1 MeV $Kr^{+}$ ions to a fluence of approximately $3x10^{17}$ ions $m^{-2}$ is shown in the images presented in Figure 3; the original primary channel is the lighter region that extends across the image. The dislocation density is low in this region although there are clear signs of debris in the form of complete as well as half loops. With continued straining, cross-slip from the primary channel occurs and new dislocations are generated from the boundary between the primary channel and the defect-hardened matrix; arrowheads indicate examples of expanding half loops. The deformation is now concentrated outside the primary channel with new sources of dislocations being responsible for widening.

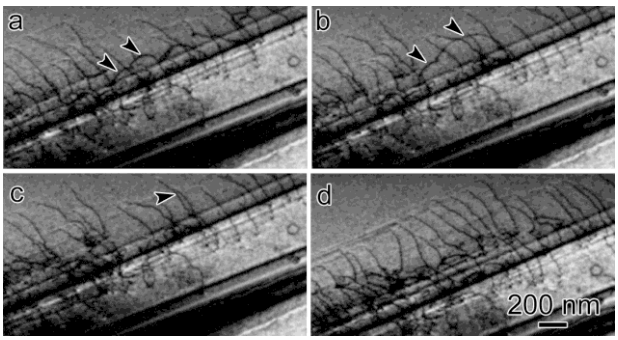


Figure 3. Evolution of defect free channel with half loop tracked by arrow head. The half loop eventually comes into contact with the foil surface in panel c, splitting into dislocation segments that continue on a path parallel to the original slip system. Snapshot times are 19.6, 20.1, and 85.7 s.

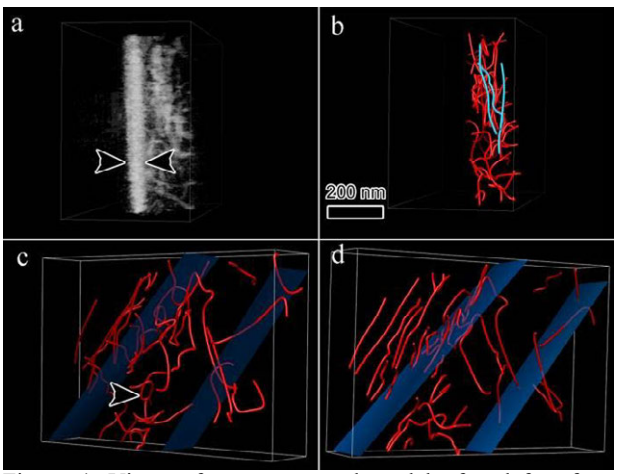


Figure 4. Views of tomogram and model of a defect free channel. a highlights the FIB induced damage. b highlights the elongated dislocations in blue. A helical dislocation is indicated in c. Blue planes indicate the channel boundaries.

As the sample was originally in the form of a bar with dimensions of 12.5x2.5 mm, a section of interest was removed from the electron transparent region by using focused ion beam (FIB) machining and attached to a copper grid using a platinum weld. Images were collected in bright-field mode every degree over an angular range of 76°. As before, the images were reconstructed into a tomogram, which was then used to form a 3D model of the interaction with the approximate location of the channel-matrix boundary included as blue planes (Fig. 4).

Inspection of the tomogram itself shows a high density of defects from the FIB machining process concentrated on one surface of the sample and extending approximately 35 nm from it (Fig. 4a). Notable features of the model include the complex dislocation shapes, including helical-shaped dislocations within the primary channel indicative of dislocations cross-slipping to overcome strong barriers. Also seen in the tomogram are elongated dislocations lining the

channel boundaries and occupying different slip planes (Fig. 4b). These dislocations can increase the complexity of the channel-matrix boundaries by tangling with dislocations cross-slipping from the channels. The interactions between these dislocations and other cross-slipped dislocations could serve as the source of the half-loops seen in Figure 3. Significant dislocation debris is still present in the channel interior, perhaps instigating the dislocation cross-slip from the channel.

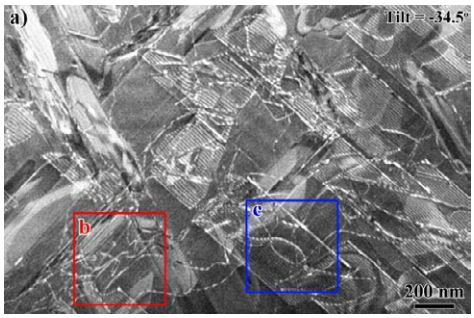

Figure 5. TEM micrograph of dislocations interacting with precipitates in Al-Cu. Two spots are highlighted for comparison with the model.

A final example shows dislocation/precipitate interactions in an Al-4.5%Cu alloy. The TEM micrograph in Figure 5 shows that the dislocation/precipitate interactions are highly complex and cannot be resolved using only two-dimensional projections. A tilt series with an image acquired every 2° over a tilt range of 82° was used in the reconstruction. Figure 6 shows a view from the 3D model, with select interactions shown at higher magnification and precipitates colored according to their respective {001} habit planes.

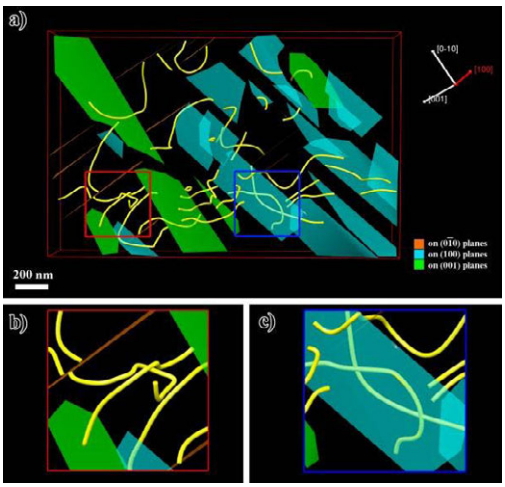

Figure 6. Model of the interactions shown in Fig. 5. Two areas of interest are magnified.

The model shows that dislocations are often pinned at the ends at precipitates, obstructing their motion through the matrix and leading to entanglement of the dislocations. Extensive cross-slip and bowing is observed around the precipitates, suggesting the mechanisms by which the dislocations bypass the precipitates. The dislocation shown in Figure 6c appears to lie on an (001) plane, which varies from the {111} planes that dislocations in an FCC matrix are expected to occupy, presumably due to the high levels of stress associated with the dislocation/precipitate interactions.

## Conclusions

Diffraction-contrast electron tomography can be profitably applied to understanding complex dislocation interactions with a number of obstacles, including, as shown in this paper, precipitates, twin boundaries, and irradiation defects. Further clarity and versatility can be added to these tomograms by constructing a 3D model using the tomogram as a base for the model. Details of dislocation interactions, such as complex morphologies, line directions, slip planes, and interaction points, while difficult to resolve in two-dimensional projections traditionally associated with electron microscopy, can become a simple matter to resolve once a proper model of the interaction is constructed.

## Acknowledgements

This work was supported by the US Department of Energy, Office of Basic Energy Sciences, Division of Materials Science under award No. DEFG-02-08ER66525 for investigation of

dislocation interactions with irradiation defects and award No. DEFG-02-07ER46443 for development and application of electron tomography.

## References

1. B.F. McEwen, et al., *Principles and Practice in Electron Tomography*, in *Methods in Cell Biology*. 2008, Academic Press. p. 129-168.

2. P.A. Midgley and R.E. Dunin-Borkowski, "Electron tomography and holography in materials science," *Nat. Mater.*, 8 (4) (2009), 271-280.

3. J.S. Barnard, et al., "Three-dimensional analysis of dislocation networks in GaN using weak-beam dark-field electron tomography," *Phil. Mag.*, 86 (29-31) (2006), 4901-4922.

4. J. Kacher, G.S. Liu, and I.M. Robertson, "*In situ* and tomographic observations of defect free channel formation in ion irradiated stainless steels," *Micron* (2012), DOI: 10.1016/j.micron.2012.01.017

5. J.P. Kacher, G.S. Liu, and I.M. Robertson, "Visualization of grain boundary/dislocation interactions using tomographic reconstructions," *Scripta Materialia*, 64 (2011), 677-680.

6. G.S. Liu and I.M. Robertson, "Three-dimensional visualization of dislocation-precipitate interactions in a Al-4Mg-0.3Sc alloy using weak-beam dark-field electron tomography," *J. Mater. Res.*, 26 (4) (2011), 514 -522.

7. M. Tanaka, et al., "Crack tip dislocations revealed by electron tomography in silicon single crystal," *Scripta Materialia*, 59 (8,) (2008), 901-904.

8. M. Tanaka, et al., "Transition from a punched-out dislocation to a slip dislocation revealed by electron tomography," *J. Mater. Res.*, 25 (2010), 2292-2296.

9. M. Tanaka, et al., "Sequential multiplication of dislocation sources along a crack front revealed by HVEM-tomography," *J. Mater. Res.*, 26 (4) (2011), 508 -513.

10. G.S. Liu, "Time resolved and three-dimensional study of dislocation-particle interactions in aluminum and copper alloys," Dissertation. 2011, University of Illinois.

11. T.C. Lee, I.M. Robertson, and H.K. Birnbaum, "In situ transmission electron microscope deformation study of the slip transfer mechanisms in metals," *Metal. Trans. A*, 21A (9) (1990), 2437-2447.

12. M. Briceño, et al., "Effect of ion irradiation-produced defects on the mobility of dislocations in 304 stainless steel," *J. Nucl. Mater.*, 409 (1) (2011), 18-26.

1st International Conference on 3D Materials Science
*Edited by: Marc De Graef, Henning Friis Poulsen, Alexis Lewis, Jeff Simmons, George Spanos*
***TMS (The Minerals, Metals & Materials Society), 2012***

# The Microstructure of RR1000 Nickel-Base Superalloy: The FIB-SEM Dual-Beam Approach

S A Croxall[1], M C Hardy[2], H J Stone[1], P A Midgley[1]

[1]Department of Materials Science & Metallurgy, University of Cambridge, Pembroke Street, Cambridge, CB2 3QZ, UK.
[2] Rolls-Royce plc, PO Box 31, Derby, DE24 8BJ, UK.

Keywords: FIB-SEM, Superalloy, 3D, Serial Sectioning

## Abstract

Nickel-base superalloys are aerospace materials that exhibit exceptional mechanical properties and corrosion resistance at very high temperatures. RR1000 is used in discs in gas turbine engines, where temperatures reach in excess of 650°C with high mechanical stresses. Study of the microstructure at the micron and sub-micron level has conventionally been undertaken using scanning electron microscope images, often meaning the underlying 3D microstructure can be inferred only with additional knowledge. Using a dual-beam workstation, we are able to interrogate directly the 3D microstructure using a serial sectioning approach. The 3D data set, typically $(10\mu m)^3$ in volume, reveals microstructural detail with lateral resolution of circa $8nm$ and a depth resolution dictated by the slice thickness, typically $50nm$. Morphological and volumetric analysis of the 3D reconstruction of RR1000 superalloy reveals microstructural details hitherto unseen.

## Introduction

Analysis of the microstructure of nickel-base superalloys, at the micron and sub-micron level, has been traditionally undertaken using images acquired on a scanning electron microscope. Whilst this gives 2D information of the revealed surface, the 3D microstructure has to be inferred with additional knowledge. Many 3D characteristics of a material, such as the number of precipitates and precipitate size distribution, can be measured in 2D, but require assumptions for the full 3D estimates to be obtained. There are, however, many morphological characteristics that can be measured only in 3D, such as the true shape of individual precipitates.

Serial sectioning is a technique where successive slices of material are removed with images recorded of the revealed surface, slice-by-slice. This process is repeated until the required volume of the sample is investigated giving a stack of 2D images that represent the 3D material. This can be achieved using a dual-beam focused ion beam (FIB) scanning electron microscope (SEM), with the FIB used to remove the slices of the material and the SEM capturing images of the revealed surfaces [1]. If this is a manual process the technique is very time consuming and prone to errors especially with the slice thickness [2]. However, in recent years there has been an increase in the application and use of FIB-SEM serial sectioning for 3D microstructural characterisation as technology has advanced allowing fully automated data acquisition. There has been an increase in of desktop computing power to allow rapid processing of the large data sets gathered via serial sectioning [3].

RR1000 is a nickel-base superalloy used for high pressure disc rotors in gas turbine engines in which temperatures can reach in excess of 650°C and where high mechanical stresses

are commonplace [4]. The microstructure of the material is linked intrinsically to the mechanical properties it possesses; 3D analysis should offer new insights into the relationships between the different microstructural elements. In this work, different methods for image acquisition, image processing and 3D reconstruction are investigated to determine the feasibility and value of imaging nickel-base superalloys in 3D. Using nanoscale serial sectioning, the 3D microstructure is reconstructed post-facto, allowing for subsequent 3D volumetric and morphological analysis.

## Sample Material and Equipment

RR1000

Table I. RR1000 Chemical Composition (Weight Percent)

| Element | Ni | Co | Cr | Mo | Ta | Ti | Al | B | C | Zr | Hf |
|---|---|---|---|---|---|---|---|---|---|---|---|
| Wt% | bal | 18.5 | 15 | 5 | 2 | 3.6 | 3 | 0.015 | 0.027 | 0.06 | 0.5 |

RR1000, with a composition shown in Table I, exhibits $Ni_3Al$ $\gamma'$ precipitates, with an $L1_2$ structure dispersed within a Ni $\gamma$ matrix with an $A1$ structure. The alloy is produced via powder metallurgy using argon gas atomisation, with the $\gamma'$ varying in size from $1\mu m$ to $5nm$ depending on the heat treatment and cooling rates applied [5]. In this investigation, forged material was given a super-solvus heat treatment: forged RR1000 was solution heat treated at 1170°C for 4 hours, cooled at 1°C/min, and then aged for 12 hours at 800°C. The cooling rate, notably slower than than those in disc forgings, was chosen to yield large precipitates that show dendritic morphology at a scale suitable for testing the 3D imaging capabilities of the FIB-SEM, Figure 1.

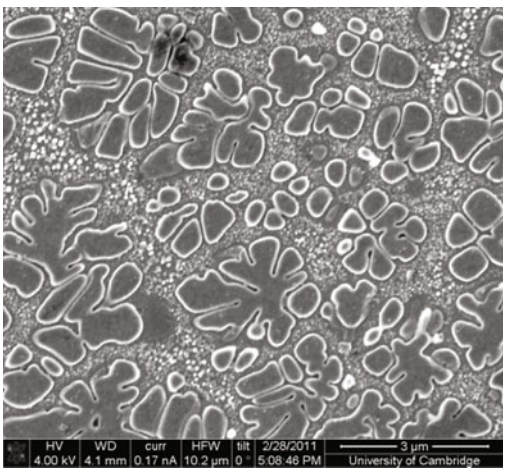


Figure 1: Secondary electron 2D micrograph of the RR1000 sample used in this investigation. The $\gamma'$ are visible as the "flower-like" shapes. An electrolytic etch has been applied to preferentially remove the $\gamma$ phase, leaving the $\gamma'$ in relief.

Dual-Beam FIB-SEM

The microscope used in this investigation is an FEI Company Helios Nanolab 600, which features a field emission gun SEM and a FIB column, using $Ga^+$ ions, at 52° to the vertical [6], see Figure 2. The electron column has a quoted resolution of $1.6nm$ at $5kV$ at the coincident working distance of $4mm$, while the FIB gives a resolution of $5nm$ at $30kV$ with a working distance of $16.5mm$.

Sample Preparation, Image Optimisation and Serial Sectioning

The samples were prepared using a precision saw to slice off small slices from the bulk material before being mounted on standard aluminium SEM stubs. As the experimental technique does not require a smooth surface, no further polishing is required and the samples are mounted in the Helios for the fine scale sample milling.

Before the serial sectioning can commence, a volume of interest needs to be prepared that will have an imaging surface that is parallel to the FIB and visible to the SEM for imaging. The preparation method involves tilting the sample to 52° so that the surface is perpendicular to the FIB. A region of interest $15\mu m$ x $20\mu m$ was selected and a protective layer of platinum deposited to protect it during the rough milling stage. Trenches are then milled out around three edges of the region of interest to stop redeposition of material during the serial sectioning and to allow an unobstructed view of the imaging face by the SEM, Figure 2.

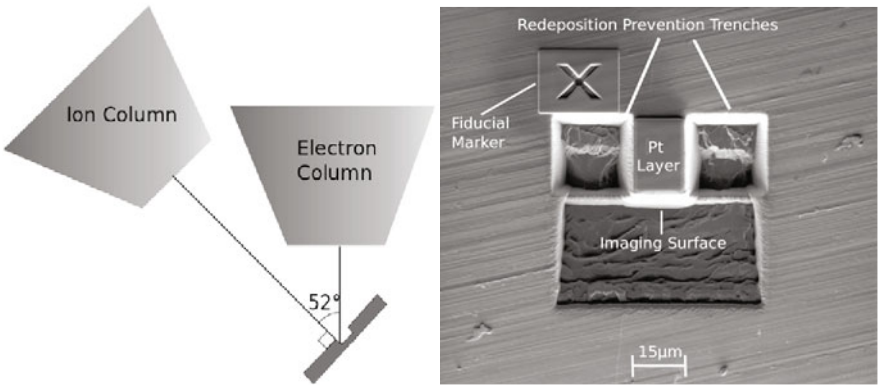


Figure 2: *Left*: Schematic geometry of the fine sample preparation for serial sectioning in a FIB-SEM. *Right*: FIB image of the region of interest after rough milling.

Various detectors can be used while imaging with the electron beam during serial sectioning. The simplest signal in principle for detecting the contrast between the $\gamma$ and $\gamma'$ is from backscattered (BS) electrons, as this gives contrast directly dependent on the elemental composition of the features being imaged. However, due to the geometry of the imaging conditions, there is a significant loss of imaging signal as some BS electrons do not reach the in-column Thru-the-Lens Detector (TLD). To counter this, the Helios is used in the ultra-high resolution (UHR) mode in which a magnetic immersion lens helps to focus type-II secondary electrons (SE) up the column to the TLD detector. Type-II secondary electrons are generated by interactions of the electrons with the sample and this signal contains the compositional information. The best imaging conditions were found to be with an electron beam current of $0.69nA$, accelerating voltage of $5kV$, an image size of 2048x1768 pixels, dwell time of $30\mu s$ and horizontal field width of $17\mu m$.

The serial sectioning consists of two main stages. Firstly the Ga ion beam is used to remove a thin layer of material from the imaging face, 50nm in this investigation, with the aid of a fiducial marker to counter any drift of the stage. Once the slice has been milled, the electron beam is used to capture an image of the revealed surface using the conditions described above. In total, 283 slices were acquired over 22 hours, of which 224 were used in the final reconstruction.

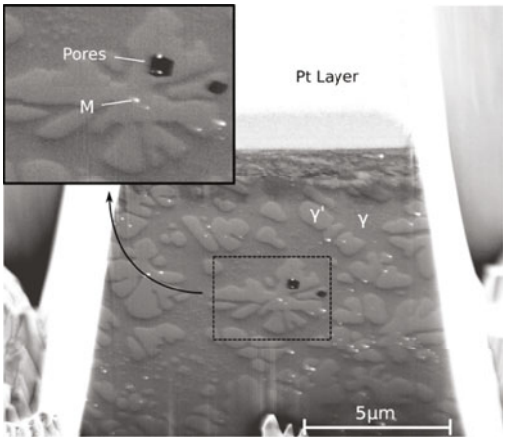


Figure 3: An unprocessed secondary electron image from the serial sectioning of RR1000 alloy. The inset shows a magnified part of the image. The "flowers" are $\gamma'$, the white dots are likely to be carbides/oxides and the black regions are pores. The image is recorded at 52° tilt.

Figure 3 shows one of the unprocessed images taken from the serial sectioning run. The first step is to align all the slices to remove any stage drift and crop the images to include only the area of the face that is of interest. With a data set of 224 images, and without any drift correction on the SEM images, the drift of the sample with regards to the field of view is such that the total stack needs to be split up into smaller stacks of approximately 50 images. The StackReg plugin for ImageJ can then be used to align the smaller stacks before they are combined. These are then cropped to the area of the face that is free from any "curtaining" in the middle of the imaging face. The final stage is then to adjust the image brightness and contrast, and the whole stack normalized to get comparable intensities throughout the stack.

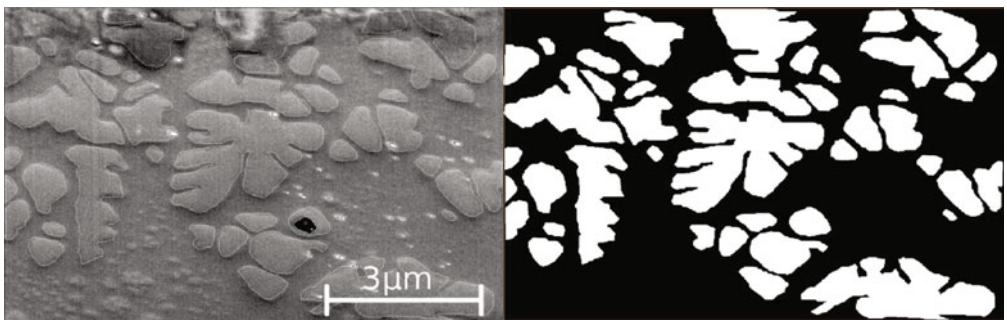


Figure 4: The segmentation and binarisation process to enable the 3D reconstruction of the $\gamma'$ precipitates of RR1000.

For segmentation and reconstruction, specialist software Avizo®Fire is used. The processed images need to be segmented into their separate components, primarily here the $\gamma'$ precipitates and the bright spots (carbides/oxides) that appear in each slice. Due to the complex nature of the variations in intensities across the imaging face, simple global thresholding could not be used, and the data set had to be segmented manually, see Figure 4. Once

the features were segmented, binary image stacks were produced individually for both the $\gamma'$ and carbides/oxides.

The next stage is to reconstruct the surfaces of the $\gamma'$ and this is delivered by linking the precipitate features in sequential slices and forming 3D representations; the use of a built-in smoothing algorithm accounts for the lost data between the slices. Finally, the voxel size needs to be input to give the correct relationship between the three dimensions and care must be taken to account for the angle of the imaging face to the electron beam. The final reconstruction was generated for both the $\gamma'$ and carbides/oxides separately, giving a total volume of 9.5$\mu$m x 8.7$\mu$m x 11.3$\mu$m, Figure 5.

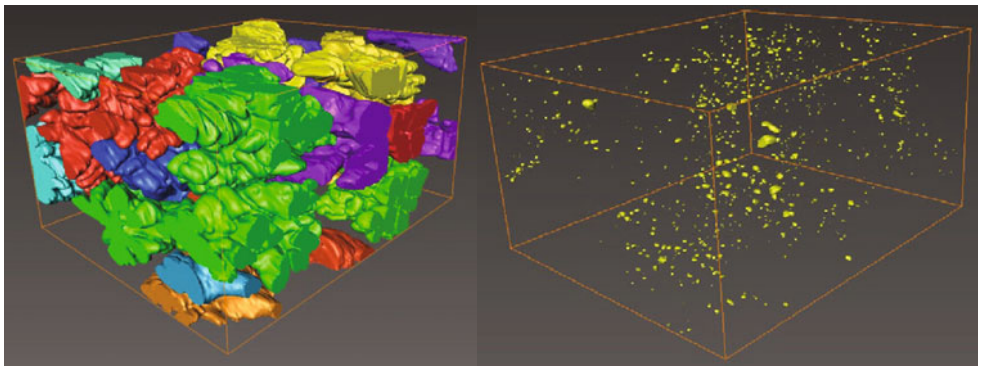

Figure 5: Reconstruction of the $\gamma'$ and "bright spot" microstructure of RR1000. The bounding box measures 9.5$\mu$m x 8.7$\mu$m x 11.3$\mu$m, the precipitates are coloured to distinguish individual precipitates. The small precipitates on the right are most likely tantalum and/or hafnium carbides and/or oxides.

## Results and Discussion

Aviso® Fire offers a great deal of built-in functionality in terms of 3D analysis of the reconstructions. The software is able to separate each individual precipitate and perform volumetric measurements. This is important as at this stage there are many single voxel precipitates that are artifacts of the segmentation and reconstruction process; these can be removed by filtering out precipitates under a minimum, physically meaningful, size. This is also useful for the study of individual precipitates, or groups of precipitates. By overlaying the reconstruction of the bright spot features, the relationship between the two microstructural elements can be visualised. The volumetric data can be used quantitatively, for example, by plotting the surface area of the precipitates against precipitate volume, Figure 6. This plot shows that the smaller precipitates follow the growth expected for a spherical precipitate with $A \propto V^{2/3}$. As the precipitates get larger, their growth becomes more dendritic with the surface area increasing at a faster rate, alluded to by the linear nature of the graph at high volumes. Future work will include full characterisation of the dendritic growth and the implications this has on the mechanical properties of the alloy.

## Conclusion

We have demonstrated how FIB-SEM can be used to reconstruct 3D morphology and distribution of precipitates in RR1000 nickel-bas superalloy. Quantitative 3D analysis of the $\gamma'$ precipitates has given insight into the development of dendritic morphology. Other image

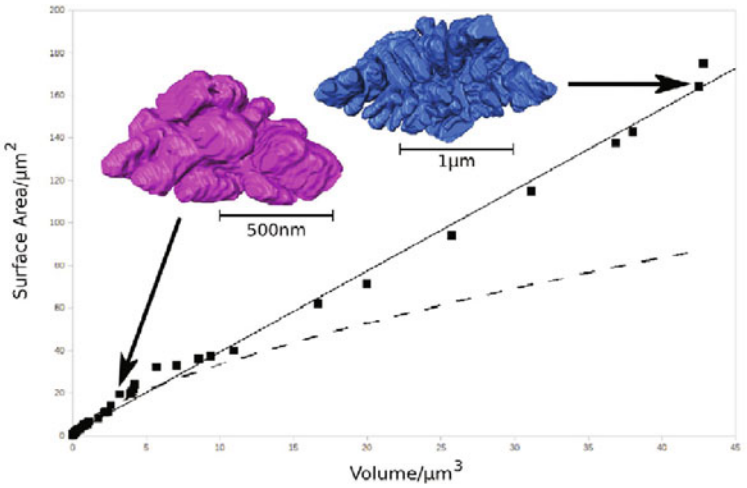


Figure 6: Graph showing the precipitate volume plotted against the surface area (data points). The standard of a sphere of increasing radius is used as a reference (dotted line). Two precipitates are shown (not to scale), and their corresponding data points are indicated by arrows.

modes and acquisition conditions need to be explored more fully, but already the wealth of data provided by the FIB-SEM technique is enabling a better understanding of the microstructural development of RR1000 and its relationship with the underlying mechanical properties.

## Acknowledgments

The authors would like to acknowledge the support provided by the University of Cambridge, EPSRC and Rolls-Royce plc. PAM acknowledges funding from the ERC under grant number 291522 3DIMAGE and the EPSRC grant number E012477.

## References

[1] Dunn, D. N., Kubis, A. J., and Hull, R. Quantitative Three-Dimensional Analysis Using Focused Ion Beam Microscopy pp. 281–300 Springer (2005).

[2] Groeber, M. A., Haley, B. K., Uchic, M. D., Dimiduk, D. M., and Ghosh, S. January 2006 *Materials Characterization* **57**, 259–273.

[3] MacSleyne, J., Uchic, M. D., Simmons, J. P., and Graef, M. D. August 2009 *Acta Materialia* **57**, 6251–6267.

[4] Reed, R. C. (2006) The Superalloys: Fundamentals and Applications, Cambridge University Press, .

[5] Collins, D. M., Heenan, R. K., and Stone, H. J. (2010) *Metallurgical and Materials Transactions A* **42(1)**, 49–59.

[6] Young, R. J. and Moore, M. V. Dual-Beam (FIB-SEM) Systems: Techniques and Automated Applications pp. 247–268 Springer (2005).

1st International Conference on 3D Materials Science
*Edited by: Marc De Graef, Henning Friis Poulsen, Alexis Lewis, Jeff Simmons, George Spanos*
***TMS (The Minerals, Metals & Materials Society), 2012***

# 3D ANALYSIS OF PHASE SEPARATION IN FERRITIC STAINLESS STEELS

Joakim Odqvist[1], Jing Zhou[1], Wei Xiong[1], Peter Hedström[1], Mattias Thuvander[2], Malin Selleby[1] and John Ågren[1]

[1]Department of Materials Science and Engineering, KTH Royal Institute of Technology, SE-10044, Stockholm, Sweden

[2]Department of Applied Physics, Chalmers University of Technology, SE-41296, Göteborg, Sweden

Keywords: Phase separation, Atom Probe Tomography, Phase-field modeling

## Abstract

The embrittlement of ferritic stainless steels during low temperature aging is attributed to the phase separation with Fe and Cr demixing. The small scale of the decomposed structure with only minor compositional fluctuations and short distances between the enriched and depleted regions has been a challenge for quite some time. A wide selection of experimental and modeling tools have been used to quantify these types of structures. These analyses often focus on rather late stages of decomposition where the mechanical properties are already seriously affected. The recent advance in 3D tools like phase-field and atom probe tomography have created a need for good quantitative procedures of evaluating the structure and also to link results from the continuum approach to the individual atom measurements. This work aims at addressing this need.

## Introduction

The phase separation of Fe-Cr alloys at low and intermediate temperatures, historically known as the 475°C embrittlement, has been studied extensively both experimentally and theoretically, see e.g. [1-4] and the references therein. Due to the small difference in atomic size between Fe and Cr and the nanoscale structure experimental investigation of phase separation in the early stages using electron microscopy and XRD has been a challenge. However, atom probe tomography (APT) has opened up possibilities to perform atomic-scale studies of short-range ordering and clustering effects [5]. On the theoretical side phase separation has been modeled with the Cahn-Hilliard equation [2,4,6,7] and the Monte Carlo (MC) technique, see e.g. [8]. Both the continuum and atomistic treatments have their advantages and disadvantages: for the Cahn-Hilliard equation additional elements and the effect of stress are easily added, but a quantitative comparison with APT is more challenging. On the other hand, in the MC technique simulation of higher order systems and the influence of stress are not so straightforward to handle while comparison with APT is easier.

In the present work phase separation in one binary Fe-Cr alloy is simulated using the Cahn-Hilliard approach coupled with a recently improved thermodynamic description of Fe-Cr [3]. A quantitative comparison of the wavelength of compositional fluctuations in simulations and APT is estimated using different methods.

## Atom Probe Tomography (APT)

Experimental Details

The Fe-Cr alloy was produced by vacuum arc melting and casting of a 600g ingot. Before any aging treatments the sample was homogenized at 1100°C for 2h under argon and subsequently quenched in brine. Aging treatments were performed at 500°C for up to 1000h. Samples for APT were cut into square sectioned rods 20 x 0.3 x 0.3 $mm^3$ and subsequently sharp needle-like samples were prepared using the standard two-stage electro-polishing method. A LEAP 3000X HR$^{TM}$ (Imago Scientific Instruments, USA) equipped with a reflectron for improved mass resolution was used for all APT measurements. The ion detection efficiency is about 37% and the experiments were made in voltage pulse mode (20% pulse fraction, 200 kHz, evaporation rate 1.5%) with a specimen temperature of 55K.

Methods of Analysis

In the present work focus was on the evaluation of the wavelength of the compositional fluctuations in Fe-36 at.% Cr after aging at 500°C for 100 h using three different methods: the autocorrelation function (ACF) [9], fast fourier transform (FFT) and the radial distribution function (RDF) available in the software IVAS 3.4.3.

## 3D Simulation Of Phase Separation In Binary Fe-Cr

In order to simulate phase separation in binary Fe-Cr the ordinary diffusion equation needs to be modified to account for local gradients in composition which enters through the Gibbs energy functional

$$G = \frac{1}{V_m}\int_V \left( G_m(x_{Cr}, T) + \frac{\kappa^2}{2}\left|\nabla x_{Cr}\right|^2 \right) dV \tag{1}$$

Where the integration is taken over the volume $V$ of interest, $V_m$ is the molar volume here assumed to be constant, $G_m$ is the molar Gibbs energy, $x_{Cr}$ is the mole fraction of Cr and $\kappa$ are the so-called gradient energy coefficient. The variational derivative of eq. (1) with respect to $x_{Cr}$ inserted into the Onsager linear law of irreversible thermodynamic gives us

$$J_{Cr} = -L_{CrCr}\nabla\left(\frac{\delta G}{\delta x_{Cr}}\right) = -\frac{L_{CrCr}}{V_m}\nabla\left(\frac{\partial G_m}{\partial x_{Cr}} - \kappa^2\nabla^2 x_{Cr}\right) \tag{2}$$

Where $\mu_{Cr}$ and $\mu_{Fe}$ are the chemical potentials for Cr and Fe respectively. $L_{CrCr}$ denotes the phenomenological coefficient which are related to the atomic mobilities [10]. Eqs. (1) and (2) combined with the continuity equation results in a modified diffusion equation usually called the Cahn-Hilliard equation [6,7].

$$\frac{1}{V_m}\frac{\partial x_{Cr}}{\partial t} = -\nabla \cdot J_{Cr} \tag{3}$$

It should be emphasized that no linearization of eq. (3) was performed and the atomic mobilities were allowed to change with composition. Eq. (3) was solved numerically using a semi-implicit Fourier-spectral method [11] on an equidistant grid. The derivatives of the chemical potentials were obtained from Thermo-Calc through a Fortran based programming interface using a recently improved thermodynamic description for the Fe-Cr system [3]. Cahn and Hilliard [6] assumed that the gradient energy coefficient was proportional to the regular solution parameter. This was adopted also in the present work, i.e.

$$\kappa = \frac{\Omega_{CrFe} l^2}{2} \tag{4}$$

Where $\Omega_{CrFe}$ is the regular solution parameter, taken from [3], $l$ is the interatomic distance set to 0.25nm. The atomic mobilities were estimated from a fit between composition amplitudes from APT and simulations using a newly developed technique described elsewhere [12]. Simulation results for Fe-36 at.% Cr aged at 500°C during 0, 10, 100 and 180 h are shown in Fig. 1.

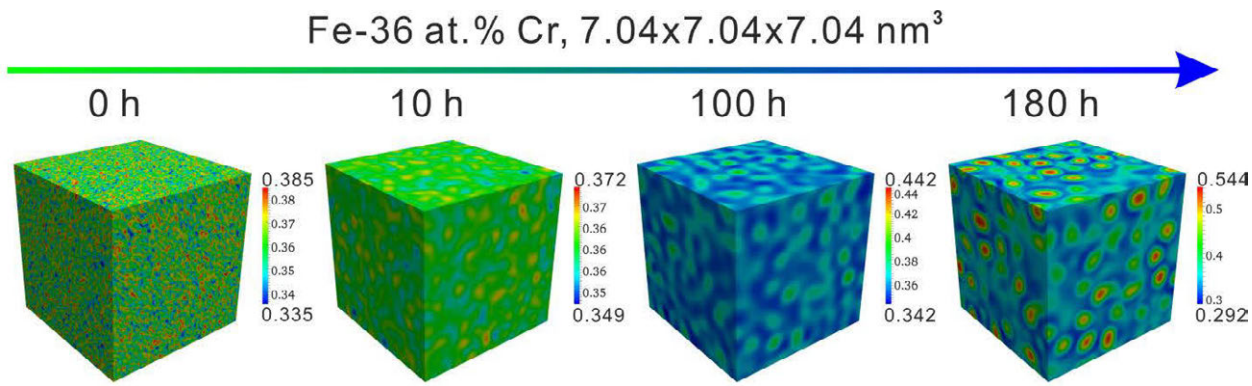


Fig. 1. Simulation of the evolution of phase separation in Fe-36 at.% Cr during aging at 500°C. The red and blue color denotes Cr-rich and Fe-rich areas respectively.

**Quantitative Comparison Between Simulation And APT**

The results from evaluation of the wavelength from simulation and APT data using ACF, FFT and RDF are shown in Figs. 2-4. In Fig. 2 the ACF in 1D was used, but it was applied continuously throughout the simulated and experimental volume by stepping in the y and z direction while measuring in the x-direction. The results from each step was then added together, hence the smooth curves in Fig. 2. This procedure thus involves the full 3D data and should give a considerably more accurate estimation of the wavelength compared to a 1D ACF in a random direction. In fact, if the 1D ACF was applied to a couple of random directions in the experimental data the estimated wavelengths were in the range 3-5 nm. The first maxima of the ACF indicate the wavelength of the compositional variation [1]: 5 nm and 1.2 nm for APT and simulation respectively, see Fig. 2.

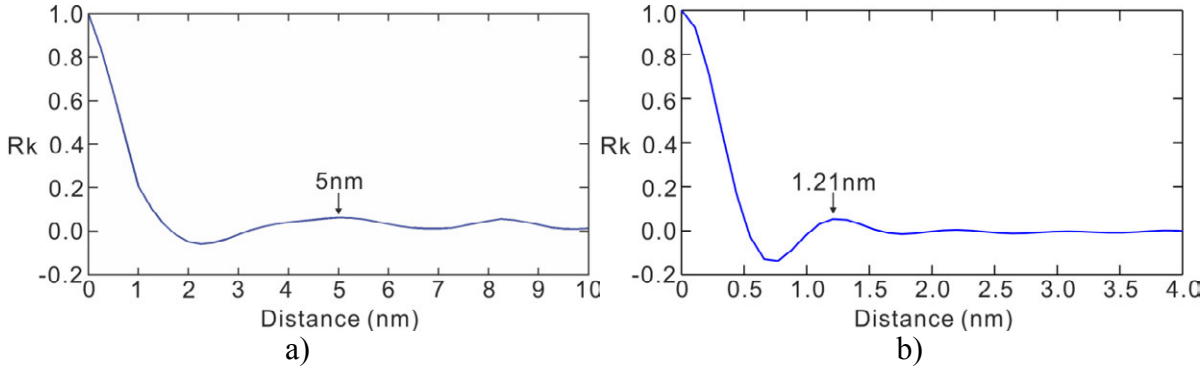


Fig. 2. Results from the autocorrelation function ($R_k$) for a) APT: λ≈5 nm and b) Simulation: λ≈1.2 nm. After aging Fe-36 at.% Cr at 500°C for 100 h.

The same procedure as for the ACF was used for the FFT i.e. the FFT in 1D was used repeatedly in the whole volume, see Fig. 3. In order to find the most dominant wave from the spectrum i.e. the fastest growing wave, integration under the different peaks was performed. For APT it was found that the spatial frequency should be between 0.2044 and 0.2166 $nm^{-1}$, and 0.7032 and 0.7172 $nm^{-1}$ for the simulation, see the magnified spectrum in Fig. 3. The arithmetic mean for each case was chosen to represent the frequency of the fastest growing wave i.e. 0.21 $nm^{-1}$ for APT and 0.71 $nm^{-1}$ for the simulation corresponding to a wavelength of 4.8 nm and 1.4 nm respectively.

In Fig. 4 only the RDF for the APT data is shown since no information on the position of individual atoms is available from the simulation. The RDF represents the average radial concentration profile measured from each atom of the species selected; in Fig. 4 the RDF for Cr-Cr is shown. The high values at short distances is an indication that Cr wants to cluster to Cr i.e. there is phase separation of Fe and Cr. If the concentration is normalized with the bulk concentration the RDF will approach unity for a random distribution of Cr atoms.

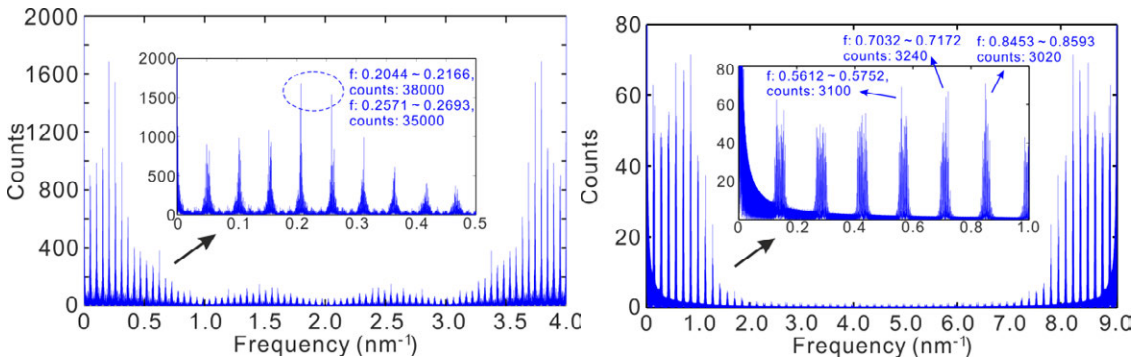


Fig. 3. Results from FFT for a) APT: λ≈4.8 nm and b) Simulation: λ≈1.4 nm. After aging Fe-36 at.% Cr at 500°C for 100 h.

It is interesting to note that the estimated wavelength from the APT data is rather consistent around 5 nm for all three methods and 1.2-1.4 nm for the simulated data using ACF and FFT. The ACF in 1D applied with the stepping procedure described above seems to perform just as well as the more advanced RDF method, which is believed to be a more accurate method.

Under the assumption of sinusoidal compositional fluctuations, small in amplitude, Hillert [13] introduced the concept of a critical wavelength ( $\lambda_c$ ), such as below this wavelength fluctuations would decrease and disappear. For the present case this assumption gives $\lambda_c$ =0.98 nm. Hillert also showed that the wavelength of the fastest growing wave is given by $\lambda_{max} = \sqrt{2}\,\lambda_c$ . Inherent in this result is the assumption of an isotropic material. Inserting the calculated $\lambda_c$ gives $\lambda_{max} \approx 1.4$ nm, in good agreement with the FFT result for the simulation. This good agreement should not come as a surprise since the effects of coherency stresses and anisotropy in elastic properties were not included in the modeling. In reality the fluctuations should be more pronounced in the elastically soft direction. However due to the small misfit between Fe and Cr this effect should be small.

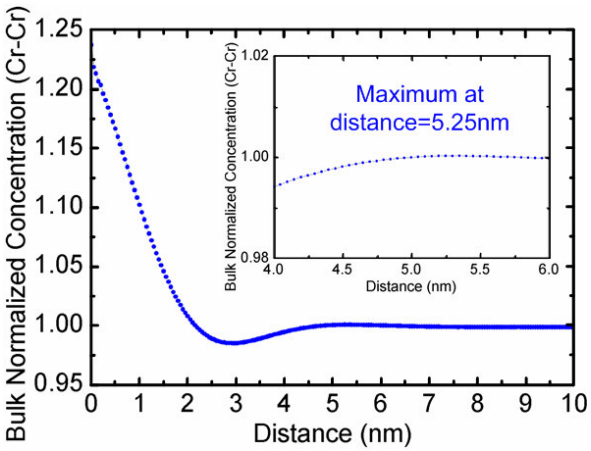


Fig. 4. Results from RDF for APT: λ≈5.2 nm. After aging Fe-36 at.% Cr at 500°C for 100 h.

## Concluding Remarks

In the present work a quantitative comparison of the estimated wavelength of compositional fluctuations during phase separation of a Fe-Cr alloy from APT and simulations has been performed. The large difference in the wavelength estimated from APT and simulation could be due to several reasons. For example, the gradient energy coefficient is assumed to be constant in the simulation, see eq. (4). The gradient energy coefficient is a weight factor that determines how large the energy penalty will be for having a too sharp interface between Fe-rich and Cr-rich regions i.e. the whole gradient term is a measure of the interfacial energy. It is possible that a composition dependent gradient would bring the estimated wavelength from simulations closer to the experimental values. In addition, the Cahn-Hilliard equation is deterministic in the sense that no noise due to thermal fluctuations is accounted for when time > 0, instead a stochastic variant of the eq. (3) should be solved. All this will be explored in future studies.

## Acknowledgements

This project was supported by the VINNEX centre Hero-m, financed by the Swedish Governmental Agency for Innovation Systems (VINNOVA), Swedish industry and KTH (Royal Institute of Technology) JO and MT also acknowledges the support from the Swedish Research Council (VR, Grant No. 621-2009-5289).

## References


[1] J. M. Hyde , M. K. Miller, M. G. Hetherington, A. Cerezo, G. D. W. Smith and C. M. Elliott, "Spinodal decomposition in Fe-Cr alloys: experimental study at the atomic level and comparison with computer models – II. Development of domain size and composition amplitude", *Acta Metall. Mater*., 43 (1995), 3385-3401.

[2] W. Xiong, K. Asp Grönhagen, J. Ågren, M. Selleby, J. Odqvist and Q. Chen, "Investigation of spinodal decomposition in Fe-Cr alloys: Calphad modeling and phase field simulation", *Solid State Phenom*. 172-174 (2011), 1060-1065.

[3] W. Xiong, P. Hedström, M. Selleby, J. Odqvist, M. Thuvander and Q. Chen, "An improved thermodynamic modeling of the Fe-Cr system down to zero Kelvin coupled with key experiments", *Calphad*, 35 (2011), 355-366.

[4] P. Hedström, S. Bagsheikhi, P. Liu and J. Odqvist, "A phase-field and electron microscopy study of phase separation in Fe-Cr", *Mater. Sci. Eng*. A, 534 (2012), 552-556.

[5] M.K. Miller and E.A. Kenik, "Atom Probe Tomography: A technique for nanoscale characterization", Microsc. Microanal., 10 (2004), 336-341.

[6] J.W. Cahn and J. E. Hilliard, "Free energy of a nonuniform system. I. Interfacial energy", *J. Chem. Phys*., 28 (1958), 258-267.

[7] J. W. Cahn, "On spinodal decomposition", *Acta Met*., 9 (1961), 795-801.

[8] C. Pareige, M. Roussel, S. Novy, V. Kuksenko, P. Olsson, C. Domain and P. Pareige, "Kinetic study of phase transformation in a highly concentrated Fe-Cr alloy: Monte Carlo simulation versus experiements", *Acta Mater*., 59 (2011), 2404-2411.

[9] M. Kendall, A. Stuart and J. K. Ord: *The Advanced Theory of Statistics* ($4^{th}$ Ed. Griffin & Box, London, 1983).

[10] J.-O Andersson and J. Ågren, "Models for numerical treatment of multicomponent diffusion in simple phases", *J. App. Phys*., 72 (1992), 1350-1355.

[11] L.Q. Chen and J. Shen, "Applications of semi-implicit Fourier-spectral method to phase field equations", *Comp. Phys. Comm*., 108 (1998), 147-158.

[12] W. Xiong and J. Ågren, unpublished research, 2012.

[13] M. Hillert, "A solid-solution model for inhomogeneous systems", *Acta Met*., 9 (1961), 525-535.

1st International Conference on 3D Materials Science
*Edited by: Marc De Graef, Henning Friis Poulsen, Alexis Lewis, Jeff Simmons, George Spanos*
***TMS (The Minerals, Metals & Materials Society), 2012***

# MICRO-COMPUTED TOMOGRAPHY, A 3D TOOL FOR NON-DESTRUCTIVE VISUALISATION AND ANALYSIS

E. Bongaers[1], R. Van den Bosch[2]

[1] SkyScan, Kartuizersweg 3b, 2550 Kontich, Belgium.
[2] University of Antwerp, Department of Physics, Groenenborgerlaan 171, 2020 Antwerp

Keywords: micro-computed tomography, 3D visualization, microstructure, porosity, rocks, geological materials

## Abstract

Micro-Computed Tomography (microCT) is a powerful technique to visualize the microstructure of various materials, both biological as non-biological, in a non-destructive way. By means of x-rays the internal structure is revealed on a micro- or nanometer scale. As an example this paper will focus in the study of pores and pore networks in rocks for oil exploration. The resulting dataset of a micro-CT scan is a set of thin, virtual slices through the object. 3d analysis software can extract unique numerical characteristics, such as internal porosity, size distribution for pores or grains, etc. Visualisation software shows a realistic 3D object on the screen, Micro-CT has an added value and can provide new information in 3D, leading to new insights in materials and processes.

## Introduction

In many applications (foods, packaging materials,..) open and closed porosity, pore networks and pore connectivity are crucial parameters requiring 3D evaluation. Obtaining 3D information of the internal microstructure of an object is possible by means of micro-CT. A material that is placed between an x-ray source and detector, can partially absorb or transmit x-rays, depending on its density. In this way a 2D radiographic projection image is created. By rotating the sample, a series of 2D projection images is acquired. Backprojecting these projection images allows the reconstruction of the crossectional slices of the sample, now containing spatially resolved information. The stack of crossectional images, i.e. virtual slices true the object, reveals true 3D information of the internal microstructure of the material. 3D image analysis of this image stack can provide answers to all porosity questions, but results should be carefully interpreted. To this end, 3D analysis offers plenty of tools as will be shown by means of 2 rocks as example datasets.

## Methods

The SkyScan 1173 (Kontich, Belgium) is a desktop micro-CT scanner with a polychromatic x-ray source of 130 kV. A flatpanel detector of 2400 pixels allows achievement of pixel sizes down to 5-6 micrometers. The samples were scanned at 12 micrometer/pixel. Projection images have been reconstructed by means of NRecon software with an NReconServer engine. SkyScan software CTAn is used for image analysis. Surface rendering is performed by means of SkyScan software CTVol.

## Results & Discussion

Figure 1 shows the reconstructed crossections of the 2 sandstone samples. Sandstone 2 (bottom) shows a significantly larger connectivity between the pores and an increase in overall porosity in comparison with sandstone 1 (top). A basic porosity analysis is already sufficient to illustrate this, as shown in methodology 1.

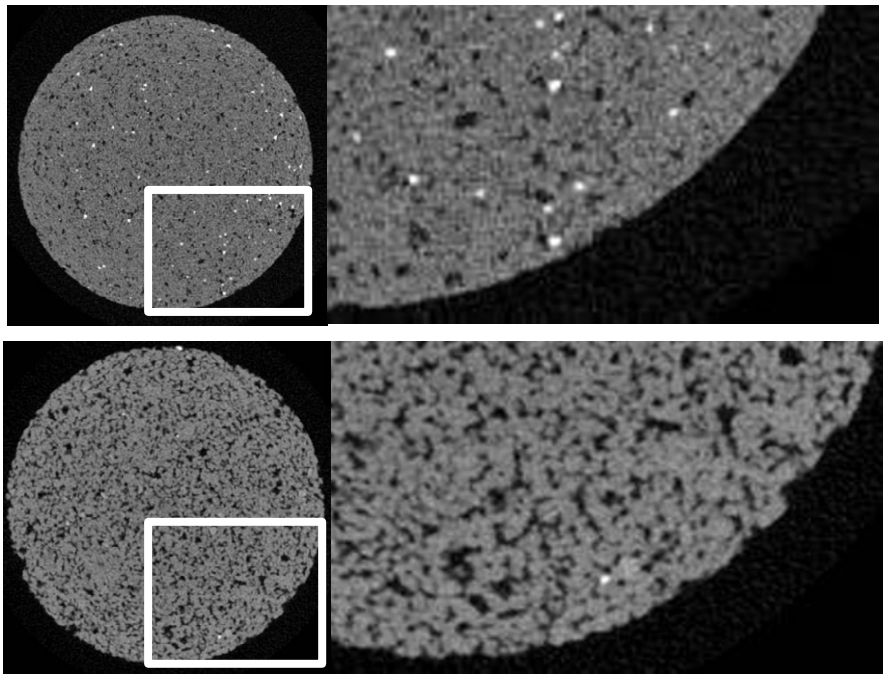

Figure 1. Reconstructed view of cylindrical sandstone samples, the inset of the crossection on the left is shown at higher magnification on the right.

Methodology 1: Analysis of open and closed porosity

Firstly, a region of interest (ROI) is selected to avoid air outside the sample negatively impacting porosity analysis results. Note that all operations are shown on a 2D slice, but are performed on a 3D dataset.

By means of thresholding raw images are converted to binary images (figure 2), in which the object pixels are white, and the pixels, representing pores, black. Images have been despeckled to remove black speckles due to noise. White speckles have been removed by means of a sweep operation which removes all objects except the largest one, i.e. the sandstone matrix. Image analysis is performed by CTAn on selected pixels, i.e. white, better known as "object". Within this object, CTAn can identify pores, as being a number of black pixels, surrounded by white pixels. It can distinguish between bubbles (closed pores) or connecting channels (open pores), giving you information about the porosity network. A 3D analysis of this data is presented in the table below, confirming the higher open porosity and larger overall porosity.

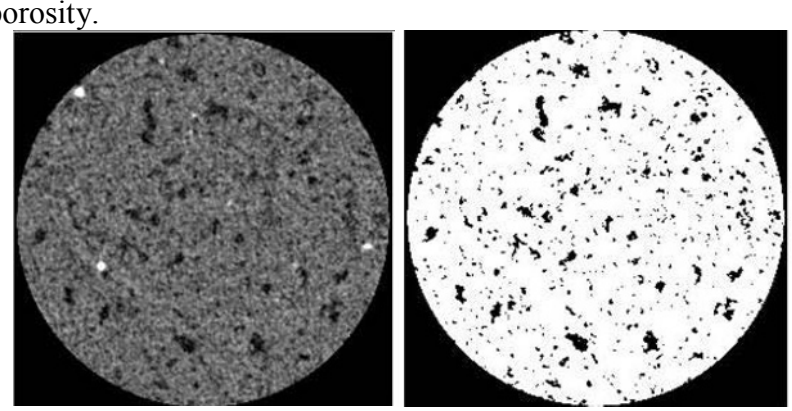

Figure 2. Crossection before and after image analysis steps in methodology 1.

Table 1. 3D Analysis

| | Sandstone 1 | Sandstone 2 |
|---|---|---|
| Total VOI volume | 52.8 $mm^3$ | 50.7 $mm^3$ |
| Object volume | 50.0 $mm^3$ | 43.8 $mm^3$ |
| Number of closed pores | 22074 | 2410 |
| Volume of closed pores | 2.32 $mm^3$ | 0.33 $mm^3$ |
| Closed porosity | 4.43 % | 0.75 % |
| Volume of open pore space | 0.45 $mm^3$ | 6.59 $mm^3$ |
| Open porosity | 0.85 % | 13.0 % |
| Total volume of pore space | 2.77 $mm^3$ | 6.92 $mm^3$ |
| Total porosity | 5.25 % | 13.6 % |

Methodology 2: Distribution of Open Porosity

To focus on the distribution of open porosity throughout the sample, CTAn offers a built-in plugin by means of which the closed pores can be removed. Only open pores, which are in contact with the image boundary, will remain present in the dataset (see figure 3 below).

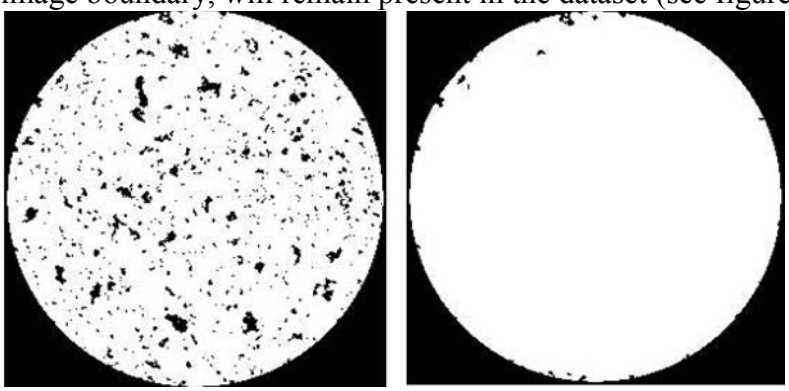

Figure 3. Crossection before and after removing the closed pores by means of CTAn.

A 2D analysis will calculate porosity parameters for each individual slice of the dataset. The remaining pores are open in 3D, but when considering a 2D crossection, they can be either open or closed. Therefore in this 2D analysis the total porosity is considered, defined as the pore volume with respect to the object volume. The distribution of the (3D) open pores throughout the sample is shown in following figure.

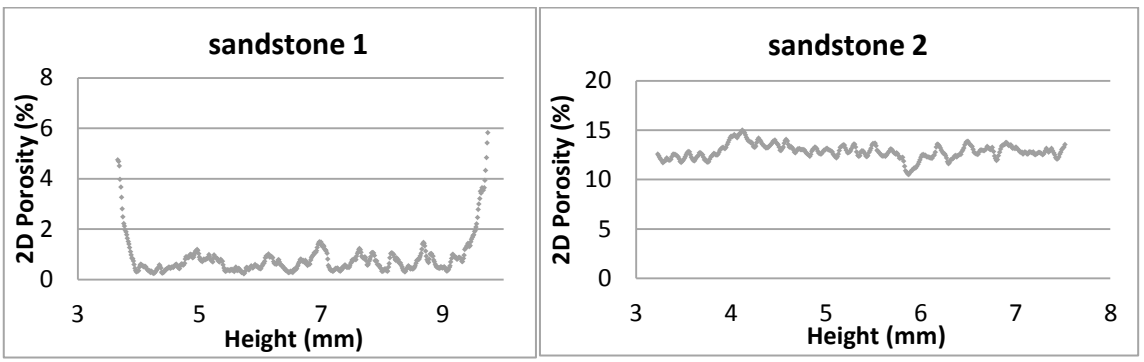


Figure 4. Open porosity in function of the height of the sandstone samples.

In sandstone 1 the open porosity is especially present at the upper and lower slices of the sample. For sandstone 2 the open porosity is homogeneously distributed throughout the

sample, representing a bulk material property. The effect in sandstone 1 is caused by virtually cutting the sample with the VOI, cutting through the closed pores. By reslicing the dataset the 2D analysis can be repeated on the new stack of slices, resulting in a distribution of open pores in function of any desired direction. The figure below shows the result for 2 perpendicular directions throughout the diameter of the cylindrical shape (referred to as width and depth). The open porosity is no characteristic of the bulk material, but an artifact caused by the finite dimensions of the sample.

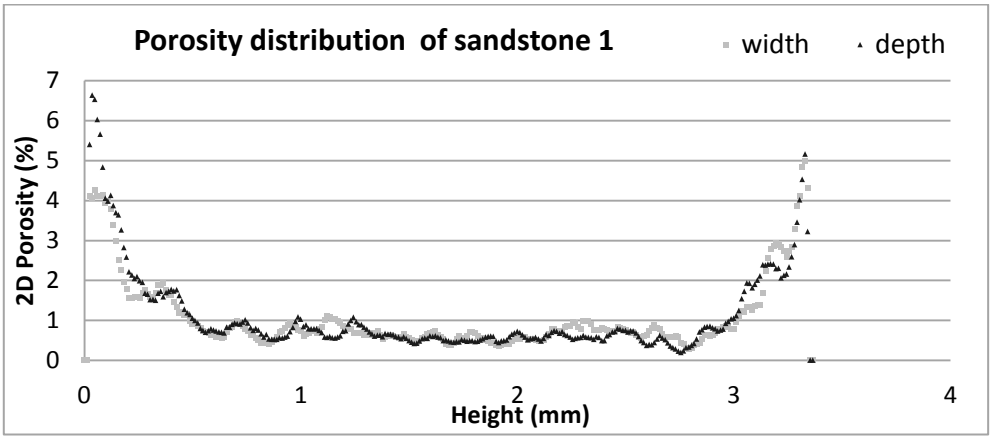


Figure 5. Open porosity distribution throughout the diameter in sandstone 1.

The percentage of closed porosity is calculated with respect to the object volume, being the binarized object and the closed pores, excluding the open pores. It is a material property, as opposed to open porosity or total porosity, which are calculated with respect to to entire VOI volume. From the formulas below (1-3) can be seen that the total porosity does not equal the sum of open and closed porosity. A different methodology is required to reduce the artificially opened pores.

$$\%\ Closed\ Porosity = \frac{Closed\ Pore\ Volume}{Object\ Volume + Closed\ Pore\ Volume} \quad (1)$$

$$\%\ Open\ Porosity = \frac{Open\ Pore\ Volume}{VOI\ Volume} \quad (2)$$

$$\%\ Total\ Porosity = \frac{Closed\ Pore\ Volume + Open\ Pore\ Volume}{VOI\ Volume} \quad (3)$$

Methodology 3: Advanced Porosity Analysis

In this section we will eliminate the open porosity artifact in sandstone 1 Firstly, the ROI is eroded by one pixel in 2D, meaning that the boundaries of the circle shaped ROI will move one pixel inward In this way a slightly smaller ROI is created. Secondly, a bitwise operation is performed to replace the image with a copy of the smaller ROI (image=copy ROI). Next, the original ROI is reloaded (2). The smaller circle can now be subtracted from the bigger circle to create a one-pixel boundary for our object by means of the bitwise operation "ROI=ROI sub image'(3). The original image can now be reloaded (4) and thresholded and despeckled (5) as discussed in the basic porosity analysis. When considering the 'image inside the ROI', one can see black speckles. These are the pores in the sample boundary, causing incorrect open porosity value. Now the crucial step in removing this unwanted effect merges the one-pixel boundary with the image by means of the operation 'image=image OR ROI' (6). No more open pores are present. Finally, before proceeding to the analysis, the original ROI can be reloaded (7). A 3D analysis can now be performed with the results in the table below.

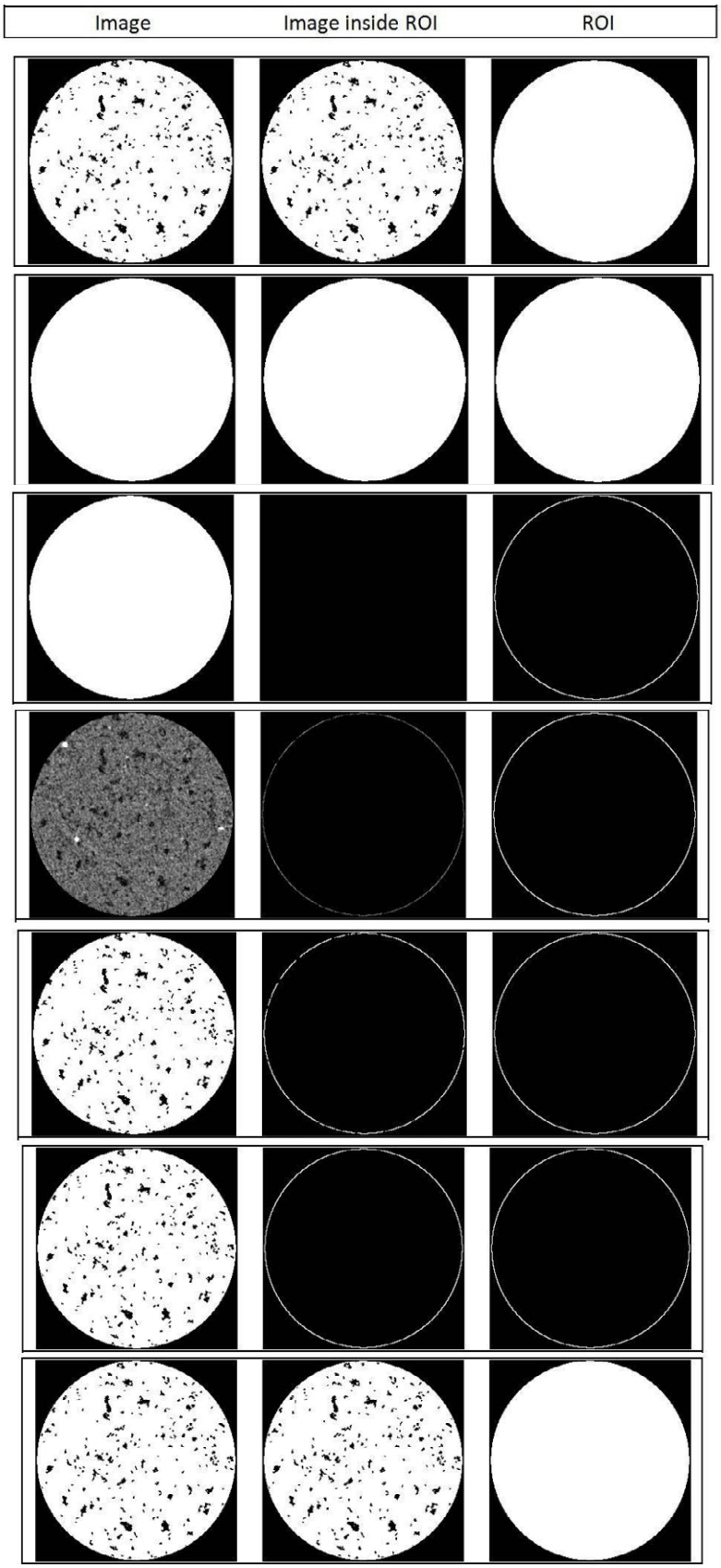


Figure 6. 3D image analysis steps in methodology 3.

Table 3. 3D analysis.

| | |
|---|---|
| Total VOI volume | 52.8 $mm^3$ |
| Object volume | 50.1 $mm^3$ |
| Number of closed pores | 23857 |
| Volume of closed pores | 2.58 $mm^3$ |
| Closed porosity | 4.90 % |
| Volume of open pore space | 0.12 $mm^3$ |
| Open porosity | 0.23 % |
| Total volume of pore space | 2.70 $mm^3$ |
| Total porosity | 5.11 % |

By adding the closed one-pixel boundary to the image, open pores are transformed into closed pores, increasing the open porosity. The remaining 'artificial' pores, located at the top- and bottom slices, can be removed by adding a slice on the top and bottom of the dataset.

Surface rendered 3D models can be created in between the analysis steps. These models can be loaded into CTVol and in this way a distinct visualization of the sample is possible. Figure 7 illustrates the difference between the two sandstone samples. Open pores are visualized in green and closed pores are colored red. The matrix of the sandstone has been made slightly transparent. For the first sample the open pores (green) are only present at the boundaries of the sample The 2nd sandstone sample shows the open porosity (green) is present throughout the sample, not just at the edges. Some closed pores (red) can be found inside the matrix of the sandstone.

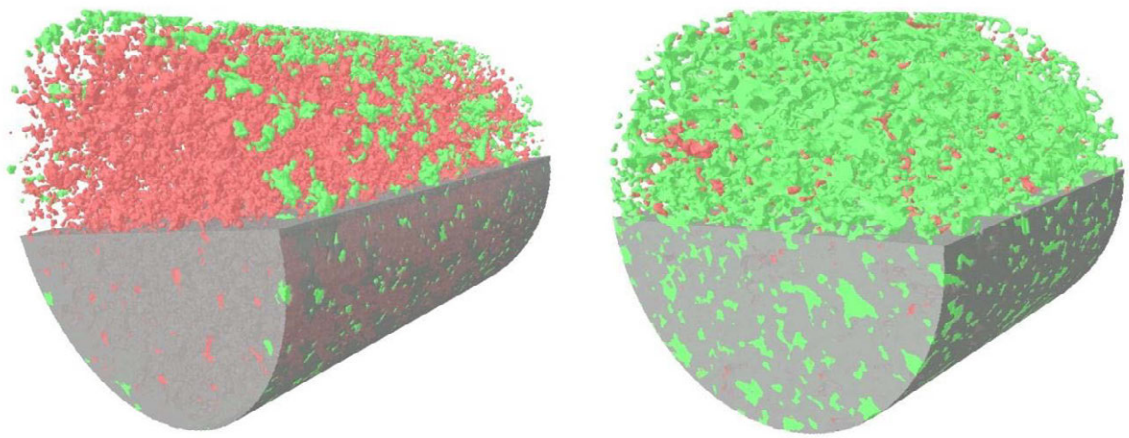

Figure7. 3D model of the 1st (left) and 2nd (right) sandstone sample.

## Conclusion

SkyScan Micro-CT is a useful tool to gather information on porosity networks, pore size, pore distribution,… In this work different methodologies to perform specific porosity analysis, have been explained by means of a demonstrative example. Additionally, 3D surface rendering using CTVol, proved to be a useful asset in order to visually interpret the data.

1st International Conference on 3D Materials Science
*Edited by: Marc De Graef, Henning Friis Poulsen, Alexis Lewis, Jeff Simmons, George Spanos*
***TMS (The Minerals, Metals & Materials Society), 2012***

# SEM-BASED ELECTRON TOMOGRAPHY OF TURFS COMPRISED OF LINEAL STRUCTURES

**O.M. Fakron[1], D.P. Field[1]**

[1]School of Mechanical and Materials Engineering, Washington State University, Pullman, Washington 99164-2920

## Abstract

In recent years, electron tomography (reconstruction of three-dimensional information from a tilt series of bright field images obtained in the TEM) has attracted the attention of electron microscopists and materials researchers. In this research the electron tomography technique has been extended to imaging loosely intertwined lineal structures from secondary electron images in the SEM. The expected application is to investigate the structure of carbon nanotube turfs before and after deformation. For imaging, the specimen was tilted from -10 to 60 degrees by one degree steps. Three dimensional images were reconstructed for a test sample of fine steel fibers by conventional electron tomography software. The technique is shown to be able to reasonably reconstruct the three dimensional features of the turfs and to extract features such as density and tortuosity.

## Introduction

Recent developments in nanostructures have brought to light exceptional electromagnetic, thermal, and optical properties of a class of nanostructures formed of disordered, intertwined, one-dimensional, structural units (nanowires, nanobelts, nanotubes) of carbon nanotubes, and GaN and SiO2 nano-wires, springs, and others. Such disordered assemblies are named turfs [1]. Applications include thermal switches, flat panel displays, hard disc drives, solar collectors, and chemical and biological sensors. Complete topological characterization of such structures requires either stochastic and stereological approaches [2], or three-dimensional imaging. Dual beam, SEM/FIB instruments have made remarkable progress in recent years and have enabled three-dimensional imaging of a multitude of structures. Because of the small scale of the nano-structured turfs and their relatively fragile nature, it is not possible to image these features using standard three-dimensional, parallel serial sectioning techniques. Even if the structures were somehow impregnated first with a polymer based space-filler, the morphology of the structures would be altered by the impregnation and subsequent ion beam milling required for imaging. Finally, simple imaging of stereo pairs, as is often done in the SEM to recreate the surface topography of a bulk specimen, cannot be performed with reasonable results on such specimens because the technique necessarily assumes a fully connected surface structure. A typical secondary electron image of a carbon nanotube turf obtained using a field emission SEM is shown in Figure 1. In recent years, electron tomography has enabled the three-dimensional characterization of features observed in TEM foils by tilting the specimens about an axis and reconstructing the 3-D images from a reduced tilt series [3].

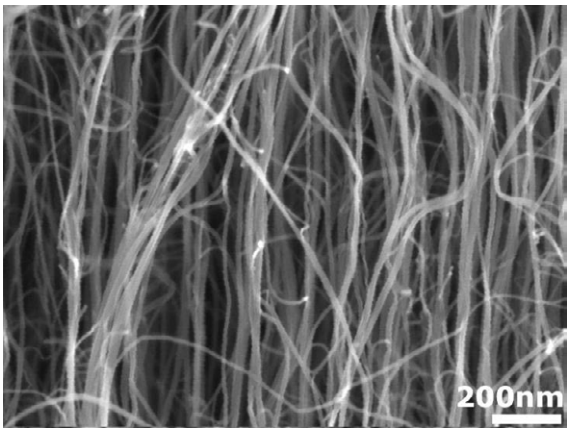


**Figure 1.** Typical SE image of a carbon nanotube turf structure [2].

In electron tomography there are three steps in obtaining three-dimensional images. First, data acquisition in obtaining a tilt series of images is required. The tilt series might consist of single axis tilt, dual axis tilt, or conical tilt. The second step is alignment and reconstruction of the images to construct the tomogram. Most alignment methods are cross-correlation using fiducial markers. There are also many methods for constructing the projected images such as the weighted back projection (WBP) method, the algebraic reconstruction technique (ART), and the simultaneous iterative reconstruction technique (SIRT). The final requirement is image enhancement that consists of two steps: de-noising and image filtering. After these methods are performed, the three dimensional model can be obtained [4].

The main target of this work is to develop a tool that can reconstruct three dimensional (3D) images from a tilt series of projected 2D SEM images and to get three dimensional data from the constructed images. EM3D is powerful software developed for use in standard TEM based tomography and is used in 3D image reconstruction and Chimera software will be used in 3D image visualizing and getting 3D data. Here in the technique is demonstrated using a steel wool sample. Characterization of the steel wool sample is demonstrated by finding tortuosity, tube diameter, and lineal density.

## Experimental Details

The procedure uses three steps: 1) take images by SEM, 2) construct a three dimensional image by EM3D electron tomography software [5] and 3) visualize the created three dimensional images. After obtaining the images the positions of the lineal features are identified in a semi-automated way, getting the (X,Y,Z) position at various locations along the feature. From the information obtained we determine fiber diameter and calculate the tortuosity of each fiber analyzed. It is also often possible from these data to fit an equation to each feature so that the structures may be included in mathematical models of structure evolution .We have adopted an approach that uses a single axis tilt series of images. The construction method is a filtered back projection algorithm. In an imaging system, the point-spread function describes the image of a single point as it results after using a perfect point as input to the system. An imaging system should be a combination of optical and digital systems. In this system the image of the object is created on a photographic plate or CCD camera. The image will then be transferred to the

computer by the digitizer, will be processed by the algorithms, and finally the processed images will be saved [6].

A series of seventy images were obtained over a range of 70 degrees about a single axis by taking a secondary electron image every one degree. Figure 2 shows representative images at tilting angles of -10° and 35°. The incomplete tilt series necessarily results in a lack of information in certain parts of the structure that are shaded by the features to the point that the back part of the feature is not viewed. For lineal structures such as those in steel wool and also in CNT turfs, the cross-section of the fiber can be considered to be circular and the mid-line of the feature is used to obtain measures of the path followed by each fiber. Using these rather reasonable assumptions, the complete 3D information of the structure can be obtained from the partial tilt series. The tilting angle range should be as high as possible to avoid a missing wedge effect on the reconstructed 3D image. In the ideal case the tilting range should be 360̊. In TEM tomography the tilting range of 360̊ provides a perfect 3D image. It is possible to have this range because the sample stage is able to rotate 360̊ [7]. In SEM tomography the tilting angle range is 180̊, but the maximum tilting angle range is 70 degrees. Because the sample stage can't rotate over a range of more than 70 degrees there is a missing wedge around 110̊ caused by the limitations of SEM tomography.

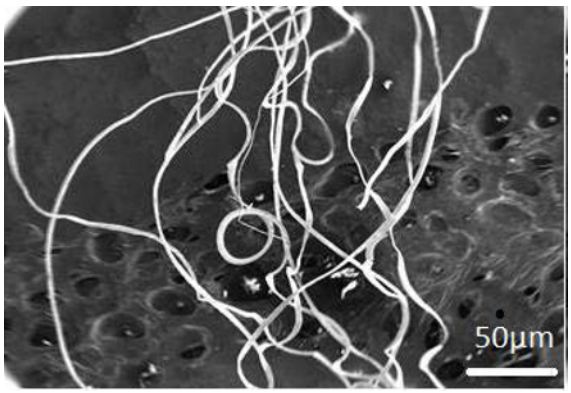


**Figure 2.** (a) Steel wool sample at tilting angle (-10)

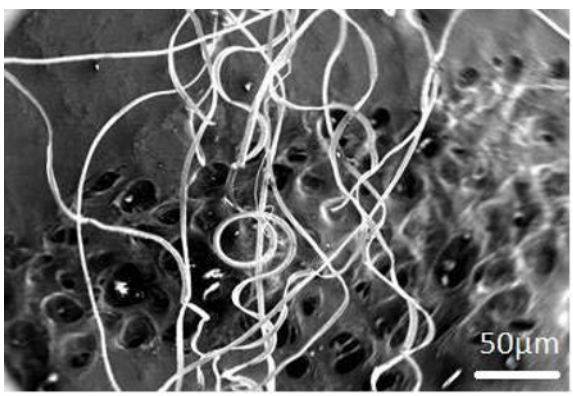


**Figure 2.** (b) Steel wool sample at tilting angle (35)

Three dimensional images were constructed from an imported series of projected 2D SEM images. Visualization software (Chimera) was used in visualizing the created three-dimensional images and in obtaining (X, Y, Z) coordinates of various points. Figure 3 shows a representative reconstructed 3D image of the steel fibers [8].

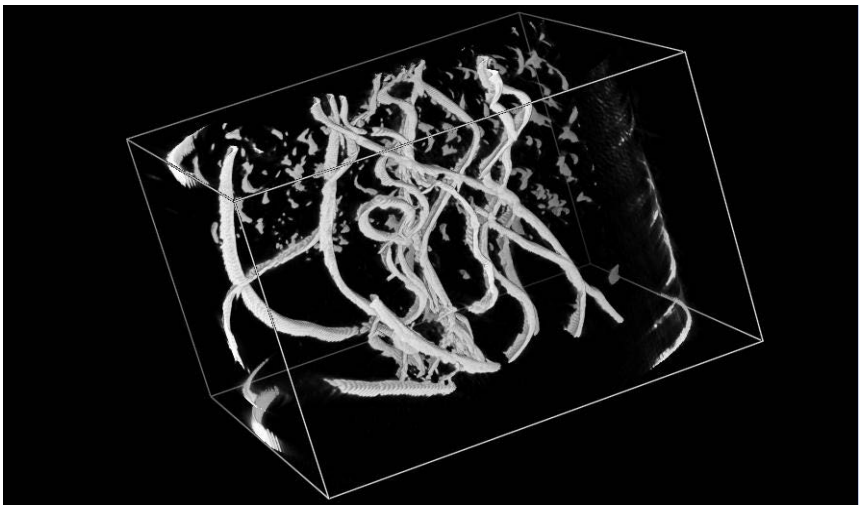

Figure 3. Projected image of the steel wool structure.

## Results and Analysis

Various features of the structure are potentially of interest. These include lineal density, fiber diameter distribution, and tortuosity. Each of these measures will have an influence on the mechanical response of the turfs. The fiber diameter distribution can be obtained from 2D images so the under-determined regions in the image have no consequence. In the present analysis tortuosity, $\tau$, is defined simply as the ratio of the total length along the curved fiber ($G$) versus the minimum point to point distance ($L$):

$$\tau = \frac{G}{L} \tag{1}$$

To measure the tortuosity of a given lineal feature, the length along the feature must be determined. This is done by using a semi-automated, point and click, procedure to indicate several points along a feature at which the coordinates in three-dimensions are identified. The length between each pair of points is summed up and divided by the shortest distance between the first and last point indicated along the feature. In the following example, there were 17 points identified along a given steel fiber in the steel wool sample. One definition of tortuosity is given by Eq. (1) and results in a value of 1.4 for the fiber analyzed in the present example (using the obtained data). .

The density of the structure can be determined by using the fiber diameter to obtain cross-sectional area and multiplying by the total length to find the volume of the features. This is

divided by the total volume analyzed to obtain a density. One definition of tortuosity is given by Eq. (1) and results in a value of 1.4 for the fiber analyzed in the present example. The density of the structure can be determined by using the fiber diameter to obtain cross-sectional area and multiplying by the total length to find the volume of the features. This is divided by the total volume analyzed to obtain a density.

To quantify the structure such that it can be used in models of structure evolution and mechanical response, each of the features discussed must be quantitatively determined and represented. One simple way of identifying the positions of all fibers is to represent them in some equation such as a cubic spline or polynomial fit. Matlab was used to fit the data from Table 1 to an equation to obtain a mathematical representation of the fiber. One equation that had a reasonable fit has the form:

$$z = a + b\sin(m\pi xy) + c\exp\left[-(wy)^2\right], \tag{2}$$

For the fiber analyzed, the coefficients were determined (with 95% confidence) as: $a$ = 43.89, $b$ = -0.398, $c$ = 0.9755, m = 0.5097, and $w$ = 0.2446.

## Summary

In this research the electron tomography technique has been extended for use on analysis of lineal structures in the SEM. The technique has three main steps, taking partial tilt series of images, reconstructing the projected images and obtaining the 3D images. From these images a wealth of information can be obtained in quantifying the character of the lineal features. This includes measurement of true tortuosity and local curvature as well as obtaining density and distributions of various additional measures. These can be used in tracking the evolution of the turf structures or in comparing against models of structure evolution.

## Acknowledgments

The authors are grateful for the assistance of Prof. Ian Robertson, Stephen House and Josh Kacher for some initial guidance in determining the best approach to this problem. We also acknowledge financial support of the CMMI division of the US National Science Foundation under grant number 0856436.

## References


1. C.M. Carter, R.F. Richards, S.Dj. Mesarovic, C.D. Richards, D.F. Bahr, C. McClain, J.Jiao *J. Mat. Sci*. 41 (2006) 7872-7878
2. H. Malik, K.J. Stephenson, D.F. Bahr, and D.P. Field, *J. Mat. Sci*. 46 (2011) (*doi: 10.1007/s10853-010-5192-y*)
3. L. Gan, (2008). "Electron Tomography: Methods for Three-Dimensional Visualization of Structures in the Cell," 2nd Edition. Edited by Joachim Frank." *MICROSCOPY AND MICROANALYSIS 14(4): 370-371.*
4. Paul A. Midgley and Rafal E. Dunin-Borkowsk Nature Materials 8, (2009) 271-280.
5. EM3D 2.0 Ress DB, Harlow ML, Schwarz M, Marshall RM, McMahan UJ (1999) "Automatic acquisition of fiducial markers and alignment of images in tilt series for electron tomography." *J Electron Microsc* (Tokyo) **48** (3): 277-87. PMID 10425746
6. Michael Radermacher. "Weighted Back-projection Methods", *Electron Tomography*, 2006.
7. Bánsági, Jr., T.; Steinbock, O., CHAOS **18**, 026102 (2008) 1-8.
8. UCSF Chimera—a visualization system for exploratory research and analysis. Pettersen EF, Goddard TD, Huang CC, Couch GS, Greenblatt DM, Meng EC, Ferrin TE. *J Comput Chem.* 2004 Oct;25(13):1605-12

# AUTHOR INDEX
# 1st International Conference on 3D Materials Science


## A
Adachi, Y. ..... 37
Adrien, J. ..... 61, 203
Ågren, J. ..... 221
Amato, K. ..... 73

## B
Barbuto, A. ..... 165
Barbuto, T. ..... 13
Bassman, L. ..... 189
Bernthaler, T. ..... 177
Blandin, J. ..... 203
Boller, E. ..... 203
Bongaers, E. ..... 227
Borgenstam, A. ..... 19
Bracarense, A. ..... 177

## C
Caceres, C. ..... 79
Callahan, P. ..... 195
Cao, S. ..... 125
Chapman, M. ..... 195
Chen, X. ..... 125
Croxall, S. ..... 215
Cutler, B. ..... 97

## D
Deal, A. ..... 13, 165
De Graef, M. ..... 147
Di Michiel, M. ..... 203
dos Santos, V. ..... 177

## E
Eden, T. ..... 43
Enomoto, M. ..... 107

## F
Fakron, O. ..... 233
Fang, M. ..... 85
Feng, N. ..... 91
Ferry, M. ..... 189
Field, D. ..... 233
Fife, J. ..... 131
Fontoura, S. ..... 183

## G
Gandin, C. ..... 67
Gant, A. ..... 25
Gaytan, S. ..... 73
Gee, M. ..... 25
Gholinia, A. ..... 19
Glicksman, M. ..... 97
Glowinski, K. ..... 119
Godfrey, A. ..... 31
Golay, D. ..... 189
Grandhi, R. ..... 49
Green, N. ..... 131
Griffiths, W. ..... 131
Groeber, M. ..... 49, 113, 195

## H
Hagström, J. ..... 19
Hanlon, T. ..... 13, 165
Hardy, M. ..... 215
Hedström, P. ..... 19, 221
Henein, H. ..... 67
Herlach, D. ..... 67
Hernandez, J. ..... 73
Huang, Y. ..... 13, 165

## I
Ikeda, T. ..... 125
Ilbagi, A. ..... 67

## J
James, R. ..... 125
Jensen, D. ..... 1
Jiang, Y. ..... 85, 91
Jones, H. ..... 25
Juul Jensen, D. ..... 31

## K
Kacher, J. ..... 209
Karlsson, O. ..... 19
Keller, T. ..... 97
Khatibi, P. Delshad ..... 67

## L
Laflen, B. ..... 13, 165
Lewis, D. ..... 97
Lhuissier, P. ..... 203
Li, D. ..... 171
Liu, G. ..... 209
Loughnane, G. ..... 49
Lu, S. ..... 85

## M
MacDonald, N. ..... 31
Maire, E. ..... 61, 203
Martinez, E. ..... 73
Mauricio, M. ..... 177, 183
McMahon, C. ..... 189
Medina, F. ..... 73
Midgley, P. ..... 215
Mingard, K. ..... 25
Monteiro, M. ..... 177
Morawiec, A. ..... 119
Murr, L. ..... 73

## N
Nagasekhar, A. ..... 79
Nakayama, M. ..... 37
Neal, B. ..... 137

## O

Odqvist, J. ..... 221
Oikawa, T. ..... 107
Ojima, M. ..... 37

## P

Paciornik, S. ..... 177, 183
Pessoa, E. ..... 177
Pilotto, D. ..... 183
Prill, T. ..... 159
Pushkareva, M. ..... 61

## Q

Quadir, Z. ..... 189

## R

Ramirez, D. ..... 73
Redenbach, C. ..... 153
Riley, M. ..... 49
Robertson, I. ..... 209
Rowenhorst, D. ..... 13
Ru, H. ..... 85
Russ, J. ..... 137
Ryu, S. ..... 171

## S

Salvo, L. ..... 203
Sato, N. ..... 37
Scheel, M. ..... 203
Schladitz, K. ..... 153, 159
Schreiber, J. ..... 43
Schryvers, D. ..... 125
Schuren, J. ..... 113
Scott, M. ..... 195
Selleby, M. ..... 221
Shade, P. ..... 113
Shah, M. ..... 49, 195
Shindo, P. ..... 73
Shiveley, A. ..... 195
Simmons, J. ..... 147
Smid, I. ..... 43
Snyder, J. ..... 125
Soe, B. ..... 189
Spinelli, I. ..... 13, 165
Spowart, J. ..... 195
Srinivasan, R. ..... 49
Srivastava, V. ..... 125
Stone, H. ..... 215
Stormvinter, A. ..... 19
Suery, M. ..... 203

## T

Thuvander, M. ..... 221
Turner, T. ..... 113

## U

Uchic, M. ..... 49, 195

## V

van den Bosch, R. ..... 227
Vecchio, I. ..... 153

## W

Waggoner, J. ..... 147
Wang, S. ..... 147
Wang, Y. ..... 37
Weck, A. ..... 61
Wicker, R. ..... 73
Wieser, C. ..... 159
Winiarski, B. ..... 19
Withers, P. ..... 19

## X

Xiong, W. ..... 221

## Y

Yu, L. ..... 85, 91
Yue, Y. ..... 131

## Z

Zhang, B. ..... 79
Zhang, Y. ..... 31
Zhou, J. ..... 221

# SUBJECT INDEX
# 1st International Conference on 3D Materials Science


## 3
3D ..... 215
3D Characterization ..... 49
3D EBSD ..... 189
3D Image Analysis ..... 153
3D Microscopy ..... 195
3D Microstructures ..... 73
3D Techniques ..... 1
3D Visualization ..... 227
3DXRD ..... 1

## A
Abrasion Simulation ..... 25
Al Alloys ..... 131
Alignment ..... 165
Aluminum ..... 31
ANSYS ..... 91
Appearance ..... 147
Atmozation ..... 67
Atom Probe Tomography ..... 221

## B
Bending-dominated Behavior ..... 79
Boolean Model ..... 159

## C
Carbide ..... 107
Carbon Steels ..... 19
Carbonate Rocks ..... 183
Challenges For 3D Science ..... 1
Compatibility ..... 125
Continuous Tomography ..... 203
Cooling Schedule ..... 171
Correlation ..... 171
Cracks ..... 177
Crystal-Plasticity ..... 113

## D
Damage Evolution ..... 203
Differential Geometry ..... 37
Digital Microscopy ..... 183
Dislocations ..... 209
Dual-phase Steel ..... 37

## E
EBSD ..... 165, 195
EDS ..... 195
Electron and Laser Beam Melting ..... 73
Electron Backscatter Diffraction ..... 189
Electron Tomography ..... 209
Entrainment Defects ..... 131

## F
Fast Multiscale Clustering ..... 189
FIB Tomography ..... 159
FIB-SEM ..... 25, 215
Finite Element Analysis ..... 43
Finite Elements ..... 113
Focused-ion-beam ..... 125
Fracture ..... 61
Fragmentation ..... 43
Fully Automated Serial-sectioning Microscope ..... 37

## G
Geological Materials ..... 227
Geometric Characterization ..... 119
Geometric Model ..... 153
Grain Boundary ..... 31, 119
Grain Boundary Deformation ..... 113
Grain Growth ..... 107
Grain Size ..... 49
Graph Cut ..... 147

## H
Harmonic Analysis ..... 137

## I
In Situ ..... 203
In-situ Tensile Test ..... 61
Innovation Cathode Cell ..... 91
Interface ..... 119
Intermetallic Network Microstructure ..... 79
Invariant Moments ..... 137
Iron Alloy ..... 107

## J
Johnson-Cook ..... 43

## L
Lorentz Force ..... 91
Low Angle Boundaries ..... 189

## M
Machine Vision ..... 137
Macroscopic Boundary Parameters ..... 119
Magnesium Alloys ..... 79
Martensite ..... 19
Materials Microstructures ..... 159
Metals and Alloys ..... 73
Micro-computed Tomography ..... 227
Micro-tribology ..... 25
Micro-truss Lattice ..... 79
Microbands ..... 189
Micromechanical Properties ..... 85
Microstructure ..... 49, 227
Microstructure Reconstruction ..... 171
Microtomography ..... 67
Monte-Carlo Simulation ..... 159

## P
Pearlite ..... 37
Phase Separation ..... 221
Phase-field Modeling ..... 221
Pinning Effects ..... 107
Plasticity ..... 43
Polymer Foam ..... 153
Porosity ..... 177, 183, 227
Precipitates ..... 125
Propagation ..... 147

Protrusion/retrusion ..... 31

# Q

Quantitative Analysis ..... 159

# R

Random Closed Set ..... 153
Recrystallization ..... 1, 31
Rocks ..... 227

# S

Scanning Electron Microscopy ..... 159
Segmentation ..... 147, 189
Serial Sectioning ..... 19, 49, 195, 215
Shape ..... 147
Shape Classification ..... 137
Shape Descriptors ..... 137
SiC/Fe-20Cr Co-continuous Composites ..... 85
Simulated Annealing ..... 171
Slice-and-view ..... 125
Solidwork Simulation ..... 85
Sphere Packing ..... 153
Stochastic Process ..... 171
Stretch-dominated Behavior ..... 79
Success of 3D Science ..... 1
Superalloy ..... 215

# T

Three-dimensional Microstructure ..... 19
Tomography ..... 233
Topology ..... 37, 147
Transmission Electron Microscopy ..... 209

# U

Undercooling ..... 67
Underwater Weld ..... 177

# V

Void Growth ..... 61

# W

WC/Co Hardmetals ..... 25
Weighted Voronoi Tessellation ..... 153
Widmanstatten ..... 125

# X

X-ray Microtomography ..... 183
X-ray Tomographic Microscopy ..... 131
X-ray Tomography ..... 61

# µ

µCT ..... 177